GEOINFORMATICS FOR TERRAIN CHANGE STUDIES IN TECTONICALLY ACTIVE KUTCH REGION, INDIA

Ph.D. THESIS

by

SUMAN SOURAV BARAL

DEPARTMENT OF EARTH SCIENCES
INDIAN INSTITUTE OF TECHNOLOGY ROORKEE
ROORKEE-247 667 (INDIA)
JULY, 2017

GEOINFORMATICS FOR TERRAIN CHANGE STUDIES IN TECTONICALLY ACTIVE KUTCH REGION, INDIA

A THESIS

Submitted in partial fulfilment of the requirements for the award of the degree

of

DOCTOR OF PHILOSOPHY

in

EARTH SCIENCES

by

SUMAN SOURAV BARAL

DEPARTMENT OF EARTH SCIENCES
INDIAN INSTITUTE OF TECHNOLOGY ROORKEE
ROORKEE-247 667 (INDIA)
JULY, 2017

INDIAN INSTITUTE OF TECHNOLOGY ROORKEE
ROORKEE

CANDIDATE'S DECLARATION

I hereby certify that the work which is being presented in this thesis entitled "**GEOINFORMATICS FOR TERRAIN CHANGE STUDIES IN TECTONICALLY ACTIVE KUTCH REGION, INDIA**" in partial fulfilment of the requirements for the award of the Degree of Doctor of Philosophy and submitted in the Department of Earth Sciences of the Indian Institute of Technology Roorkee, Roorkee is an authentic record of my own work carried out during the period from December, 2011 to July, 2017 under the supervision of Dr. Arun K. Saraf, Professor, Department of Earth Sciences and Dr. Josodhir Das, Associate Professor, Department of Earthquake Engineering, Indian Institute of Technology Roorkee, Roorkee.

The matter presented in the thesis has not been submitted by me for the award of any other degree of this or any other Institute.

(SUMAN SOURAV BARAL)

This is to certify that the above statement made by the candidate is correct to the best of our knowledge.

(Arun K. Saraf)
Supervisor

(Josodhir Das)
Supervisor

Date:

Abstract

Naturally occurring events such as earthquake causes impulsive deformations inside the earth as well as on the surface. Measurement of deformation rate on ground is a tedious job as it would require meticulous detailed observations within short time involving lot of sophisticated instrumentation and manpower. However, microwave (RADAR) remote sensing technique endowed with special capability of all time and weather condition imaging and measuring the distance of object (on earth surface) from the satellite. This microwave technique, where Synthetic Aperture Radar (SAR) images are used to quantify the extent of ground deformations, is known as Interferometric Synthetic Aperture Radar (InSAR or IfSAR) and Persistent Scatterer Interferometry (PSI). PSI is a radar-based technique that belongs to the group of differential SAR image interpretation.

Land deformation studies based on InSAR has been in practice, however, in only 2000 the Permanent Scatterer Interferometry (PSI) technique was first developed by a research team at the Politecnico di Milano (POLIMI), Italy. The principal aim of this development was to overcome the limitation of temporal and geometrical decorrelation of synthetic aperture radar (SAR) interferometry. Though geodetic observations, such as aseismic and co-seismic InSAR studies, have provided important insights into the earthquake deformation cycle for inter plate regions for different parts of the world, however prior to this work little post seismic intra plate tectonic deformation observations have been made by researchers for Kutch region, India. The present study intends to provide an improved understanding of the earthquake deformation cycle for the unstable continental plate region of Kutch rift basin.

This study is the systematic effort, using satellite based InSAR, PSI, multispectral image, digital elevation models supported by topographical, geological, tectonic and earthquake information to observe and interpret surface deformation associated with tectonic processes for the Kutch rift basin India. The work is motivated by the relatively incomplete understanding of the post-seismic ground changes due to the occurrence of large intensity, damaging, earthquake in Bhuj on 26th January 2001 as well as subsequent earthquakes and earlier tectonically affected geological set up.

The landscape of Kutch is one of the most unique examples of tectonically active intraplate region enduring rift reversal. Since geological time, the basin has never attained

stability and is continuously subjected to many phases of tectonic deformations. In an active tectonic belts the potentially seismogenic zones are indicated by major faults. These faults bear certain geomorphic signatures which can explain the origin, stress condition and geometry of the fault and therefore survey across active faults can reveal idea about paleo-seismic events.

The devastating earthquake of magnitude 7.7Ms (IMD) / 7.7Mw (USGS) that struck Bhuj on January 26, 2001 is an example of such seismic activity. As per report, the event had caused maximum uplift of approximately 1.57±5 meters near the epicenter. Widespread liquefaction and corresponding deformations were reported in the epicentral area around Bhuj and Bhachau city after the earthquake. The Rann of Kutch earthquake of 1819 was the severest in the region which caused visible faulting on the earth surface and created a high mound. This earthquake was followed by a large number of aftershocks which continued for nearly eight years.

By means of morphometric analysis, realistic synthetic two-pass InSAR and PSI technique the region has been carefully examined for neotectonic activity aided by generation of suitable time series interferograms from SAR image pairs for Kutch area. As reported by Institute of Seismological Research (ISR), Gujarat, the small scale deformation distributed in the Kutch rift basin are some of the least investigated using InSAR and the present study demonstrates the capability of the technique to provide important observations on small-magnitude post-seismic events. Ground deformation (change) is expressed in terms of negative i.e. ground has moved towards satellite and positive i.e. ground has moved away from the satellite in the line-of-sight direction (LOS). The multi-year time-series of descending InSAR data from the Envisat, ALOS-PALSAR and Sentinel 1-A satellite are used and inter-seismic ground deformation which is estimated in the Kutch region is up to ±15 to 30 mm/yr in the satellite-to-target line-of-sight direction.

Initially a series of interferogram produced from Envisat and ALOS-PALSAR satellites images for a time period of 2003 to 2010 are used to investigate long-term surface deformation processes for the Kutch, India. A deformation pattern could be detected across the Kutch mainland, Island area and the KBF and KMF associated areas to the South of Banni plains in the Central Kutch basin. Further the geomorphic study of the different basin suggests expected neotectonic activity along with presence of numerous faults as observed from optical and

microwave images. The estimated deformation may be occurring consistently with the marked faults. In this study InSAR and PSI datasets (one pair ALOS PALSAR, four pair Envisat ASAR, three pair Sentinel 1-A and eleven scenes of Sentinel 1-A) have been utilized to analyse the nature of ground deformation in the Kutch region.

The ALOS-PALSAR data pair of years 2007 and 2010 have been analysed for the area bounded by Kutch Mainland Fault (KMF) and Katrol Bhuj Fault (KBF) supposed to have going through relaxation phase of a stressed crustal layer. Three different regions in the study area illustrated countable significant fringes, indicating different amount of positive and negative ground deformations (-35cm, -35cm and 24cm) to the north and east of Bhuj city. The two interferogram images generated from Envisat dataset between 2003-05 indicate an episodic ground change followed by a negative and positive ground deformations. The interferogram derived from 2003-05 pair indicates resultant subsidence in the mentioned area along with a positive prominent change (subsidence) on ground to the NE, NW and south of Bhuj. Further deformation map generated followed by interferogram images from 2003 and 2005 Envisat data pair deciphers a positive ground deformation up to 17 cm in and around the Bhuj region covering mostly the Mainland region of Kutch basin. Elevation profile along the locations of deformation are drawn for SRTM (2000) and ALOS PALSAR (2007) DEM. Further an elevation difference is calculated employing change detection technique for the Bhuj area between the two DEMs, indicating a relative elevation variation between 2000 and 2007 for Bhuj.

The interferograms generated from Sentinel 1-A data pairs showed a small scale ground deformation. In order to study more precisely the PSI technique has been deployed to observe the terrain change over one year period. The interferogram generated from Sentinel 1-A data pair reveals a positive deformation of about 18 mm, followed by a small scale ground deformation up to mm scale around Bhuj, in the upper mainland, along KMF, KBF fault zones and along the IBF in Khadir mound and along the major lineament cross cutting the KMF, east to the Khadir uplift. In order to compute rate of terrain change over the last few years, persistent scattering technique has been employed for central Kutch region covering Bhuj area. The PSI study reveals a negative ground displacement of 20 to 30 mm per year in the W and NW of Bhuj city to the east of Mainland along the LOS. A subsidence rate of 25-30 mm is observed in the south and east of the Anjar city from the PSI study. The Interferogram

generated based on the Envisat and Sentinel 1-A data exhibits ground deformations in the area in and around KMF and KHF. Further, as per ISR report these two faults were mapped as active.

Morphometric analysis is the quantitative assessment of form features of the earth surface and any landform unit. Tectonic features such as dislocation and displacement of mountain ridges, valleys, clearly recognisable lineaments, and drainage offsets have been identified in the Landsat true colour composite image. Also, the morphometric analysis and shaded relief models (SRMs) created from DEM, further substantiates the presence of faults. In this study the geomorphic evidences of active faults were also inferred.

A significant offset is observed to the West along KBF; a major offset in drainages is observed and marked to the extreme WWS along KBF. Another series of 3 offsets have been identified to the south of KBF roughly parallel to each other. A displacement of intertrappean beds and some other sedimentary rocks is observed to the south of KBF. A lineament is marked along the KBF having step like fashion (en-echelon). Two prominent ridge displacements are witnessed at the extreme north of KBF, which concludes the presence of fault. Further two other sets of ridge displacements are observed at the extreme NW of Kutch basin. The faults have been identified and marked on both the Landsat true colour image and Sentinel 1-A power image from which the DEM is also derived to infer the existence of faults on hillshade and aspect map. Further the faults are marked for the eight locations on a three dimensional prospective view obtained by draping high resolution Digital Globe image over the ALOS PALSAR 12.5m resolution DEM.

Hypsometric curves have been obtained for the associated drainage basins from SRTM-DEM for the eight locations where the faults have been identified. The stream length index found to be highest for two locations. The basin asymmetry factor (AF) shows a proportioned tilting towards east and west controlled by the marked fault at three locations. The Basin shape index (Bs) for three locations indicates nearly circular shape basins due to lower tectonic activity.

Finally, the present study concludes that InSAR, PSI, morphotectonic and morphometric study can make a useful contribution towards better understanding of earthquake induced effects and seismic hazard in the Kutch region, India.

Acknowledgement

First of all my eternal bow in reverence and gratitude is to **"Almighty God"** whose gracious blessing enabled me to complete my work in time. Words cannot express the depth of my gratitude for all those who directly or indirectly helped me in my endeavour.

I wish to take this opportunity to express my heartfelt deep sense of gratitude to my supervisor, **Prof. Arun Kumar Saraf**, Earth Sciences Department, IIT, Roorkee for his constant, and benevolent guidance, sustained encouragement, unlimited patience, endless advices, keen interest, judicious planning of the project, and the continual support that inspired and fuelled my research engine over the year and made me to bring this work to a successful completion. Words seem inadequate to articulate my indebtness to him for moulding me with the cologne of strong scientific lust. I am very much grateful to him for his appreciation, suggestions and constructive criticism. His overly enthusiasm, integral view on research has made an everlasting impression on me. It is matter of pride to get a unique opportunity of working with an affectionate, courageous and great professor.

I would like to express my profound gratitude to my supervisor, **Dr. Josodhir Das** for his erudite guidance and productive criticism during the tenure of my research work. Professional expertise, open discussions and constant unflinching support rendered by **Das Sir** have shaped this thesis to its present form. I'm immensely thankful to him for his patience, motivation, enthusiasm, and immense knowledge. He spared his valuable time in monitoring the work progress and providing useful tips, critical comments and precious suggestions from time to time. I could not have imagined having a better advisor and mentor for my Ph.D study.

I would like to thank the Heads of the Department of Earth Sciences, IIT Roorkee, during the tenure of my research, namely: **Prof. P. K. Gupta**, **Prof. A. K. Saraf** and **Prof. D. C. Srivastava** for their academic help and encouragement.

I express my sincere thanks, to all faculty members and Staff of Earth Sciences Department for their co-operation and support. Especially, I would like to acknowledge **Dr. S.P. Pradhan**, for his moral support and extending a helping hand throughout my research work.

I wish to sincerely acknowledgement the continuous financial support by **Council for Scientific and Industrial Research** (CSIR) and Ministry of **Human Resources and**

Development (MHRD), New Delhi supporting me as **Research fellow** without which it would have become difficult to take up this work.

I convey my heartfelt and esteemed sense of gratitude for **Mrinmoy Da**, **Kanika Mam**, **Gaurav** and **Sushant** for their helping hand during my period of research work. I am also grateful to **Zia, Eirin** for their immense help and cooperation at each and every step of my research. I extend my deep sense of appreciation to my loving juniors **Arun, Ajit, Debasmita, Pratap** and others for their respect, affection, and wholehearted cooperation and for keeping my morale high.

I would like to thank **Nair Ji**, **Mohd. Aslam Ji** and **Rakesh Ji** for their open-hearted support and administrative help during the course of my stay at Roorkee. A special place holds for (Late **Rahil Ji**). His constant round the clock lab support and tea-breaks will always be part of my fond memories.

It's my fortune to gratefully acknowledge the support of one special person **JeJe Babu** for his constant motivation, guidance and also been the inspiration in this journey.

I feel a sense of unique pleasure to pen down my feelings for my loving **Baba, Bou, Bapa and Maa** whose ineffable love, selfless sacrifice, moral support, loving inspiration and faith in me, has always made things simpler and life more worthy to live.

I am truly thankful to the almighty for having **Bhai, Bhauja, Chhua Bhai, Maman Apa, Bubun, Lulu and Mama** for their affectionate supports and encouragements.

Last but not the least I would like to express my heartfelt thanks to my beloved wife **Samiksha** for her selfless love, sacrifice, moral support and encouragement in every phase of life. Without her help and co-operation I would never have reached this mile-stone.

Last but not the least I thank all those who have helped me directly or indirectly at various stages of this work.

Thank you all...

Thank you God

(Suman Sourav Baral)

Table of Contents

List of Figures

enlarged aspect map of location ‘f’ showing the effect of fault

List of Tables

ABBREVIATIONS

Sr. No.	Abbreviation	Full Form
1	ADORE	Automated DORIS Environment
2	ALOS	Advanced Land Observation Satellite
3	ASAR	Advanced Synthetic Aperture Radar
4	ASC	Amateur Seismic Centre
5	ASTER	Advanced Spaceborne Thermal Emission and Reflection Radiometer
6	BIS	Bureau of Indian Standards
7	CYM	Cyan-Yellow-Magenta
8	DEM	Digital Elevation Model
9	DInSAR	Radar Differential interferometry
10	DORIS	Delft Object-oriented Radar Interferometric Software
11	ENVISAT	Environmental Satellite
12	ESA	European Space Agency
13	ESRI	Environmental Science Research Institute
14	ETM	Enhanced Thematic-Mapper
15	FCC	False Colour Composite
16	GIS	Geographic Information Systems
17	GPS	Global positioning system
18	GSI	Geological Survey of India
19	HC	Hypsometric Curve
20	IMD	Indian Meteorological Department
21	InSAR	Interferometric Synthetic Aperture Radar
22	ISR	Institute of Seismological Research
23	JAXA	Japan Aerospace EXploration Agency
24	KMF	Kutch Mainland Fault
25	LISS	Linear Imaging Self Scanning Sensor
26	MM	Modified Mercalli
27	PALSAR	Phased Array type L-band Synthetic Aperture Radar
28	PSI	Persistent Scatterer Interferometry
29	RADAR	Radio Detection and Ranging
30	RAR	Real Aperture Radar
31	SAR	Synthetic Aperture Radar
32	SEISAT	Seismotectonic Atlas of India and its Environs
33	SLC	Single Look Complex
34	SRM	Shaded Relief Model
35	SRTM	Shuttle RADAR Topographic mission
36	USGS	United States Geological Survey

Chapter 1

Introduction

1.1 Preamble

The ever developing techniques of remote sensing have the prospective to contribute and support human research in assessing natural processes and events occurring frequently on the earth's surface. Remote sensing provides synoptic and repetitive coverage, unbiased recording of earth's surface and events, cost effective technique, takes very less time and produces multi-spectral data. Geographic Information Systems (GIS) provides proficient analysis of natural hazard effects, tracing emergency areas, assisting in rehabilitations etc. Apart from identifying damaged areas, remote sensing also allows monitoring of the earth on a real time basis for impending signs of a disaster (Gupta, 2000; Tronin, 1996 and 2006). The earth's changes in topography can unfold many unidentified natural processes related with earthquakes happening due to tectonic/fault movements. Any deformation occurring on the land surface in a tectonically active region can be observed regularly that might be a manifestation of earthquakes.

As earthquake studies have improved progressively, remote sensing has become an integral part of earthquake disaster management. Till now, some major factors like non-availability of good resolution data for the damaged area, cost of high resolution data, temporal resolution (revisit cycle of a satellite), lack of knowledge in this field viz., complexity of the phenomenon called 'earthquake' were the hindrances to such studies.

Among all natural phenomena, earthquakes are possibly the most devastating one and remained a captivating part of research interest for the scientists. An earthquake is a sudden movement in the earth, caused by the immediate release of strain that has accumulated over a long time. This transient natural force has created havocs in history of mankind, destructing life, economy, property, thus pausing the development of the earthquake struck region for a long time. Most of the earthquakes initiate at plate boundaries, where the plates of the earth's crust (called lithospheric plates) are converging, diverging or sliding past one another, Sometimes few earthquakes also originate due to volcanism etc. The most powerful earthquakes are associated with plate boundaries and plate subduction zones are responsible for more than half of the world's seismic events.

Now, remote sensing is the most widely used technique to study natural and Earth's surface processes. In this field, we can utilize two or more data sources together to get more environmental information rather than extracting from separate data sources individually (Cracknell, 1997, 1998). Several researchers (Jasrotia, *et al*., 2007; Krishna, 1996, 2005; Mansor, *et al*., 1994; Pati, 2005; Pati *et al*., 2008; Pirasteh *et al*. 2009 and 2010; Tripathi, *et al*., 2000; Tripathi & Singh, 2000; Chaudhary & Aggarwal, 2009; Maiti & Bhattacharya, 2009) have been using remote sensing techniques and GIS for various studies worldwide. Sensors on-board satellites having sensing abilities in different bands of electromagnetic spectrum permit the user to interpret various earth objects and physical phenomena with more accuracy and reliability. Earthquake studies using different remote sensing techniques have found many directions and have proven its utility in different realms of life and property. In disaster management, optical remote sensing has been widely used. High spatial resolution remote sensing data provide very minute observation of the affected region which helps the rescuer to plan and reach to the affected people in a very effective manner. However microwave remote sensing [Interferometric Synthetic Aperture Radar (InSAR)] is undoubtedly most noble remote sensing application in earthquake studies. The InSAR based deformation studies are useful in determining the deformation suffered by the part of earth during an earthquake event, which may be attributed as aseismic, co-seismic and post-seismic events.

1.2 Remote Sensing in Earthquake Studies

The systematic and synoptic Earth observation was provided by the remote sensing technology. Applications of remote sensing technology have different characteristics like synoptic view, unbiased multispectral recordings, continual observations etc. which compensate the insufficiency in earthquake stations on the ground and develop present system of earthquake monitoring and forecasting (Ziqi *et al*., 2001). Earthquake is a dynamic process and finally the stress-strain process results into a shock (so called earthquake sequence), which initiates a few days or weeks before the main shock and continues many days after it as aftershocks (Hayakawa *et al*., 2000). Generally it causes deformation of earth's crust, terrain slope failures and alteration of physical-chemical characteristics in stress affected region and neighbouring areas, before or during the earthquake. These types of alterations lead to the release of several types of energy disturbing earth's surface and atmosphere i.e. thermal precursors, ionic clustering in the atmosphere etc.

In hilly and rugged terrain one of the prominent affects due to an earthquake is landslide occurrences. An earthquake of higher magnitude triggers extensive landslides creating

extremely hazardous conditions to road/rail network and habitations. There are several examples of river obstruction due to landslide. Remote sensing technique can be utilized efficiently and effectively to study and monitoring the landslides.

One of the most severe geological hazards is earthquake, due to which the socio-economic conditions of many countries in the world have been threatened and influenced by causing intense damages and casualties (Jasrotia 2007; Mansor *et al*., 2007; Tripathi & Soomro, 2007; Pirasteh *et al*., 2008). In natural sciences, the observation of the Earth from the space has found many utilities, but it is only in the last decades that technological advances have been made, which is also extended to land deformation and liquefaction studies (Canuti *et al*., 2004; Ferretti *et al*., 2001; Ferretti *et al*., 2011; Hong *et al*., 2007; Martha *et al*., 2010; Mantovani *et al*., 1996; Massonnet & Feigl, 1998; Scaioni *et al*., 2014; Singhroy, 1995; van Westen *et al*., 2008). Massonnet *et al*., (1994) first established the utility of SAR differential Interferometer technique in surveying 28 June 1992 Landers (Mw 7.3) earthquake's co-seismic displacement. Satellite based InSAR technology prospered in the 1990's. It is based on the base line interferometer and phase information, has many advantages in crust's vertical displacement measurement (Ziqi *et al*., 2001). Radar Differential interferometry (DInSAR) and Persistent Scatterer Interferometry (PSI) technique, due to its high sensitivity to dynamic transformation, high spatial along with spectral resolution and wide covering area has advantage over InSAR. The precision of generated interferometric pattern was improved by eliminating topographic phase from earthquake interferogram (Zebker *et al*., 1994). This post-seismic research has aroused the 'geophysicists' interest widely. Now a day Envisat, ERS-2, RADARSAT, Sentinel-1A, ALOS-PALSAR2, JERS-1 etc. satellites offer large numbers of original data for DInSAR and PSI research. The Differential Interferometry Synthetic Aperture Radar (DinSAR) technique was used to detect ground deformation after the Sichuan earthquake (Stramondo *et al.,* 2008). DInSAR has been well recognised as a remote sensing technique to measure land displacement because of the resolution and accuracy provided by the technique (Stramondo *et al*., 2006, Bayuaji *et al*., 2010). Further advantage of DInSAR is that the method allows the study in large areas that are inaccessible by means of ground-based observation methods, such as the application of global positioning systems (GPSs) and leveling measurements (Raucoules *et al*., 2007).

In 2000 the Permanent Scatterer (PSI) technique was first developed by a research team at the Politecnico di Milano (POLIMI), Italy. The principal aim of this development was to overcome the limitation of temporal and geometrical decorrelation of synthetic aperture radar

(SAR) interferometry. At the same time, this new technology also overcomes the limitation of atmospheric effects, which can significantly degrade the accuracy of the interferometric results (Ferretti *et al*., 2000, Ferretti *et al*., 2001). The spatial density of PS is much higher than the grids that are produced by the traditional point based methods, like levelling surveying and Global Positioning System (GPS) technology. This implies that the PS technique can be used as an operational tool to measure ground deformation with a high accuracy and a high spatial PS grid density. Meanwhile, a number of modified techniques are developed to further improve the PS technique.

1.3 Morphotectonics and Morphometry

Morphotectonics describes the study of short and long-term surficial evidences of tectonic activity. The earth's asthenosphere of endogenous mechanism resulting out of the tectonic activity is always characterized by relative movements such as uplifting, subsidence and translation of the parts of the crust. The continuous weathering and erosion process leads to formation of landforms manifesting the control of tectonics. Morphotectonics is the combination of geometry and tectonic activity to describe landforms primarily at continental, sub-continental as well as local scales, whereas structural geomorphology deliberates the passive influence of geological structure on landforms. Morphotectonics bring out the influence of earth movements on landform evolution. It comprises of the study of origin of mountains, drainage patterns, erosion surfaces, and sediments on land and offshore. These types of existing and newly developed morphotectonic features can be examined by using geoinformatics comprising multi-sensor images, topographic maps, field data, multi-date remotely sensed data, DEMs, GIS, visual interpretation and advanced digital image processing techniques.

In tectonically active regions, significant topographical change can be directly observed from direct field observation. However, the regions where rate of tectonism is mild or very slow can be well studied by analysing the morphometric indices. Streams and drainages are able to record even negligible tectonic deformation. Tectonic activities are often demonstrated by characteristic geomorphological attributes such as linear valleys, erosional surfaces, slope-breaks, ridgelines, regional anisotropy and tilt of terrain. Analysis of optical and microwave remote sensing data sets with the derived digital elevation models by means of numerical geomorphology, gives a means for recognizing fractures, faults and characterizing the tectonics of an area in a quantitative way. Morphometric parameters like drainage basin asymmetry, river sinuosity, slope gradient index, hypsometry, stream length gradient index etc. are key indicators of neotectonic activities prevailing in a region.

1.4 Concept of Morphotectonic Analysis

The relationship between geomorphology and tectonics is the base to understand the landscape evolution for the morphotectonic study. The associated tectonic features can be well studied by the interpretation of various surface expressions. These observations compare the morphological structure of geomorphic markers such as drainage systems, courses of river, volcanic landscapes and mass movements with joint orientations along with fault movements. These are the major indicators of neotectonic changes.

Remote sensing can be a very useful tool in the evaluation of various morphotectonic parameters. A synoptic view is provided by the satellite images and capable of producing information regarding the areas which are inaccessible and unreachable during field surveys due to topographic factors, climatic factors and dense vegetation. Availability of high resolution satellite images presenting even different minor topographies; distinctly give opportunity to look into details of occurred modification if any. On the basis of image interpretation elements such as tone, texture, pattern, shape, size etc., and geotechnical elements such as vegetation, land use, land cover, drainage etc., meaningful interpretation of satellite images can be done. Remote sensing technique provides us different data product and implementing GIS techniques makes it extremely effective. Hence, these two techniques are complementary to each other. By using GIS, several maps like geomorphological, geological, structural, drainage etc. can be easily prepared for morphometric and morphotectonic evaluation of any region. GIS technology is digital, spatial and generic. Further, GIS provide platform to handle all the information effectively which are georeferenced (having latitude / longitude information). The GIS technique has the unique capability by means of overlaying and superimposing different layers of images in a single map and therefore, it becomes easy to analyse the impact of one parameter on another. For example river morphology and drainage pattern are very sensitive to neo-tectonic activities, and both can be easily extracted by remote sensing and GIS approach.

1.5 The 26 January, 2001 Bhuj Earthquake

In India, the most disastrous earthquake in the post-instrumental era is the Bhuj earthquake (Mw=7.7) which caused extensive damage to the settlements and heavy casualty. This event had caused maximum uplift of approximately 1.57±5 meters near the epicenter (Chandrasekhar *et al*., 2004). The Kutch region has experienced 90 seconds of strong shaking, followed by several minutes of moderate shaking (Iyengar and Raghu Kanth, 2002; http://asc-india.org/lib/20010126-kachchh.htm).

It is reported that the Bhuj region has been experiencing moderate earthquakes in the form of aftershocks occurred between the years 2003 to 2005, after main event (Figure 1.1). Figure 1.1 further shows the study area along with the tectonic set up of Kutch, Gujarat. Figure 1.2 gives information on the affected areas even at the Talukas level. The Bhuj earthquake source is bounded from both sides by Nagar Parkar Fault and Kathiawar (Bodin and Horton, 2004). At the western margin of the Indian plate rifting was controlled by the NE-SW trend of the Delhi (Precambrian) fold belt which swings to E-W in Kutch. In the post rifting stage, footwall (formed during the rifting) has been uplifted along EW trending major fault line due to compressional tectonic forces in the Kutch region of Gujarat. As a result of this, formation of highland and intervening plain lands occurred. At the same time a change in the nature of the major faults occurred from normal to reverse and slip the block laterally as it got tilted towards south (McCalpin and Thakkar, 2003). Kutch region has been experiencing earthquakes in the past and are well documented. Figure 1.3 shows overall earthquake occurrences along with the tectonics of the larger Gujarat region.

Widespread liquefaction and corresponding deformations were reported in the epicentral area around Bhuj and Bhachau city (McCalpin and Thakkar, 2003). Unconsolidated Holocene sediments are present in the Ranns and the plains of Banni which served as vast grounds for liquefaction (Figure 1.4). Also, lateral spreads, sand blows, and water spouts, mainly between the Pacham, Khadir Uplift and the eastern part of the Mainland Uplift were accompanied. Rajendran *et al*., 2001 has documented many of the features and provide the post-earthquake study.

Many mud-volcanoes in the Rann of Kutch have dimensions of hundreds of meters and one covers a 5 km diameter stretch of the southern Rann with dark sand and mud. Numerous ancient river channels were illuminated by a pock mark pattern of sand vents, and some have clearly flowed, and breached their old channels. Figure 1.4 displays liquefaction suffered by the Kutch region. Deformation of alluvial units along the Mainland fault's northern edge, due to extensional and compressional movement, resulted in ground surface faulting, sand boils, and surface bulging due to compression. A total extension of approximately 2 km of surface rupture occurred for the Kutch Mainland Fault about 18 km northwest of Bhachau. Figure 1.5 shows terrain deformation through road subsidence, large ground cracks and surface evidence of earthquake rupture.

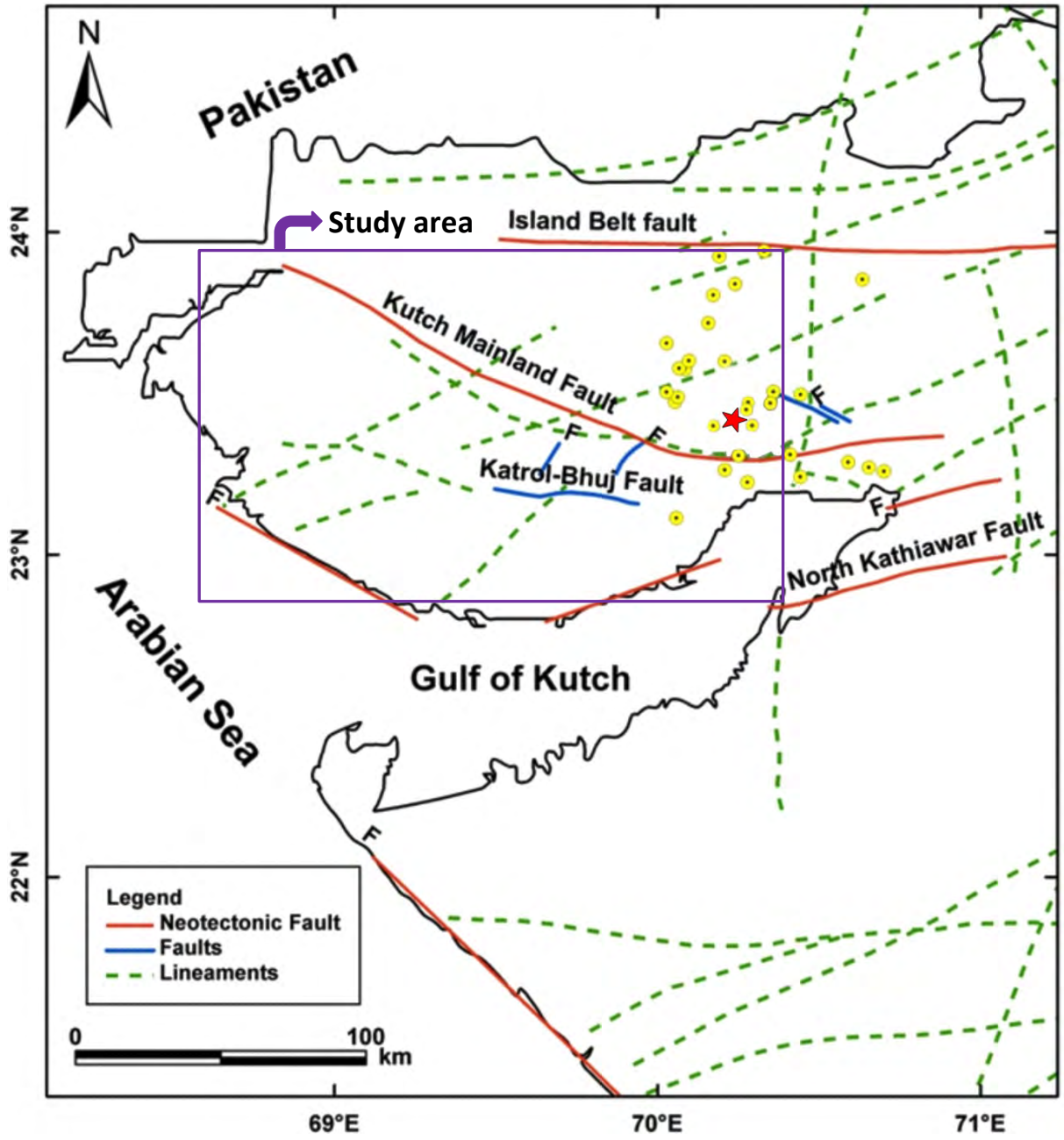

Figure 1.1: Tectonic set up of Kutch, Gujarat. Red star indicates the location of epicentre of main shock; Yellow circles indicate earthquake (between 2.7 - 4.5 Mw) occurred between the years 2003-05.

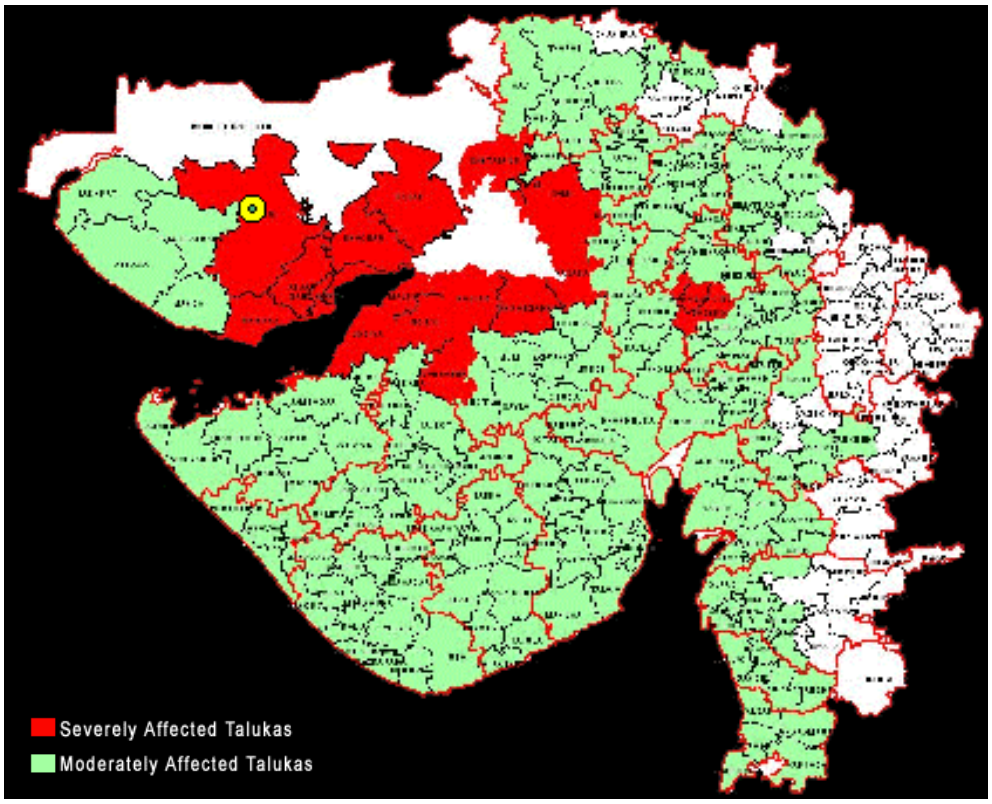

Figure 1.2: 2001 Bhuj earthquake intensity Source: Gujarat state disaster management authority, (http://gujarat-earthquake.gov.in/final/seismic.html).

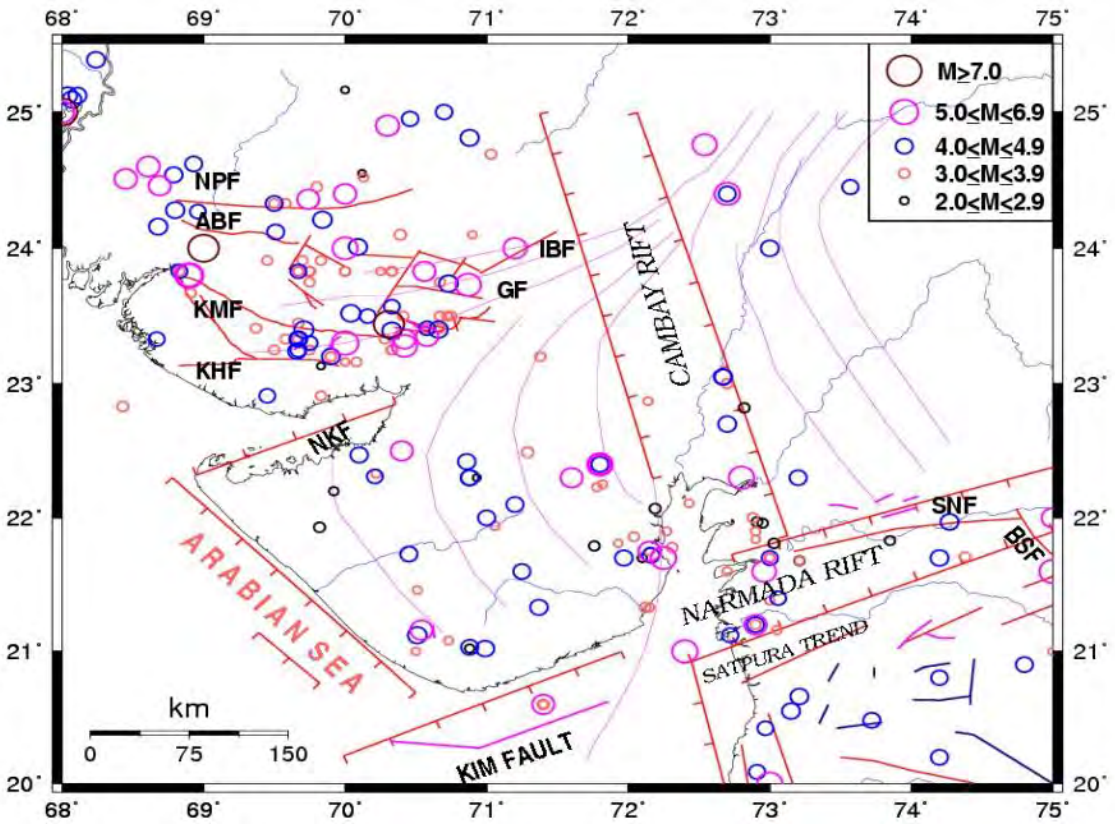

Figure 1.3: Felt earthquakes from historical times to 2009 (ISR 2010).

Figure 1.4: Nature of liquefaction caused by Bhuj earthquake (ISR 2010).

Figure 1.5: Terrain deformations due to the Bhuj 2001 earthquake (ISR 2007).

Large scale masonry structures around the Anjar city have been destroyed as a result of Bhuj earthquake (Figure 1.6). Single and multi-story buildings collapsed in Bhuj city due to the tremor.

The aftershock data collected by the Middle America Earthquake Centre, infers that the co-seismic hidden fault for this earthquake was dipping 40-50° south and projected fault surface would lie north of the Bharodiya village, where two key fracture directions were described by the located aftershocks (Kayal *et al*., 2002). One was trending NE and the other NW, the rupture meets at a zone of 10km south from the 2001's main earthquake epicentre. Further, the study was carried out based on SW and SE dipping reverse faulting based on the NW and NE cluster of events respectively (Kayal *et al*., 2002). On the basis of analysis of 600 aftershocks records employing local network (Figure 1.7), Mandal *et al*., 2004 suggested that the causative fault for Bhuj earthquake was a hidden EW trending reverse slip fault with south dip. This fault is located about 25 km north of the KMF and named as North Wagad fault (Figure 1.7). Mandal *et al*., 2004 also estimated that the earthquake's nucleation depth was approximately 20-30 km in the central part of the aftershock zone and the propagation was 10 km towards the surface.

Studies also indicate that the Kutch region also experienced neotectonic movements. Two major phased of Quaternary tectonic uplift could be detected. The Early E-W trending faults records Quaternary tectonics and these faults were more active during Early Quaternary (Thakkar *et al.*, 1999). The Late Pleistocene phase took place along the NNE-SSW to NNW-SSE trending transverse faults. Malik *et al.,* 1999 suggests that most large Holocene earthquakes have occurred along transverse faults as indicated by the Neotectonic landforms of the area. Neotectonic effects have been observed at different locations of Bhuj and Anjar city (Figure 1.8).

Figure 1.6: (a) Most stone houses in the old town of Bhuj collapsed, (b) Damage to cut stone and lime mortar masonry building in old Bhuj, (c) Taksila Apartments, Bhuj. Both 5-story buildings collapsed due to soft story effects, (d) Damage to the RCC building (http://peer.berkeley.edu/pdf/2713_Other200104GujaratEQTR0101.pdf accessed on 28-04-2017).

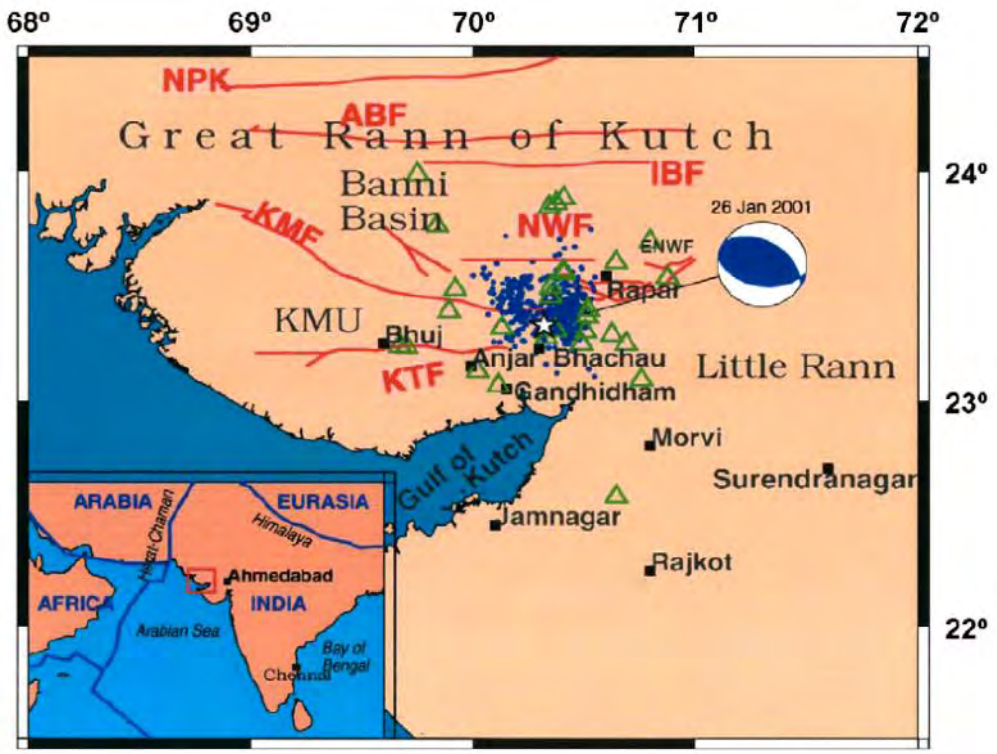

Figure 1.7: Tectonic features of the Kutch region, the epicentral location of Bhuj earthquake (white star), epicentral locations of 600 aftershocks (blue solid circles) recorded employing 28 seismographs (marked by solid triangle) and the USGS focal mechanism solution for the 2001 Bhuj mainshock, Kutch mainland uplift (KMU). Major faults (red lines): ABF, Allah Bund Fault; IBF, Island belt fault; KMF, Kutch mainland fault; KTF, Katrol hill fault; NPK, Nagar Parkar fault; NWF, North Wagad fault. (Source: Mandal *et al*., 2004).

Figure 1.8: Field photographs showing neotectonic effect of soft rocks at Bhuj (upper) and Anjar (lower).

1.6 Research Objectives

Most earthquakes are expected at the convergent plate boundary e.g., between the Indian plate and the Eurasian plate boundary. However Kutch is situated at an intraplate zone, where earthquake takes place frequently. In addition the Gujarat earthquake is an excellent example of liquefaction, causing buildings to 'sink' into the ground which gains a consistency of a liquid due to the shear stress generation during the earthquake. The current research work has its basis on ability of remote sensing technique along with other geo-information in deciphering rapidly and efficiently any changes occurring on the Earth surface. Natural phenomena like devastating earthquake takes place at any place of the world needs immediate attention and rigorous scientific study where most visible effects are destruction to the houses, land deformations, liquefaction etc. Further taking into account many geomorphic indices are helpful in identifying neotectonic activity at a local to regional scale. Many such effects can be studied with the help of remote sensing technique and in view of applicability of the technique a study on neo-tectonics and effect of earthquake has been conceived and employed in case of Kutch region. So the key objectives of this study are,

a) Understanding the geological, tectonic and seismic set up of the study area.
b) Geoinformatics in analysing the deformation process caused by tectonic movement and recent earthquakes.
c) Ground deformation information based on SAR Interferometry.
d) Persistent Scatterer technique for ground movement.
e) DEM and terrain representation.
f) Morphometry in establishing effect of slow and gradual tectonic deformation.
g) Identification of faults and landforms based on optical and radar satellite images and DEM.

1.7 Organization of Thesis

The thesis has been organized in eight chapters including this chapter of introduction. Basic purposes of each chapter have been discussed below:

- **Chapter-2:** Background and case study, which includes earthquakes, InSAR, drainage morphometry and morphotectonic studies. Tectonic locations like inter and intra plate boundary regions are the most seismically active zones. In India, there are five important seismic zones, according to the vulnerability of a region to any intensity of earthquake. These explanations as given by different workers around the world have been discussed in it.
- **Chapter-3:** Discusses the regional geology and tectonic setup of the Kutch region of Gujarat.
- **Chapter-4:** Introduces different remote sensing data sets and description of the processing techniques applied to 'Identification of earthquake induced surface deformations using SAR Interferometry techniques' for Bhuj earthquake. An overview of methodology has also been discussed.
- **Chapter-5:** Discusses identification of earthquake induced liquefaction effects even after many years of main shock using ALOS PALSAR SAR image pair of 2007 and 2010.
- **Chapter-**6 Describes the time series land deformation analysis and observations made using Envisat and Sentinel 1-A SAR images of 2001-2016, along with validation from the correlation of SRTM and ALOS PALSAR DEM for Bhuj. Further it deciphers about the neotectonic activity around the Kutch rift basin from PSI study.
- **Chapter-7:** Discusses about the interpretation of faults from satellite images and the geomorphic evidences of active faults in Kutch, Gujarat using Remote Sensing and GIS.
- **Chapter-8:** Summarizes the analysis, observations and the conclusions drawn from the study.

Chapter 2

Earthquake, Remote Sensing and terrain deformation studies: A Review

2.1 Introduction

Sudden change on our Earth's surface is essentially caused by earthquakes. Magnitude of terrain deformation obviously is governed by the size of earthquake. This type of terrain change can be effectively detected and measured by the microwave remote sensing technique. However, to decipher gradual and slow rate of ground modification morphometric analysis may be employed. The first part of this chapter includes global and India's seismicity followed by introduction of the concepts of RADAR (Radio Detection and Ranging), Synthetic Aperture Radar (SAR), Interferometric Synthetic Aperture Radar (InSAR) and application of InSAR data in crustal deformation studies. Whereas the second part discusses the application of morphometric and morphotectonics to understand slow tectonic movements.

2.2 History of Earthquake Studies

Earthquakes play a major role in mountain building and tectonic activities. Earthquakes are responsible for large scale disaster and loss of life and economy.

2.2.1 Causes of Earthquakes

The study of earthquakes is quite new and rigorous. Until perhaps the 18th century, the actual cause of earthquakes was little understood. However it is well-known that tectonics plays a vital role in initiating an earthquake.

Now it is understood that the earth's surface is comprised of about a dozen large plates that move relative to one another. Tectonics causes the deformation on the earth's crust due to the force and the resultant structural with geological features. Plates spreading away from each other causing divergent plate margin, if sliding (grinding) past in opposite direction producing transform faults and if striking each other causing converging boundary and subduction zones. Oceans occupy most of the spreading zones. Along Mid-Atlantic ridge, Eurasian plate is spreading apart from North American plate. Generally spreading zones have shallow depth

earthquakes (within 30km from surface), (http://pubs.usgs.gov/gip/earthq1/where.html). The major continental and oceanic plates which include North American Plate, Australian-Indian plate, South American Plate, Antarctic plate, African plate, Arabian plate, Caribbean plate, Eurasian plate, Cocos plate, Nazca plate, Juan de Fuca plate, Philippines plate, pacific plate and Scotia plate (Figure 2.1). These plates comprise of smaller sub-plates. Most earthquakes of the world happen at these plate margins.

Earthquake location and the kinds of ruptures produced, defines these plate boundaries where Inter-plate (plate-boundary) earthquakes are more common than Intra-plate (within plate) earthquakes out of which less than 10% earthquakes are Intra-plate earthquakes. Weakened boundary regions become interior part of plates due to constant movement of plate boundaries. These internal zones of weaknesses within continents can release accumulated strain in the form of earthquake which may be a response to stress initiating at either deeper crust or at the edges of plate. (http://pubs.usgs.gov/gip/earthq1/where.html).

2.2.2 Historical Seismicity

The 1177 BC China earthquake was the earliest earthquake for which there is descriptive information available. Earliest reported Europe earthquakes are in 580 BC but some descriptive information is available for the earthquake that happened in mid-16th century. Though earliest known American Earthquake is in Mexico in late 14th Century and in Peru in 1471, details of their effects are not well documented.

A series of three earthquakes in New Madrid, starting from 16 December 1811, second on 23 January 1812 and a third on 7 February 1812 rocked North America. The aftershocks sustained for a long time. The earthquake of magnitude 8.0 was felt as far as Boston and Denver, but fortunately could not cause much destruction as the region was sparsely populated. In 1906 the San Francisco earthquake is one of the most destructive earthquakes in North American History which claimed the lives of 700 people. This earthquake was followed by fire killing almost 700 people and leaving city in ruins. The earthquake of Alaska happened on 27th March 1964 which was of greater magnitude than that of San Francisco Earthquake, as it has released twice energy than San Francisco earthquake but loss of property in Alaska was less as it was sparsely populated. Table-2.1 gives a few most destructive earthquakes in history. Table-2.2 gives the major earthquakes in India (http://neic.usgs.gov/neis/eqlists/eqmosde.html).

2.2.3 Earthquakes of Gujarat

From historical time the peninsula Indian state of Gujarat, along with Maharashtra has affected from frequent earthquakes, both deadly and damaging. All the earthquakes are intraplate events where numerous active faults have been identified (Dasgupta *et al*., 2000). Gujarat has experienced series of earthquakes from 18^{th} century i.e. February 1705 Bhavnagar-Gogha, 16 June 1819 Rann of Kutch (M_w 8.2), 13 August 1821 Kheda-Nadiad, 20 July 1828 Bhuj-Anjar, 26 April 1848 Disa, 29 April 1864 Dewan-Khambat, January 1903 Kunria (M_w 6), 29 August 1936 Surat (Intesity III for 30 sec), 1940 Umia-Luna area (M_w 5.8), 14 June 1950 Tharad-Jhajham (M_w 5.6), 21 July 1956 Bhadreshwar-Anjar (M_w 6), 23 March 1970 Ankleshwar-Bharuch (M_w 5.4), 28 January 2001 Suvi-Rapar (M_w 5.8), 07 March 2006 Mouna (M_w 5.5), 20 October 2011 Sasan Gir (M_w 5) (Source: http://asc-india.org/seismi/seis-gujarat.htm#3). The above historical earthquakes have been shown in figure 1.3 of chapter 1.

Among the above described Indian earthquakes, the 1819 Rann of Kutch earthquake happened on 16 June having a predicted magnitude from 7.7 to 8.2 and a maximum observed intensity of XI (Mercalli intensity scale). It resulted a minimum 1,543 casualties. The earthquake produced an area of subsidence which lead to the formation of Sindri Lake and further the zone of upliftment to the north about 6 km wide, 80 km long, and 6 m high dammed the Koree River. The earthquake caused a great surface deformation as well as a land stretching of 90 kms which was uplifted about several metres, named as Allah Bund. Beside this the 1956 Anjar earthquake was devastating and a remarkable one.

Table 2.1: Most deadly historical earthquakes recorded in the world (http://earthquake.usgs.gov/earthquakes/world/historical.php).

Date	Location	Mw (USGS)	Deaths	Comments
22 December 0856	Damghan, Iran	-	200,000	-
23 March 893	Ardabil, Iran	-	150,000	-
9 August 1138	Aleppo, Syria	-	230,000	-
September 1290	Chihli, China	-	100,000	-
1268	Silica, Asia Minor	-	60,000	-
23 January 1556	Shensi, China	8	830,000	-
November 1667	Shemakha, Caucasia	-	80,000	-
11 January 1693	Sicily, Italy	-	60,000	-
18 November 1727	Tabriz, Iran	-	77,000	
1 November 1755	Lisbon, Portugal	8.7	70,000	Great tsunami
4 February 1783	Calabria, Italy	-	50,000	-
28 December 1908	Messina	7.2	70,000 to 100,000	Deaths from earthquake & tsunami
16 December 1920	Gansu, China	8.6	200,000	Major fractures, landslides
1 September 1923	Kwanto, Japan	7.9	143,000	Great Tokyo fire
22 May 1927	Near Xinjiang, China	7.9	200,000	Large fractures
25 December 1932	Gansu, China	7.6	70,000	-
30 May 1935	Quetta, Pakistan	7.5	30,000 to 60,000	Quetta almost completely destroyed
5 October 1948	USSR (Turkmenistan Ashgabat)	7.3	110,000	-
31 May 1970	Peru	7.9	66,000	$530,000 damage rock slides, floods
27 July 1976	Tangshan, China	7.5	255,000 (official)	Estimated death toll as high as 655,000
20 June 1990	Iran	7.7	50,000	Landslides
17 August 1999	Izmit, Turkey	7.6	17,118	-
26 January 2001	Gujarat, India	7.6	20,023	-
25 April 2015	Gorkha, Nepal	7.8	16,808	-

Table 2.2: Location of Past Major Earthquakes in India the magnitudes are as provided by Maps of India (http://www.mapsofindia.com/maps/india/majorearthquake.html).

Date	Location of Epicenter		Place	Magnitude (Mw)
	Latitude(°N)	Longitude(°E)		
16-06-1819	23.6	68.6	Kutch, Gujarat	8.0
10-01-1869	25	93	Near Cachar, Assam	7.5
30-05-1885	24.1	74.6	Sopor, J & K	7.0
12-06-1897	26	91	Shillong Plateau	8.7
04-04-1905	32.3	76.3	Kangra, H. P.	8.0
08-07-1918	24.5	91.0	Srimangal, Assam	7.6
02-071930	25.8	90.2	Dhubri, Assam	7.1
15-01-1934	26.6	86.8	Bihar-Nepal Border	8.3
26-01-1941	12.	92.5	Andaman Islands	8.1
23-10-1943	26.8	94.0	Assam	7.2
15-08-1950	28.5	96.7	Arunachal Pradesh-China Border	8.5
21-07-1956	23.3	70.0	Anjar, Gujarat	7.0
10-12-1967	17.37	73.75	Koyna, Maharashtra	6.5
19-01-1975	32.38	78.49	Kinnaur, H. P.	6.2
06-08-1988	25.13	95.15	Manipur-Myanmar Border	6.6
21-08-1988	26.72	86.63	Bihar-Nepal Border	6.4
20-10-1991	30.75	78.86	Uttarkashi, Uttrakhand	6.6
30-09-1993	18.07	76.62	Latue-Osmanabad, Maharashtra	6.3
22-05-1997	23.08	80.06	Jabalpur, M. P.	6.0
29-03-1999	30.41	79.42	Chamoli District, Uttrakhand	6.8
21-01-2001	23.41	70.23	Kutch, Gujarat	7.7

2.2.4 Seismic Zones around the World

Up to early 20th century seismologists had mixed and wrapped picture of earthquake distributions since their knowledge was confined up to the continent of their residence. Through technology, as 20th Century advanced, efforts of global seismograph network to trace earthquake started becoming a reality. This provided more developed recording and cataloguing for earthquakes occurring world over. In the year 1990 for international data exchange, around 3300 seismographic observations were available. Some of the agencies like ISC and NEIC are assembling regional as well as global catalogues. These catalogues are helpful for calculations of earthquake hazard and provide source of tectonic deformation studies around the world. From ancient times, it is understood from experiences that some regions are more susceptible to earthquake while others are less prone. This improved cataloguing has given flawless picture and backing to this idea. As a result, bifurcation of regions into seismically active and seismically stable zones can be prepared. Based on estimated earthquake locations, it is found that earthquakes happen in regions which are confined in a narrower zone and are surrounded by relatively stable regions. As per Plate Tectonics, global epicentres distribution is correlated to lithospheric plate boundaries. (Figure 2.2). Plate boundary earthquakes are also identified as interplate Earthquakes.

"Ring of Fire" is the World's most active region which corresponds to margins of Pacific Ocean. 80% of world's largest earthquakes and 90% of world's total earthquakes occur along "Ring of Fire." Large magnitude earthquakes take place along this region from Aleutian Islands to Southern Chile in Americas and from New Zealand to Kamchatka peninsula in Asia. Throughout the long region, along margins of South & Central America, besides shallow earthquakes, intermediate and deep shock takes place. Another seismically active large region is Himalaya-Alpine-Mediterranean which ranges from west to east. For this region, Northern part is Eurasian plate and southern region is plates of Africa, Arabia India and Australia. This zone have all types of earthquakes i.e. shallow, intermediate and deep earthquakes which accounts for 6% of total world's earthquake and 17% of world's major earthquakes. Third region is shaped by earthquakes located on oceanic ridges that form margins of oceanic plates (e.g. East Pacific Ridges, Mid-Atlantic Ridge) etc. Here, shallow depth earthquakes are concentrated in thin bands succeeding trend of oceanic ridges (USGS Earthquakes).

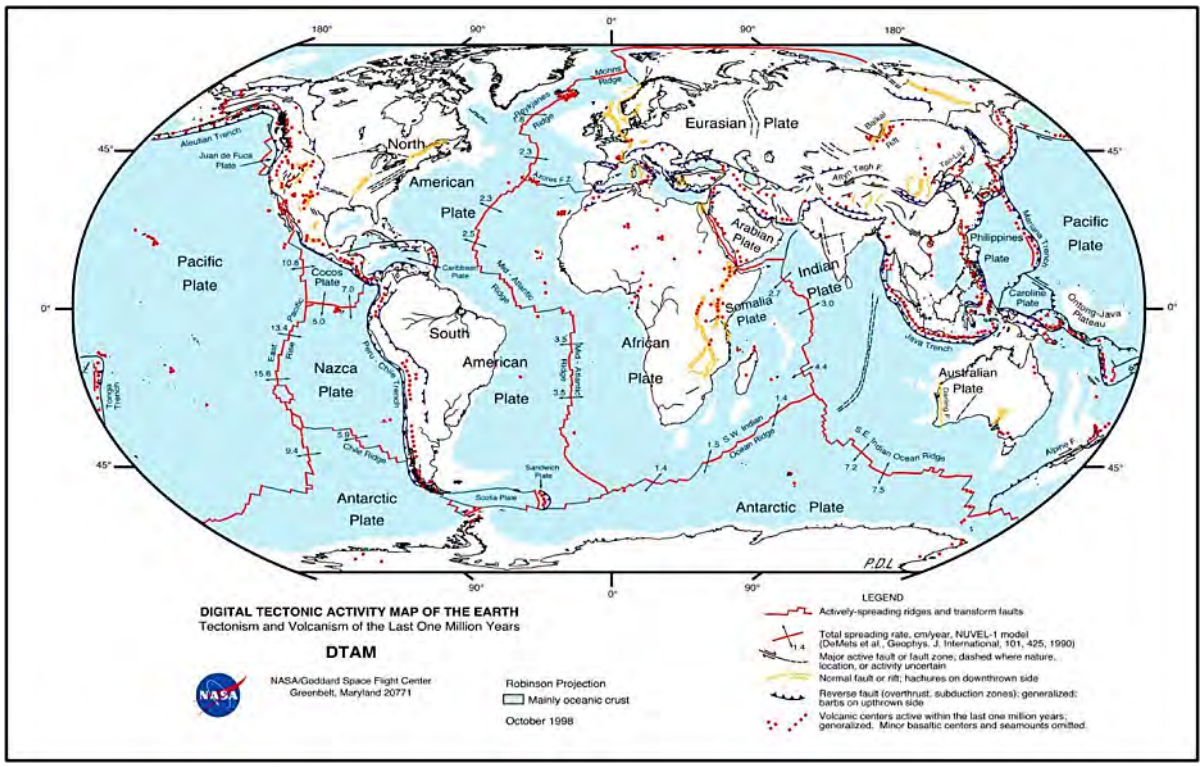

Figure 2.1: Tectonic Activity Map of the Earth showing tectonism and volcanism of the last one million years (Source: http://www.globalchange.umich.edu/globalchange1/current/lectures /evolving_earth/evolving_earth.html).

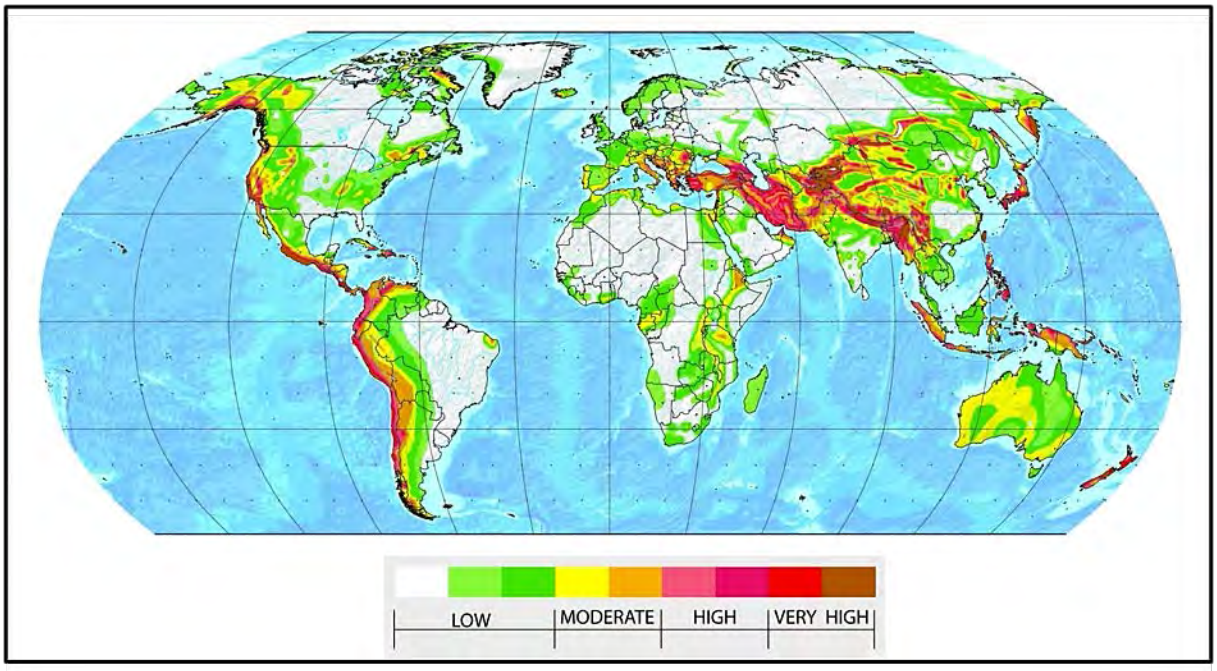

Figure 2.2: Global seismic hazard map. The different colours indicate the level of seismic risk Source: (http://xrds.acm.org/article.cfm?aid=1247243).

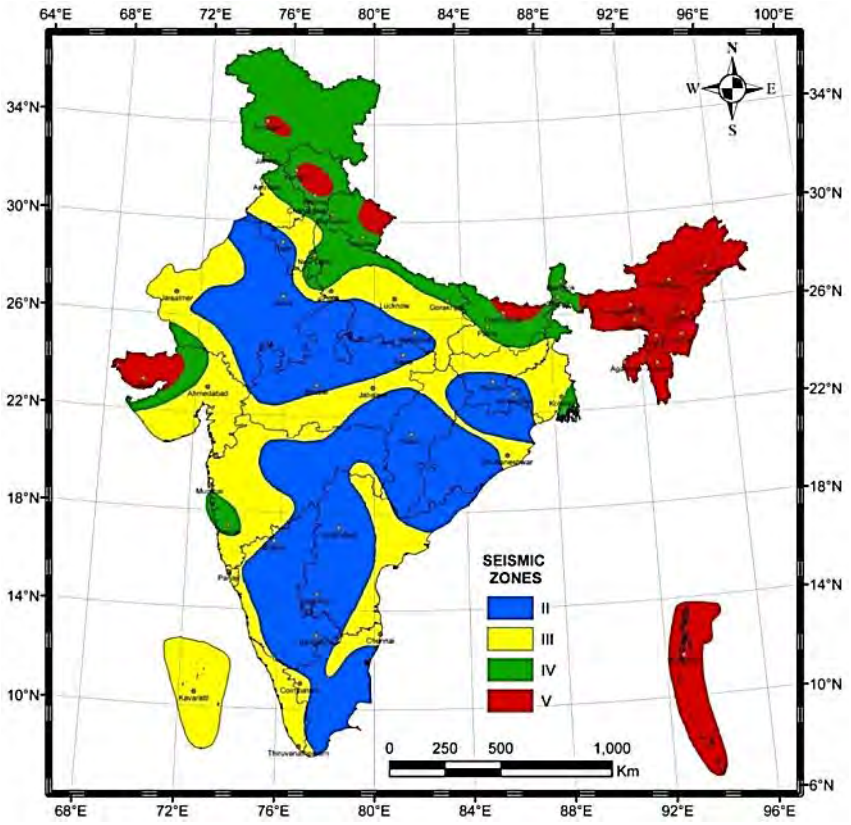

Figure 2.3: Indian Seismic Zone map as per IS : 1893 (part-1) - BIS 2002, Criteria for Earthquake Resistant Design of Structures; general Provisions & Buildings, Bureau of Indian Standards, New Delhi.

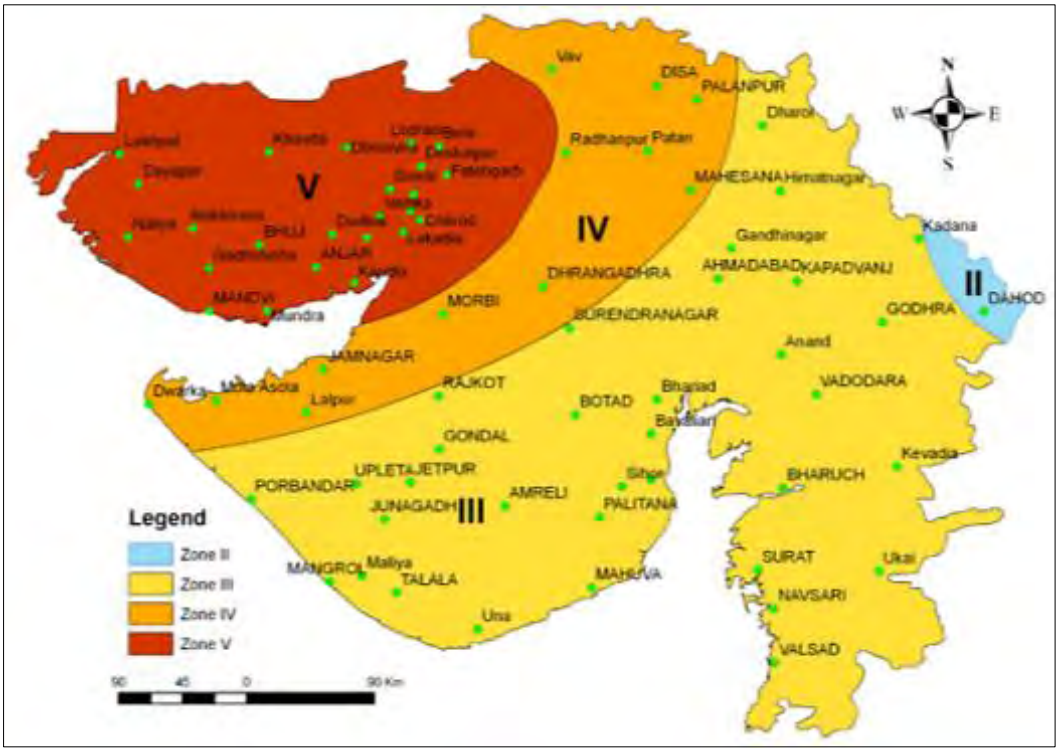

Figure 2.4: Gujrat Seismic Zone map as per ISR 2010 report.

2.2.5 Seismic Zones in India

Due to the difference in ecological conditions, the effect of earthquake damage also varies with different locations. Thus seismic zone mapping is essential to get the information of these regions. As per 1970 version of zone map, India have been subdivided into five categories such as Zone I, II, III, IV, V. Intensities in these zones defined in terms of maximum Modified Mercalli (MM) intensity. The intensity experienced in these zones were V or less, VI, VII, VIII and IX and higher respectively. Northern (some areas) and north-eastern parts of Himalaya and Kutch were categorized in zone V. In due course of time based on seismo-tectonics and country's seismicity, seismic zone map is reviewed timely based on the acquired experience. In 1962, India's first seismic zone map was prepared, next revised in 1967 and then in 1970. Again in 2002 the map was revised (Figure 2.3) making India with only four zones (Zone-II to Zone-V). Areas in zone-I in 1970 version of seismic zone mapping were upgraded to Zone-II in 2002 version. Also, peninsular region zone mapping have been improved. India's seismic Zone Map presents seismic zones of India (large scaled view) (Murthy, 2004). As per the ISR report, the Gujarat region has been divided into four seismic zones among which the Kutch rift comes under the zone V (Figure 2.4).

2.3 Microwave remote sensing

The development of differential RADAR interferometry can be more or less grasped by a basic advancement stream as Radio Detection and Ranging (RADAR), Synthetic Aperture RADAR (SAR), Interferometric SAR (InSAR), Differential Interferometric SAR (DInSAR) Persistent scatterer interferometry (PSI) techniques have been developed. The historical backdrop of RADAR can be followed back to nineteenth century in which the huge disclosure of radio waves and electromagnetism by Maxwell and Hertz changed the world (Woodhouse, 2006). Gradually, significant developments in the Radar technology resulted to the evolvement of advance technologies like InSAR, DInSAR and PSI. Coherent Radars which have the capability to receive both phase and amplitude information of ground played an important role in the advancement of RADAR imaging. Initially an artificial long antenna was designed to acquire SAR images which worked on the principle of Real aperture RADAR (RAR). But later the antennas were synthesized with a phase array pattern so called Synthetic aperture RADAR (SAR). Initially a SAR system supported satellite was launched in June 1978 for ocean studies (Hanssen, 2001). This led to the use of different SAR system facilitated satellites which turn into an essential requirement data source for many applications. Yet SAR's incapability to differentiate two entities at the same range but from different positions has grown public

interest. This lead to the invention of multi RADAR satellite sensors mounted on one platform which has the capability to acquire image from two different positions at the same time (Hanssen, 2001). This idea, along with the use of phase information paved the way for interferometry (Hanssen, 2001). So it became possible to obtain distance as well as angular measurements with two SAR images (Hanssen, 2001).

2.3.1 Synthetic Aperture Radar (SAR)

After the radar observation of Venus and the Moon in the 1960s, followed by a SAR imaging technique developed in the 1950, the Seasat satellite was introduced with the combined effort of NASA and JPL in the year 1978, (Gens and Van Genderen, 1996) which was the first Earth observing space-borne SAR system. Conceptually SAR operates within the microwave to radio wave regime where the transmitted signal towards the target is received which is coherent in nature (i.e. Phase preserving) backscattered broadband radio signals, at microwave frequencies, operates in the X, C, S, L or P bands (Elachi, 1988; Curlander and McDonough, 1991; Bamler and Hartl, 1998) (Table 2.3).

2.3.2 SAR observations

Table 2.3: Microwave radar frequencies and their respective wavelengths.

Band	Frequency (GHz)	Wavelength (cm)
P	<0.3	100
L	1-2	15-30
S	2-4	7.5-15
C	4-8	3.75-7.5
X	8-12	2.5-3.75

2.3.3 InSAR

It was Graham who used the SAR system in an interferometric mode to generate topographic maps in the year 1974 (Graham, 1974). Cloud and poor sunlight was a great hindrance in the data collection by aerial photography as well as through optical satellite imaging. So RADAR technology is introduced, which has the capability to overcome the restrictions posed by aerial photography which works in connection with all-weather electronic systems. The RADAR was expected to perform two functions. The acquired image

will have a good resolution so that can differentiate the various entities and landscapes to be mapped. Second the determination of position of an object from the sensor considering its three dimensional accuracy with sufficient number of points to define the terrain surface. So the RADAR technology used in acquisition of reasonable resolution image of the topography and RADAR interferometry helped in the measurement of three dimensional positions.

The San Francisco Bay area of 11 sq. Km was mapped by Zebker and Goldstein (1986) using interferometric technique in the year 1986. Two different images were obtained by two antennas in the flight direction of the aircraft. Interferogram was generated using the two images with baseline 11m subsequently performing co-registration of the two images at pixel by pixel a height map was generated followed by a coherence map. Thus the cartographically accurate map of the height of the illuminated terrain is derived.

Li and Goldstein (1990) demonstrated the repeat-pass method of InSAR with satellite data in the year 1987. This give rise to exceptionally useful terrain information and to demonstrate the same a particular data set obtained by the SEASAT SAR was used. The fringes obtained from the generated interferogram resembled predictable topographic contours where the fringes were consistent following the conventional topography of study area. This study was focused on terrain mapping followed by a conventional SAR with a single antenna in a repeat ground-track orbit.

InSAR technique with repeat-pass method was also established by Gabriel and Goldstein in the year 1988. Here SIR-B sensor was used to carry out the Interferometric process mounted on two separate orbits with a small inclination angle. In order to restrict the baseline length imaging site has been picked close to the crossover point along two orbits. Crossed orbit interferometry was proposed as a useful extension for SAR Interferometric usual methods.

In the year 1993, Madsen, Zebker and Martin used the C-band RADAR data to generate rectified topographic maps. They established a new processing scheme which featured motion compensation, absolute phase retrieval and 3D location. Using extreme aircraft motion under adverse conditions the performance of the new processor was evaluated. DEMs obtained using optical stereo method was compared with RADAR derived topographic maps to evaluate the accuracy.

Digital Elevation Models (DEMs) are used in many applications such as in seismic source modelling, topographic mapping and rainfall-runoff studies etc. InSAR is a very well

established technique for generating high resolution DEM from space borne and airborne data (Okeke, 2006). Shuttle RADAR Topographic mission (SRTM) DEM is a very good example for the SAR derived DEM.

Gens and Van Genderen (1996) carried out a review of the issue, techniques and applications of SAR interferometry. The article discusses the various potential applications of SAR interferometry such as digital elevation modelling, slope measurement, topographic mapping etc. Further it includes influence of the atmosphere which hinders the quality of InSAR data.

2.4 History of InSAR Techniques in deformation studies

In Synthetic Aperture Radar (SAR) microwaves with cloud penetrating imaging capabilities are there. Its 'Interferometric configuration' (InSAR) is one of the most effective technologies for identifying crustal deformations by recording the phase differences of microwave pulses acquired by SAR before and after deformations occurred in the same area produced by either subsidence or uplifting of the ground. The technique has proven capability of measurement of alterations in deformation up to centimetres over time span ranging from days to years. The SAR Interferometry has been successfully used in several applications e.g. earthquake induced deformations, subsidence due to mining activity, landslides and over exploration of groundwater, volcanic activity based deformations , tsunami monitoring etc.

In past two decades researchers have used InSAR technique extensively to measure and detect seismically induced ground deformations which are initiated by crustal faulting. (Massonnet *et al*. 1994; Wright *et al*. 2001; Jacobs *et al*. 2002,; Yarai *et al*. 2004; Stramondo *et al*. 2005; Satyabala and Bilham 2006; Satyabala, 2006; Ge *et al*. 2008).Researchers also study the effects of tectonism on ground deformation due to main rupturing. The use of pre- and post-earthquake SAR images is termed as co-seismic InSAR studies. Saraf *et al*. 2012 studied the post seismic ground deformation caused due to the 2001 Bhuj earthquake (Mw 7.7) (epicentre is 23.41° N, 70.23° E as reported by USGS). The event was triggered by reverse faulting along a hidden fault and a large scale ground deformation has been caused which were occurring in Kutch (Gujrat, India). Origin of this event found to be located along ruptured fault at about 16 km depth causing maximum destruction in eastern region of Bhuj. A ground deformation around the Kunjisar village in Bhuj located about 7 km north of Bhachau was indicated by preliminary studies of Oct. 2003- Nov. 2004 and Nov. 2004- Oct. 2005 InSAR data. The relative crustal deformation taking place within two different time spans i.e. between the Oct.

2003- Nov. 2004 and Nov. 2004- Oct. 2005 could be worked out. The 2003-04 interferogram images exhibited an uplift of ≈ 8 cm around Kunjisar village and ≈ 25 cm and ≈ 5 cm in the two other areas situated north to Kunjisar. Whereas, the 2004-05 interferogram image indicated a subsidence of ≈ 17 cm in Kunjisar area and also subsidence of ≈ 25 cm and ≈ 5 cm in the two areas of north and northwest of Kunjisar, respectively. The ground uplift during 2003-04 probably indicates that the last phase of ground deformation followed by the onset of subsidence during 2004-05 as the ground began to experience dilation phase.

2.5 Persistent Scatterer InSAR (PSInSAR)

The PSI technique is an alternative to image stacking techniques where pixels have stable phase characteristics over long periods of time. This technique allows the refinement of topographic models (or more generally look-angle models) on a pixel by pixel basis and spatial filtering approaches which exploit the knowledge those atmospheric signals are highly correlated over short distances.

This method is referred to as Persistent Scatterer InSAR (PSInSAR). The PSInSAR analysis technique is useful for the observation of slow deformation processes, such as long term subsidence due to fluid extraction (Schmidt and Burgmann, 2003); landslides (Hilley *et al*., 2004) and inter-seismic deformation (Lyons and Sandwell, 2003). The PSInSAR techniques generally involve the issues of selection of image pair (i.e. type of image pair), analysis of InSAR, pixel based image co-registration, Persistent Scatterer Candidate (PSC) followed by pixel identification, spatial and temporal modelling of phase interpretations for atmospheric signal, residual topographic error and satellite trajectory error, temporal (or 3-D) phase unwrapping and deformation estimation.

The PSInSAR method was first established by Ferretti *et al*. (2000) and later further developed by Colesanti *et al*. (2003a). Usually PSInSAR techniques generate a sparse distribution of observations over a scene, where the technique has been demonstrated for linear and seasonal deformation with estimated precisions of 0.1-0.5 mm/yr. The typical number of detected persistent scatter is about 120 to 400 PS/km^2 in urban areas and 15 to 50 PS/km^2 in rural areas (Colesanti *et al*., 2003a). In these approaches, deformation is typically estimated simultaneously with concern parameters (including atmospheric and residual topography signal), where the signal components are separated by exploiting their spatial and temporal characteristics. The method has been successfully used for baseline separations in excess of the critical baseline (i.e. a $B_\perp$ of $\pm$ 1600 m for ERS) (Ferretti *et al*., 2001).

2.6 Example: Nepal Earthquake

Earthquakes in Himalaya are responsible for the ongoing tectonic collision of north bound Indian plate against the Eurasian plate. The Nepal earthquake on 25th April 2015 (Mw 7.7, focal depth ≈ 8km) is reported to be the most disastrous earthquake in the last decade causing extensive damage to the settlements and heavy casualty. In sequel to the above cited earthquake, the region has experienced another major earthquake (Mw 7.3, focal depth ≈ 15km) on 12 May 2015 (Figure 2.5). The initial earthquake occurred in the village of Barpak in the Gorkha district with approximately 80 km NW of Kathmandu and the second event struck near Dolakha southeast of Kodari. The occurrences of the two earthquakes were reported to be relatively shallow depth (USGS). The focal mechanism of Nepal earthquake suggests compressional WNW-ESE trending thrust, where fault has not broken the surface. The earthquakes caused a rupture along the Main Himalayan Thrust (MHT) locked line up to Main Boundary Thrust (MBT) covering Main Central Thrust (MCT), and portions of Lesser and higher Himalaya (GSI Report, 2015). These two earthquakes caused approximately 8000 casualties and 22000 injuries (EERI, 2016). These earthquakes also affected moderately northern part of India which includes eastern Uttar Pradesh, north Bihar and north Bengal bordering Nepal where 80 casualties were reported (Rai *et al*., 2015, Baral *et al*., 2016).

Every strong seismic event causes a series of sequel earthquakes which are known as aftershocks usually last for several weeks and even months until frictional ground equilibrium is re-attained in the rupture zone. Though the frequency of the aftershocks generally decreases with time, this process is by no means smooth and continuous. Over 672 aftershocks have been recorded following the April 25 main shock that occurred in the vicinity of the Kathmandu Valley (EERI, 2016). Most of the aftershocks were reported to be relatively shallow depth of less than 15 km below the Earth's surface. Based on co seismic InSAR study many researchers proposed ground deformation up to 1m for the Kathmandu valley using Sentinel 1-A and ALOS PALSAR-2 SAR images. SAR interferometry is the highly accurate technique to measure the ground deformations made by an earthquake event. However, it is very challenging due to generally unavailability of suitable interferometric data pairs having minimum baseline.

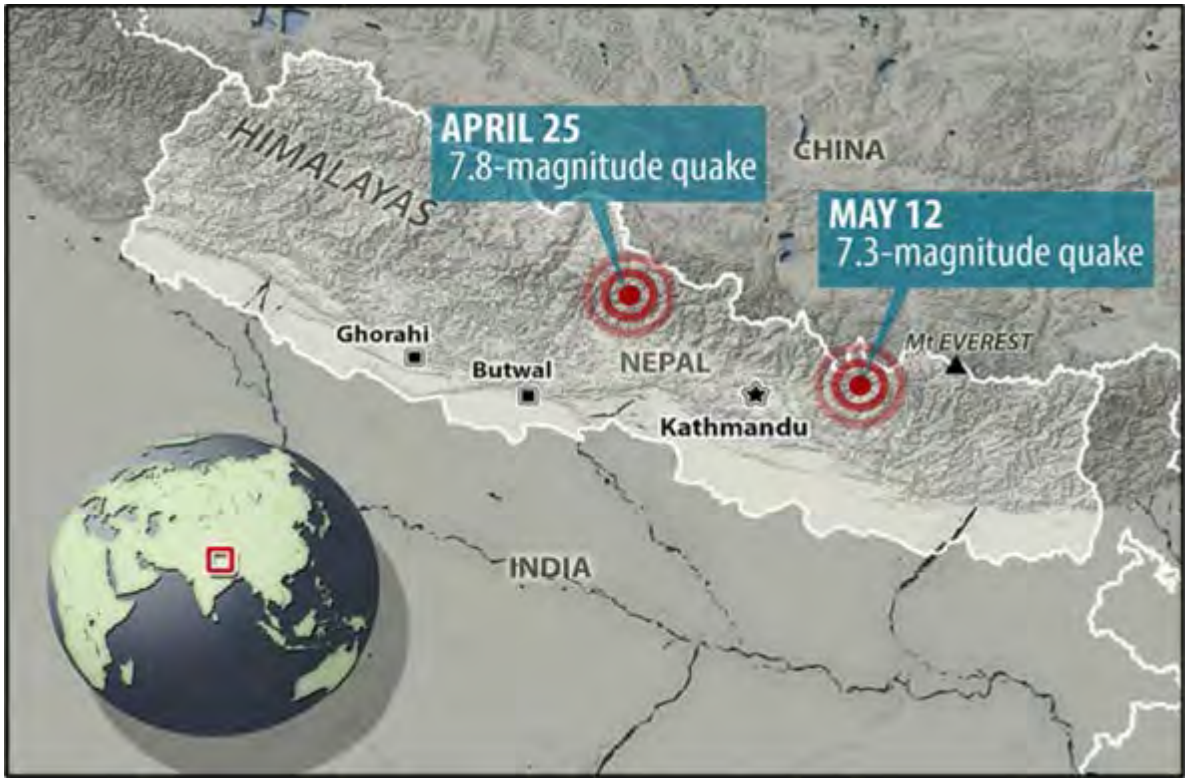

Figure 2.5: Location of 25 April, 2015 and 12 May, 2015 Nepal earthquakes. (Source: informationOverload-http://informoverload.com/wp-ontent/uploads/2015/05/ASAH_L.jpg).

2.6.1 InSAR Study (Post-seismic)

As a part of research work and to apply the interferometry technique post seismic deformation study has been done in case of Nepal 2015 earthquake. Earlier co seismic interferogram images were generated by many researchers using 9th April 2015, 17th April 2015, 29th April 2015, 3rd May 2015, 6th May 2015 and 18th May 2015 SAR images acquired by Sentinel-1A over the Kathmandu region (ESA Sentinel Online, 2015; Grandin, 2015; Yague-Martinez *et al*., 2016).

Accounting to the post seismic InSAR study, it was proposed that deformation up to 20 to 30 mm was taking place in Kathmandu valley even after few months of the main earthquake events. In case of Bhuj and Nepal earthquake post ground settlement and the related deformation becomes significant. In this study to site an example of post seismic surface deformation several data pairs of Sentinel 1-A image (Table 2.4) of the Copernicus mission by ESA are used for the interferometric study based on InSAR technique.

Table 2.4: Detail of Sentinel 1-A InSAR pairs for Nepal

Satellite	Acquisition Date	Orbit No.	Perpendicular base line in m	Time difference (In Days)
Sentinel-1A (InSAR)	03 May2015 (master)	5757	71.92	492
	06 Sept 2016 (slave)	12932		
	20 July 2016 (master)	12232	28.92	48
	06 Sept 2016 (slave)	12932		
	06 Sept 2016 (master)	12932	18.59	24
	30 Sept 2016 (slave)	13282		

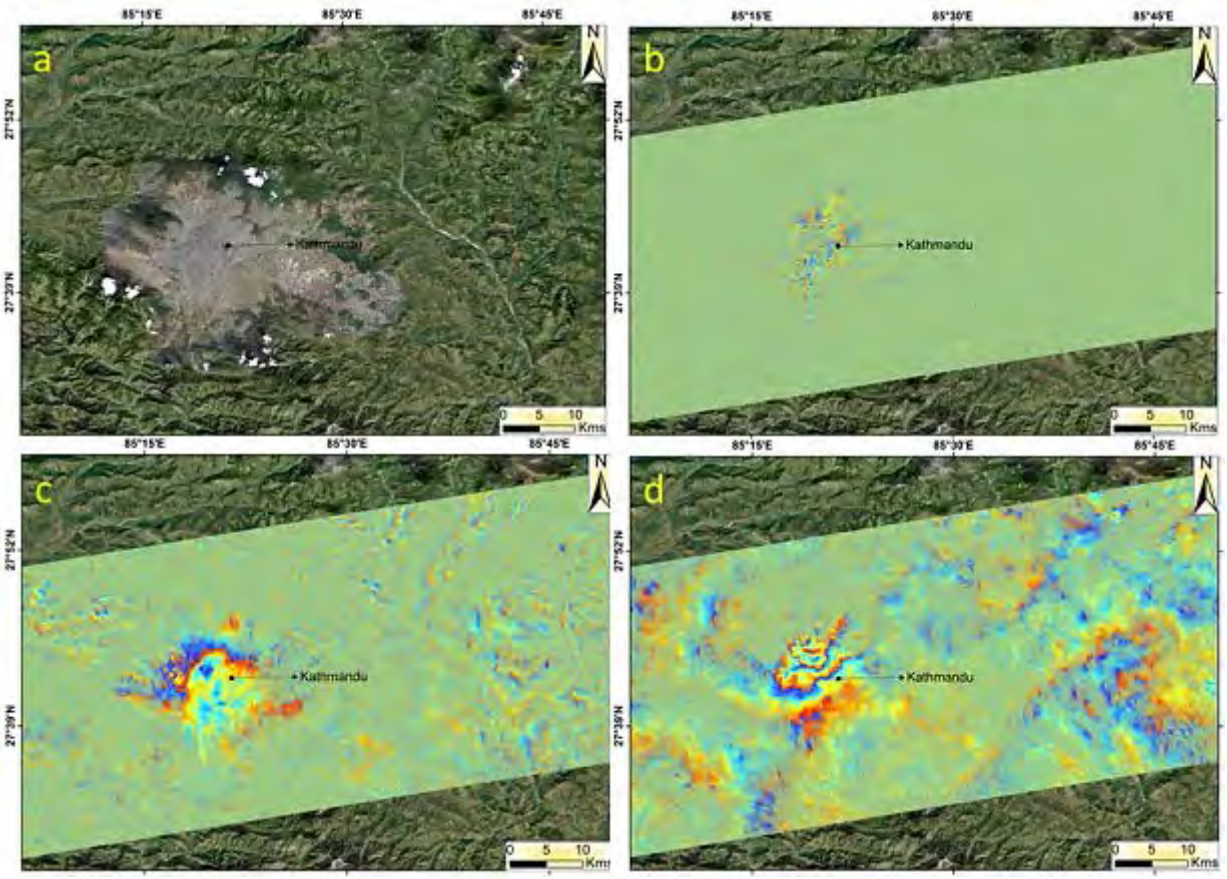

Figure 2.6: (a) Shows the location of Kathmandu valley, (b) Interferogram generated from 03 May 2015 and 06 Sept 2016, (c) Interferogram generated from 20 July 2016 and 06 Sept 2016, (d) Interferogram generated from 06 Sept 2016 and 30 Sept 2016.

Based on InSAR study the generated interferogram shows some deformation in terms of closely spaced number of fringes up to few mm in figure 2.6(b), as the SAR pairs are of large duration (492 days separation). In second case (Figure 2.6-c) the fringes are quite broad and show slow deformation (48 days separation). For the third pair (Figure 2.6-d), though the duration is of 24 days the deformation rate is comparatively high in terms of wide number of fringes. The interferograms clearly indicates post ground settlement in the Kathmandu valley.

2.7 Example: L'Aquila Earthquake (Co-seismic)

The L'Aquila earthquake took place on 6th April 2009 of Mw 6.3 (focal depth 8.8km). The epicentre was near L'Aquila, the capital of Abruzzo which is 75km west of Pescara (Italy), 85km in Rome's (Italy) North-East, 115km in Perugia's (Italy) South-East and 145km of Ancona (Italy). This earthquake was felt all over Central Italy. Around 300 people were died, 1000 injured and 66,000 made homeless and thousands of buildings were damaged and destroyed. Figure 2.7 shows epicentral location of 6 April, 2009 L'Aquila earthquake of Mw 6.3 (USGS).

In this case also interferometry technique tested and in order to have confidence in InSAR processing, much before the occurrence of Bhuj earthquakes of 2001, a sample datasets of Envisat-ASAR of 6th April 2009 L'Aquila earthquake was processed to generate interferogram and study the earthquake induced ground deformations. The above InSAR analysis has facilitated to analyse Bhuj earthquake datasets of Sentinel-1 satellite with ease.

In this study, SAR data pairs of Envisat satellite were processed. By using two SAR data pair interferogram images have been generated. The Interferogram was generated using 01 Feb 2009, 12 April 2009 and 11 March 2009, 15 April 2009 SAR data pair. Topographical effect was removed by using SRTM DEM. SAR data pairs are shown in Figures 2.8 and 2.9 respectively. Generally three interference fringe colour codes are generated which are cyan (C), yellow (Y) and magenta (M). In all the fringes, yellow colour remains in the middle part bordered by cyan and magenta. The specific arrangement of these colour codes disclose the nature of dislocation occurred on the ground. Each interferometric fringe corresponds to 2.8 cm ground deformation (half of the C band wavelength used, i.e. 5.6 cm) in the radar line of sight. In order to estimate upliftment or subsidence number of developed fringes in any area is to be multiplied with the 2.8 cm.

By using 1 Feb, 2009 and 12 April, 2009 data pair, the first interferogram image is generated (Figure 2.8) and it has been noticed that well defined interference fringes have developed (Figure 2.8). Interferogram indicates two lobes of deformation. Reading these fringes range from north to south in left lobe, the order of colours is CYM, the subsidence of about 25cm was indicated in that region. These fringes correspond to 25 cm of negative ground deformation. In right lobe a high damage was experienced using Envisat pre- and post-earthquake data pair of 1 Feb, 2009 and 12 April 2009 SAR, ground variations occurred between these two dates.

Second interferogram image (Figure 2.9) has been generated by using 11th March 2009 and 15th April 2009 data pair. It has been noticed that interference fringes have developed (Figure 2.9) exhibiting clear geometry. The order of colours fringes is CYM, which infers that subsidence of about 25 cm occurred in that region.

2.8 Optical Remote Sensing

Remote sensing in visual and infrared spectral range provides vital information about the terrain features in the image form. These features are then interpreted by thematic specialists to understand and carry out the necessary interpretation. Role of remote sensing in geomorphology has been extensively covered by several workers such as Fairbridge, 1968; Verstappen, 1977; Sabins, 1997; Lillesand, and Kiefer, 2000; Drury, 1998; Gupta, 2003; Ramasamy, 2005; Smith and Pain (2009); Tronin *et al.* 2002. Landform studies tries to understand the genesis of relief of the earth's surface and several aspects of geomorphology are the manifestation of geological processes (Krishna & Rai, 1996; Maiti & Bhattacharya, 2011; Pati *et al.* 2006; Chaudhary & Toleti, 2006). Terrain is the amalgamation of landform, ecology, vegetation cover, human action, natural and tectonically disturbed landscape. These effects can be interpreted very effectively through remote sensing technique and any modification that occurs on the landscape is expressed efficiently through temporal coverage of the same area.

Table 2.5: Envisat ASAR L'Aquila Dataset used in analysis of ground deformation.

Pair	Date	Time	Track	Orbit
1	01.02.2009	09:24:28	079	36205
	12.04.2009	09:24:27		37207
2	11.03.2009	20:47:46	129	36756
	15.04.2009	20:47:42		37257

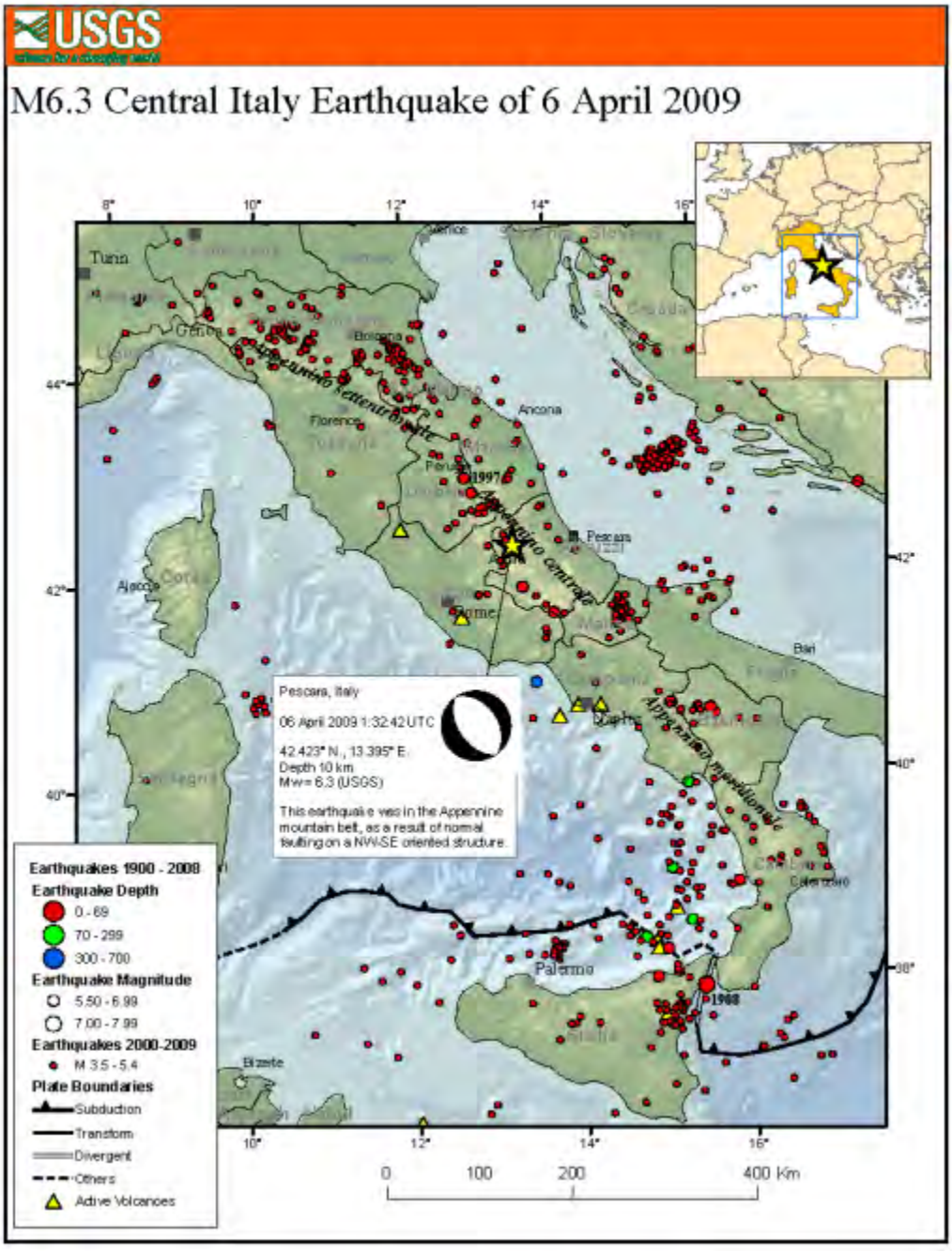

Figure 2.7: Epicentral location of 6 April' 2009 L'Aquila earthquake of Mw 6.3 (Source- USGS- earthquake.usgs.gov).

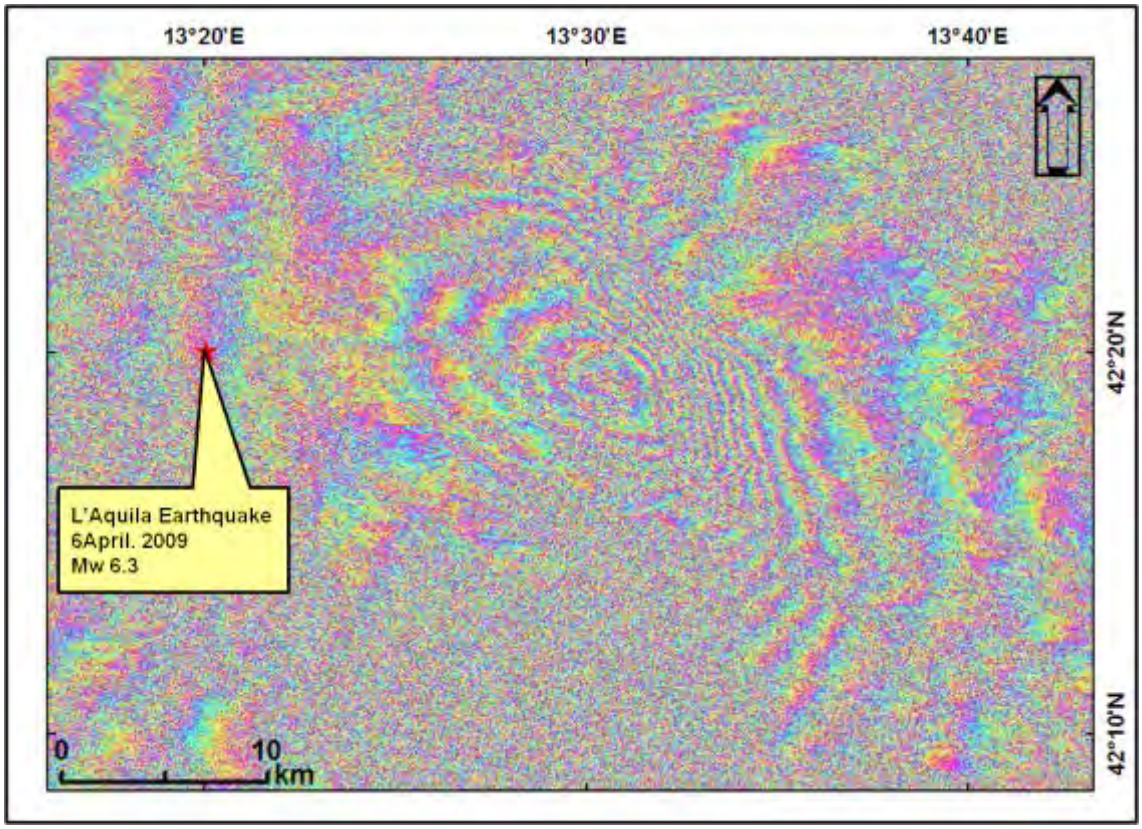

Figure 2.8: Interferogram of 6 April 2009 L'Aquila Earthquake using 1 Feb 2009 and 12 April 2009 pre-and post- earthquake SAR data pair.

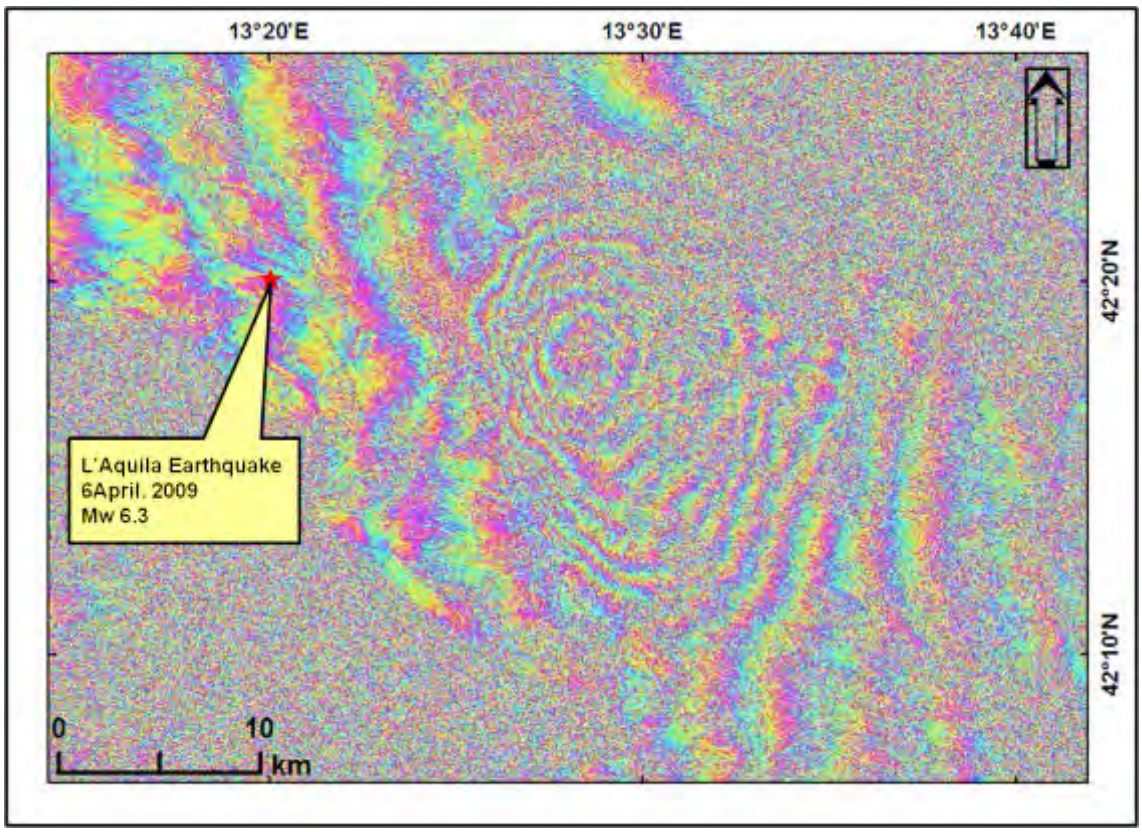

Figure 2.9: Interferogram of L'Aquila Earthquake using 11 March 2009 and 15 April 2009 pre-and post- earthquake SAR data pair.

Better spatial and spectral resolution of the satellite images that is available today generates higher contrast level among the objects thereby facilitating convincing identifications and interpretations. Less than 1m resolution images are today providing every detailed information of the features whereas 15 and 30m resolution image can produce significant information about the terrain covering larger areas. Further, one can study satellite images of various spatial resolutions. Spectral multi-bands such as visible and infrared ranges are generating images of the objects differently as the earth features are differently sensitive to the different wavelengths. The users are in a position to choose a particular spectral band data or in a combination depending on the requirements. Moreover, digital enhancement can also be carried out to make particular feature more prominent than the surroundings. According to Higgitt and Warburton (1999) the remote sensing technique can provide insight in geomorphology in four ways; (i) new application for geomorphology, (ii) improved accuracy in measurement, (iii) new data and new ideas for investigation and (iv) development of data processing capabilities. Digital image processing and terrain analysis has become an essential requirement in land and forest management (Slaymaker, 2001). Remote sensing based quantitative assessment of the geographic distribution of major landforms is done by Bocco *et al*., (2001). Rao (2002) has studied geomorphology of the foothills of Siwaliks (Doon valley), Mahanadi Brahmani delta system and Kanha national park area using remote sensing technique.

Kutch region of Gujarat as represented using different satellite and different resolutions (Landsat 1, 4, 7 and 8) from 1978 to 2014 to depict the terrain nature (Figures 2.10 to 2.14). Figure 2.10, 2.11, 2.12, 2.13, 2.14 and 2.15 are the FCC image from 80m, 30m, 30m, 30m and 5.8m spatial resolution MSS, TM, ETM, OLI and LISS IV MX images form Landsat-1 (1978), Landsat-4 (1989), Landsat-7 (2001), Landsat-8 (2014) and Resourcesat-1 (2007) respectively. Figure 2.14 is a true colour composite of Google Earth Digital Globe image. These temporal images show the effect of better spatial and spectral resolution with time. Figure 2.16 a, b, c & d are the enlarged small part of the above images (Figures 2.10 to 2.14) showing effect of improved resolution in imaging technology.

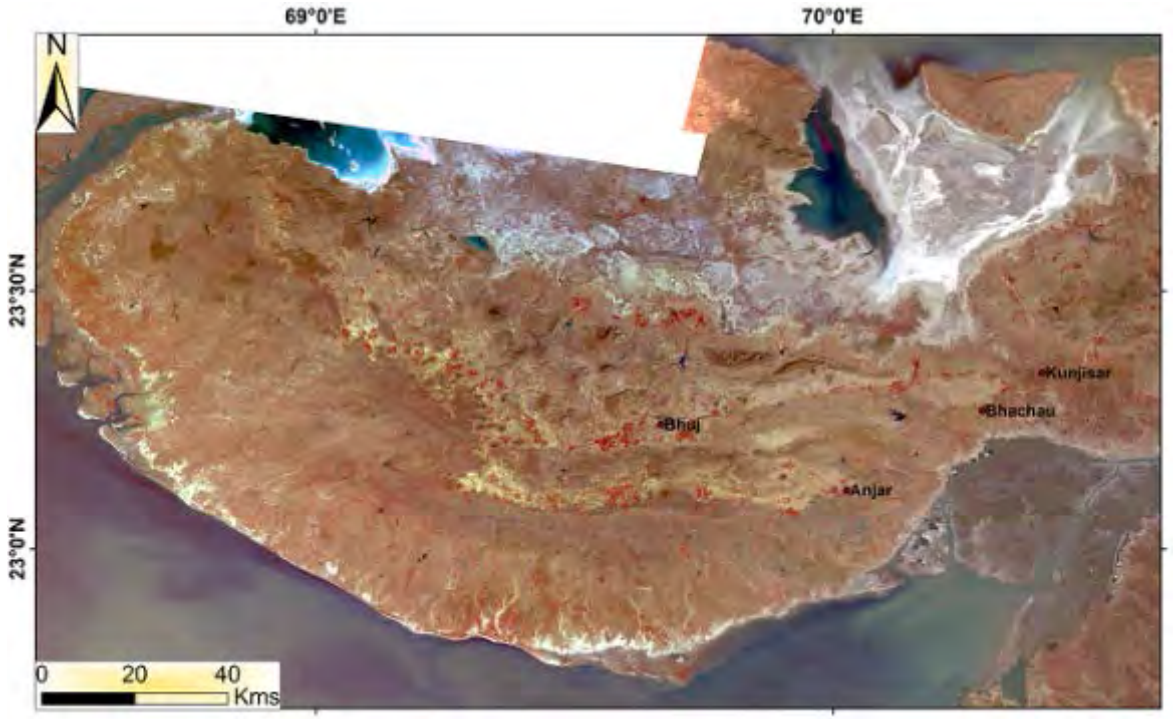

Figure 2.10: Mosaic FCC Image of Landsat-1 MSS image of 1978.

Figure 2.11: Mosaic FCC Image of Landsat-4 TM image of 1989.

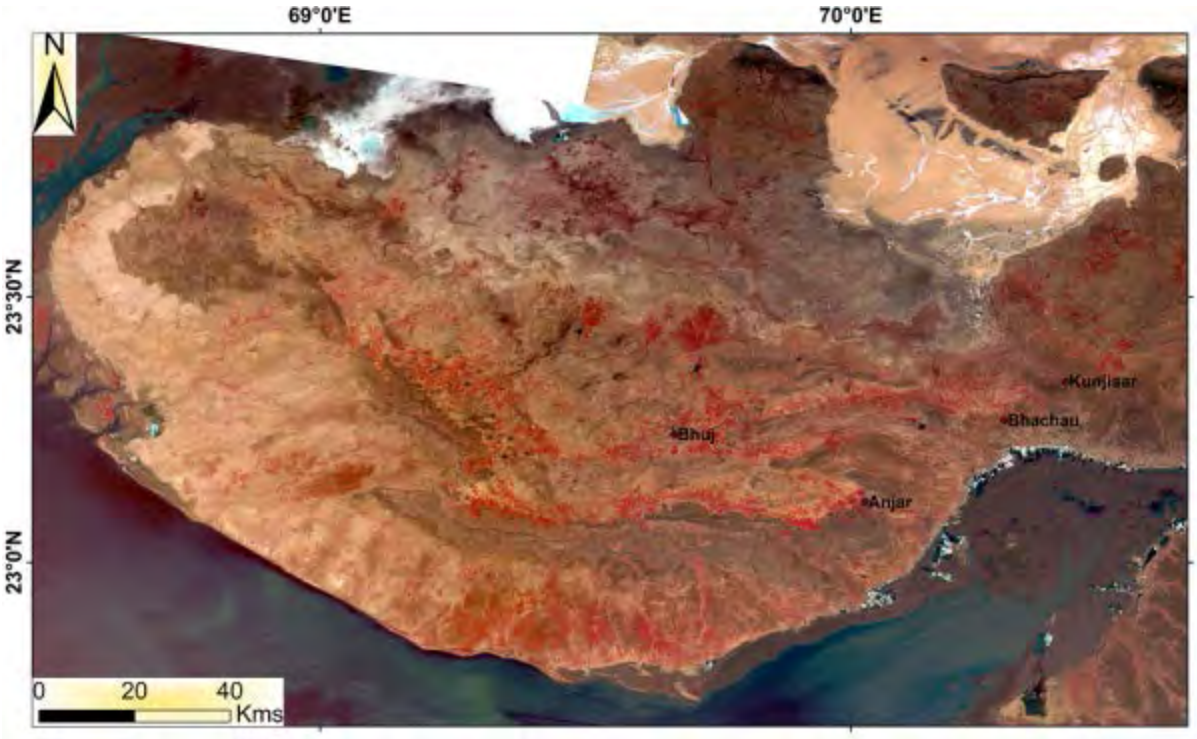

Figure 2.12: Mosaic FCC Image of Landsat-7 ETM image of 2001.

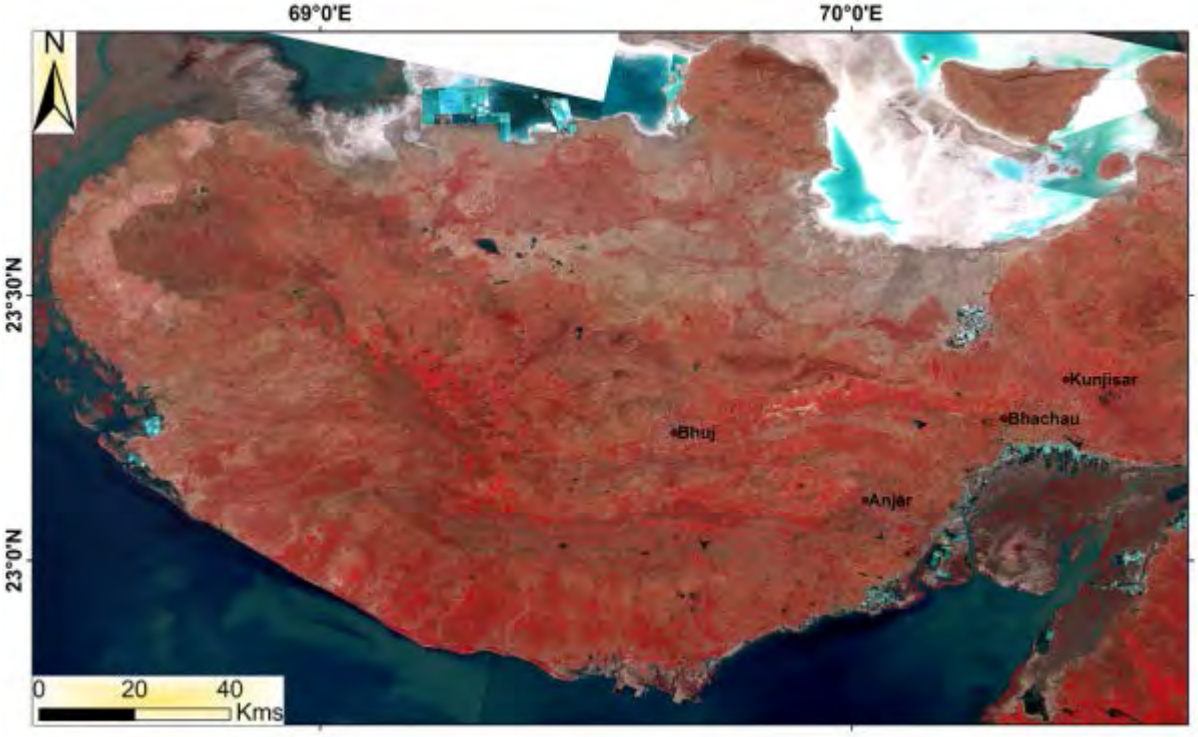

Figure 2.13: Mosaic FCC Image of Landsat-8 OLI image of 2014.

Figure 2.14: True colour composite Google Earth Digital Globe image.

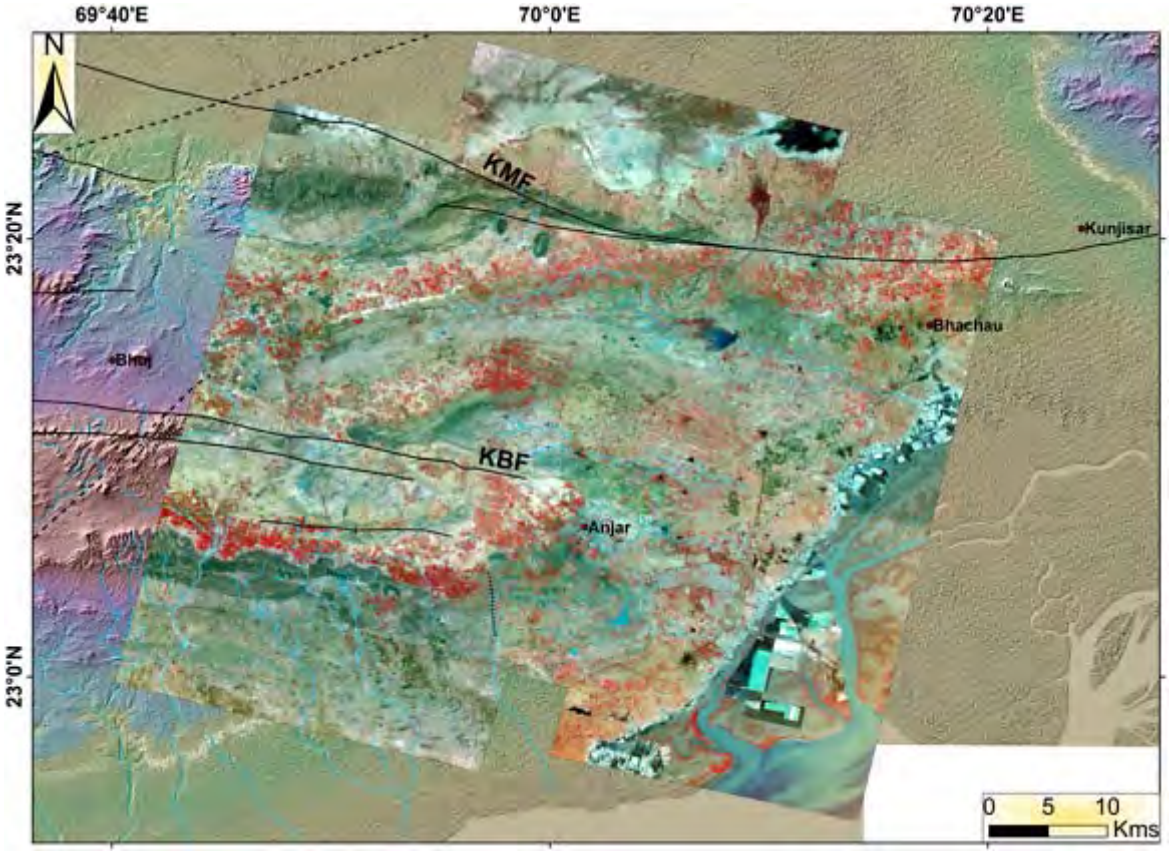

Figure 2.15: Mosaic FCC image of LISS 4 MX of eastern Kutch region covering Anjar and Bhachau area.

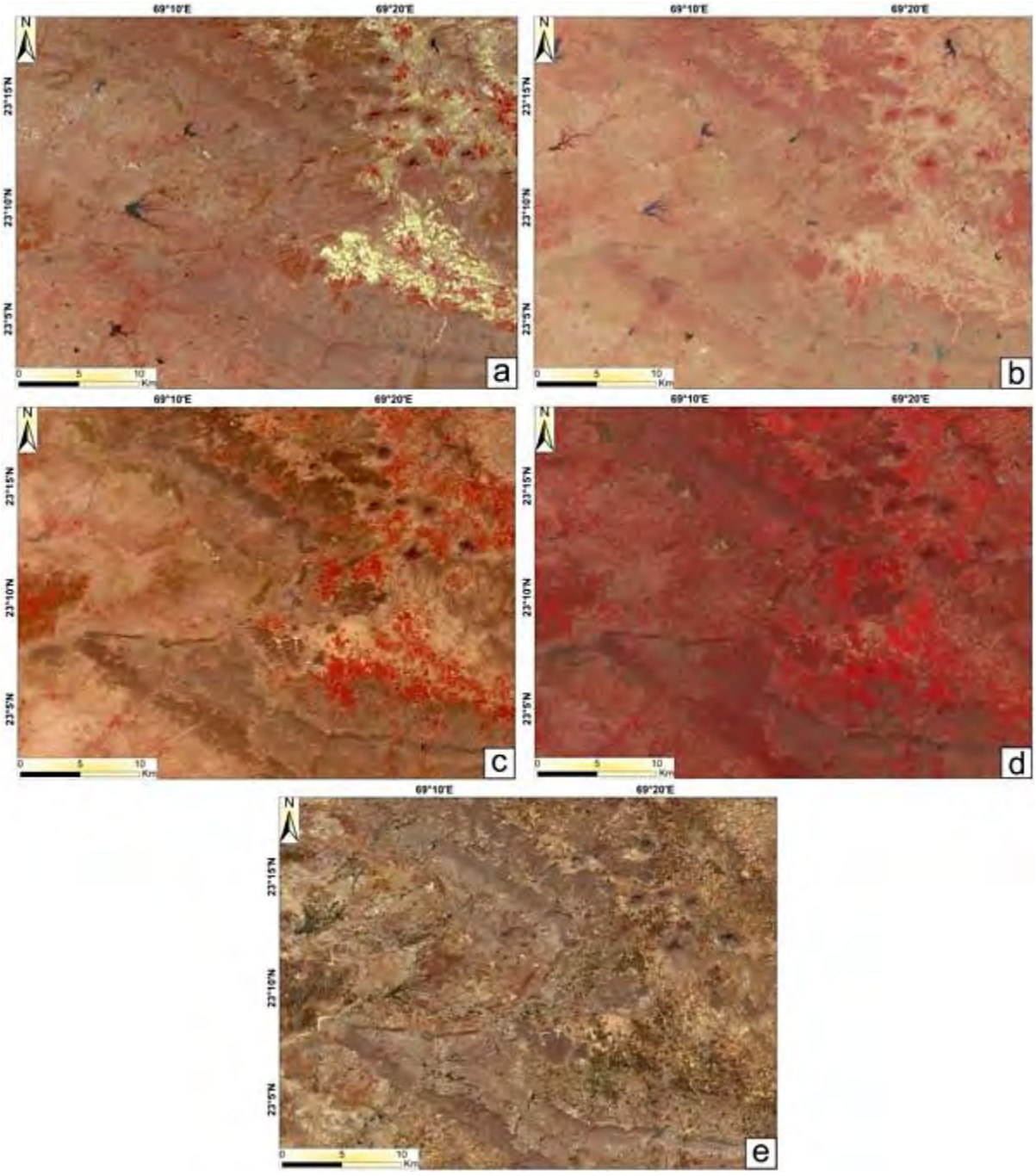

Figure 2.16: Showing effect of improved resolution in optical remote sensing.

2.9 Morphotectonics and Morphometry

Morphotectonic integrates topography and tectonic activity to describe landforms generally at continental, sub-continental and even at local scales. It includes the study of mountains, drainage patterns, erosion surfaces, and sediments on land and offshore. In recent years, substantial advances have been made in the fields of morphotectonics, and neotectonics especially with the advancement of remote sensing technique. Further, the with the help of satellite geodesy and application of geophysical tools for dating quaternary materials combined with wide range availability of high resolution digital topography have developed our ability to resolve the impacts of active tectonics and surface processes on sculpting the Earth's surface. Recently, many earth scientists have shifted emphasis from classical geologic, structural and tectonic explorations to investigations of neotectonics and landscape evolution, further increasing our understanding of surface kinematics and the consequential surficial change expressed as the land surface morphology.

The morphometric studies have now been combined by studies of the relationship between global tectonics and geomorphic evolution. Oilier (1981) has proposed the term 'evolutionary geomorphology' for this portion of earth-science. In recent years, in the field of remote sensing and GIS, researchers stressed primarily on the deformed landforms for morphotectonics. With the availability of digital elevation model, high resolution satellite data and topographical maps it becomes possible to extract little variations.

2.10 Geomorphic constraints on the active tectonics

In the last decades, the urge towards the development of quantitative geomorphology has shown the way from improved statistical and mathematical models to define different geomorphic processes (Scheidegger, 1961; Evans, 1972; Anhert, 1973; Mark, 1975). A varied range of work has outlined the utility of quantitative geomorphic estimations in interpreting morpho-evolutionary processes in the tectonically active regions (Avena *et al*., 1967; Buonasorte *et al*., 1991; Pike, 1993; Lupia Palmeiri *et al*., 1995, 1998, 2001; Centamore *et al*., 1996; Jasrotia *et al*., 2012; Maiti, 2013). Quantitative methodologies have shown their utility in detecting neotectonic effect on geomorphic processes through the application of statistical parameters (Keller *et al*., 1982; Ciccacci *et al*., 1986; Mayer, 1990; Cox, 1994; Merritts *et al*., 1994; Belisario *et al*., 1999; Currado and Fredi, 2000).

Study of interior tectonic forces that shape the topography of the earth surface is very difficult. Hence, most researchers have used digital topography to search for the symptom of active deformation preserved in the local geomorphology. The active tectonics and landscape evolution of the southern Taiwan on the basis of drainage anomalies and deviation of major river systems have been studied by Ramsay *et al*. (2007). Active normal faults evolution in Greece is revealed by geomorphology and drainage pattern (Goldsworthy and Jackson, 2000). Walker and Jackson (2002) have identified 3 km horizontal fault offset of Gawk fault, a major intra-continental strike slip system in SE Iran from well preserved geomorphology.

2.11 Tectonic features and Neotectonics

By using various techniques and parameters morphometric analysis is carried out. Study on intensity of tectonic activities prevalent in any region becomes important. Hantke & Scheidegger (1998) carried out morphotectonic study of Massacre Island in Indian Ocean on the basis of alignment (strike, trend) of joints, valleys, ridges, faults, and lineaments. Jain *et al*. (1998) studied the neotectonics of western India using the evidence from deformed quaternary fluvial sequences of Mahi River in Gujarat. Based on several geological-geophysical and geomorphological methods a morphotectonic analysis of the relief of Iberian Peninsula (IP) is studied by Cotilla and Cordoba (2004) so as to build up a morpho-structural sketch. From their observation, they described that earthquake occurrence in the Iberian Peninsula is mainly due to the concentration of stress around morphotectonic zones and great seismic activity is found near the second and first order lineaments. Devi and Singh (2006) investigated the morphotectonics of the Arunachal Himalaya on the basis of neotectonic deformation of Ganga Lake located in Itanagar capital complex.

It has been studied and well explained that earthquake occurrence in Hispa niola is related with the stress concentrations in the vicinity of morphotectonic zones (Cotilla *et al*., 2007). A comparative morphotectonics in the Himalayan foreland and the fore-arc of southwest Japan was proposed by Kimura (2004). Mukherji and lyer (1999) studied morphotectonics and volcanic of the central Indian Ocean and explained that a distinct relationship occurs between the morphotectonic forms and the volcanic and perceived two types of volcanic activities. Morphotectonic study of Psathopyrgos active fault, which is located at the western end of Corinth Rift, Greece was conducted by Tsimi *et al*. (2007). Their observations suggested that these areas have experienced very recent uplift and strong down cutting due to bi-directional fault development. The tectonism has been a major controlling mechanism for topographic and

landscape development have been demonstrated by neotectonic study of different regions (Garcia-Melendez *et. al*., 2003; Dumont *et. al*., 2005).

2.12 Geomorphic marker and associated deformation

Geomorphic markers are identifiable landforms, surfaces or linear features that provide a reference frame for deformational history. According to Marshall and Anderson, 1995, they can be easily compared with their modern counterparts for variation in morphological parameters. Reconstruction of deformed markers is essential for reliable results.

To document faulting and folding, river terraces are commonly used as geomorphic markers (Molnar *et al*., 1994; Rockwell *et al*., 1984). River terraces are very useful in evaluating the vertical as well as horizontal deformation. Alpine glaciation fluvial terraces have been used to compare with moraines associated with glacial advances or still stand for years (Penck and Bruckner, 1909). The terrace crossing the San Andreas Fault in California near Cajon pass potentially illustrates the complex nature of terrace formation (Weldon, 1986). The comparison between terrace surface and the modern day stream gradient, states that it appears to have been warped more than 30m, although it is not physically dislocated along fault. Dating of sediments indicates that both the initiation of aggradation and incision are diachronous. River terraces which are same as alluvial fans do not immediately or uniformly changes in controlling parameters like sediment supply, discharge, rock uplift rate and base level lowering (Humphrey and Heller, 1995). Surface processes may tend to transform the appearance of alluvial fans (McFadden *et al*., 1982; Ritter *et al*., 1993). Whipple and Dunne (1992) observed that many arid alluvial fans are dominated by deposition from debris flows. Even surfaces with considerable roughness, can be used as effective markers, because in spite of its irregularities the average surface gradient can be defined (Avouac and Peltzer, 1993), and offset of the gradient by faulting can be readily predictable. Lava flows, landslides, debris flows, and erosional surfaces can provide excellent markers (Weldon, 1986; Small and Anderson, 1998). In central Asia, Tien Shan is regionally extensive erosion surface which was bevelled across Paleozoic rocks and suppressed by Cenozoic sedimentary rocks (Chediya, 1986; Sadybakasov, 1990). It offers an exceptional sign for recording faulting and folding of ranges that grows above the surrounding terrain (Burbank *et al*., 1999). A location for standardizing the amount of erosion is not only the erosion surface but itself the uncomfortable surfaces that has encountered beneath it (Small and Anderson, 1998). The displacement along ridge

crests across strike-slip faults and through courses of river can evidently record lateral offsets (Beanland and Clark, 1994).

2.13 River responses to the active tectonics

Alluvial rivers are very sensitive to the variation of slope gradient of a region. By the process of aggradation and degradation along fault line, streams respond to vertical displacement. Aggradation and degradation can be seen on the upstream from the horst and the downside part of the horst respectively (Cartier and Alt, 1982). In the course of a river slow rates of upliftment can cause more channel adjustment by widening and meandering (Ouchi, 1985). DEMs are capable to provide a framework followed by conceptual and empirical models among stream power, channel gradient and the form and dynamics of water channel systems. The shape changes at critical values of gradient, stream power, and sediment load (Schumm and Khan, 1972). Hooke (1995) has studied the adjustment to meander cut-offs on the River Bollin and River Dane, NW England.

2.14 Drainages and stream networks anomalies

By analysing the drainage basin asymmetry, neotectonic activity of a region can be understood followed by young and weakly consolidated sediments (Cox, 1994) if the drainage pattern is sensitive indicator of active tectonics (Jackson and Leeder, 1994). Tectonic deformation results shift in river channel, change in channel slope, position, and variation in fluvial processes, hydrological characteristics and channel morphology of a river system.

Local scale variation in regional slope can cause anomalous drainage pattern. Experimental studies showed that parallel drainage pattern form on the slopes greater than 2.5 percent, whereas dendritic pattern forms on the gentler slopes (Philips and Schumm, 1987). Changes of entire drainage network, with the effect of sloping, are described by Sparling (1967). Topography and drainage system in regions of active deformation results in aspects of faults growth (Cracknell & Hayes, 1991; Medwedeff, 1992; Mueller and Tailing, 1997; Delcaillau *et al*., 1998; Tate *et al.*, 2002; Burbank and Anderson, 2001; Husson and Mugnier, 2003; Delcaillau, 2004; Gupta and Ellis, 2004).

Different Geomorphic indices are capable in detecting landform responses to neo-tectonic activity and deformational processes and therefore have been broadly used as a recognition tool to describe sectors deformed by active faults (e.g., Seeber and Gornitz,

1983; Brookfield, 1998; Keller and Pinter, 2002; Chen *et al*., 2003; Kobor and Roering, 2004).

Morphometric indices are the proxy indicator of dynamic tectonic prevailing in the regions where the changes are gradual and drainage anomalies are not prominent (Pedrera *et al*., 2009). Some geomorphic indices have been established as basic identifying tools to recognise areas undergoing rapid tectonic deformation. The most useful tools in studies of active tectonics are the hypsometric integral, stream sinuosity, drainage basin asymmetry, stream-gradient index, slope gradient index, mountain front sinuosity, basin elongation ratio and ratio of valley floor width to valley height (Keller and Pinter, 1996). Stream sinuosity, proposed by Muller (1968) helps in understanding the ongoing tectonical activity of a region (Susan, 1993). The channel-gradient reflects the slope change of a stream longitudinal profile, which may reflect tectonic activities (Merritts and Vincent, 1989; Rhea, 1989; Marple and Talwani, 1993; Brookfield, 1998). Hypsometry is the relative ratio of an area at different elevations within a river basin and may be sensitive to various forcing factors such as lithology, tectonics and climate (Lifton and Chase, 1992). The stream length-gradient index (SL index) has been commonly used to investigate gradient change of a stream longitudinal profile and is believed to reflect stream power (Hack, 1973). Generally, it is very sensitive to changes in channel slope and is applied to evaluate relationships between rock resistance, topography and possible tectonic activity, (Keller and Pinter, 1996). Basin elongation ratio is proposed as one of the proxy indicators of recent tectonic activity (Cuong and Zuchiewicz, 2001, Bull and McFadden, 1977).

2.15 Remote Sensing and GIS approach in morphotectonic analysis

Geomorphology and landform characteristics can be well understood from remote sensing images of high and coarse resolution images. Spatial information obtained from aerial photographs, satellite data topographic maps along with morphotectonic indices can well describe tectonic history of a region (Keller, 1986). Significant development in resolution of satellite data and advancement in GIS resources has enabled researchers to carry out quantifiable and more precise analysis of various landforms. Verrios *et al*. (2004) carried out morphotectonic study for Eliki fault zone to correlate active tectonics with erosional processes using topographic maps and aerial photographs. Cuong and Zuchiewicz (2001) studied the morphotectonic characteristics of Lo River fault near the Tam Dao in North Vietnam. Jain and Verma (2006) applied integrated remote sensing and GIS technique to identify geomorphology, slope, and vegetation index to assess neo-

tectonic potential in Bundi-lndergarh sector of Rajasthan. Morphotectonics of Anandpur Sahib area of Rupnagar district (Punjab) was studied by Bhatt *et al*. (2007) using remote sensing and GIS approach.

Using Remote Sensing data products, Dalati (1994) has studied the tectonic of EI-Rouge Depression, NW of Syrian Arab Republics. Ramasamy (2006) and Ramasamy *et al*., (2011) studied mega drainage characteristics, tectonic, hydrological and geomorphic anomalies based on satellite images for whole peninsular India.

Morphological analysis of topographic features, like minor faults and lineaments, has long been applied in structural and tectonic studies (Hobbs, 1912; Frisch, 1997). Satellite images show great ability as a tool for mapping and correlation of alluvial geomorphic surfaces (Gillespie *et al*., 1984; Kahle *et al*., 1984; Anderson and Beratan, 1993, 1994; Chaudhary *et al*., 1996).

2.16 DEM based morphometric studies

DEMs derived from microwave (SAR Images) and optical images have several applications in various fields. The potential of DEMs for solving a wide spectrum of applied and theoretical problems has long been known (Evans, 1972). Its simple data structure and widespread accessibility have made it a popular tool for land characterization. DEMs derived from the ASTER (Advanced Spaceborne Thermal Emission and Reflection Radiometer) stereo data (GDEM), Shuttle Radar Topographic Mission (SRTM) and ALOS-PALSAR (Advance Land observing satellite with Phased Array type L-band Synthetic Aperture Radar) geo-corrected is now freely available for whole world with a resolution of 90m, 30m and 12.5m in 3 arc and 1 arc second tiles. These products can be very useful for research purposes as well as to supply basic topographic mapping data for poorly mapped areas (Rabus *et al*., 2003). SRTM-DEM's Accuracy assessment is carried out by various workers using different approaches (Sun *et al*., 2003; Miliaresis *et al*., 2005; Kocak *et al*., 2005; Sharma *et al*., 2010; Baral *et al*., 2016). DEM has a vital role in morphotectonic analysis as they are most widely used for representing topography. Moreover, DEM also displays the tectonically affected topography in better way. Most of the morphometric studies applying DEM use shaded relief models jumbled with remotely sensed data products over a wide region (Florinsky, 1998; Chorowicz *et al*., 1999). For better understanding three dimensional perspective views with image drape (Le Turdu *et al*., 1995) has been used by researchers. Chorowicz

et al. (1991) used DEM to calculate dip and strike from geological maps. Koike *et al*. (1998) calculated fault plane geometries from DEMs. Florinsky (1998) studied the connection between fault type and landform followed by use of curvature maps to recognize and characterize fault line. Onorati *et al*., (1992) used aspect and slope calculations in a regional morphotectonic investigation.

Jordan *et al*. (2005) suggest a technique for the reliable application of digital terrain analysis technique to classify tectonic phenomenon from geomorphological parameters in Hungary and NW Greece. Zizioli (2008) studied the DEM-based morphotectonics analysis of Western Ligurian Alps exhibiting a typical drainage network related to the geological events. They have used advance GIS based approach to extract the morphotectonic lineaments, drainage characteristics and neotectonics of the Lingurian Alps.

Chapter 3

Regional Geology, Tectonics and Geomorphology of the study area

3.1 Introduction

The landscape of Kutch is one of the most unique examples of active intraplate region enduring rift reversal. The basin formed in early Jurassic time which is marginal cratonic in nature and later on received sediments, as the Indian plate was moving north-eastward after the rifting (Biswas, 1982 and1987). Since that time, the basin has never attained stability and is continuously subjected to many tectonic deformations. The basin has thick fill of sediments of Mesozoic and Cenozoic which is intervened by the Deccan Trap. The Cenozoic rocks of Kutch are exposed for about 3000 sq. km. as a semi-circular outcrop fringing the Deccan basalt. The rift basin is filled with syn-rift middle Jurassic to Early Cretaceous sediments and post-rift filled sediments characterized by Late Paleocene to Pliocene and Quaternary sediments. The Deccan Trap volcanism and post-rift inversion uplift marks the Late Cretaceous to Early Paleocene break in sedimentation. Based on the Litho, Bio, and Chrono- stratigraphy, many researchers developed new stratigraphy concept with different conceptual models. The Kutch rift basin comprises of major and minor faults, lineaments and scarps. Based on the elevation pattern of the basin, it is divided into different high and low lands along with typical characterized plains.

3.2 Geologic and Tectonic Setup

The Kutch basin in Gujrat, Western India is a pericratonic rift basin in Western continental margin of India (Figure 3.1). Geologically, the Gujarat region is represented by Precambrian to Recent rock formations and probably the geological evolution initiated sometime in the Triassic period coinciding with the rupturing of Gondwanaland. The Kutch region played a significant role in the Mesozoic and Cenozoic times marked by intense tectonic activities. Because of folding and faulting, the Mesozoic sedimentary rock mass is forming higher uplifted areas. These highlands are surrounded by the gently dipping Tertiary strata forming plains of the region (Biswas, 1980). The base of the Mesozoic strata is well exposed in Meruda Hill of the Great Rann (Biswas and Deshpande, 1970). Various uplifted lands occurring extensively in Kutch Mainland are constituted by the Mesozoic rocks (Figure 3.1).

Kutch and Saurashtra region (Gujarat, India) has mainly occupied by Deccan trap rocks. The Deccan volcanism caused reactivation of the Narmada geofracture and rifting of the Western Continental Margin (Figure 3.2). The Saurashtra region is configured by fractures related to the three major bisecting rift trends viz., Delhi (NE-SW), Narmada (ENE-WSW) and Dharwar (NNW-SSE) and represent a horst structure (Biswas, 1987). The coastal sides of the landmass are bounded by faults. A NW-SE trending fault which is part of West Coast Fault System marks the S-W coast line (Merh, 1995) and the northern side is marked by the E-W trending Gulf of Kutch fault. The southern coast is aligned with the Narmada geo-fracture. The Saurashtra region has been affected by numerous lineaments. ENE-WSW trending lineaments are also affecting the trap rock in the region. These fractures control some of the river courses. Closely spaced ENE-WSW trending cluster of lineaments affects the trap rock of this region and the rocks are sliced by these features in particular fashions.

The north-western margin has been placed alongside with the Sind-Baluchistan geosynclinal belt (Biswas, 1987). This tectonic set up comprises of block faulting and folding along the marginal region. A series of uplifts along the master faults marks the Kutch region and folded, faulted and igneous rock intruded Mesozoic strata of the region. Faulted margins of the uplifts are marked by narrow linear zones of structural folds. Further, this tectonised zone is also recognised by different features like the occurrence of a string of asymmetric domes, igneous intrusions, brachy anticlines (Karanth *et al*., 2001). The Kutch mainland's northern limit is the WNW-ESE trending Kutch Mainland Fault and this fault was responsible for southward tilting of the mainland. In the south, the Gulf of Kutch fault is bounded by the Kutch mainland. Other prominent faults of the region are Little Rann of Kutch fault system, Katrol Bhuj Fault, and Island Belt Fault which played significant role in the post-Mesozoic geological evolution (Figure 3.4). It is believed that several features control the post-Mesozoic geological and geomorphological evolution of Kutch mainland (Biswas, 1980, 1982, Biswas and Deshpande, 1970) namely, Vigodi Fault, Katrol Hill Fault, Little Rann of Kutch Fault system, Bhujpur Fault, Naira River Fault, Vinjhan Anticlinal nose, Vinjhan Fault, and Narayan Sarovar Antclinal nose, Kothara embayment, Gulf of Kutch embayment, Bhachau Anticlinal nose (Figure 3.4). They controlled the geomorphological evolution and the post-Mesozoic geological evolution.

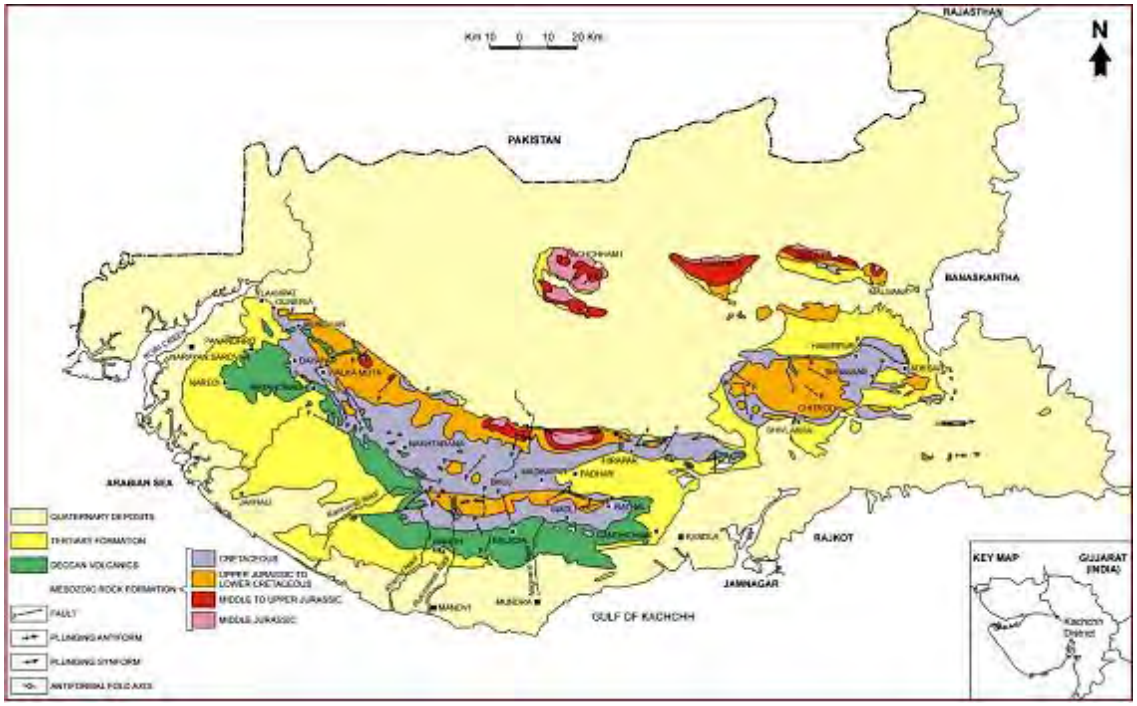

Figure 3.1: Overview of the geological and tectonic settings of Kutch region (Source: GSI, 2001).

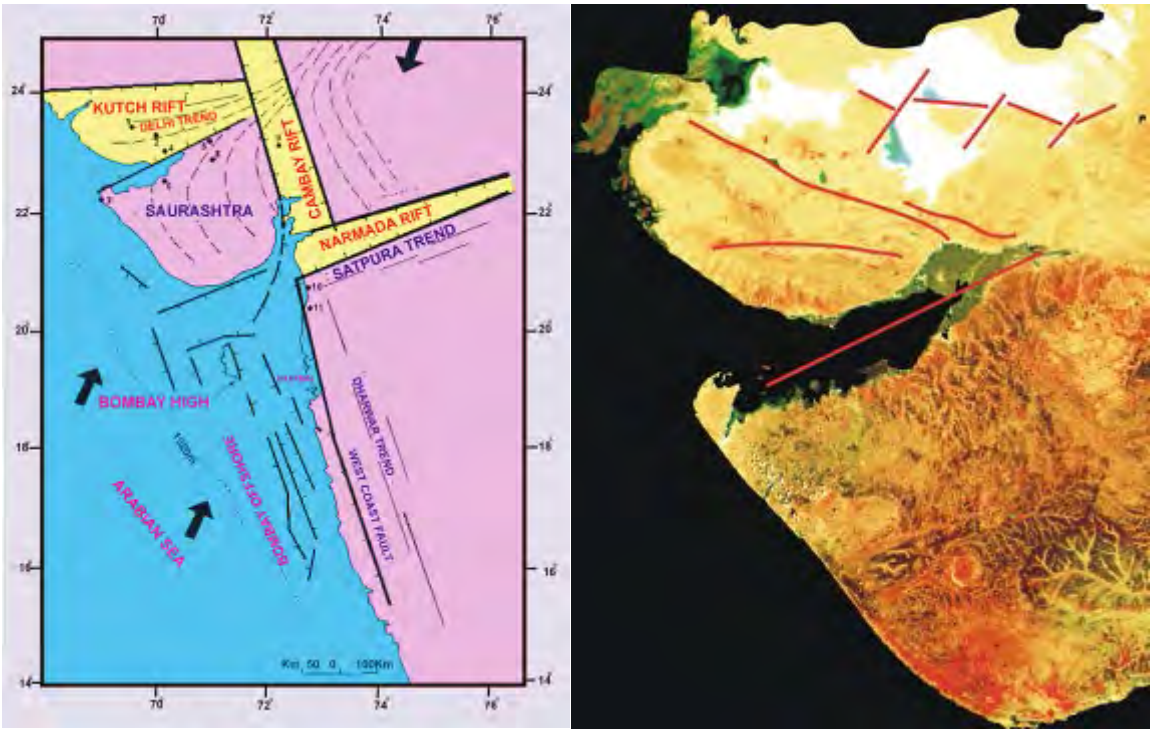

Figure 3.2: Rift system of Western India and major Precambrian trends (Left), Kutch rift and Saurastra shown on true colour Landsat satellite image (Right) (Biswas, 2005).

The Cambay graben bounded by the curvilinear marginal faults on two flanks is a significant subsurface tectonic feature of the region (at the eastern side of the study area). In the eastern side of the fault a high throw is present. Faulting magnitude is as much as 3000-5000m in this graben in the Deccan trap (GSI, 2003). Due to extension of marginal rifting along Dharwar trend the Cambay graben has formed (Biswas, 1982). This was formed due to the fracturing of Kathiawar land from Kutch mainland and bounded by the Cambay rift in the east and Kutch rift in the north. Geophysical data reveals that Bharuch has the deepest basin part and the trap surface is delineated at around 6000 meters. En-echelon faults paralleling the Dharwar trend and the Aravalli and Narmada trends are covering this graben. It is also found that the due to right lateral movement, the Cambay basin is displaced westward along the Son-Narmada fault. Currently thick sequence of Tertiary sediments fills the Cambay basin beneath the alluvial cover.

3.3 Geomorphic feature

The Kutch landscape is characterised by highlands surrounded by low lands (Figure 3.4 and 3.6). The lowlands are intervening sediments filled half-grabens whereas highlands are tilted uplifts along the faults. Highland are characterised by hilly terrain with peripheral coastal plains where the intervening lows are extensive mud and salt flats (playas and salinas). There are marked six high lands: Kutch Mainland in the south, Wagad in the east, Pachham, Khadir, Bela and Chorar in the north forming an E-W chain of small highlands. These four islands are referred as “Island Belt” (Biswas, 1971) (Figure 3.3). The major structural lows are Gulf of Kutch between peninsula and Mainland, Banni grass land between Mainland and Pachham and Great Rann of Kutch between Island Belt and Nagar Parkar Ridge. In the Eastward ending with the mudflat, is named as the Little Rann of Kutch, between Kathiawar and Wagad highlands (Figure 3.6). The characteristic rocks exposed in the highlands are of Mesozoic (Middle to Upper Jurassic) bordered by the Tertiary and Quaternary rocks.

3.3.1 Kutch Mainland uplift (KMU)

It is the biggest uplift in Kutch rift basin (Figure 3.4). The uplift plunges west (Lakhpat and Narayan sarovar noses) towards Arabian Sea and on the East towards little Rann of Kutch (Bhachau and Anjar noses). The block is tilted towards south along KMF. The uplift is marked by four structural zones: Northern Range Deformation Zone (NRDZ), Charwar Range Deformation Zone (CRDZ), Vigodi Gugriana Khirasra Deformaton Zone (VGKDZ) and Peripheral platform having peripheral plains with Tertiary strata (Biswas, 2016).

3.3.2 Wagad Uplift (WU)

The WU is marked along the South Wagad Fault in the Eastern part of Banni plain (Figure 3.6) is the second large uplift in the basin. It is an E-W trending large domical uplift bound by faults with acentral dome. Chobari nose occurs on the west and Adesar nose occurs on the east. The WU is defined by three structural zones i.e. South Wagad Fault Zone (SWFZ), Central Zone and Northern Zone (Biswas 2016).

3.3.3 Island Belt Uplift (IBU)

The IBU comprises of four south tilted blocks i.e. Pachham Uplift, Khadir Uplift, Bela Uplift, Chorar Uplift, from west to east (Figure 3.3). These are the part of E-W oriented fault blocks of IBU, north of KMU and WU (Figure 3.4). This blocks show typical characteristics of shifting, rotation and differential tilting. The PU is located north of KMU with an orientation of NW-SE, KU to the north of KMU with E-W orientation, BU on the north of WU with orientation WNW-ESE and the CU is the smallest uplift in the IBU located at the north-eastern corner of Kutch rift basin with orientation NE-SW.

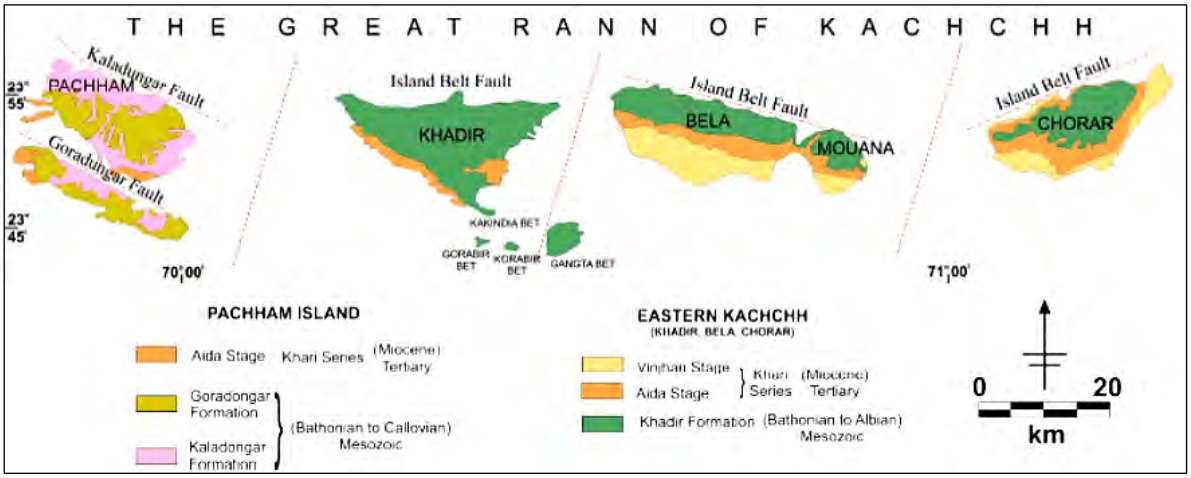

Figure 3.3: Location and Geological map of the IBU showing two distinct lithostratigraphic units; Pachham Island and Eastern Kachchh (Khadir, Bela and Chorar) (Biswas and Despande, 1970).The Island Belt Fault (IBF) is displaced by major transverse faults.

3.4 Seismo tectonic boundaries (Faults)

The structure of Kutch Rift possesses six major E-W striking intra rift faults i.e. Kutch Mainland Fault (KMF), Katrol Hills Fault (KHF) or Katrol Bhuj Fault (KBF), South Wagad Fault (SWF), Gedi Fault (GF), Goradongar Fault (GDF) and Island Belt Fault (IBF). The associate rift bounding faults are Nagar Parkar Fault (NPF) and North Kathiawar Fault (NKF) respectively on the north and south of the rift basin. The geometry of the marginal flexures which are affected by zone of parallel late generation faults infers about the surface location of the faults. The common geometry seen in all the uplifts associated with the faults is knee and ankle bend fold with a short, near vertical faulted fore limb and gently dipping, long back limb (Figure 3.4).

3.4.1 Nagar Parkar Fault (NPF)

The fault marks the northern boundary of the rift basin and is defined by the boundary between basement and rift sediments. The fault is drawn along a prominent geomorphic high with Allah bund, in the western part of the basement, is not well exposed. Allah bund is a ridge comprised of Holocene sediment uplifted during 1819 earthquake. The interpreted location of the NPF is further supported by the sharp boundary between the dune of Thar Desert and mud flat of great Rann of Kutch. This is an important transfer fault between rift and foreland basin (Biswas, 2016).

3.4.2 North Kathiawar Fault (NKF)

Though the fault is not exposed, it is postulated approximately along the northern straight edge of Saurashtra on the basis of geomorphology. The southern boundary of Gulf of Kutch is an elevated plateau of Saurashtra which is bounded by faults in all other sides. The Gulf attains maximum depth near the plateau which progressively deepens southward. The fault is presumed to be passing offshore along the northern edge of Saurashtra and is located between Gulf of Kutch and Saurashtra plateau (Biswas, 2016).

3.4.3 Kutch Mainland Fault (KMF)

It is marked as the longest fault in Kutch rift basin, which extends about 120 km from the north-western corner of Mainland near Ghuneri to Bhachau on the east (Biswas, 2016). Its location is indicated by escarpments and hog back ridges of hard beds facing Banni plains on the north (Figure 3.6). A zone of propagated second order faults is exposed along the foot of

the marginal escarpment, named as the KMF zone. In this zone upturned tertiary strata are juxtaposed with steeply down folded Mesozoic strata. The fault gradually disappears out towards the east, north of the Bhachau and does not continue south of WU. On the west the fault continues for some distance across the Rann of Kutch (Figure 3.4).

3.4.4 South Wagad Fault (SWF)

The fault is genetically related to KMF strike slip faulting and responsible for right lateral slip of Wagad block with respect to mainland block. It is the east ward continuation of KMF. A pull apart basin is formed due to transitional movement between KMF and SWF is named as Samakhiali graben. It is suggested that the basin is now a transfer zone undergoing transpressional movement attributed by complicated subsurface structure (Biswas, 2016).

3.4.5 Katrol Hills Fault (KHF) and Goradongar Fault (GDF)

Unlike KMF or IBF, both these faults are not rift fault and have no control on syn-rift sediment accommodation. These are post rift reverse faults where down thrown and up thrown sides are well exposed with repetition of Mesozoic strata (Biswas, 2016). The KHF and GDF uplifted blocks are also tilted to the south with a narrow deformation zone along the faulted up edges. The faults divide the uplifts into two south tilted blocks i.e. Northern range and Katrol hill blocks in KMU and Kaladongar and Goradongar in PU (Figure 3.4). The upthrown side marks the Charwar (Katrol) hill range against the plain of Bhuj low. The KHF strikes E-W parallel to KMF (Figure 3.6). The KHF is a strike slip fault. The GDF strikes NW-SE, uplifting the southern part of PU as Goradongar hills (Figure 3.4). The geometry and characteristic of the fault is same as that of the other faults.

3.4.6 Island Belt Fault (IBF)

IBF is not well exposed along the northern edge of the island. It is presumed to be concealed under the Rann sediments. Its presence along the four northern islands is indicated by clear escarpment and marginal folds facing plains of the great Rann of Kutch to the north (Biswas, 2016).

3.4.7 Gedi Fault (GF)

This fault separates Bela Horst (BU) and north tilted Wagad block. GF strikes E-W with upthrow of BU on the north. It shows the same geometric characteristic as that of the other master faults (Biswas, 2016).

Kutch region is present between the Indian subcontinent and the Asian plate along the India-Pakistan border within 400 km of the active plate boundary zone (Shah *et al*., 2004). Tectonic geomorphology shows that this region lies in a transition zone between the stable continental interior of Peninsular India and the active plate margin. Mesozoic tectonic events caused the formation of the Kutch aulocogen which was formed during the break-up of Gondwanaland and the northward drift of the Indian plate. The break-up resulted the evolvement of the rift which was controlled by a series of normal faults. A large number of grabens and horsts are formed due to the relative movements along these faults. A change from extensional tectonic environment to the compressional environment has taken place in the NS direction, around 40Ma ago (Rajendran *et al*., 2001). This was subsequently followed by Indian and Asian plate collision. East-trending folds and faults that deform Mesozoic clastic deposits and Deccan Trap basalts, Tertiary sedimentary units, and Quaternary terrace and alluvial/intertidal sediments are the major structural features of the Kutch region. The major faults in the region are the E-W trending Katrol Hills fault (KHF), Nagar Parkar Fault (NPF), Kutch Mainland fault (KMF), South Wagad Fault (SWF), Island Belt fault (IBF), and the Allah Bund fault (ABF) (Figure 3.4). Geological cross sections across central and eastern Kutch rift along the median high deciphers the attitude of different faults (Figure 3.5) Kutch Mainland Fault probably got reactivated on 26th January 2001. This Kutch region was a part of diffused India-Asia plate boundary or a transition area between stable portion of peninsular India and the plate boundary which can be suggested by active thrust belts and folds. The Kutch region can be categorised as a unique seismological setting of “Rifted Stable Continental Region (SCR) extended crust” (Sharma, 2001). Figure 3.7 shows different geological formations viz., Deccan Trap, Tertiary and Mesozoic occurrence along with the topography as displayed by the DEM. Subsurface nature of faults, affected sedimentary formation and corresponding topography are shown in a geological cross section (Figure 3.8).

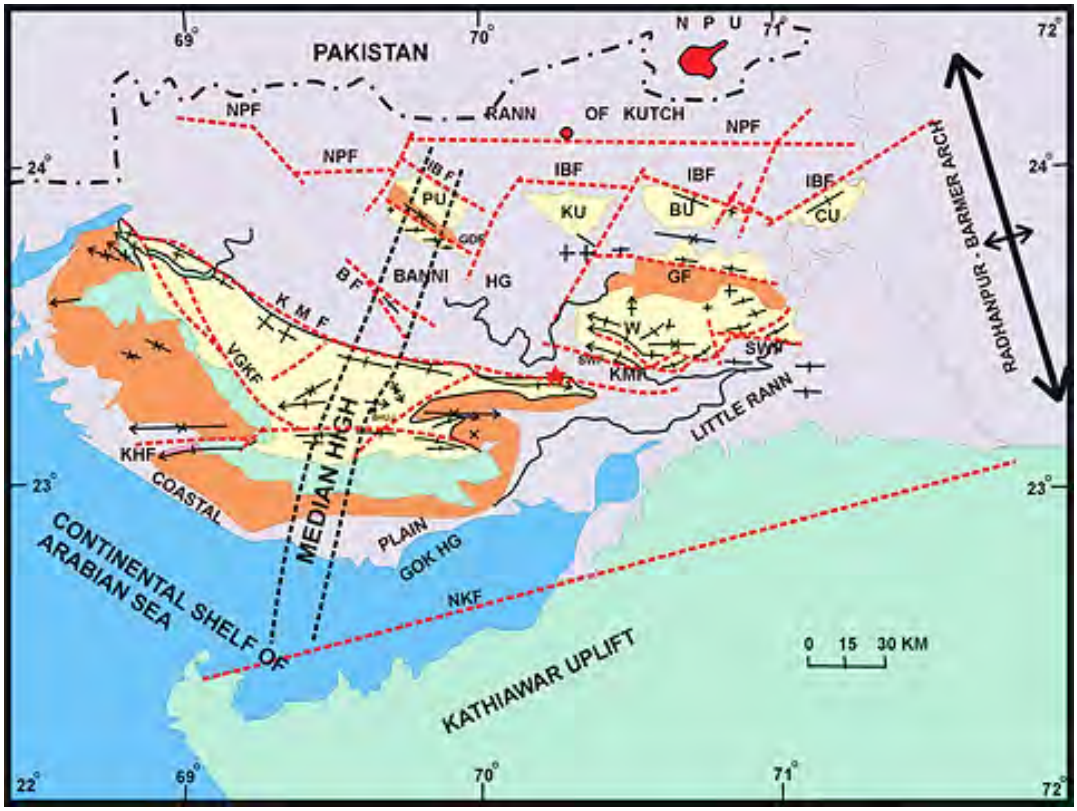

Figure 3.4: Tectonic map of Kutch with the major faults: Kutch Mainland fault (KMF), Vigodi Fault (VGKF/VF), Katrol Hill Fault (KHF), Little Rann of Kutch Fault system, Bhujpur Fault (BF), Island Belt Fault (IBF), Goradongar Fault (GDF), South Wagad Fault (SWF), North Kathiawar Fault (NKF), Gedi Fault (GF), Nagar Parkar Fault (NPF). Uplifts: Pachham Uplift (PU), Khadir Uplift (KU), Bela Uplift (BU), Chorar Uplift (CU) (Biswas, 2005).

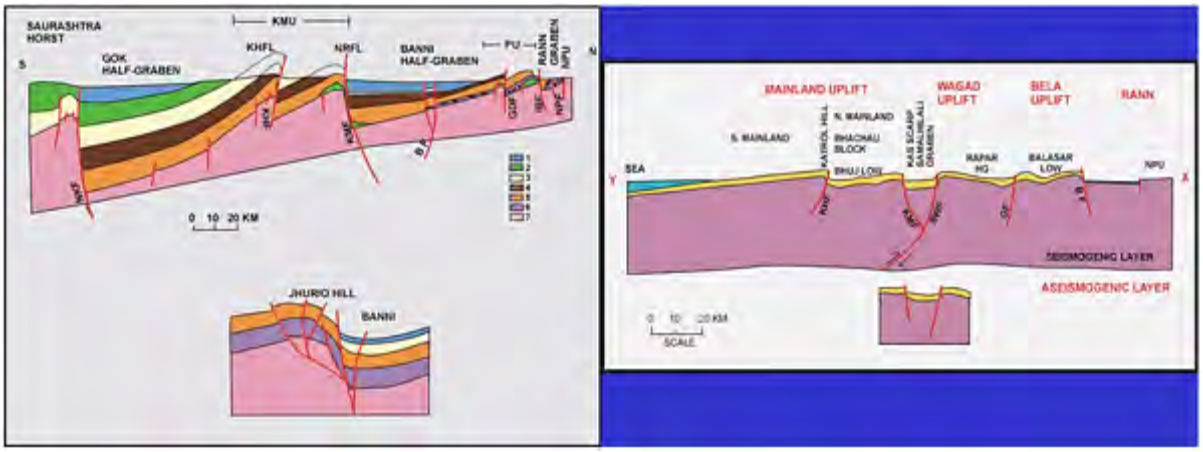

Figure 3.5: Geological cross section across Kutch basin along axis of Median High (Figure 3.4) KHFL- Katrol Hill Flexure. NRFL - Northern Range Flexure. Box index: 1- Quaternary and Tertiary; 2- Deccan Trap/intrusive; 3- Lower Cretaceous; 4- Upper Jurassic; 5- Mid. Jurassic; 6 Lower Jurassic-Upper Triassic; 7- Precambrian. (Biswas, 2005).

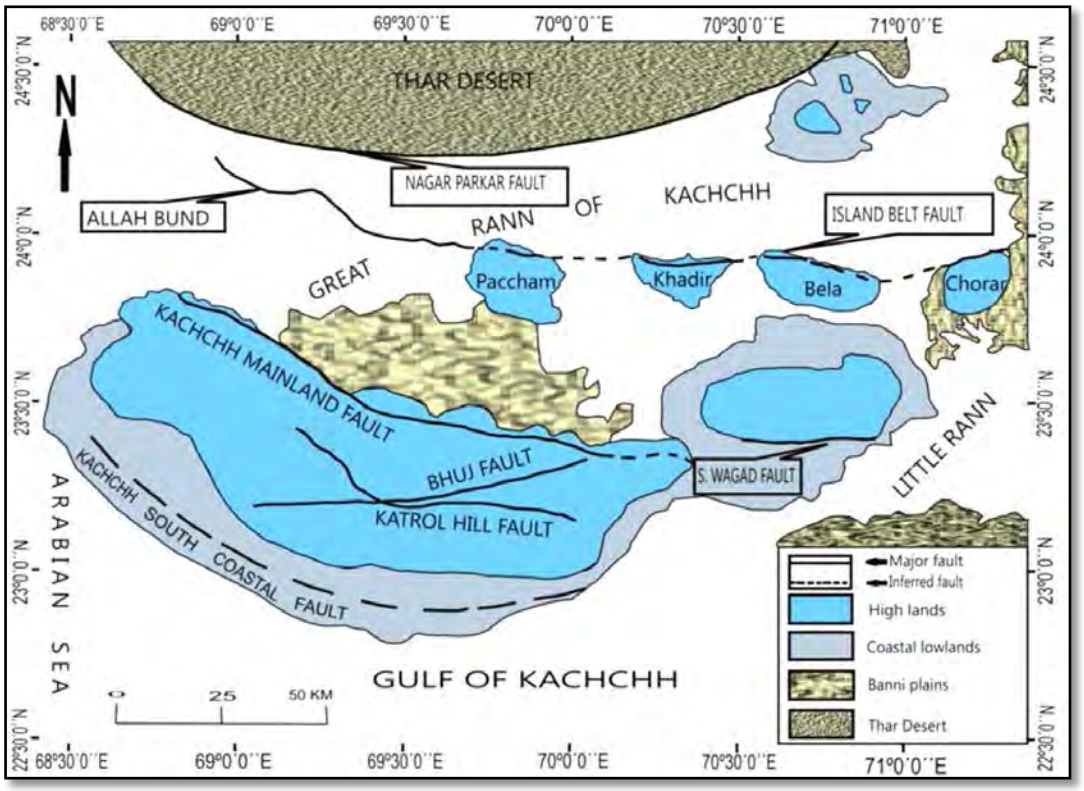

Figure 3.6: Geomorphic map of the Kutch region, Indian subcontinent, showing disposition of the major landforms in the area (Roy *et al*., 2012).

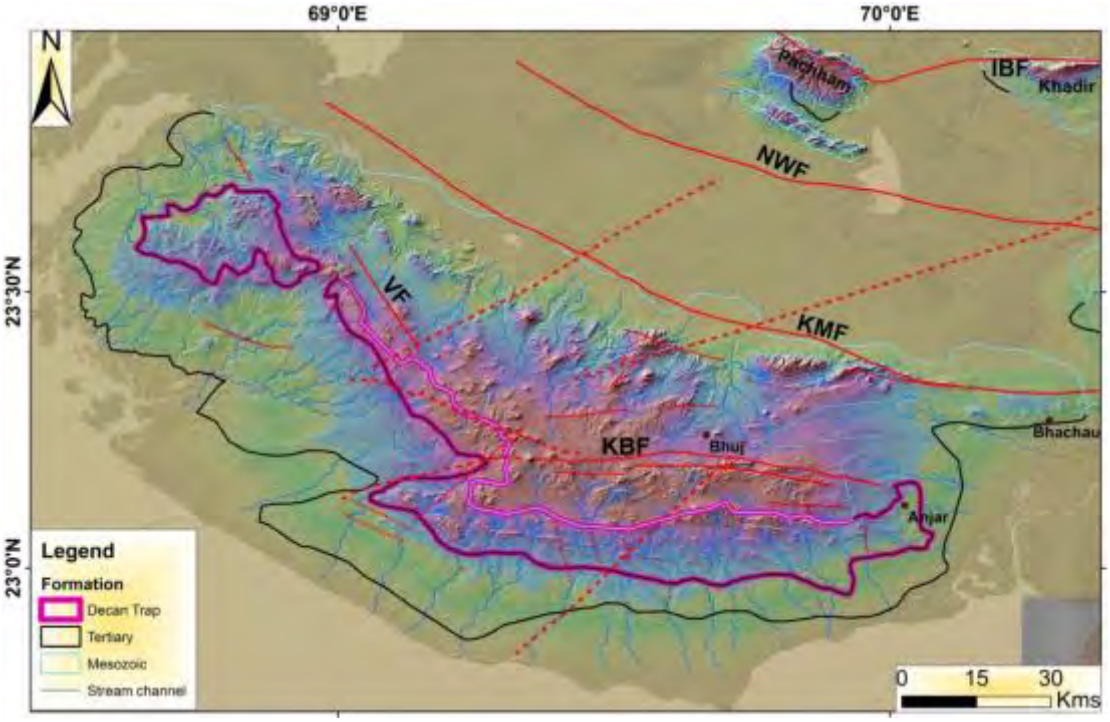

Figure 3.7: Hillshade map derived from ALOS PALSAR DEM with formations, major faults and lineament.

Geological evidence for the above described exposure of low angle reverse faults is the cause for tectonic reversal and also can be confirmed by the thrust type focal mechanism obtained for the 2001 Kutch event (USGS) as well as the 1956 Anjar earthquake. The stress field which is in the N-S to NNE-SSW direction can be considered to be responsible for the reversal of movement and the ongoing deformation (McCalpin and Thakkar, 2003).

3.5 Neotectonics and Seismicity

Characteristic landscapes are formed in Kutch region and still exhibits neotectonic movements. Two major phases of Quaternary tectonic uplift took place in this region. Along the E-W trending faults the Early Quaternary tectonic activity and along the NNE-SSW to NNW-SSE trending transverse faults the Late Pleistocene phase took place. As evidenced by miliolites overlapping the colluvial deposits along the Katrol Hill Fault/ Katrol Bhuj Fault during Early Quaternary, the E-W trending faults were more active (Thakkar *et al*., 1999). According to lithological setting due to differential uplift along E-W faults, viz. the KMF and KHF the present configuration of the landscape came into being during the Early Quaternary. The Early Quaternary physiographic setting has been modified by the Late Pleistocene-Holocene tectonic activity along transverse faults (Thakkar *et al*., 1999).

Neotectonic landforms of the area indicate that along transverse faults most large Holocene earthquakes have occurred (Malik *et al*., 1999). Neotectonic geomorphology also supports the current setup. It appears that the major tectonic activity of Mainland Kutch was confined to the KMF and KHF or KBF. But at the same time, a large number of earthquakes also occurred along transverse faults, specifying that the latest phase of tectonic activity was more along the transverse faults. Stress of compressive nature has been transferred from Kutch Mainland Fault to the transverse faults in this region (Thakkar *et al*., 1999). It happened due to the blocking of the Indian plate in the NE. The transition in tectonic environment between extensional and compressional is also the reason for the activity of transverse strike-slip faults in Kutch (McCalpin and Thakkar, 2003).

The earthquake occurred along a tectonic boundary on 26 January 2001 is characterized by high seismic activity. The movement of the Indian tectonic plate in a north and northeast direction after collision with the Eurasian and Arabian tectonic plates is the cause of seismic boundary. India plate drifted northward as this process has continued for millions of years. (Source: http:// www.geocities.com/.../ 8361/Quake2001India.html).

Falling in the Zone-V according to the seismic zoning map of India, Kutch region is seismically very active (Figure 3.9). The 1819 Kutch earthquake (Mw 7.5) which occurred in the Rann of Kutch near the India-Pakistan border during historic time and the 1956 Anjar earthquake (Mw 6.0) of instrumental period are the major events in the study area. The epicentre of Anjar earthquake was 40 km away from the 2001 Bhuj earthquake's epicentre. It occurred on the KMF (one of the southern boundary of the Kutch rift) at a focal depth of 15 km and whereas the 1819 earthquake occurred on the northern boundary of the Kutch rift about 140 km NW of the 2001 event. It was caused by the thrust motion on a north-dipping fault which can be depicted by morphological evidence of maximum uplift of about 6m in 1819 showing a northerly slope (Oldham, 1926; Bilham, 1998; Rajendran and Rajendran, 1999). A large number of small scaled earthquakes were also reported along major fault lines.

Tectonic reversal has also been reported by USGS after 2001 Bhuj and 1956 Anjar earthquakes. The stress field oriented in the N-S to NNE-SSW direction is responsible for this reversal of movement and the ongoing deformation (Rajendran *et al*., 2001).

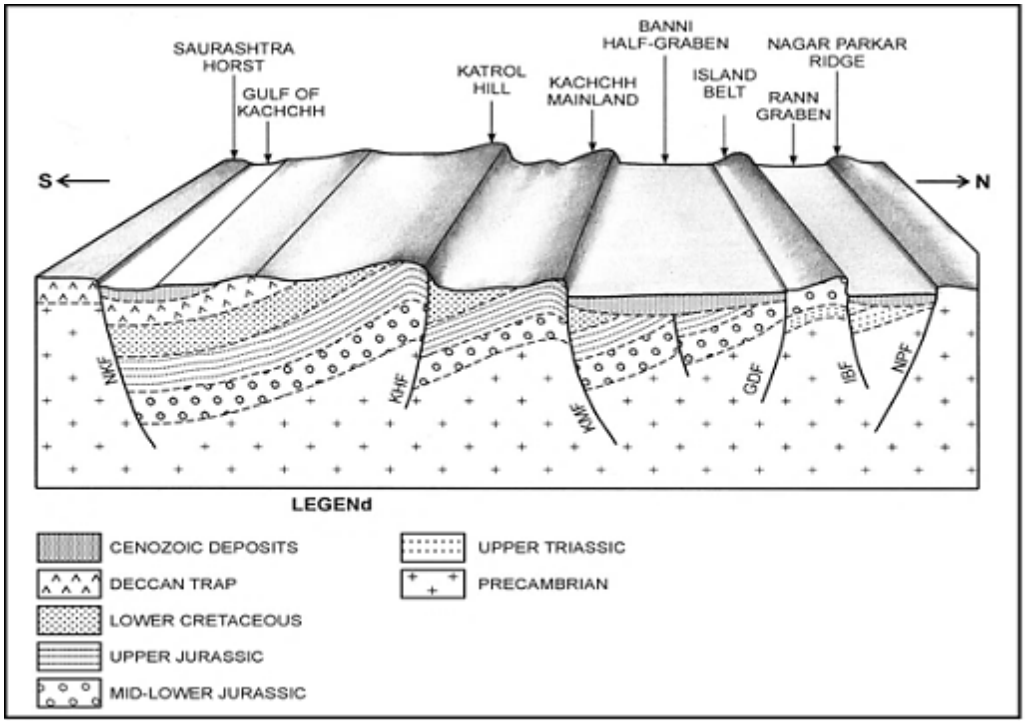

Figure 3.8: Geological section (vertical view) showing series of faults and geological formations. (Pande, 2007).

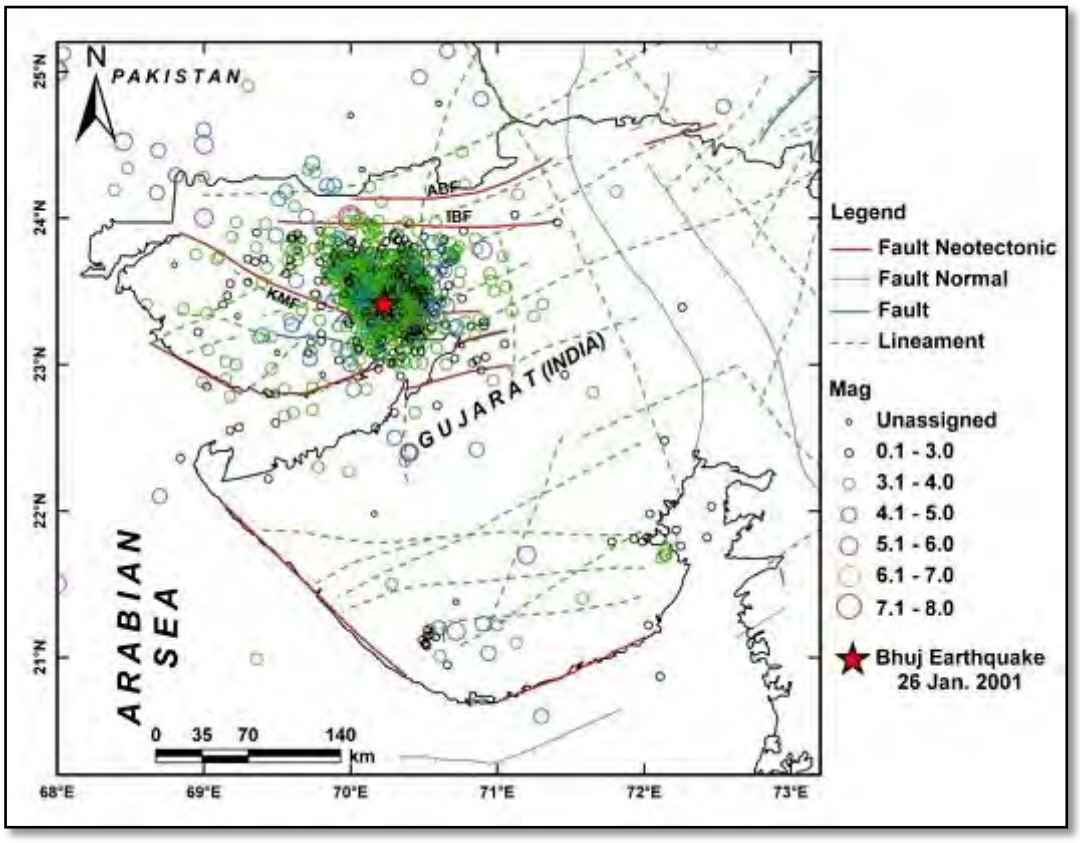

Figure 3.9: Seismotectonic set up of the Gujarat region. ABF-Allah Bund Fault, IBF-Island Belt Fault, KMF-Kutch Mainland Fault. Earthquake occurrence is from 1668 to 2016 (GSI, 2000).

Chapter 4

Data and Methodology

4.1 Introduction

Now-a-days satellite images (both optical and microwave) are available in diverse temporal, spatial and spectral resolutions after the advent of diverse remote sensing techniques and consecutive advances in remote sensing system, data communication and processing technologies. Different applications involve remote sensing data with particular resolution at which the scientific studies can be carried out. Hence the essential aspect is to lay less importance upon the image resolution than the application or to lay no importance on one specific resolution and accept relatively medium or high spatial resolution satellite images.

The main objectives of this study is to analyze 2001 Bhuj earthquake induced land deformation, liquefaction and neotectonic activity employing microwave and optical remote sensing data sets followed by estimation of earthquake induced ground deformation using InSAR technique, geomorphometric study and ground truthing / field validation.

4. 2 Data Used

For understanding the 2001 Bhuj earthquake related ground deformation, liquefaction and ground settlement along with the neo-tectonic activity from the morphometric study, remote sensing data (especially SAR images) have been used extensively. However the Remote sensing SAR data and other data products used in this research are as follows:

a) Maps (Topographic, Geological and Seismotectonic)
b) Landsat-7 and 8 datasets (from USGS, Earthquake Hazards Program)
c) Google Earth satellite images (from Google Earth)
d) Digital Elevation Model (DEM) (from CGIAR-CSI, USGS and JAXA website)
e) Envisat data (from European Space Agency (ESA)
f) Sentinel-1 data (from European Space Agency (ESA)
g) ALOS PALSAR-1 (from Earth Observation Data Utilization promotion Platform JAXA)

4.2.1 Maps

4.2.1.1 Topographic Maps

Survey of India topographic maps (1:50000 scale and 1:25000) have been used for the present study. The topographic maps for the study area were first georeferenced. These have provided with the information on locations of several places (town/villages) which served as an important guide.

4.2.1.2 Geological Map

The geological map obtained from Geological survey of India (GSI) and then was georeferenced. The Geological map has been used to identify geological features, rock units and geologic strata where the attributes are shown by colour or symbols to indicate where they are exposed at the surface.

4.2.1.3 Seismotectonic Atlas of India

The seismotectonic maps abbreviated as SEISAT were obtained from GSI, seismotectonic atlas of India and its environs. The maps for the study area were georeferenced using ArcGIS version 10.2 and the major faults, minor and major lineaments were digitized.

4.2.1.4 Seismic Data

The seismic data from past to present has been collected from the United States Geological Survey (USGS), Amateur Seismic Centre (ASC), Indian Meteorological Department (IMD).

4.2.2 Landsat-7 and 8

Landsat program is a cooperative attempt of the NASA and USGS. The first satellite was launched on 23rd July, 1972. Continuous image coverage of the Earth's surface has been provided by Landsat satellites. NASA has been developing sensors, spacecraft and launching the satellites including their performance validation. On the contrary, USGS has been developing the ground systems and operating the satellites, as well as management of data reception, archiving and distribution. The Landsat-7 enhanced thematic mapper (ETM) is available which has almost similar characteristics as that of Landsat-8. Since late 2008,

Landsat-8 data is available for public free of cost. Carefully calibrated Landsat images provide consistent inventory of the Earth's surface globally. The most current Landsat-8 was launched on 11th February, 2013. In this work, Landsat-8 datasets were acquired from the USGS (http://earthexplorer.usgs.gov). Landsat satellite has two instruments: Operational Land Imager (OLI) and Thermal Infrared Sensor (TIRS). Approximate scene size of Landsat-8 is 170 km N-S by 183 km E-W (http://landsat.usgs.gov/landsat8.php).

4.2.3 Landsat-8 technical detail

In different frequency ranges of the electromagnetic spectrum, Landsat-8 senses the Earth's surface representing a color. However, all frequency ranges are not visible to human eyes. These ranges are known as bands and Landsat-8 is capable of sensing 11 bands. Frequency ranges of the bands and their resolutions are given in table 4.1.

Table 4.1: List of Landsat-8 satellite bands (Source: USGS).

Band number	Band name	Wavelength (μm)	Spatial Resolution (meters)
Band-1	Coastal	0.43-0.45	30
Band-2	Blue	0.45-0.51	30
Band-3	Green	0.53-2.59	30
Band 4	Red	0.64-0.67	30
Band-5	NIR	085-0.88	30
Band-6	SWIR1	1.57-1.65	30
Band-7	SWIR2	2.11-2.29	30
Band-8	Panchromatic	0.50-0.68	15
Band-9	Cirrus	1.36-1.38	30
Band -10	TIR1	10.68-11.10	100(30)
Band-11	TIR2	11.50-12.51	100(30)

4.2.4 Google Earth Datasets

On 11th June, 2001 Google Earth was launched. It is a virtual globe map and geographical information program. Originally the program was called Earth Viewer. The view of the Earth is generated by superimposition of satellite images and aerial photographs over Shuttle Radar Topographic Mission (SRTM) DEMs using geographic information systems (GIS) onto a 3D globe. Satellites images belonging to different time periods are provided by Google Earth (https://earthengine.google.com/datasets/).

4.2.5 Digital Elevation Model (DEM)

Digital Elevation Model (DEM) provides enormous information of various topography characteristics. When any study is being done in a highly rugged terrain a DEM becomes essential e.g. Himalaya, Alps etc. Now different types of global DEMs are available at different spatial resolutions (public domain). For example: SRTM DEM with 30m and 90m resolutions (http://srtm.csi.cgiar.org/), Advanced Spaceborne Thermal Emission and Reflection Radiometer (ASTER) Global DEM at 30m spatial resolution that cover almost the entire globe (USGS). ALOS PALSAR DEM of resolution 12.5 m and 30 m derived from ALOS PALSAR SAR and Prism images respectively has been used at various stages of present work. Further the DEM derived from Sentinel-1 SAR image pair has been used in the morphometric study.

4.2.6 Envisat ASAR

The ASAR (Advanced Synthetic Aperture Radar) datasets, acquired through the Envisat satellite are acquired from European Space Agency (ESA). In February 2002 Envisat satellite was launched by the European Space Agency. Envisat operates in various imaging modes having different angle of incidence, swath width and resolution. In this study, ASAR SLC products in image mode with swath width of 12 Km belonging to track number 234 have been used.

The sensor operates at C-band; for Advanced Synthetic Aperture Radar (ASAR) and ensures continuity with wave mode of the ERS-1/2 AMI. It is designed to enhance capability in terms of polarisation, range of incidence angles, coverage and modes of operation. This improved ability cab be confirmed by significant differences in the instrument design i.e. a full active array antenna designed with dispersed transmitting and receiving modules which

provides discrete beams, a digital waveform generation for pulse "chirp" generation, a block adaptive quantisation scheme and a ScanSAR mode of function by beam scanning with altitude. For this satellite, the radar operates within the C-band (wavelength 5.6 cm) and other technical details are shown in Table 4.2 (http://envisat.esa.int/instruments/ asar/).

Table 4.2: Technical details of ASAR

Radar Waveband	**Technical Characteristics**			**Applications**
	Accuracy	**Spatial Resolution**	**Swath Width**	
Imaging microwave radars **Waveband:** C-band with choice of 5 polarisation modes (VV, HH, VV/HH, HV/HH, or VH/VV). Frequency Range: 5.331 GHz.	Radiometric resolution in range: 1.5-3.5 dB	Polarisation modes: approx. 30m x 30m. Wide Swath mode: approx.. 150m x 150m. Global Monitoring mode: approx. 1000m x 1000m.	Image and alternating polarisation modes: up to 100 km, Wave mode: 5 km, Wide swath and global monitoring modes: 400 km or more.	Ocean and Coast (Ocean Currents and Topography) Land (Landscape Topography) Snow and Ice (Snow and Ice)

4.2.7 Sentinel-1 Data

The Sentinel-1 mission provides in a continuation to ERS and Envisat radar satellites with better performance and revisiting. The Sentinel-1 datasets obtained from Sentinel Scientific Data Hub of European Space Agency (ESA) (https://scihub.copernicus.eu/). Sentinel-1 is the latest Synthetic Aperture Radar (SAR) satellite, which was launched in April 2014 by the European Space Agency. It has several imaging modes with different incidence angle, resolution, and swath width. Data used are Level-1 Single Look Complex SLC products in image mode with swath width of 250 km, Resolution 5 x 20 m. (ESA). The list of Sentinel-1 data used for this research work has been mentioned in the respective chapters. Sentinel-1 provides day-and-night continuous images operating in C-band (center frequency: 5.405 GHz) in all weather conditions. Data products are made accessible systematically and free of charge. The data products of the satellite are distributed in the Sentinel Standard Archive Format for

Europe (SAFE). Acquisitions zones with the related polarization and mode are defined on a cyclic (12 days) basis in the observation scenarios (ESA user guide).

4.2.8 ALOS PALSAR-1

ALOS (known as "Daichi") is an Earth-observation satellite, developed and missioned by JAXA (Japan Aerospace Exploration Agency). It was manufactured by the combined effort of Mitsubishi Electric Corp and NEC, Toshiba. The first ALOS mission was lunched in the year 2006 and ended in 2011. The objectives assigned for the active microwave and optical sensor, whose high-resolution data may be used for such applications as cartographic mapping, environmental and hazard monitoring. It was intended to deliver scientific and commercial users with data of sufficient resolution so as to generate maps with 1:25,000 scale. It generates an observational data of 2.5 m horizontal resolution for topographic study, and a 3 to 5 m vertical resolution for contour mapping. However a 10 m horizontal resolution Multispectral data is needed for the classification of land cover (vegetation, forests, etc.) (http://mrs.eecs.umich.edu/sensors.html).

4.3 Softwares Used

4.3.1 ArcVIEW GIS, version 3.2a

ArcView is geographic information system (GIS) software for visualizing, managing, generating, and analyzing geographic data. (http://www.esri.com/arcview). ArcView is a powerful tool which is easy to use that brings geographic information to the desktop. ArcView makes an environment to display and query the contents of a spatial database. It allows exploring the database, exhibiting all parts of its contents, questioning, displaying or saving results and pass information or graphics on to the other applications.

4.3.2 ArcGIS, version 10.2

ArcGIS is extensively used GIS software, developed by Environmental Science Research Institute (ESRI). A very wide range of GIS tools are provided by this software. Most of the GIS operations for this research work were performed in ArcGIS version 10.2. Different locations are digitized as line and polygon vector files from Landsat images. The ArcScene extension is used to create 3D prospective view by draping high resolution satellite images over

DEM. Using the same software, all maps were prepared. A 30 user's licensed version of the software is available at Indian Institute of Technology, Roorkee which has been used for this research work.

4.3.3 Erdas Imagine version 15

This commercial software is available from Hexagon Geospatial agency. Erdas Imagine enable researchers to envision, experience and communicate geographic information. ERDAS IMAGINE offers true value, photogrammetry, consolidating remote sensing, basic vector analysis, LiDAR analysis and radar processing into a single product. Mosaicking, digitizing and classifying are executed using this software. A multi user licensed version of the software is available at Indian Institute of Technology, Roorkee which has been used for this research work.

4.3.4 SarProz

The developer of SARPROZ is Daniele Perissin. It is very advanced and resourceful software which provides a wide range of SAR, InSAR, PSI and Multi-Temporal InSAR processing tools. This software comes with a user friendly interface and scripted on Matlab software. Many processing options can be selected by the users; nevertheless, default options allow a beginner to easily tackle SAR and InSAR. Sarproz supports maximum existing satellite formats and imaging modes. However, Sarproz has no focusing module. Therefore, SLC (Single Look Complex) data are needed. SLC data can either be ordered from data providers, or focused with other software (http://www.sarproz.com/).

4.3.5 SARScape with Envi 4.7

SARscape is specially designed as a commercial software package for processing of SAR/InSAR data which works as an extension of Envi software. SARscape is mostly useful for Envisat or RADARSAT applications. SARscape is developed by Sarmap. This software can be used as fully featured, SAR processor for spaceborne SAR data.

The Basic module comprises a set of processing steps for the generation of airborne and Spaceborne SAR products based on coherence and intensity. Essential steps include SLC Image generation, Baseline estimation, DEM extraction, focusing, multi-looking, co-

registration, filtration, feature extraction including coherence and geocoding. The basic module does not contain focusing of ALOS PALSAR, RADARSAT-1 and Envisat ASAR raw data. This software is complemented by a Multi-purpose tool and optical multi-spectral data processing capabilities. A multi user licensed version of the software is available at Indian Institute of Technology , Roorkee which has been used for this research work.

4.3.6 Sentinel 1 Toolbox

The Sentinel-1 or so called SNAP-1 toolbox is freely available by European Space Agency for research and scientific studies. This tool is capable of processing different formats and levels of Sentinel-1 and other satellite SAR images from Envisat, Radarsat, ALOS PALSAR etc. (https://sentinel.esa.int/web/sentinel/toolboxes/sentinel-1). Besides this, automated DORIS Environment (ADORE) which works on Linux platform, is also used in interferometric processing.

However the data, methodology and software used have been explained in detail in the respective chapters 5, 6 and 7.

4.4 Methodology

The methodologies adopted for the study are InSAR, PSI, characterization of morphometric indices, DEM comparison by differentiating two DEMs of different times, 3D prospective view, visual interpretation etc. The methodology adopted for morphometric study has been elaborated in chapter-7. This chapter further explains the InSAR and PSI followed by RADAR remote sensing principles, RAR, SAR, microwave imaging satellites, sensor characteristics, etc. in different sections.

4.5 Concepts of Radar and SAR Interferometry

4.5.1 RADAR

Radio Detection and Ranging (RADAR) is a most common form of imaging active microwave sensors which is used to detect range, altitude, direction and speed of an object, which was secretly developed before Second World War. A passive microwave sensor detects the microwave energy naturally emitted by the object or surface related to the temperature and

moisture properties within its field of view. Active microwave sensors provide their own source of microwave radiation to illuminate the target.

Usually the radar frequency bandwidth is used between 3MHz-10.5GHz (http://en.wikipedia.org/wiki/Radar). Its usage completely depends upon the type of application. Figure 4.1 shows the position where radar wavelength bandwidth lies in full electromagnetic spectrum (e/m).The microwave region of the spectrum is quite large, compared to the visible and infrared, and there are many wavelength ranges or bands commonly used. Detailed information on microwave remote sensing technique have been discussed by Hanseen (2001), Sabins (2007), Woodhouse (2005), Baghadi and Zribi (2016), Ulaby (2013), Gupta (2003).

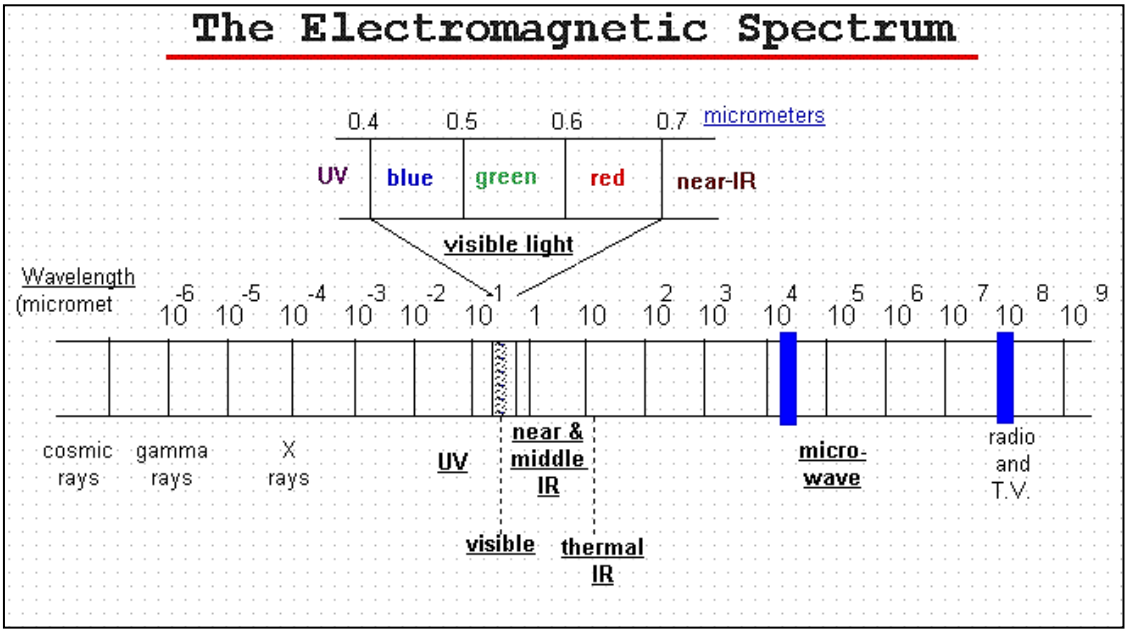

Figure 4.1: Full e/m spectrum showing relative position of bandwidth, demarcated by thick blue lines, used for radar purposes (http://en.wikipedia.org/wiki/Radar).

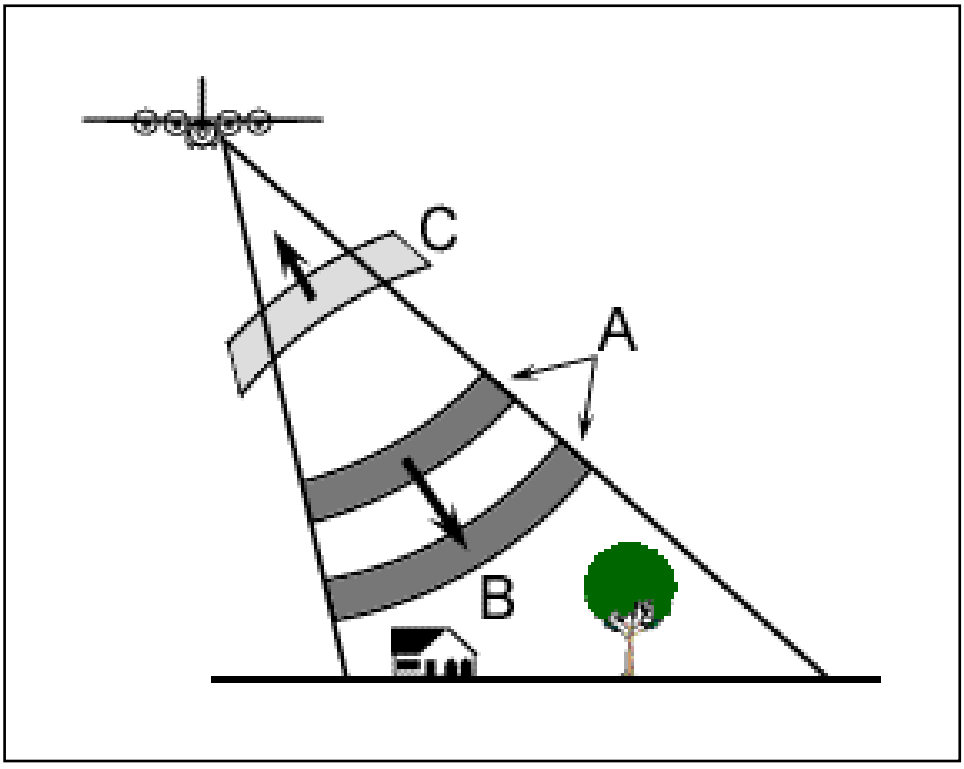

Figure 4.2: Transmission and receiving of RADAR beam (Source: http:// cct.nrcan.gc.ca/resource/tutor/).

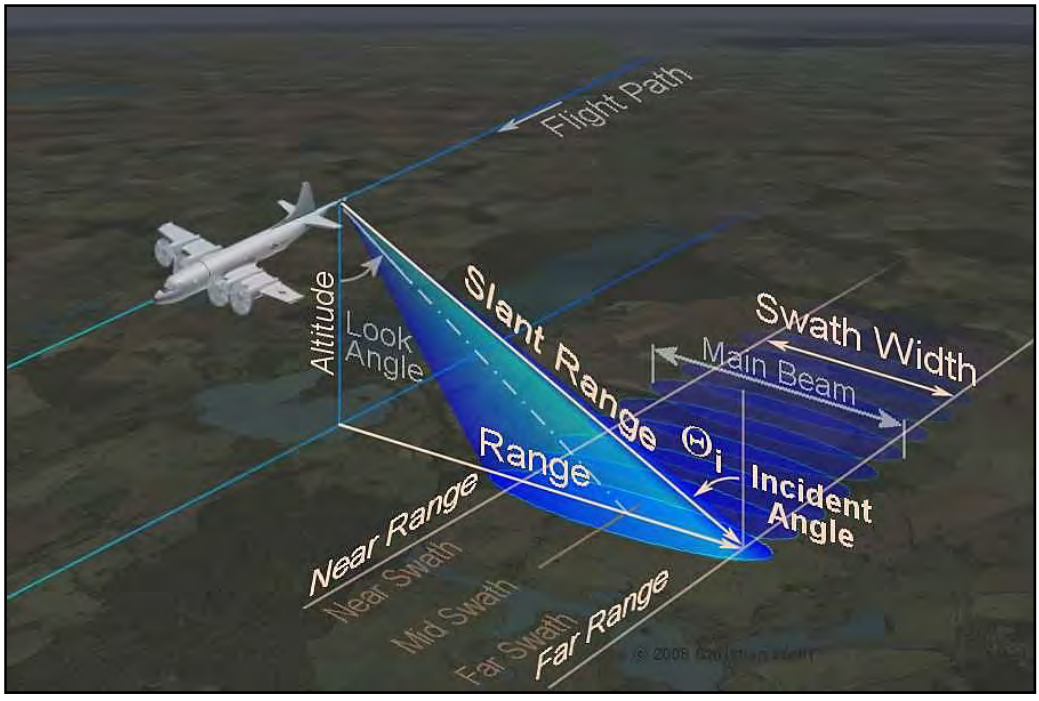

Figure 4.3: Viewing geometry of RADAR imaging technique (Source: http:// www.radartutorial.eu/20.airborne/ab06.en.html).

Essentially Radar is a distance quantifying device. Fundamentally it comprises of an antenna with a transmitter and receivers enclosed in an electronics system to process and record the data. The transmitter produces successive short pulses or bursts of microwave (A) at a regular interval which is focused by the antenna into a beam (B). The surface is illuminated obliquely at a right angle to the motion of platform by the radar beam as shown in figure 4.3. A portion of the transmitted energy reflected (or backscattered) from various objects within the illuminated beam (C) is received by the antenna (Figure 4.2). The location and the distance from the radar can be determined by measuring the delay time between the transmission of pulse and reception of the backscattered "echo" from different targets. When the sensor platform moves advance, recording and processing of the backscattered signals builds up a 2D image of the surface.

Basic radar equation, showing how the power returning to the receiving antenna (P_r) is related to different parameters, is:

$$P_r = \frac{P_t\, G_t\, A_r\, \sigma\, F^4}{(4\pi)^2\, {R_t}^2\, {R_r}^2}$$

Where,

P_t = transmitter power

G_t= gain of transmitting antenna

A_r= effective aperture (area) of the receiving antenna

σ = radar cross section or scattering coefficient of the target

F = pattern propagation factor

R_t= distance from the transmitter to the target

R_r= distance from the target to the receiver

Schematic diagram depicting working of an active radar as shown in figure 4.4 transmitter and receiver could be same or different.

Mostly RADAR uses the microwave range of electromagnetic spectrum in order to illuminate the target (Figure 4.1). The microwave region mainly consists of eight distinct bands and each waveband is used for distinct purposes.

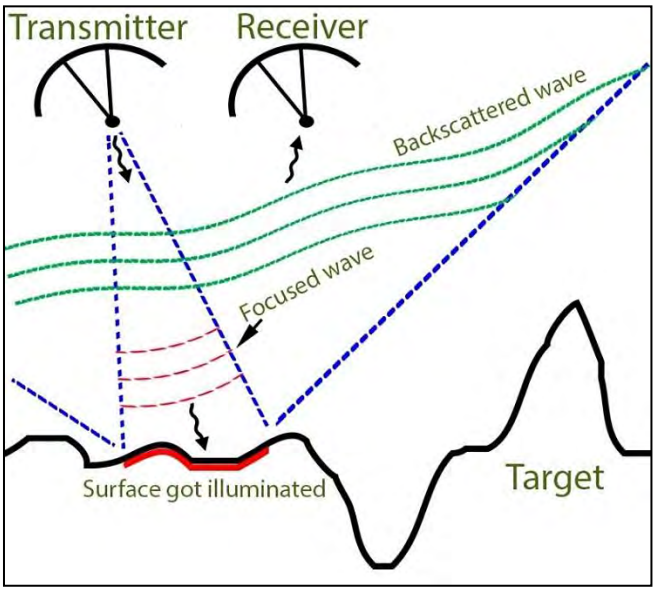

Figure 4.4: Schematic working of radar system. Target could be any surface i.e. dynamic or stationary. Focused waves are transmitted in the form of pulses, mainly when one antenna is used for transmission and reception.

The most commonly used wavebands (Table 4.3) are as follows:

Table 4.3: Most commonly used Microwave bands in InSAR

Bands	Wavelength (in cm)	Commonly used band (in cm)	Spaceborne System
P - band	30.0 - 100.0	65.0	AIR SAR
L - band	15.0 - 30.0	23.5	JERS-1 SAR, ALOS PALSAR
S - band	12.0	10.0	Almaz-1
C - band	3.8 -7.5	5.6	ERS-1/2 SAR, RADARSAT-1/2, Envisat ASAR, RISAT-2
X - band	2.4 - 3.8	3.0	TerraSAR-X-1, COSMO SkyMed
K - band	0.8 -1.1	1.2	Military domain

Table 4.4: Different SAR imaging satellite sensors with their regulating agencies

JERS-1 SAR	Japanese Earth Remote Sensing Satellite
ALOS PALSAR	Japanese Advanced Land Observing Satellite (ALOS) Phased Array L-band Synthetic Aperture Radar (PALSAR).
Almaz-1	ALMAZ-1 Russian Satellite
ERS-1/2 SAR	Earth Remote Sensing Satellite. The joint use of ERS-1 and ERS-2 SAR is called ERS- Tandem mode
RADARSAT-1/2	RADARSAT is Canada's first Earth Observation satellite
Envisat ASAR	European Environmental Satellite (an advanced polar-orbiting Earth observation satellite)
Sentinel 1-A	European Environmental Satellite
RISAT-2	Indian Radar Imaging Satellite
TerraSAR-X-1	TerraSAR-X is a German Earth observation satellite. The satellite works in the X-band and is called therefore TerraSAR-X
COSMO SkyMed	Constellation of small Satellites for the Mediterranean basin Observation (COSMO-SkyMed) is an Earth observation satellite system

4.5.2 Real and Synthetic Aperture

Real-Aperture Radar uses maximum practical length antenna (fitted to the space platform itself) to generate a narrow angular beam width in the azimuth direction.

The antenna sends the microwave beam out which illuminates an area on the ground so called footprint. The noted signal intensity depends on the transmitted energy backscattered from the ground targets within this footprint. If the length of the antenna increases, the width of the footprint decreases (Figure 4.5) (Source: http:// www.physics.nus.edu.sg.htm).

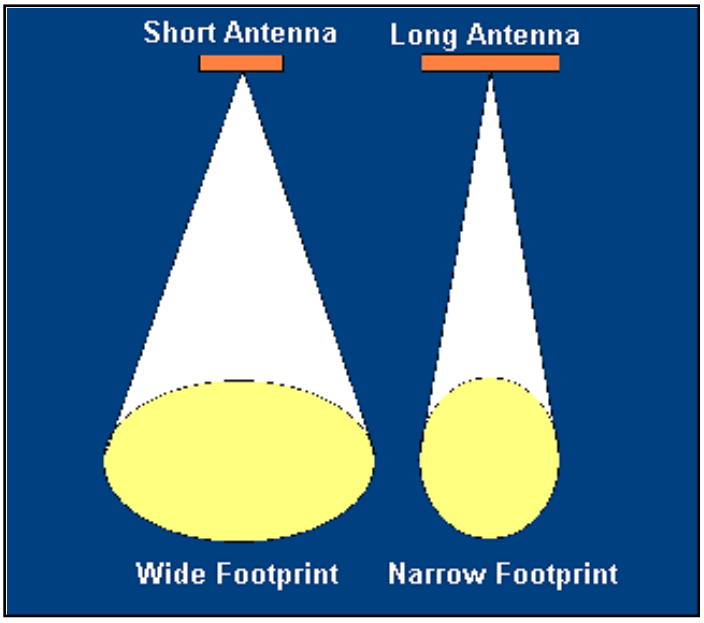

Figure 4.5: Antenna size and ground coverage (Source: http://www.physics.nus. edu.sg.htm).

In real aperture radar imaging, the size of the microwave beam sent out from the antenna limits the ground resolution. Finer information on the ground can be obtained by using a relatively narrower beam. Because the beam width is inversely proportional to the length of the antenna, i.e. the longer the antenna size, the narrower the beam width. For the space shuttle mission for radar image acquisition and DEM generation for whole earth real aperture radar system was used as shown in Figure 4.6.

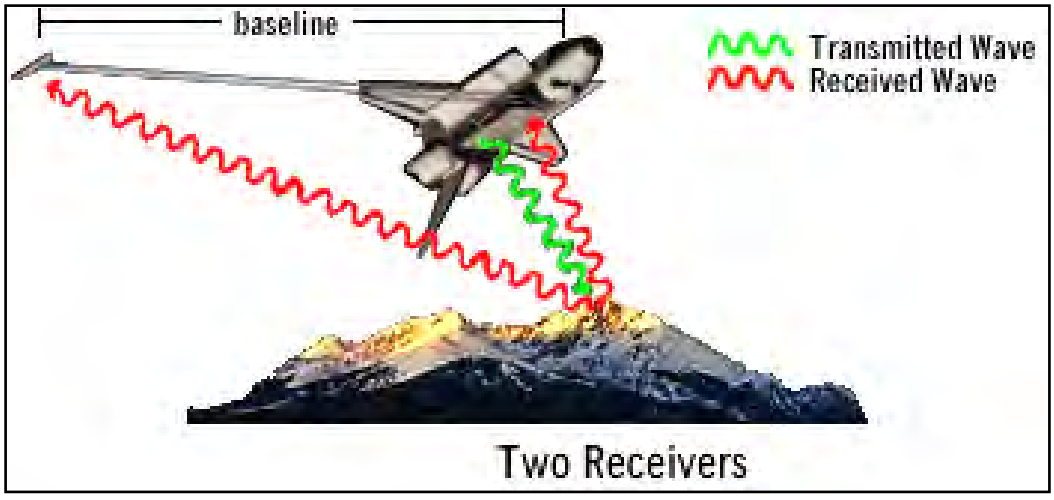

Figure 4.6: Real Aperture Radar as used by Space Shuttle in generating SRTM images (Source: http://www.jpl.nasa.gov/srtm).

A Synthetic Aperture Radar (SAR) is a coherent side looking airborne system which uses the fling path of the imaging aircraft to simulate a very large antenna or aperture electronically and that produces fine-resolution remote sensing images (Figure 4.7).

The phase and magnitude of the received signals from elements of a synthetic aperture over successive pulses are used by the signal processing. The stored data is recombined after a given number of cycles, (taking into account the Doppler effects inherent in the different transmitter to target geometry in each succeeding cycle) and creates a high resolution image of the terrain being over flown.

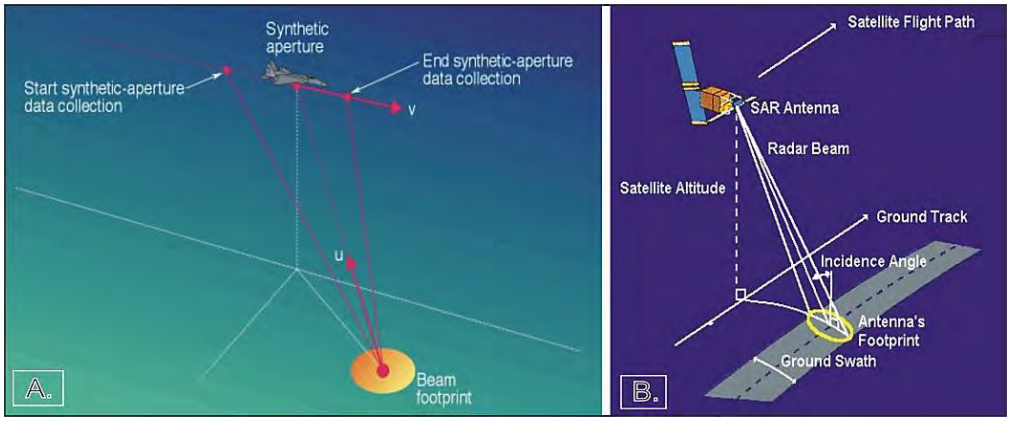

Figure 4.7: A. Synthetic Aperture Radar Imaging geometry (Source: http:// www.aero.org/crosslink/summer2004/04.html); B. Imaging geometry for a typical strip-mapping synthetic aperture radar imaging system. The antenna's footprint sweeps out a strip parallel to the direction of the satellite's ground track. (Source: http:// envisat.esa.int/handbooks/asar/CNTR4.html).

SIMULTANEOUS BASELINE **REPEAT TRACK**

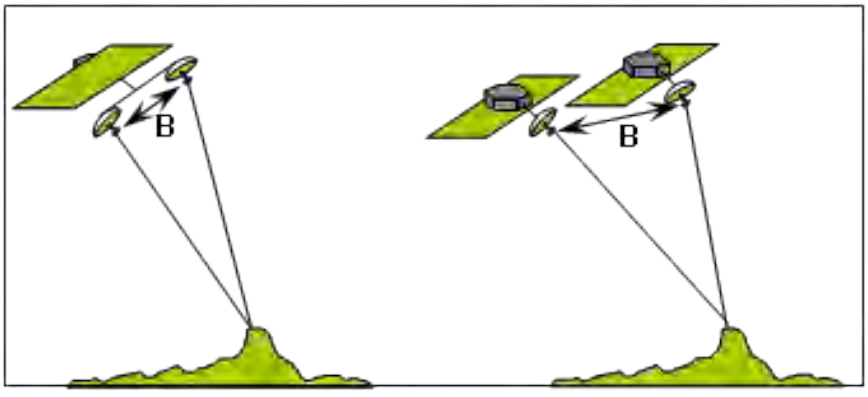

Figure 4.8: Different methods for SAR data acquisition. (Source: http://www.photogrammetry.ethz.ch/general/persons/jana/isprs/tutradar/3_radar1_1.ppt).

In synthetic aperture radar (SAR) imaging, an antenna transmits the microwave pulses towards the earth surface. The backscattered energy to the sensor is measured. Utilizing the radar principle the SAR makes an image by using the time delay of the backscattered signals. The same area can be seen from slightly different look angles. When two radars mounted on the same platform known as Simultaneous Baseline method, whereas two radars collects data at the same time or Repeat Track method, where same radar acquire data twice at different times by exploiting repeated orbits of the same satellite (Figure 4.8). The latter is the case for ERS-1, ERS-2 and Envisat. The time intervals between observations 1, 35 or a multiple of 35 days are available for these satellites (Fletcher, 2007).

SAR uses compressed pulse to get high resolution image which needs a large antenna width to acquire more azimuthal resolution (Figure 4.7 A.) The azimuth direction (v) falls on the plane where the image is focused and is perpendicular to the radar range (u). As the radar travels forward along its path, the aperture synthesis is attained by coherently integrating the reverted successive signal pulse. The azimuth resolution obtained is half of the wavelength divided by the change in angle of view during the aperture formation process. Thus, there is no loss in resolution if the same angle is covered at different altitudes.

4.5.3 Imaging Geometry of RADAR in Remote Sensing

Different parameters like surface geometry and particle size, constituting that surface along with particles dielectric constant affect the backscattered waves coming from the target. Three types of slant range distortions are associated with the SAR imaging depending upon the terrain. When slant range of two points on the target are almost equal in spite of being horizontally shifted in ground range direction, Foreshortening occurs (points a and b, Figure 4.9). On the other hand, Layover, occurs when a point, although farther from nadir in ground range direction, has small slant range as compared to another point close to nadir (points c and d, Figure 4.9). When a portion is not illuminated by transmitted waves due to obstruction by a high terrain or large structure, there happens a different situation called shadow. Figure 4.9 is best showing radar imaging geometry along with these topographic features.

Two or more synthetic aperture radar (SAR) are used by the geodetic method to create surface deformation maps or digital elevation, which uses the phase difference between the waves returning to the sensor (Figure 4.10). Amplitude and phase of the backscattered echoes from the target lying on the line of sight are recorded by SAR systems.

It has many applications in geophysical monitoring of natural hazards, for example volcanoes, earthquakes, and landslides, and it can be also used in structural engineering for precise monitoring of subsidence and structural stability.

The phase of each spot size is the sum of mainly five distinct contributions:

1. Sensor-Target-Sensor two ways travel path.
2. Interaction between incident e/m waves and ground scatterers.
3. Phase shift caused by the focusing system.
4. Phase shift because of atmospheric delay.
5. Doppler's effect.

Therefore, the phase of a single SAR image is of no practical utility. Phase difference of a single ground resolution from two slightly different viewing angle has the important role in InSAR. Phase is considered over amplitude as it is easy and precise to calculate. SAR image pair having proper baseline which can be effectively used to generate Digital Elevation Models, monitor terrain changes and improve range resolution.

SAR image is composed of real and imaginary part ($ae^{i\theta}$). Where "a" is the amplitude and "θ" is the phase calculated by scanner of a particular ground pixel. So, we use Single Look Complex (SLC) images for InSAR.

A summary of satellite SAR missions accomplished and currently working, along with most important design parameters is given in table 4.5 (Table 4.5 and 4.6 source: Hanssen, (2001)).

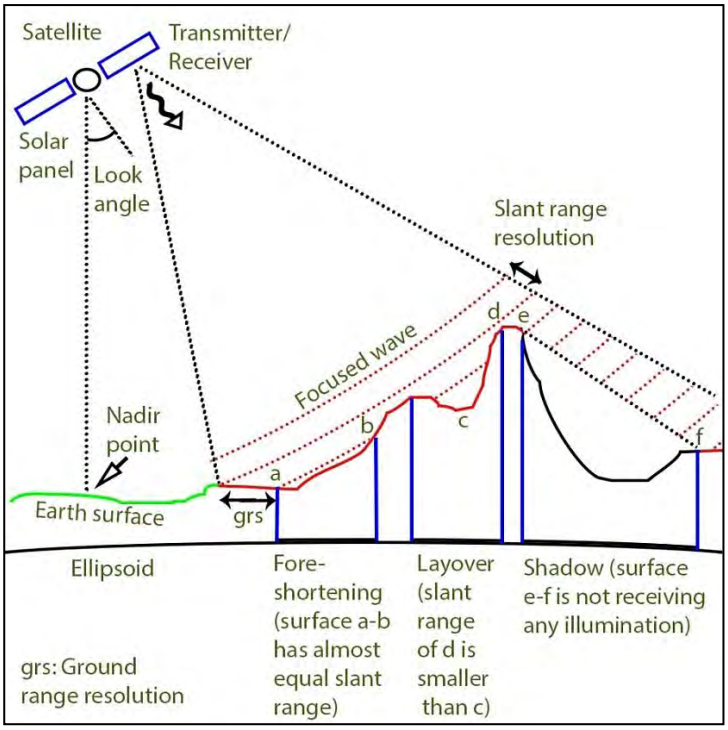

Figure 4.9: Foreshortening, layover and shadow is a topographically induced phenomena, depends on satellite orbit, look angle, elevation and ascending/descending pass mode.

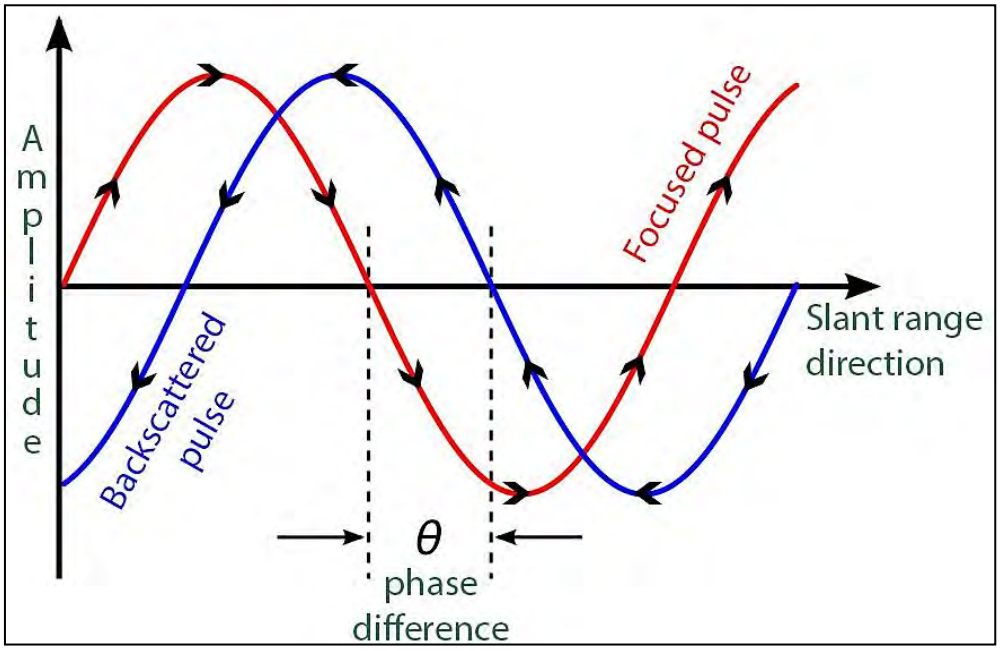

Figure 4.10: Two sinusoidal waves offset from each other by a phase shift θ. Amplitude difference will also be there but not considered and recorded for InSAR purposes. Phase difference greater than 2π cannot be calculated.

Table 4.5: Description of different SAR imaging satellites

Mission	Year	Repeat period	Height (km)	Incidence angle	Swath (km)
Seasat	1978	3	800	20,23,26	100
SIR-A	1981	NA	235	50	50
SIR-B	1984	NA	235	15-64	10-60
ERS-1	1992-92 1992-93 1993-94 1994-95 1995-2K	3 35 3 168 35	790 790 790 790 790	21,23,26 21,23,26 21,23,26 21,23,26 21,23,26	100 100 100 100 100
ERS-2	1995-	35	790	21,23,26	100
JERS-1	1992-98	44	568	26,39,41	85
SIR-C/X-SAR	Oct 1994	1	225	55	21-42
Radar Sat	1995-	24	792	20-49	10-500
SRTM	2000 2000	0 0	233 233	52 52	225 50
ENVI SAT	2001-	35	800	20-50	100-500
ALOS	2002-	45	700	8-60	40-350
Radar Sat-2	2003-	24	798	20-60	20-500
Sentinel 1_A	2014	12	693	25	250

Table 4.6: Major geological events studied using radar interferometry along with few major examples.

Events	Examples
Earthquakes	Landers earthquake, California, USA, 1992 Izmit earthquake, Turkey, 1999 Bam earthquake, Iran, 2003
Volcanoes	Vatnajokull, Iceland Etna, Italy Kilauea, Hawaii Long Valley, California, USA Galapagos
Anthropogenic subsidence/ uplift	Las Vegas, Nevada, USA, 1999 Napels, Italy, 2000 Imperial valley swelling, California, USA, 1989
Glacier/ Ice motion	Antarctica/ Patagonia Greenland.

Table 4.7: A variety of InSAR processing packages are commonly used, several are available open source or free for academic use (Source: http://en.wikipedia.org/wiki/Interferometric_synthetic_aperture_radar).

Software	Details
Gamma Software	Commercial software suite consisting of different modules covering SAR data processing, InSAR, DInSAR. It runs on Solaris, Linux, Mac, Windows OS.
DORIS (Delft Object-oriented Radar Interferometry Software)	Developed by TUDelft, DEOS group, Bert Kampes. Distributed as open source. Still under developing stage.
SARscape	Commercial software suite covering InSAR, ScanSAR focusing and Persistent Scatterers. Runs under ENVI in Linux and Windows.
GMTSAR	InSAR processing system based on Generic Mapping Tools-open source GNU General Public License
IMAGINE SAR Interferometry	Commercial processing package embedded in ERDAS IMAGINE.
Pulsar	Commercial software suite, UNIX based
RAT (Radar Tools)	PolSAR, InSAR, PolInSAR etc. Free software suite
NEST (Next ESA SAR ToolBox)	Windows, Linux, Mac, GNU GPL open source software suite
SARPROZ	Commercial software suite covering InSAR, ScanSAR focusing and Persistent Scatterers,

4.5.4 SAR (Synthetic Aperture Radar)

SAR is a technique in remote sensing which can picturise the terrain and its different structure by transmitting a radar wave from a satellite and then receiving reflection from the ground. Synthetic Aperture Radar (SAR) is a side looking radar instrument, which emits microwave radiation pulse-by-pulse and detects the backscattered amplitude and phase signals reflected from the target. The antenna transfers the radiation and then reflected back from the targets as different from the passive sensing where the signal comes from ambient illumination. The SAR image acquisition is not dependent on natural illumination and can capture image irrespective of day and night.

The transmitted radiation from radar has to reach the target on the ground and then return back to the sensor so as to form the SAR image with a travel distance 2R (Figure 4.11). At different distances the scatterers from the radar (different slant ranges) host different delays among transmitted and received radiation. As the transmitted signal is exactly sinusoidal in nature, this interval (delay) τ is corresponding to a phase change ϕ among transmitted and received signals (Fletcher, 2007).

The phase change is proportional to the two-way travel distance ($2R$) of the radiation divided by the transmitted wavelength (λ). We can say that the phase of the SAR signal is a measure of just the last part of the two-way travel path that is smaller than the transmitted wavelength.

Using one SAR image we cannot calculate elevation difference between two points having same slant range. From figure 4.13 interferometric configuration, topographic height and surface deformation can be observed by determining the geometrical and physical relationships between the phases of two signals.

Both SAR images comprises of a consistent grid with complex values, or phasors, y1 and y2, which can be converted into phase and amplitude component by means of Radar Interferometry (Hanssen, 2001).

$$y_1 = |y_1| \, exp \, (i\psi_1)$$

$$y_2 = |y_2| \, exp \, (i\psi_2)$$

For ground resolution cell P, interferometric phase difference can be written as

$$\phi_p = \psi_{1p} - \psi_{2p} = -\frac{4\Pi\Delta R}{\lambda}$$

Geometrically, the path length difference ΔR can be approximated as

$$\Delta R = B \sin(\theta - \alpha)$$

After doing a little bit trigonometry and assumptions, we derive the relationship between the height H_p above the reference body and the phase difference $\delta\phi_p$.

$$H_p = -\{\lambda\, R1p\, (Sin\, \theta p)\delta\phi p\} \Big/ \{4\, \Pi\, B\perp p\}$$

Where,

$$B_{\perp p} = B\, Cos\, (\theta_p - \alpha)$$

The initial value θ_p is found for an arbitrary reference surface (e.g., a sphere or ellipsoid).

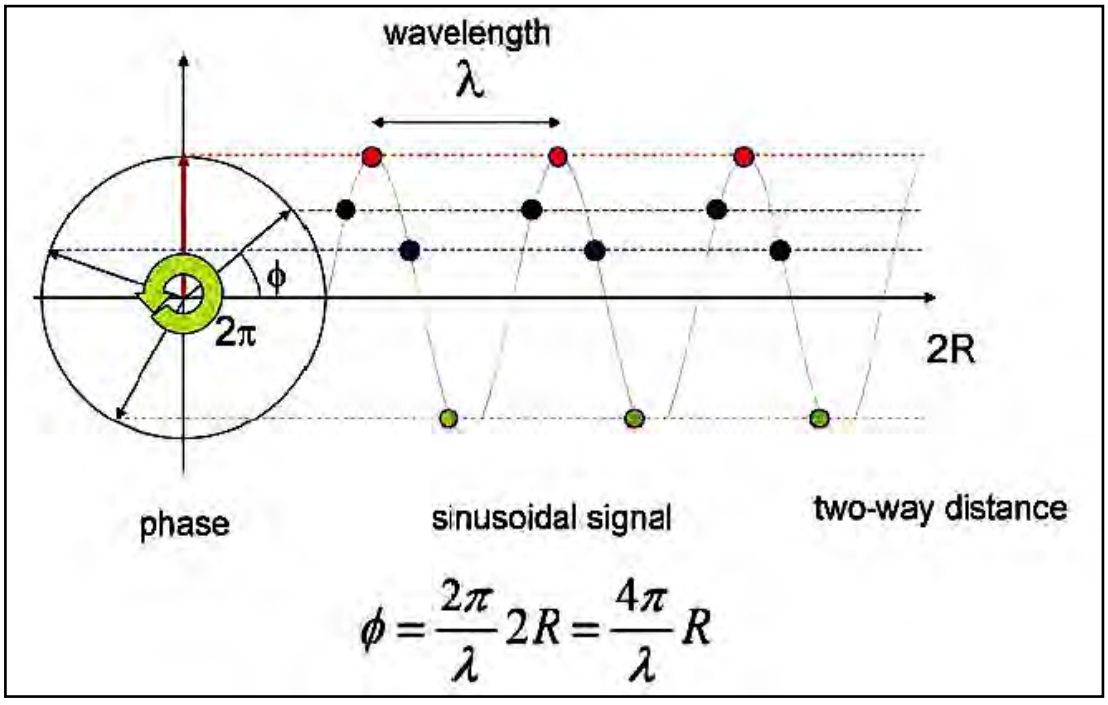

Figure 4.11: Radar sinusoidal signal and phase and two way travel (Fletcher, 2007).

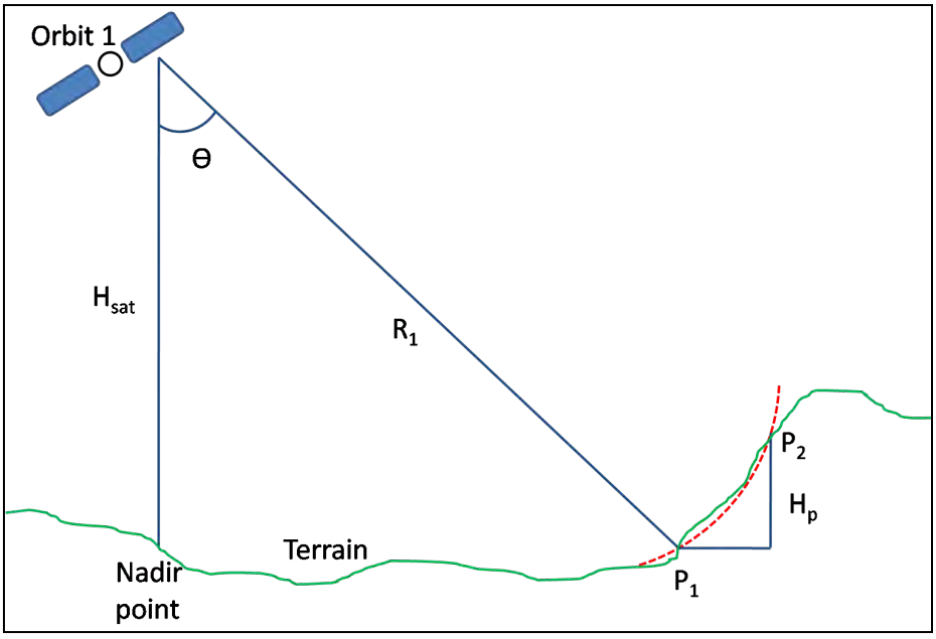

Figure 4.12: Single SAR pass geometry showing points P_1 and P_2 having equal slant range.

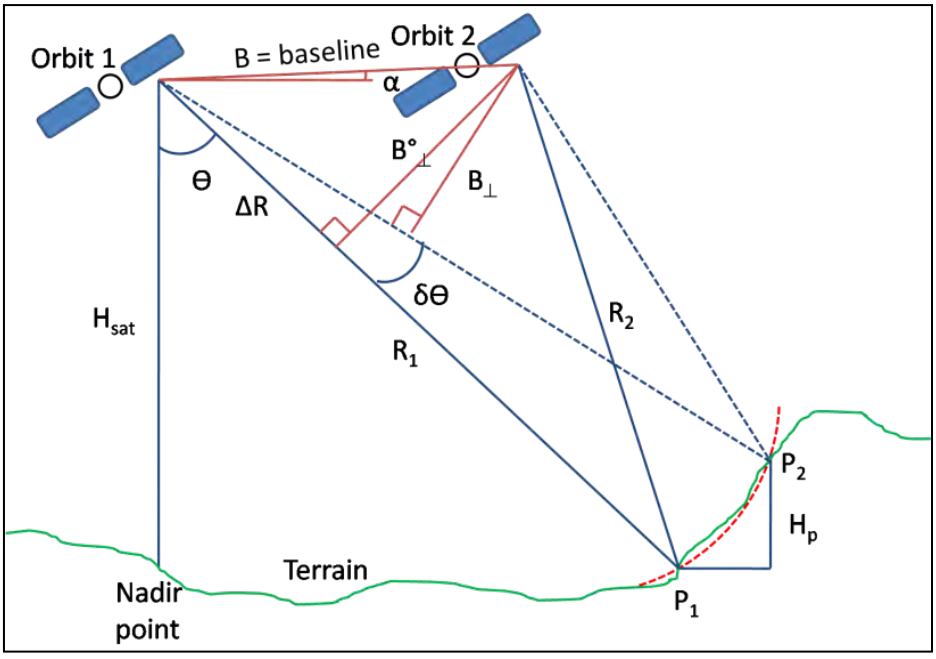

Figure 4.13: Interferometric geometry. Two orbits are being used to acquire SAR images of same ground resolution cell, having spatial and temporal baseline. H_{sat}: satellite height; θ: look angle; R_1 and R_2: slant ranges from orbit 1 and 2, respectively; H_p: elevation difference; α: elevation of orbit 2 w.r.t 1.

4.5.5 Overview of InSAR Processing

In figure 4.14, a detailed description of the InSAR and PSI processing has been shown in four divisions of block. Block 1 indicates the processing of the raw (radar and orbit) data to one more format. Block 2 comprises of the co-registration where the master image is being associated with the slave image, followed by the calculation of the reference phase of the ellipsoid. In block 3 the interferometric attributes like complex phase image and coherence are computed. Finally, block 4 shows end products (e.g., a DEM or a deformation map) are figured.

Some parameters which should be considered while selecting SAR images and processing them for interferomteric purposes are listed below:

1. Spatial baseline: Long baseline is good for highly rugged terrain. But it would be difficult to remove random noise caused due to atmosphere.
2. Temporal baseline: To retain high coherence images should be obtained during the same season. Images of rainy days or when anthropogenic activity is going on should be avoided.
3. Ascending/Descending mode: As SAR sensors follow side looking geometry, deformations in the slant range direction can be estimated precisely.
4. Satellite orbit: In order to reduce, mainly layover and shadow effect, appropriate satellites orbit should be selected for data acquisition.
5. Image polarization: Generally VV (Vertical-Vertical) polarized images have been used during most of the researches in the past, although main role in InSAR technique is played by phase difference.
6. Satellite ephemeris info: During processing it is preferred to have info regarding satellite health, stability, time of data acquisition, altitude and Doppler Effect. This data can be utilized as optional parameters to minimize systematic and random errors.
7. Image resolution: SAR image and corresponding DEM's resolution have an important role in data interpretation. DEM having fine resolution will more effectively remove phase shifts caused by topography.
8. InSAR software used: Appropriate software selection should be done because change in processing algorithms and processing steps effect errors propagation drastically.

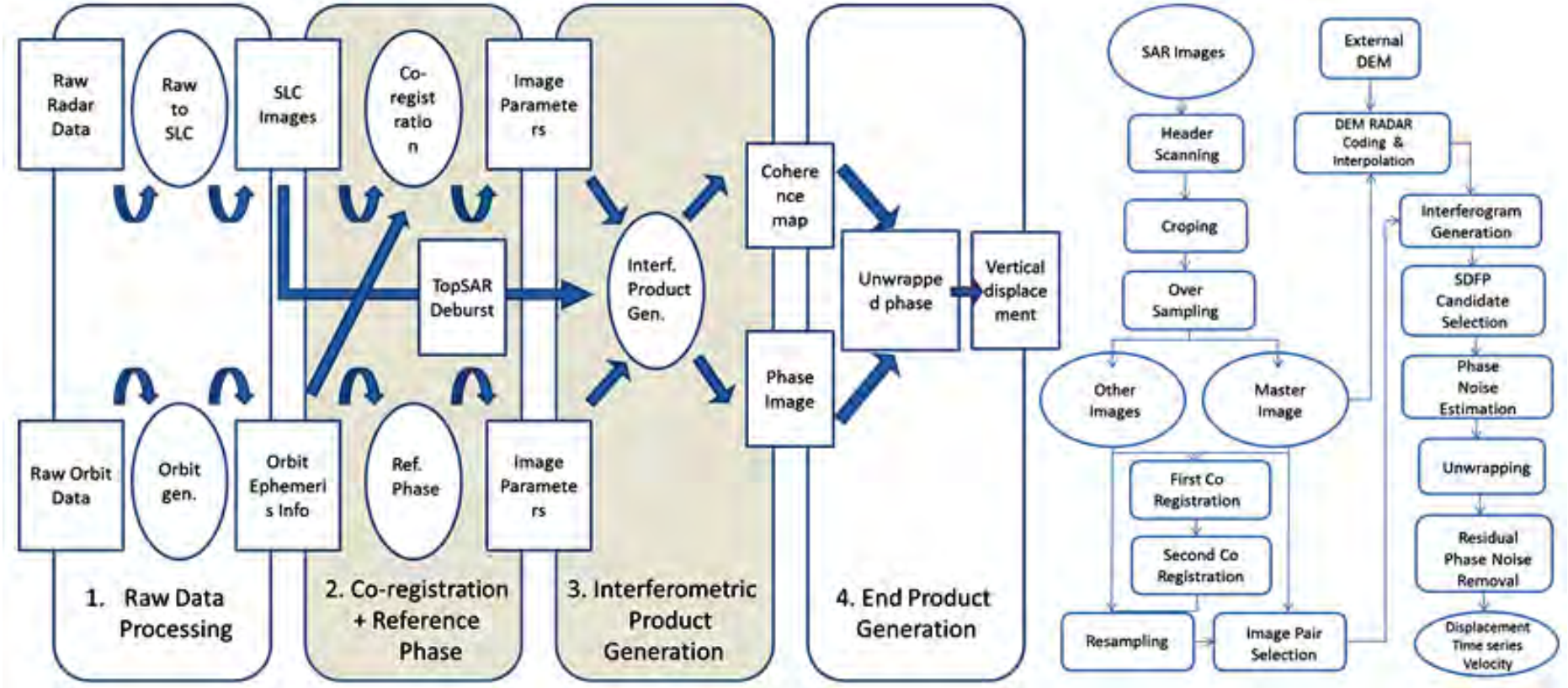

Figure 4.14: Overall processing Flowchart for InSAR (Left) (Source: http://doris.tudelft.nl/) and PSI (Right) (Source: https://www.sarproz.com/processing-modules-options/).

4.5.6 Interferometric SAR (InSAR)

As Interferometric SAR or InSAR is coherent, it allows precise measurements of the illuminated travel path. The calculation of travel path which varies as a function of the satellite location and time of acquisition allow to generate DEMs and it measures the minute surface deformations in the topography.

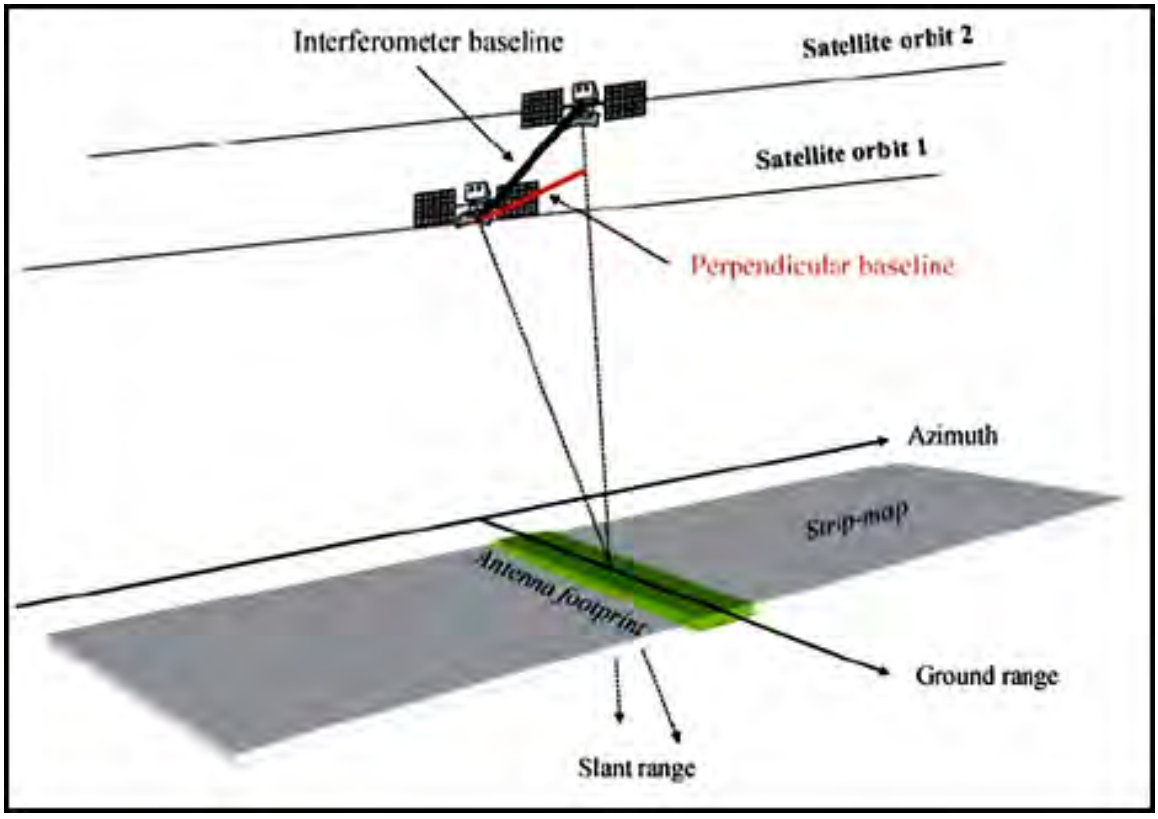

Figure 4.15: Geometry of Interferometric-SAR system (Source: Fletcher, 2007).

The distance of separation between the two satellites along the perpendicular plane to the orbit is referred as interferometer baseline (Figure 4.15) and its perpendicular projection to the slant range is marked as perpendicular baseline. The SAR interferogram is achieved by complex multiplication (pixel by pixel), the first SAR image with the complex conjugate of the second. So, the amplitude of the first image multiplied by that of the second one is the final intensity of the image, whereas the interferometric phase correspondence to the phase difference between the images (Fletcher, 2007).

4.5.7 Technique of SAR Interferometry

In radar remote sensing, generally the phase of the returned wave is used to make an interferogram. Basically radar transmits and receives microwave electromagnetic radiation with frequencies in the range of 108 -1011 Hz and corresponding wavelengths of order 1-1000 mm.

The basic principle of InSAR technique is to obtain the change in phase in the image pair of the same location obtained at period spreading over the distortion time frame. Since the active wave is delivered by the satellite, the phase is known and can be compared with the reflected signal. The phase of the return wave relies upon the separation to the ground; in fact, the way length to the ground and back will comprise of various entire wavelengths in addition to some portion of a wave. This is noticed as a phase difference or shift in the reflected wave (Figure 4.16 b and c). The phase change is the measure of the deformation along the line of sight between the two images (with orbital effects, atmospheric effects and topographic effects).

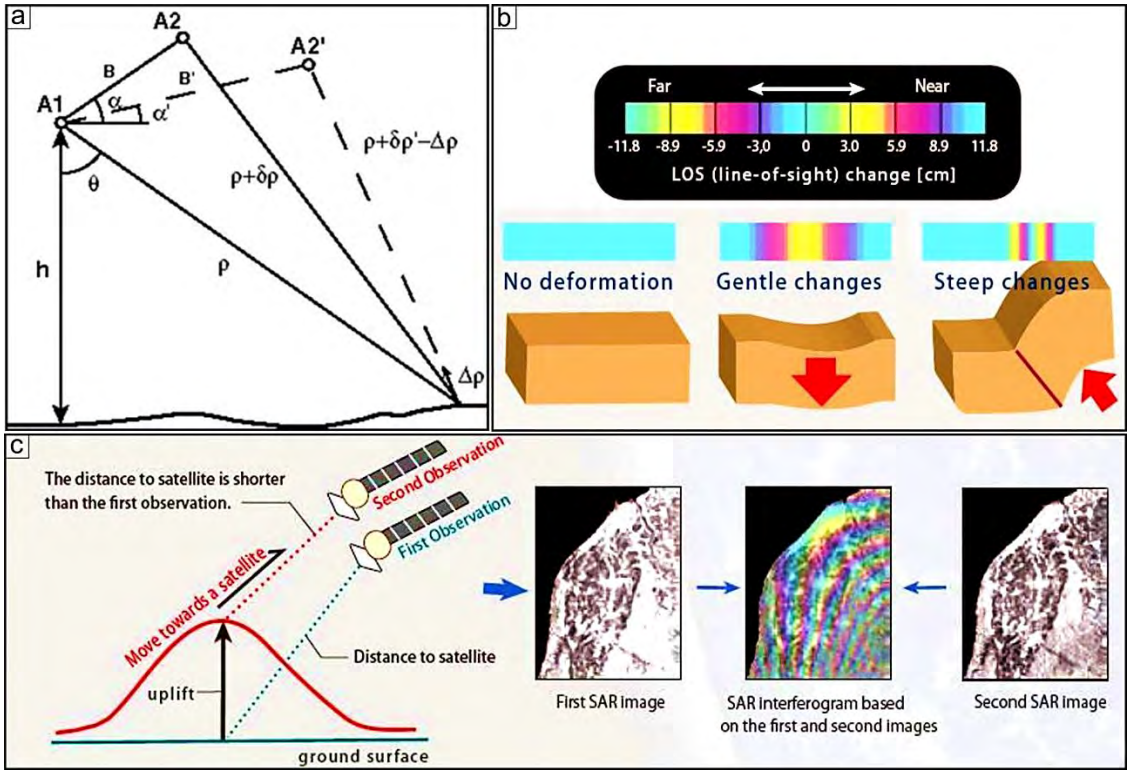

Figure 4.16: (a) Interferometric imaging geometry (Zebker *et al*., 1997), (b) Deformation pattern, (c) Configuration for InSAR acquisition (Source: http://vldb.gsi.go.jp/sokuchi/sar/).

For InSAR, the imaging places of the satellite or satellites (A1 for beginning pass and A2 for slave or auxiliary pass (Figure 4.16 a) are isolated by a point of reference B. The master satellite target ρ of an object will change by a factor of ∂ ρ for the slave image which has initiated change in phase ϕ (for two-way travel), assuming that the backscattered signal for the two frames is almost same, will be

$$\phi = (4\pi\partial\rho)/\lambda$$

This change in phase comprises of three factors i.e. the orbital, topographic, and environmental factor, which must be reduced or completely removed before the factor responsible for terrain change can be resolved.

There are two methods of deducting the topographic noise; the first one is to use a high resolution DEM, while second one is to utilize a second interferometric pair (Period of unchanged topography) which needs a minimum one more image. The DEM has to be co-registered with the radar image which relies on the ability to differentiate features in images. This method also depends upon the availability of a suitably perfect DEM for the region.

The resultant interferogram though less sensitive to topography

$$d\phi/dh = [4\pi\ B\ Cos\ (\theta - \alpha)] / \lambda\ \rho\ Sin\ \theta$$

Where θ is the look angle from nadir, λ is the radar wavelength, and α is the baseline orientation angle) than to deformation Δρ

$$d\phi/d\Delta\rho = 4\pi / \lambda$$

Since at least for satellite observations, ρ >> B and So,

$$d\phi/d\Delta\rho >> d\phi/d_h$$

The susceptibility of an interferometric pair for topographic noise is hence observed by the elevation ambiguity h_a so called as the topographic height ($\mathbf{d_h}$) required to introduce one cycle ($\mathbf{2\pi}$ radians) of phase difference ($\mathbf{d\phi}$) (Zebker *et al*., 1994).

$$h_a = (\rho\ \lambda\ Sin\ \theta) / 2B\ Cos\ (\theta-\alpha)$$

Radar that picturise Earth's surface have higher wavelengths more than few centimetres so as to penetrate through clouds, haze and precipitation. Hence they can function round the clock, irrespective of day and night in all-weather condition.

4.5.8 Factors affecting SAR Interferometry

Different factors should be considered before choosing an interferometry pair used for the study. Some of the most important factors are the following:

a. Temporal Decorrelation:

Change in vegetation growth, terrain change etc. which are referred as the Physical changes of the Earth's surface arising between a SAR data pair acquisitions leads to low coherence in phase (Gupta, 2003). This is the reason of temporal decorrelation of the data pairs and is most avoidable for processing of InSAR. The phase of the wave may vary with reflected illumination, subjected to the physical properties of the object. The reflected signal backscattered from any distinct pixel is the total influence upon phase by too many minor objects on the ground, having different distances and dielectric properties from the satellite. (http://en.wikipedia.org/wiki/Interferometric_Synthetic_aperture_radar).

b. Orbital Effects:

The InSAR pair will be more feasible if the spatial position of the image acquisition during the image capture is relatively low i.e. the images acquired by two different satellites with separate orbits cannot be linked and so a specific satellite data should be used. In general the perpendicular distance between two orbits is referred as baseline, which ranges upto few centimetres and can be measured on a scale ranging from 10 to 100 of metres. The minute changes make a great difference in phase, which should be distant from the interferogram (http://en.wikipedia.org/ wiki/Interferometric_Synthetic_aperture_radar).

c. Baseline Decorrelation:

The viewing geometry is controlled by the length of the spatial baseline. Longer baselines refer to the better relative variation in viewing geometry, which gives a better coherence and superior decorrelation. The baseline is inversely proportional to the topographic

height which needed to obtain phase change with fringes, also referred as the Altitude of Ambiguity (http://en.wikipedia.org/ wiki/ Interferometric_Synthetic_aperture_radar).

d. Atmosphere:

SAR wavelength and atmospheric condition give rise to refraction (initiating mis-registration) and artifacts in phase difference. The influence is more distinct in case of a heterogeneous atmosphere, i.e. spatially changing (Gupta, 2003). On the other hand the wave gone through a vacuum it ought to hypothetically be conceivable (subject to adequate exactness of timing) to utilise the two-way-travel-time of the wave with the phase to determine the correct separation to the ground. However the speed of the wave through the environment is lower than the speed of light in a vacuum and relies on upon air temperature, weight and the fractional weight of water vapour. Thus the interferogram created from two-pass interferometry show a more noteworthy impact of heterogeneity than do those from the three-pass interferometry. (http://en.wikipedia.org/wiki/Interferometric_Synthetic_aperture_radar). Night time acquisitions are usually less affected by atmospheric effects. However the image acquisitions should not be performed during very hot days because hot air holds much more water vapour than cold air (a major cause of atmospheric artifacts in SAR interferogram). Therefore usually Summer time is avoided for acquisition of SAR data (Hanssen, 2001).

e. Topography:

Another important source of error observed in interferogram is produced by topography. If the topographical elevation is previously known, the contribution of topographic phase can be determined and deducted. This can be achieved in two methods. In case of two pass method, elevation data from an external DEM derived from different source is used in combination with the orbital meta data to estimate the contribution of phase. However in case of three-pass interferometry two images obtained at a short time interval are used to generate an interferogram, it is supposed to be having no deformation signal and hence characterise the contribution from topography. Further the interferogram is subtracted from a third image having large time difference in acquisition so as to give the remaining phase as a result of deformation (http://en.wikipedia.org/wiki/ Interferometric_Synthetic_aperture_radar).

Chapter 5

InSAR interpretation from ALOS-PALSAR Data

5.1 ALOS-PALSAR Data Used For InSAR Study

Phased **A**rray type **L**-band **S**ynthetic **A**perture **R**adar (PALSAR) data set, acquired through the **A**dvanced **L**and **O**bservation **S**atellite (ALOS) satellite, was obtained from the **J**apan **A**erospace **E**xploration **A**gency (JAXA). PALSAR can operate at four primary modes with diverse polarizations and off nadir mode: (a) high-resolution single-polarization mode, (b) high-resolution dual polarization mode, (c) fully-polarimetric mode, (d) ScanSAR mode. Single-Polarized products in image mode with swath width of 70km and pixel spacing of 4.7m have been used for post-earthquake ground change study. Figure 5.1 shows study area for which ALOS-PALSAR data has been used. Azimuth and range resolutions are 5m and 9m, respectively. Each image comprised of basic **S**ingle **L**ook **C**omplex (SLC) image of 1.1 product code. Incidence angle is 38.7° at the scene center. These images (table 5.1) were acquired during the satellite's ascending passes.

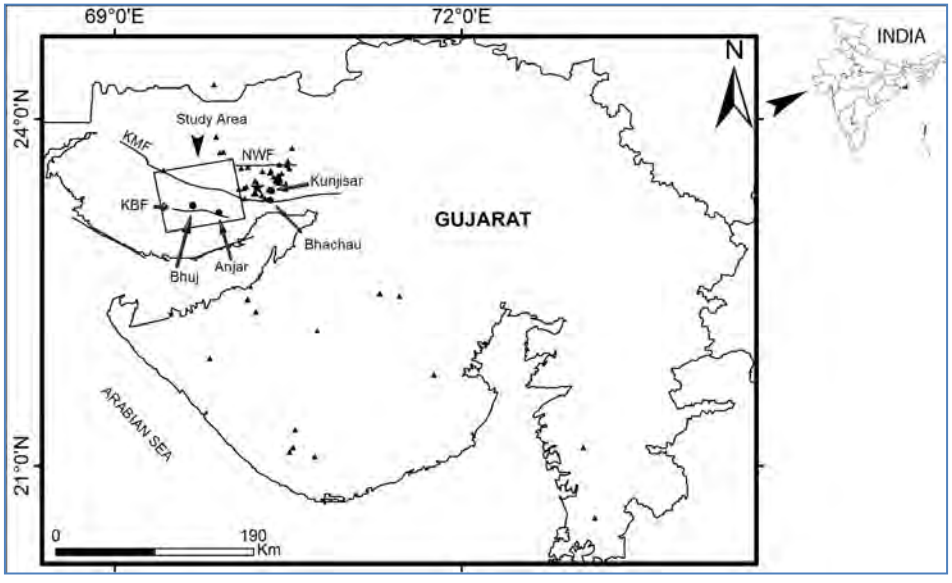

Figure 5.1: Study area covering a part of the central Kutch region of Gujarat, India. Triangles are earthquake epicenters (Mag >3.5 to 5 Mag) recorded by ISR during the year 2007-2010. Star symbol shows epicenter location of 2001, 26th January main event.

Table 5.1: ALOS-PALSAR data set for Bhuj area used in the analysis of ground deformation.

Image	Acquisition date	First pixel azimuth time (UTC)	Normal baseline (m)
Master	20th February 2007	17:55:59	889
Slave	28th February 2010	17:57:26	

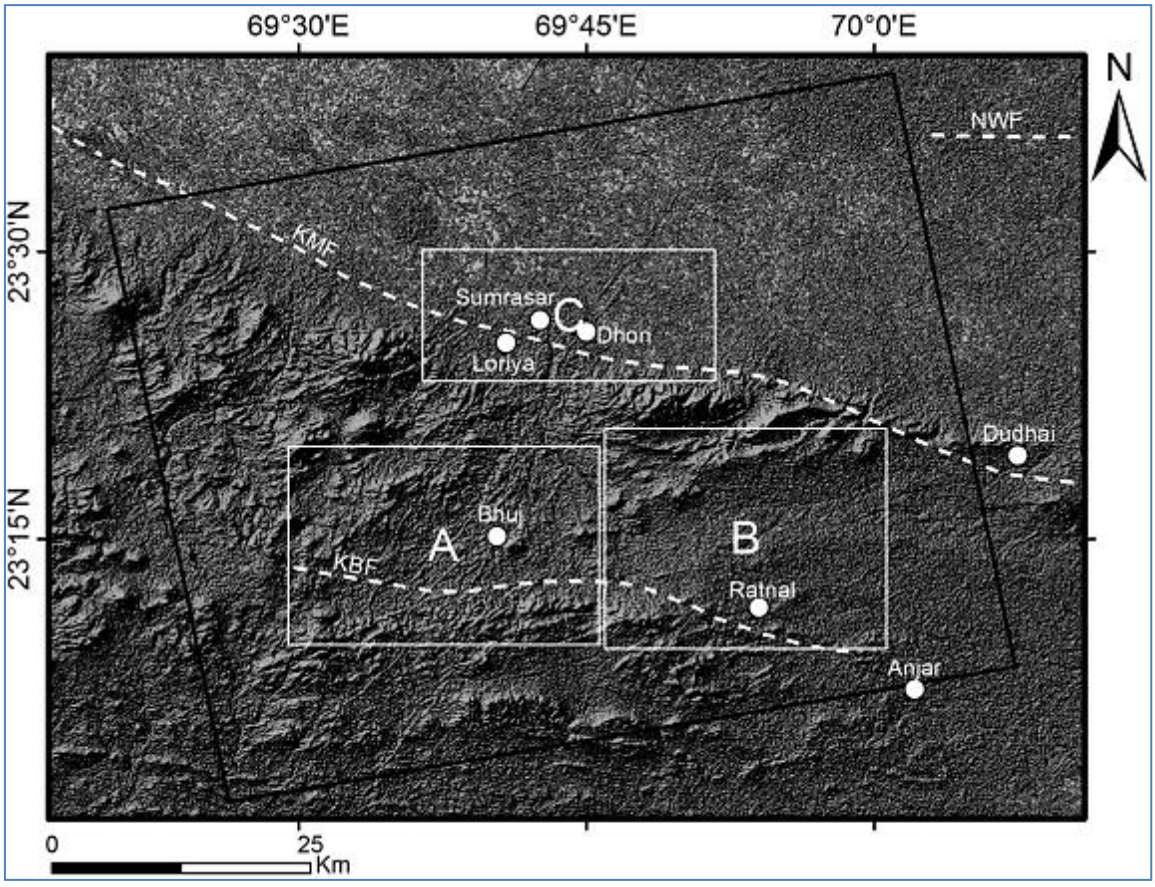

Figure 5.2: Topography of the study area as shown by shaded relief model (30m resolution) derived from ASTER-GDEM. A, B and C boxes are regions where visible countable interferometric fringes have been observed in ALOS-PALSAR data analysis (Figure 5.4) KBF-Katrol Bhuj Fault, KMF-Kutch Mainland Fault, NWF-North Wagad Fault.

Among the available ALOS-PALSAR images of the study area, a pair was selected in such a way as to keep effects of atmospheric artifacts, terrain, vegetation and effects of season of the year at minimal. The selected study area, covering about 4200km², has nearly flat topography in the eastern and northern part (Figure 5.2) with minimal drainage system, two major geological faults and few prominent lineaments (Figure 5.3). Figure 5.4 is an Enhanced **T**hematic-**M**apper (ETM) Landsat mosaic image showing the terrain characteristics. The region is semi-arid with sparse vegetation. Abrupt truncation of vegetation along two perceivable lines in the central and southern part of the study area is due to KMF and KBF, respectively (Figure 5.4).

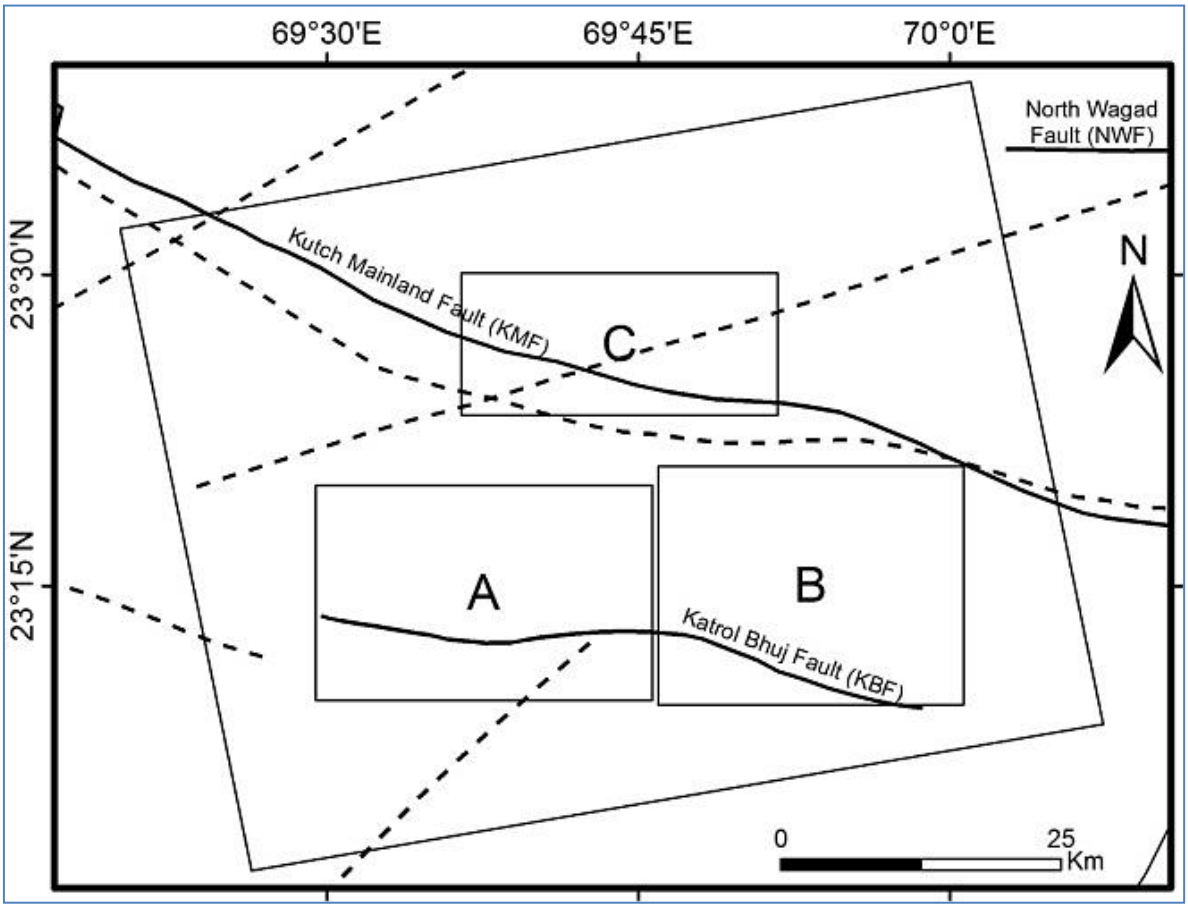

Figure 5.3: Major faults and lineaments (dashed lines) running across the SAR scene area. Blocks for which interferogram could be obtained is shown as A, B & C. Tectonic features are adopted from GSI (2000).

5.2 DORIS InSAR Processing

DORIS (**D**elft **O**bject-oriented **R**adar **I**nterferometric **S**oftware) InSAR software v4.02, developed by **D**elft Institute for **E**arth-**O**riented **S**pace research (DEOS) group, is used to process PALSAR data pair for interferometry. Automated DORIS Environment (ADORE) shell was installed on Ubuntu v12.04 to operate different interferometric steps (Figure 4.14).

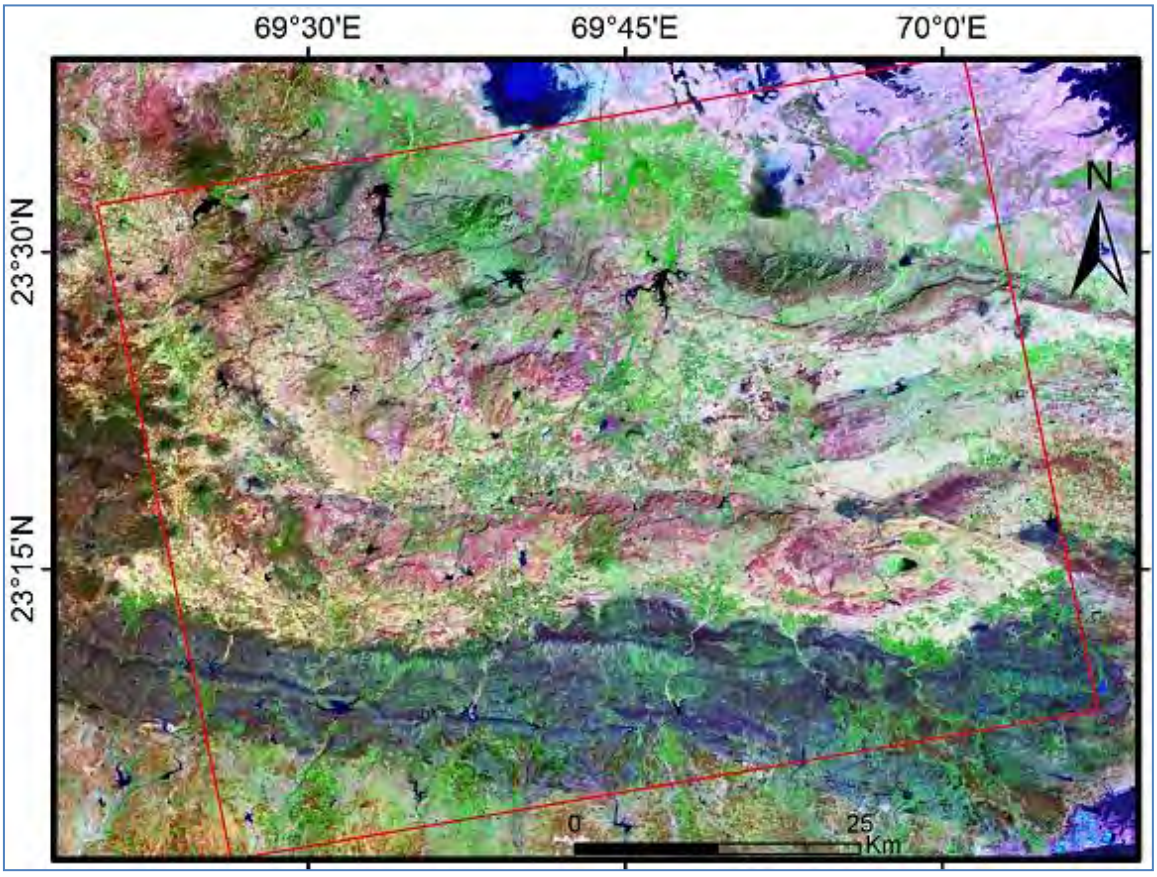

Figure 5.4: ETM-Landsat mosaic (30m resolution) covering the study area. Data was acquired between 5th June 2014 and 27th May 2014; and downloaded from GLCF website. (Source: http://glcf.umd.edu/data/landsat/).

5.3 Interpretation

Interferogram image was generated using 20th Feb. 2007 (master image) and 28th Feb. 2010 (slave image) ALOS-PALSAR data pair (Figure 5.5). For better interpretation, three blocks showing interesting features have been selected. Each interferometric fringe corresponds to about 11.8 cm of ground deformation in the satellite's line of sight (half of the L-band wavelength, i.e. 23.62 cm).

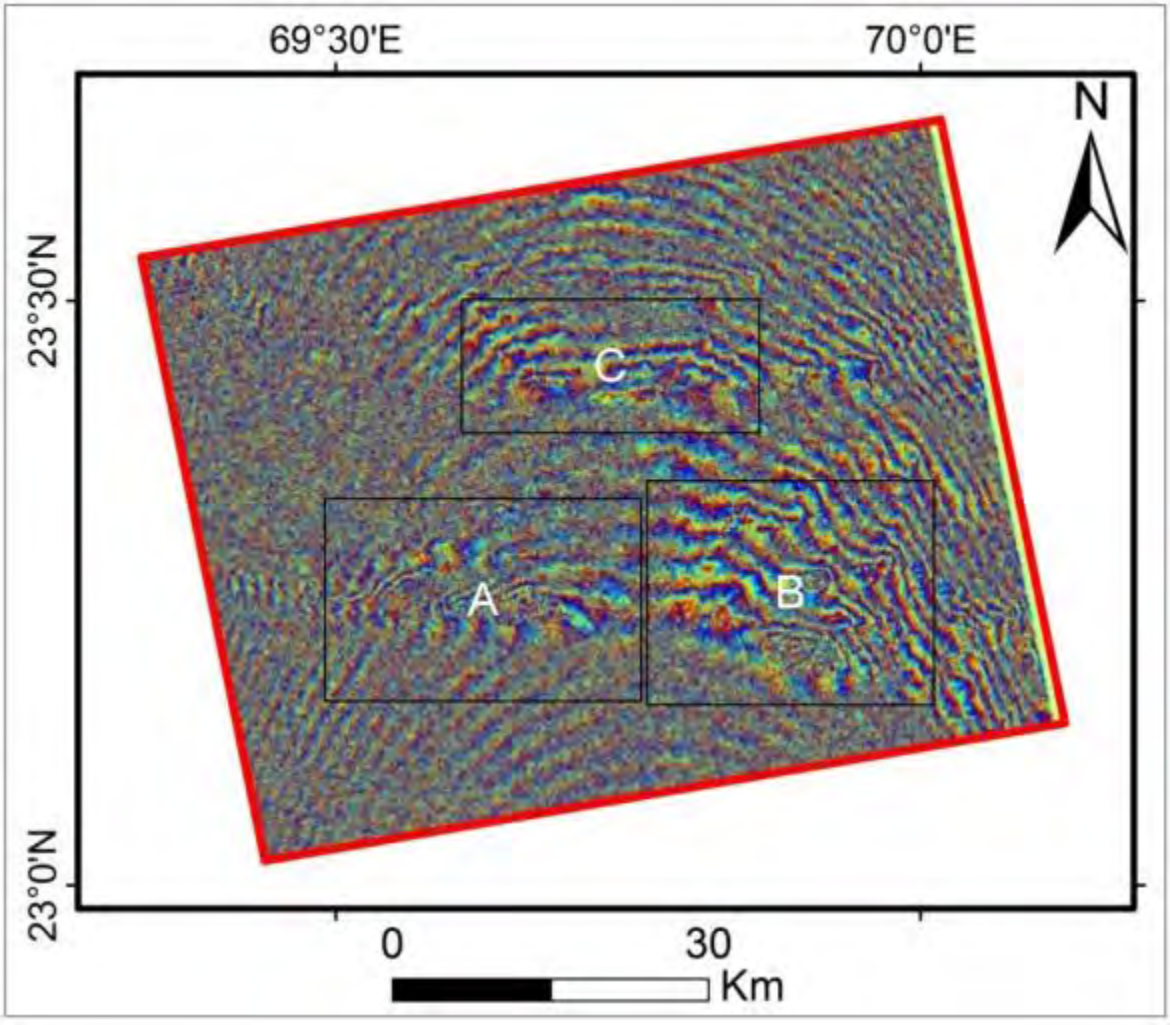

Figure 5.5: Regions covered by blocks A, B and C are showing ground deformations attributed to visible countable fringes.

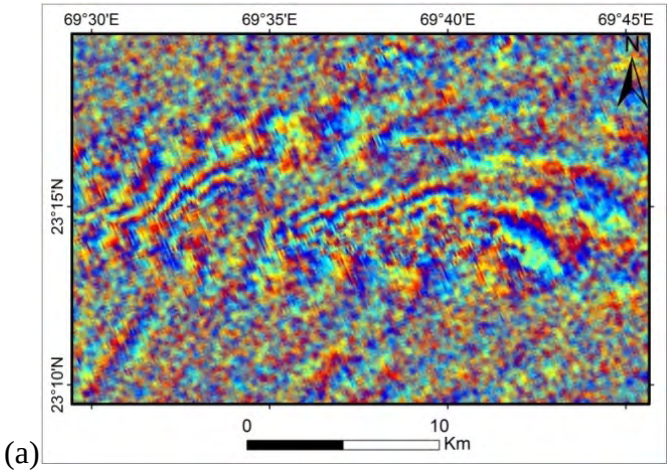

(a)

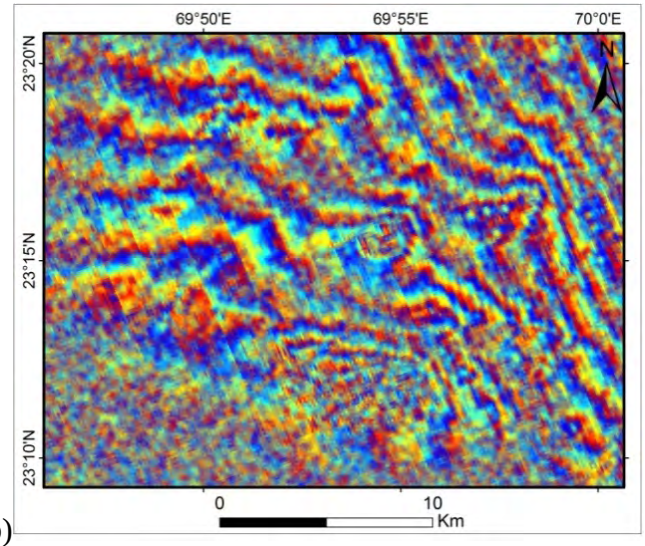

(b)

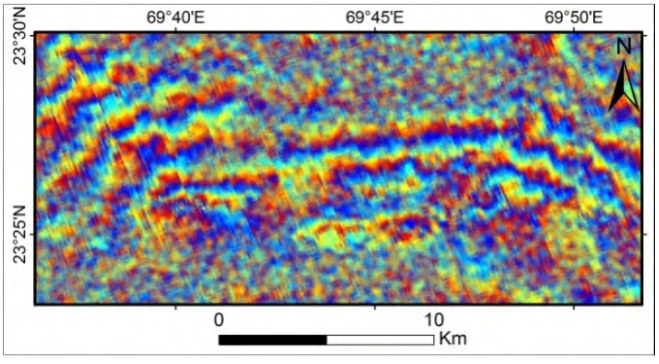

(c)

Figure 5.6: Interference fringes as developed in three blocks in the vicinity of Bhuj city at the central Kutch region of Gujarat, India. (a), (b) and (c) corresponds to the blocks shown in figure 5.5 based on the 2007-2010 InSAR pair.

Block-A, having ground coverage of 405km², is covering region around Bhuj city. Around three fringes have been observed after close inspection (Figure 5.6 (a)). Because of low coherence, interferometric fringes are discontinuous and pixilated at few places. The color pattern is **M**agenta-**Y**ellow-**C**yan (MYC) as moving from south to north, indicating a Positive deformation (Subsidence) of about 35cm on a stretch of about 10km. These fringes are abruptly terminating in the southern portion of the block-A, indicating geological feature trending from east to west.

Interesting features have been observed in block-B (area coverage about 660km²), where at the central and southern portion two loops of fringes are seen (Figure 5.6 (b)). After careful observation of the central region of the block, around two fringes having color pattern of **C**yan-**Y**ellow-**M**agenta (CYM) approaching towards the center, are noticed. This specifies a negative deformation of about 24cm along the line of sight. This interferometric observation suggests that between 2007-2010 subsidence having radius of around 1.8km has occurred. Similarly, southern region is also showing the same color pattern but because of low coherence it is not possible to read the total number of fringes. At least two visible fringes, deciphering a negative ground movement of around 24cm, can be interpreted. Since anthropogenic activity is also possible between 2007-2010, Ratnal city (Figure 5.2), with the developed circular fringes, provides valid reason for low coherence, making master and slave images interferometrically incoherent. Collectively, it can be concluded that during the selected time span the block-B, which is lying to the NW of city Anjar, has experienced positive deformations at two places. It has been reported that the central Kutch region is still experiencing liquefaction indicating subsidence effect (Figure 5.7). In the north / NE portion of the block several parallel fringes can be seen. These could be a small part of very large closed fringes covering thousands of square kilometer area, getting closely spaced as approaching towards epicenter of major earthquakes confined between the years 2007-2010 (Figure 5.1).

Block-C is lying to the north of Bhuj city and covering an area of around 440km². As moving towards north three prominent fringes having MYC color pattern have been observed (Figure 5.6 (c)). Interferometrically the region has undergone positive deformation of around 35cm as moving towards north, over a stretch of around 9km. Only upper half portion of these fringes is visible. This could happen because of geological feature close to Bhuj city, extending from east to west in the block, not allowing earthquake induced ground deformations to

propagate to the south. At places low coherence attributed to discontinuous colored fringes is due to three towns viz. Sumrasar, Loriya and Dhori lying within the study area of block-C (Figure 5.2). In case of interferometric studies, manmade structures are always act as a hindrance for good coherence (>0.4).

In the southern portion, blocks-A and B show sudden disappearances of interferometric fringes. This could happen because of crustal faulting extended to the surface, trending from SE to west in the study area. Figure 5.8 is showing KBF and KMF over the interferometric image. KBF is the primary cause for blocking the propagation of ground deformations, attributed to colored fringes, to the south of blocks-A and -B.

Similarly, block-C is also showing discontinuous fringes in the southern part which is caused due to KMF (stretching SE-NW). If combined with major geological faulting in the central Kutch region and past seismic events between 2007-2010 recorded by ISR, the synoptic view of the study area is giving appropriate explanations of sudden truncations and clustering of interferometric fringes at some places (Figures 5.2 and 5.8).

In the east and NE portion of the study area numerous subtle parallel fringes can be observed. It could be possible that only a small portion of very large fringes are visible in this current ALOS-PALSAR data. Since main seismic events (Mag >3.5 to mag 5) which took place during 2007-2010 are clustered to the east and NE to the study area (figure 5.1), liquefactions or ground deformations could be the reason for these closely spaced nearly parallel interferometric fringes. Central Kutch region has experienced at least six, five and four earthquakes event in 2007, 2008 and 2009, respectively having magnitude 4 to 5 (ISR 2009 and 2010).

The two main crustal-structural features around Bhuj and Anjar city are KMF and KBF. Due to these two structural faults, the ground deformations of upper soft crustal layer does not propagate to the south of their stretch and therefore sudden truncations of interferometric fringes have been noticed in the study area (Figure 5.8). Further, the ground change (mainly subsidence) at the selected places as inferred based on InSAR studies may be attributed to the continuing seismic activities as well as settlement of the highly water saturated ground constitute of soil/mud.

a)  (b) 

Figure 5.7: Liquefaction effect (a) Sand-blow liquefaction crater and (b) water pond near Dudhai village (figure 5.2) during May 2009 (courtesy: ISR 2010).

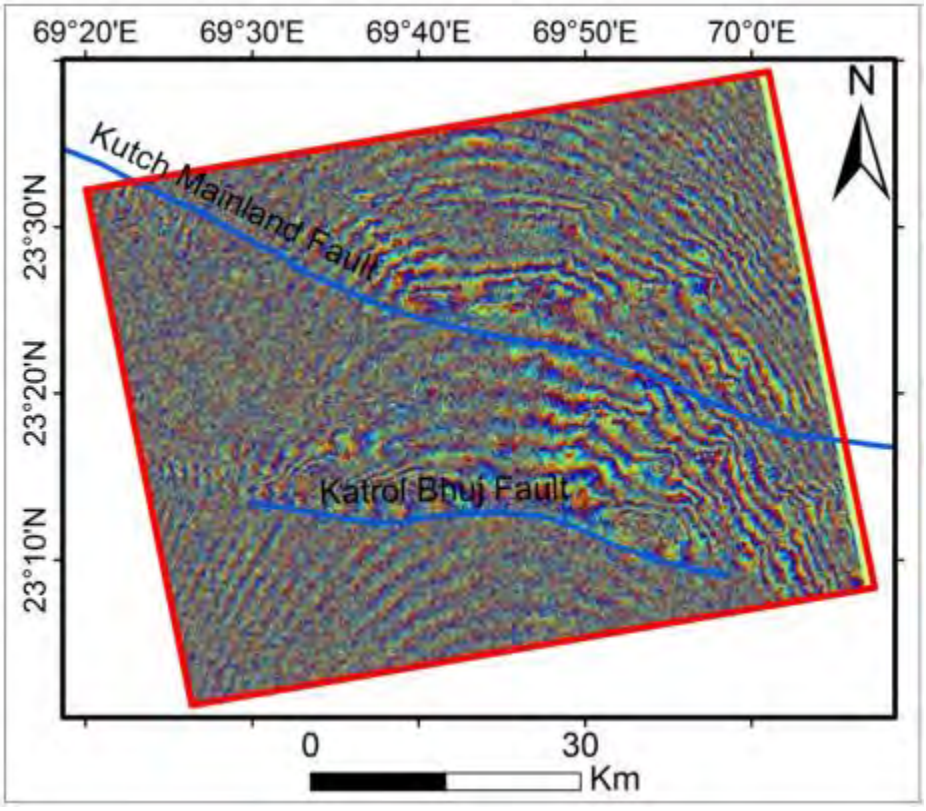

Figure 5.8: Interferometric image overlain by two major faults (KMF and KBF) of the central Kutch region, shown by blue lines.

Chapter 6

InSAR interpretation from Envisat and Sentinel datasets

6.1 Introduction

In the last decade, there is a significant development of microwave imaging satellites and sensors. On the other hand different InSAR processing software has been developed by many organizations. Earlier, most of the SAR images have to be purchased and very few was freely available with time constraint. In the present study, Envisat and Sentinel-1 SAR images have been used to study land deformation in the Kutch basin (Figure 6.1). The 2001 Bhuj earthquake, which occurred due to rupturing of a hidden reverse fault, caused large-scale ground deformation. The ground deformation in Bhuj earthquake affected region have been analyzed by Saraf *et al*., 2012 where two pairs of interferometric synthetic aperture radar (InSAR) data sets have been used for an area towards the east of Bhuj falling on near-flat terrain north of Kutch Mainland Fault (KMF).

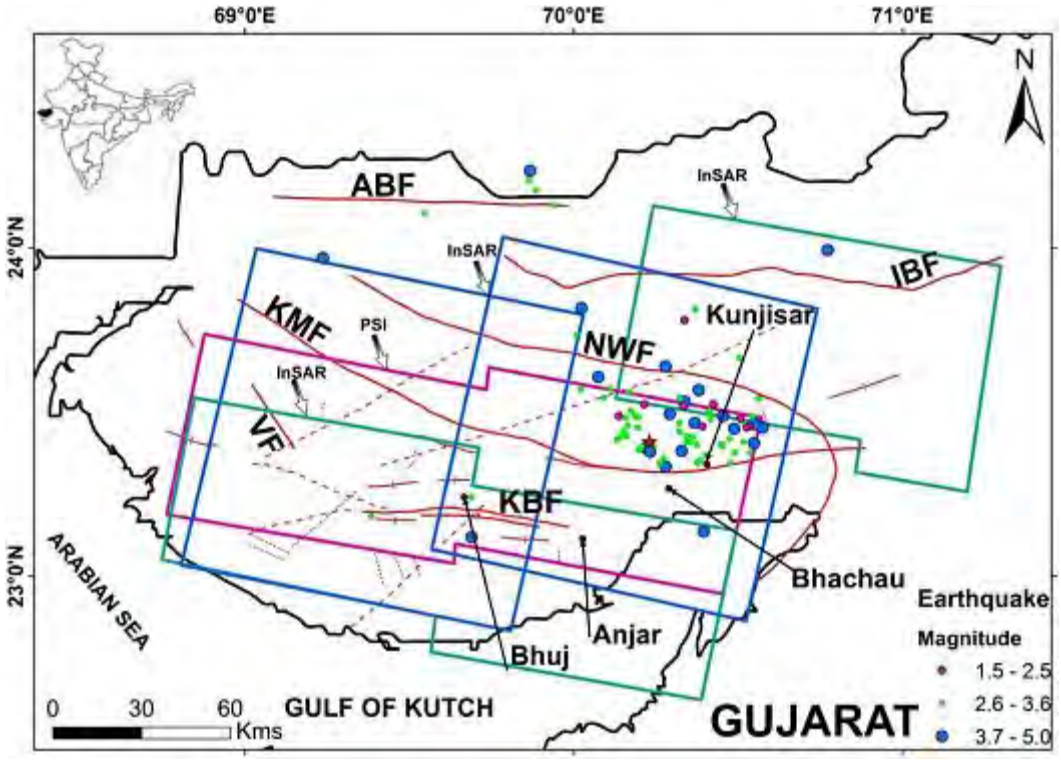

Figure 6.1: Shows the study area along with the major fault, Lineaments, anticlines with the earthquake data from 2008 to 2017 (ISR Gujrat). Envisat data (Blue box), Sentinel data (green box), PSI (pink box), Major earthquake events 2001 to 2016 (Source for tectonic features and earthquakes: SEISAT, 2000, Biswas, 2005, ISR and USGS)

6.2 The InSAR and PSI data set and processing

The suitable data set with justified perpendicular base line distance of Advanced Synthetic Aperture Radar (ASAR) data, acquired through the Environmental Satellite (Envisat) and Sentinel 1-A Interferometric Wide swath (IW) were obtained from the European Space Agency (ESA). In the present study ASAR-single look complex (SLC) and Sentinel 1-A Interferometric Wide swath (IW) products in image mode with swath width of 100 km and 250 km respectively having vertical-vertical (VV) polarization have been employed. These datasets (table 6.1) were acquired during the satellite's descending (Envisat) and descending (Sentinel 1-A) passes. Considering the effect of different attributes like atmospheric artefacts, topography, terrain changes due to vegetation and baseline length on the interferogram where utmost care was taken to select the data set provided by ESA.

The interferograms have been generated using Sarscape tool for Envisat data pair and SNAP toolbox (by ESA) for Sentinel data pair. The SAR data pairs are co-registered (pixel to pixel) followed by orbital refinement provided by ESA, then ALOS-PALSAR 12.5 m external DEM is used to perform topographical phase removal with Goldstein filtering. Further the wrapped phase is unwrapped using SNAPHU tool on a Linux platform. Then the unwrapped phase is converted to vertical displacement map using the operational wave length of the sensor (λ).

$$((\text{Unwrapped phase} * 5.6) / (-4 * \pi * \cos(\text{rad}(\text{incident\_angle})))$$

Where λ=5.6 cm is the wavelength of the C-band operating Envisat and Sentinel 1-A sensor.

Table 6.1: Envisat-ASAR and Sentinel 1-A Bhuj data sets used in the analysis of ground deformation.

Satellite	Acquisition Date	Orbit No.	Perpendicular base line in m	Time difference (In Days)
Envisat (Right pair)	25Nov 2003(Master)	9077		420
	18Jan2005 (Slave)	15089	129.07	
(Right pair)	06Oct2005 (Master)	18825		
	26Oct2006 (Slave)	24336	108.76	385
(Left pair)	02Oct2003 (Master)	8304		
	18Jan2005 (Slave)	15089	367.77	420
(Left pair)	18Jan2005 (Master)	15089		
	12Jan2010 (Slave)	41141	143.71	1820
Sentinel-1A (InSAR)	12Nov2016 (Master)	13902		
	30Dec2016 (Slave)	14602	48	48
	29Dec2014 (Master)	3927		
	07Sept2015 (Slave)	7602	19.48	252
	29Feb2016 (Master)	10154		
	19Nov2016 (Slave)	14004	32.77	264
Sentinel-1A (Persistent Scatterer)	07Sept2015 (Master)	7602		
	21July2015 (Slave)	6902	20.43	48
	14Aug2015 (Slave)	7252	4.42	24
	01Oct2015 (Slave)	7952	-36.24	24
	25Oct2015 (Slave)	8302	-25.65	48
	18Nov2015 (Slave)	8652	14.57	72
	12Dec2015 (Slave)	9002	113.56	96
	17Mar2016 (Slave)	10402	-56.27	192
	04May2016 (Slave)	11102	36.56	240
	03June2015 (Slave)	6202	84.08	96
	27June2015 (Slave)	6552	93.72	72

6.3 Persistent Scatterer Interferogram

Persistent Scatterer Interferometry (PSI) is a powerful remote sensing technique able to measure and monitor displacements of the Earth's surface over time. Precisely, PSI is a radar-based technique that belongs to the group of differential interferometric Synthetic Aperture Radar (SAR). InSAR system can identify movement on ground surface for expansive ranges with an accuracy of 3 to 24 cm and spatial resolution up to 1 m. So researchers focused on time series analyses, i.e., the use of images collected at different times for the same areas. The PS study needs a minimum of 10 to 12 scenes to process in the Sarproz software and is very much rigorous due to involvement of n number of large size scenes.

6.4 Results and Interpretation

The interferogram generated from Envisat and Sentinel 1-A scenes shows significant terrain change from 2003 to 2016. Time series surface deformational maps from 2003-04, 2004-05, 2003-05, 2005-10, 2014-15, 2016 Nov-Dec and displacement map along with PSI study infers a continuous land deformation and episodic ground settlement.

Using two suitable SAR data pairs interferogram images have been generated for different time span. The first interferogram (Figure 6.2 a) generated by using Oct. 02, 2003 and Nov. 25, 2004 where intense fringes for the island belt uplift was observed with less intense interference fringes observed in the Kunjisar area and on other parts of the image (Figure 6.2 a and b).

The second interferogram image has been generated by using Nov. 25, 2004 and Oct. 06, 2005 data pair (Figure 6.2 b). Prominent interference fringes were developed in several areas in northwest of Kunjisar and Kunjisar village area. Each interferometric fringe corresponds to 2.8 cm ground deformation (which is half of the C band wavelength used, i.e. 5.6 cm) in the radar line of sight. In order to estimate subsidence or upliftment number of developed fringes in any area is multiplied with the 2.8 cm. As the study area covers almost flat region, topographic effect may have affected least. The interference fringes developed from the first pair is very less in comparison to the fringes developed from the second pair (Figure 6.2 b).

In Kunjisar and its adjacent areas several fringes which developed in two interferogram obtained from the two interferometry pair are used for understanding the ground deformation. Commonly three interference fringe color codes are generated which are cyan (C), yellow (Y) and

magenta (M). Yellow color remains in the middle part bordered by cyan and magenta in all the fringes. The particular arrangement of these color codes reveal the nature of displacement occurred on the ground. Mostly the conventional way to analyze the interferogram is to start reading from magenta to cyan color codes. This indicates that the ground has moved closer to the satellite referred as an upliftment and the colour sequence from cyan to magenta represents a longer phase arrival to the satellite, which indicates ground has moved away from the satellite means subsidence (USGS).

Three fringes observed in the interferogram obtained using Envisat SAR data pair of Oct. 02, 2003 and Nov. 25, 2004 (Figure 6.2 a) and the fringe colour pattern MYC indicate an upliftment of about 8 cm in the Kunjisar region.

In the discussed interferogram image, interfering fringes also observed in other areas of the image north of the Kunjisar in the Pachham and Khadir mounds (Figure 6.2 a at location (A) and (C). In the extreme northern side of the image about 25 cm of negative (uplift) ground deformation [Figure 6.2 (c) A] is observed counting 9 fringes. Two circular lobes with total 2 fringes have developed indicating about 5 cm negative ground deformations [Figure 6.2 (c) B] towards the north-western part of the image. In the north-east part of the interferogram image approximately 3 fringes are formed which shows about 8 cm negative ground deformation [Figure 6.2 (c) C].

The interferogram image obtained from SAR data pair Nov. 25, 2004 and Oct. 06, 2005, shows development of approximately 6 fringes in the Kunjisar region (Figure 6.2 d). This fringe begins with the color code cyan and the sequence is cyan-yellow-magenta. Same sequence has been observed in most of the other part of the interferogram image. A positive deformation of around 17 cm may have occurred in the Kunjisar region as indicated by the developed six fringes.

Interferometric fringes are seen to have developed in other parts of the images. Mostly the fringes are formed to the northwest of Kunjisar (Figure 6.2 b). Here, almost 10 fringes have developed corresponding to 28 cm of positive ground deformation [Figure 6.2 (d) A]. Three fringes within 2 lobes have formed in the north-western part of the image, indicating about 8 cm positive ground deformation [Figure 6.2 (d) B] however in the north-eastern part of the interferogram image the fringes are difficult to read, because of low phase coherence. However, it appears that about 10 fringes are developed in this part [Figure 6.2 (d) C].

The interferogram generated from 2003 and 2005 Envisat data pair (Right) exhibits a positive prominent change on ground to the NE, NW and south of Bhuj (Figure 6.3), where deformation is revealed for Kunjisar and Island belt uplift areas in the Pachham and Khadir mounds for the same area and data pair a two phase subsidence and upliftment was observed by Saraf *et al*. 2012 in the Panchham, Khadir mounds along with some upper parts of Kunjisar village (Figure 6.4) as described above. The topographical change in the Pachham, Khadir mounds may be due to the activity of the IBF.

Further studying the deformation map generated followed by interferogram image using 2003 and 2005 Envisat data pair (left) deciphers a positive ground deformation (Figure 6.4) up to 17 cm in and around the Bhuj region (Figure 6.5) covering mostly the Mainland region of Kutch basin, which can be attributed as a post tectonic ground settlement immediately after the earthquake. The deformations have been observed along the KMF, KBF and major lineament passing across the Bhuj city. In a sequel of Envisat data pair 2005-10 (left) and 2005-06 (right) shows a low scale ground deformation (Figure 6.6) in terms of interferometric fringes. The deformation map could not be generated for this data pair due to less ground control points and high temporal period of acquisition. However comparing the interferometric image from 2003-05 with 2005-10, it can be well observed that the change in the ground topography has been reduced in the later in comparison to the earlier. In both of the interferometric images positive deformation is observed in terms of countable fringes where it shows a colored pattern of Magenta-Yellow-Cyan (MYC) as moving from south to north. The reduction in the ground deformation may be referred to the post relaxation of ground after the earthquake.

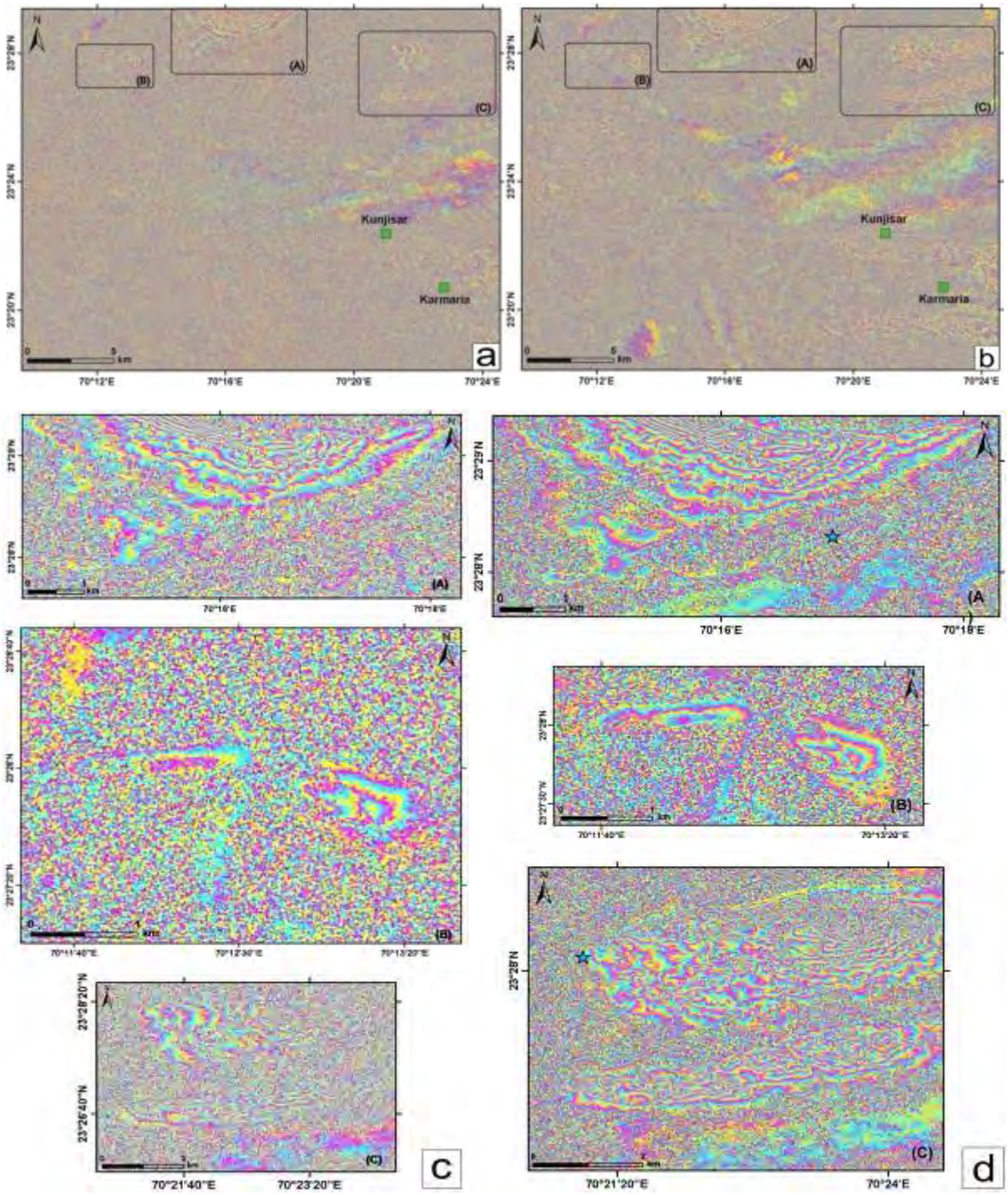

Figure 6.2: Interferogram image showing development of interference fringes in three areas (shown by boxes) towards north of Kunjisar (a) Interferogram generated from 2003-04 data pair (b) interferogram generated using 2004-05 data pair (c) Enlarged view of Interferogram of 2003-04 data pair (d) Enlarged view of Interferogram of 2004-05 data pair.

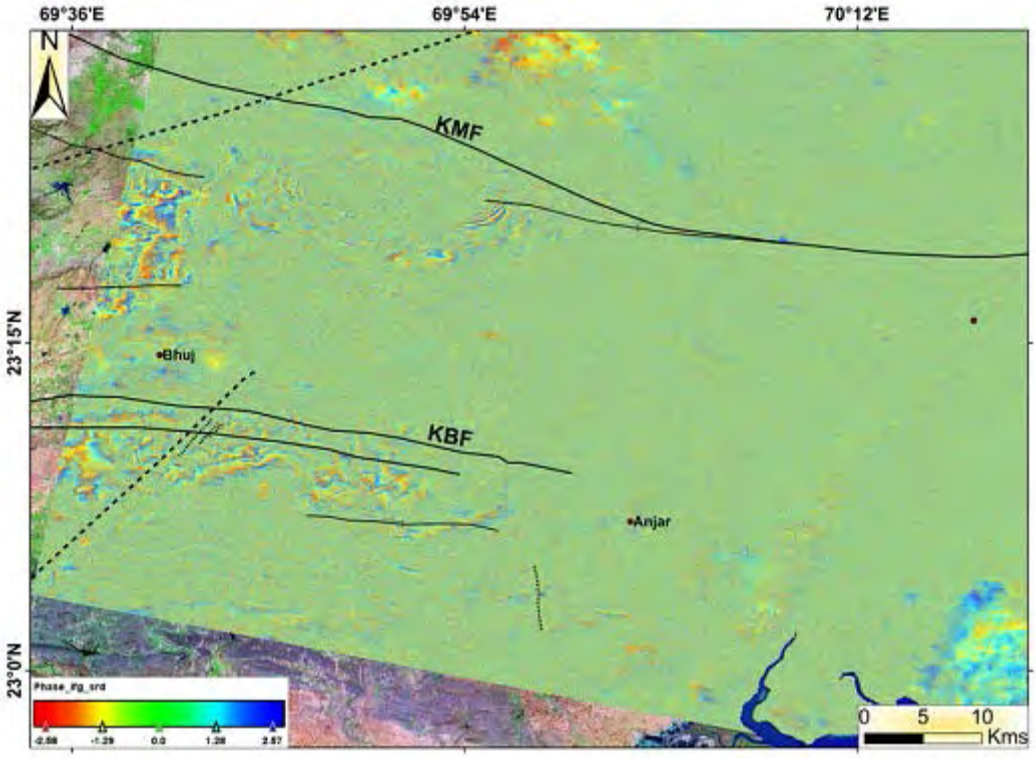

Figure 6.3: Interferogram generated from Envisat data 2003-05 (Right pair).

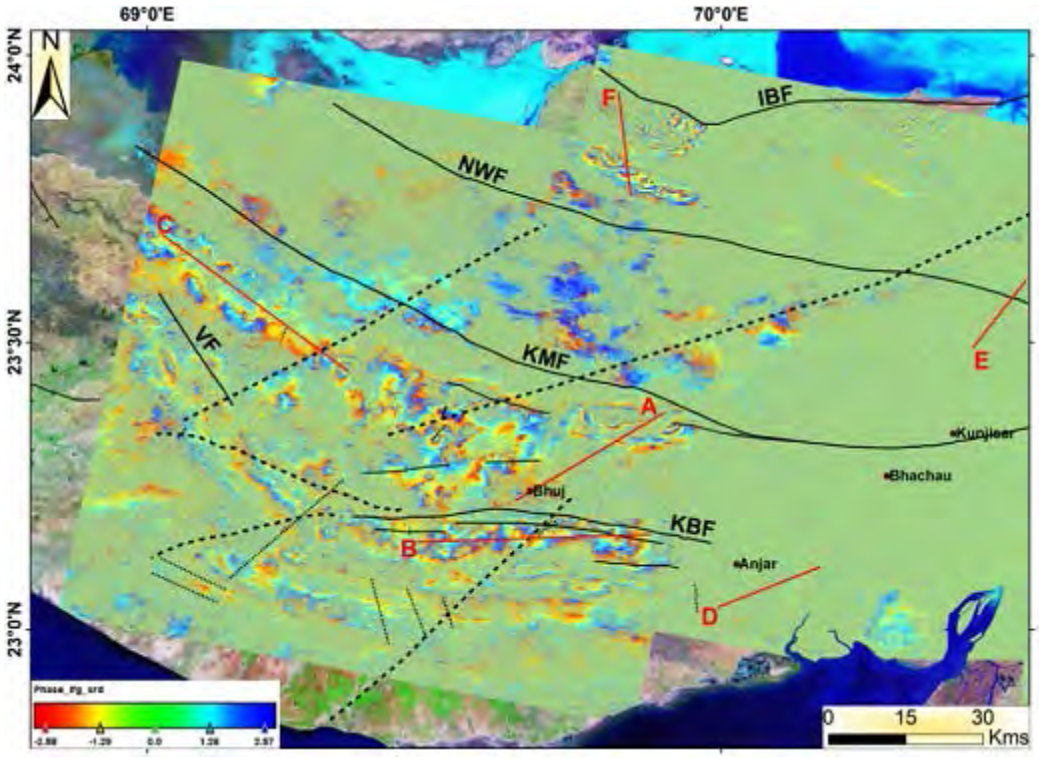

Figure 6.4: Interferogram generated from Envisat data 2003-05 (left and right pair) and red lines marked as A, B, C, D, E & F along which elevation profiles are drawn from SRTM DEM and ALOS PALSAR DEM.

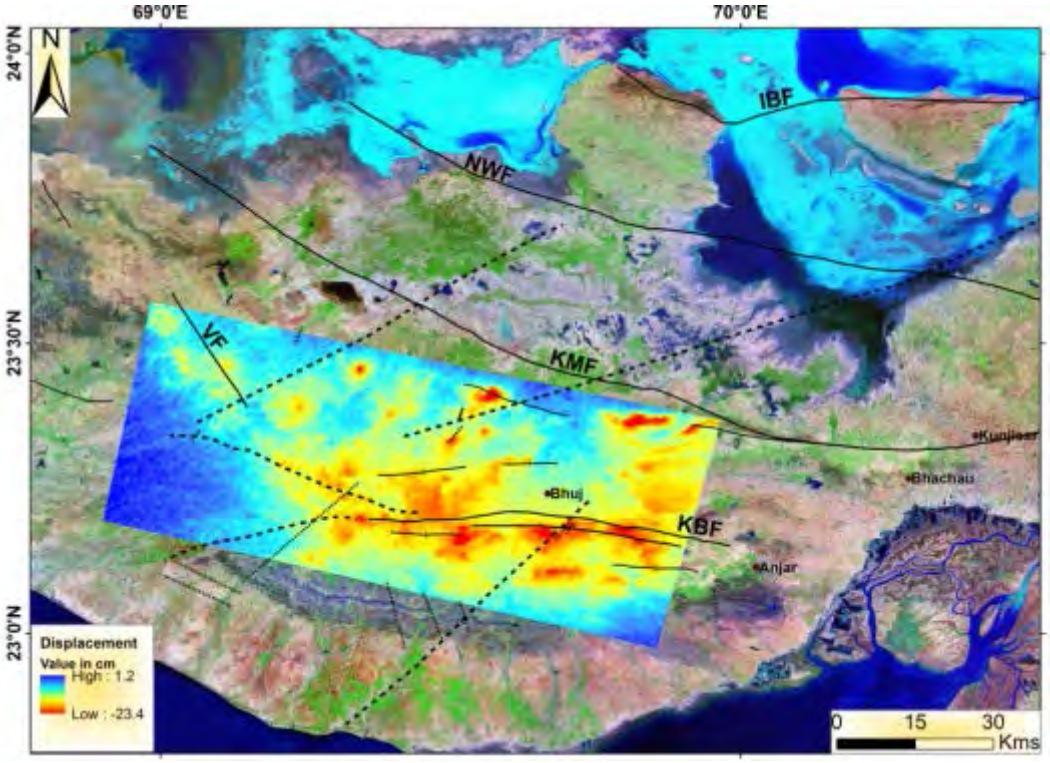

Figure 6.5: Vertical displacement map obtained from Envisat data 2003-05 (Left pair).

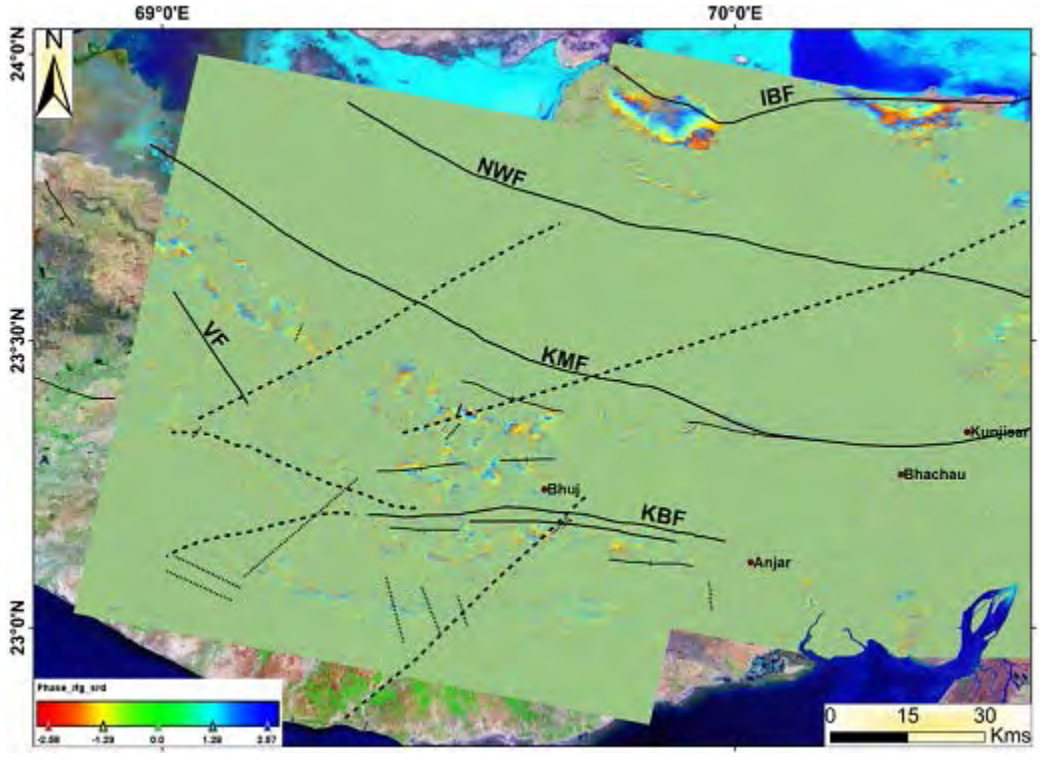

Figure 6.6: Interferogram generated from Envisat data 2005-10 (Left pair) and 2005-06 (Right pair).

6.5 DEM analysis

Elevation profile along the lines A to F are drawn using Arc GIS 3D analyst tool for SRTM (2000) and ALOS PALSAR (2007) DEM. These elevation profiles are taken for the area where terrain changes have been detected based on SAR interferogram. The profile shows elevation and trend of the curve (Figure 6.7), which is also observed in the time series interferograms derived from the Envisat SAR images. Further an elevation difference is calculated employing change detection technique for the Bhuj area between the two DEMs (Figure 6.8), which indicates a relative elevation variation in between 2000 and 2007 for Bhuj. Red toned area indicates lower elevation and blue toned area indicates higher elevation when difference has been computed between 2000 and 2007 DEMs respectively.

Further, Envisat scenes of the years 2006 and 2008 for the area as shown in the figure 6.9 indicate area of in-coherence (ISR, 2010). The earlier time series interferogram from Envisat data suggests change in terrain for the same location from coherence map (Figure 6.9). It suggests a clear view of terrain change that occurred during that period, over the studied Kutch region through the coherence change map in ISR 2010 report.

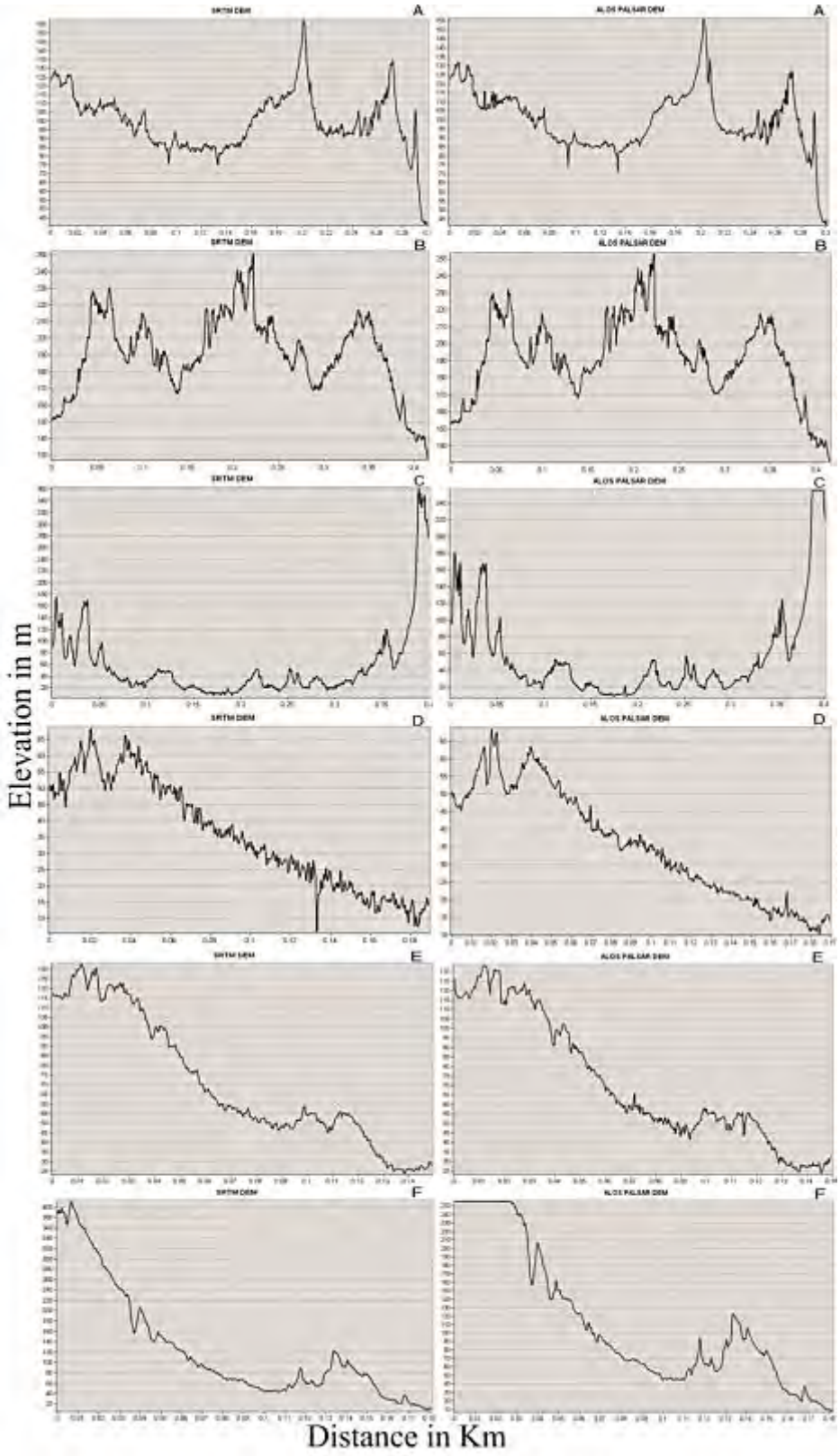

Figure 6.7: Comparison of elevation profile derived from SRTM and ALOS PALSAR DEM for A to F sections of Figure 6.4.

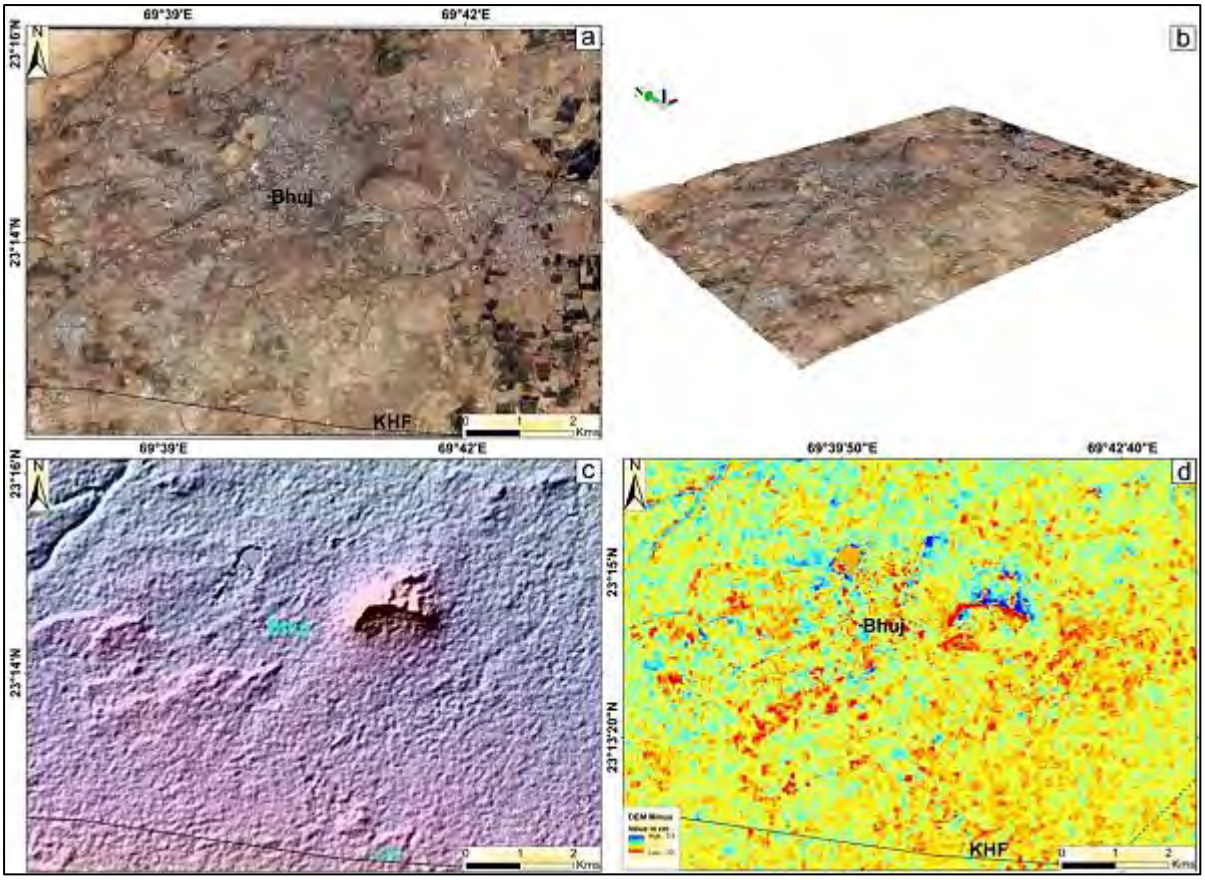

Figure 6.8: (a) Digital globe satellite map of Bhuj, (b) 3D drape view, (c) Hillshade image, (d) Difference in elevation between SRTM (2000) and ALOS PALSAR (2007) DEM for Bhuj area

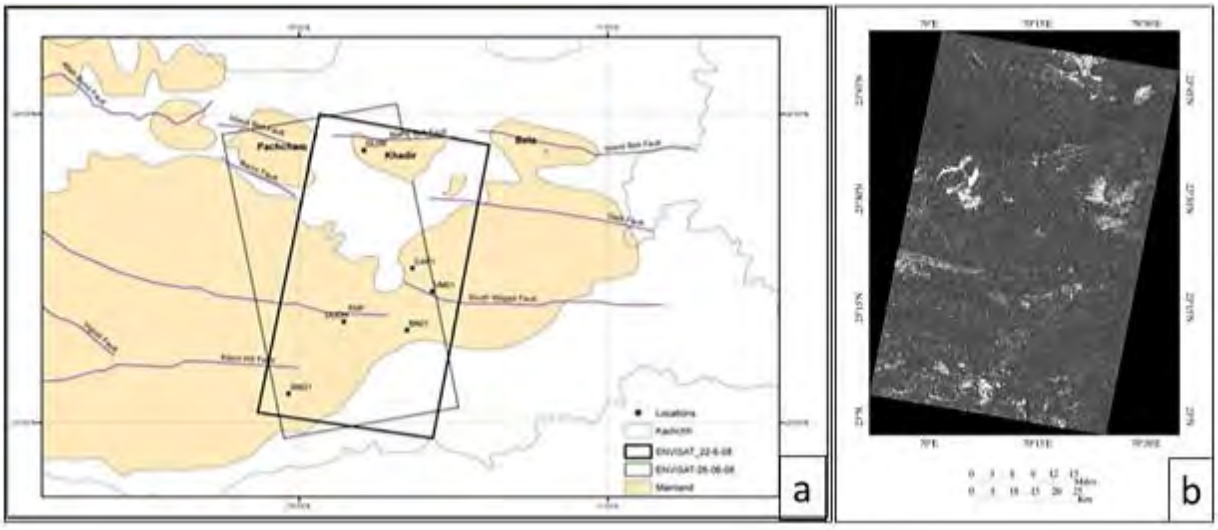

Figure 6.9: (a) Envisat Scenes (2006 and 2008) over the study area (b) Coherence image generated from multitemporal Envisat Scenes over the study area (ISR 2010). White color indicates the area of change in terrain.

6.6 Analysis from Sentinel 1-A data

Sentinel 1-A data covering the central and upper southern part of the Kutch region has been used to generate interferogram. These data set belongs to 2016 November - December and 29Dec2014 - 07Sept2015. Further 29Feb2016 and 19Nov2016 pair is used to study the ground activity along the IBF covering the Island belt uplifted areas. The interferograms generated from these data pairs showed a small scale ground movement. To study more accurately the PSI technique has been deployed to observe the terrain change over one year.

The interferogram (Figure 6.10) generated from Sentinel 1-A 2016 Nov-Dec data pair indicates a small scale ground subsidence up to 18.2 mm, which is inferred from the displacement map (Figure 6.11). The image pair with a less temporal period is very suitable for phase unwrapping and in order to obtain a displacement map the data pair has been selected with a 48 days interval. The Sentinel data pair indicates a small scale ground change for most of the same locations that has been studied using Envisat data pairs from 2003 to 2010. Again the interferogram generated from 2014-15 data pair of Sentinel 1-A image indicates small scale ground deformation up to mm scale around Bhuj, in the upper mainland, along KMF and KBF fault zones. The Sentinel 1-A 29 Feb 2016 and 19 Nov 2016 data pair indicates a small rate deformation along the IBF in Khadir mound and along the major lineament cross cutting the KMF, east to the Khadir uplift (Figures 6.12 & 6.13).

In order to compute rate of terrain change, persistent scatterer technique has been employed for central Kutch region covering Bhuj area (Figure 6.14). The persistent scattering study reveals an upward or negative ground displacement of 20 to 30 mm per year in the W and NW of Bhuj city to the east of Mainland along the LOS (figure 6.14). However the location south of the KBF region which was observed to be subsiding from InSAR study of the Sentinel data also shows a subsidence with rate of 15 to 20 mm per year. The extreme NW and NE locations of Bhuj also show a subsidence of 10 mm per year from the PSI study. However, the InSAR study reveals a change in topography for the adjacent areas of Anjar city in the large difference in temporal period of the data pair. A subsidence rate of 25 to 30 mm is observed in the south and east of the Anjar city from the PSI study of the Sentinel images over the period.

Interferogram generated based on the Envisat and Sentinel 1-A data exhibits ground deformations in the area in and around KMF and KHF. As per ISR (2010) report these two faults

are mapped as active (Figure 6.15). Hence, the observed deformation based on this study is due to the active nature of the faults.

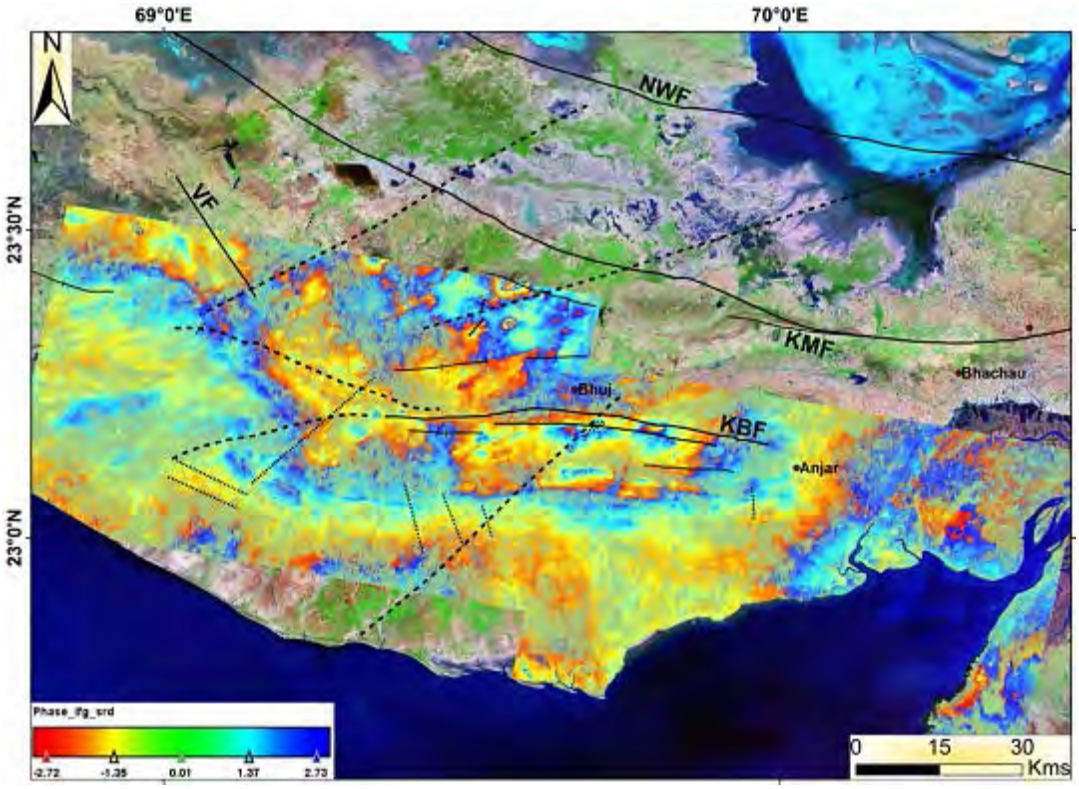

Figure 6.10: Interferogram generated from Sentinel 1-A 2016 Nov-Dec data pair.

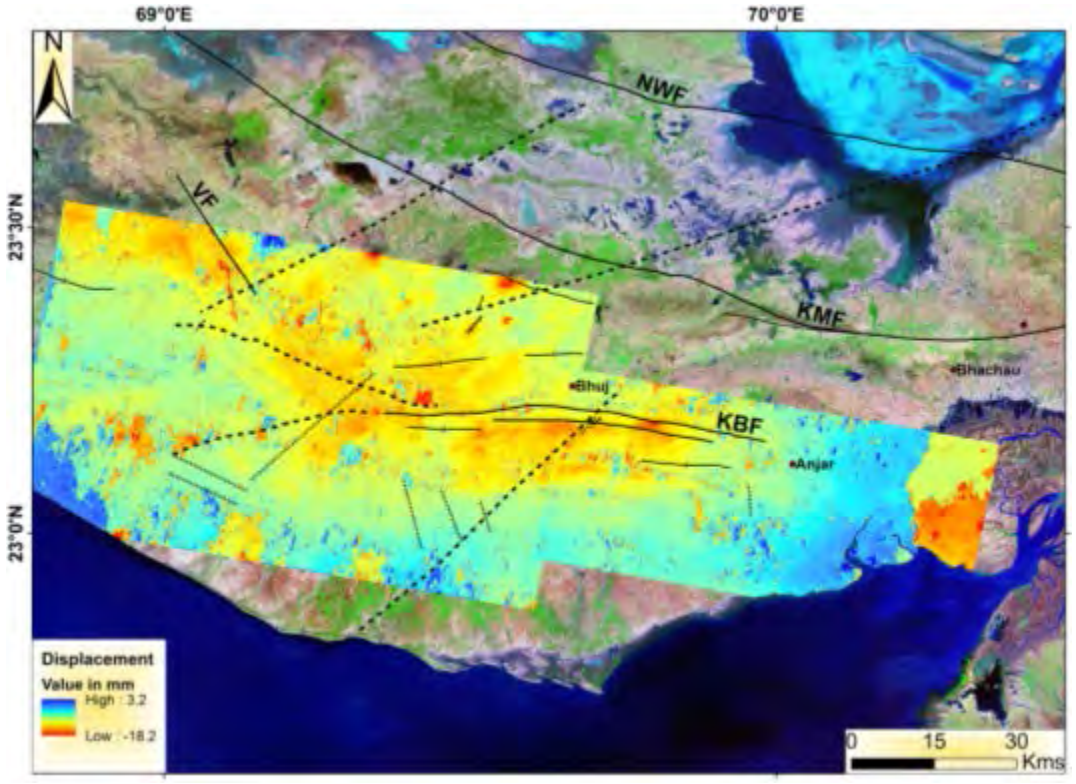

Figure 6.11: Vertical displacement map generated from Sentinel 1-A 2016 Nov-Dec data.

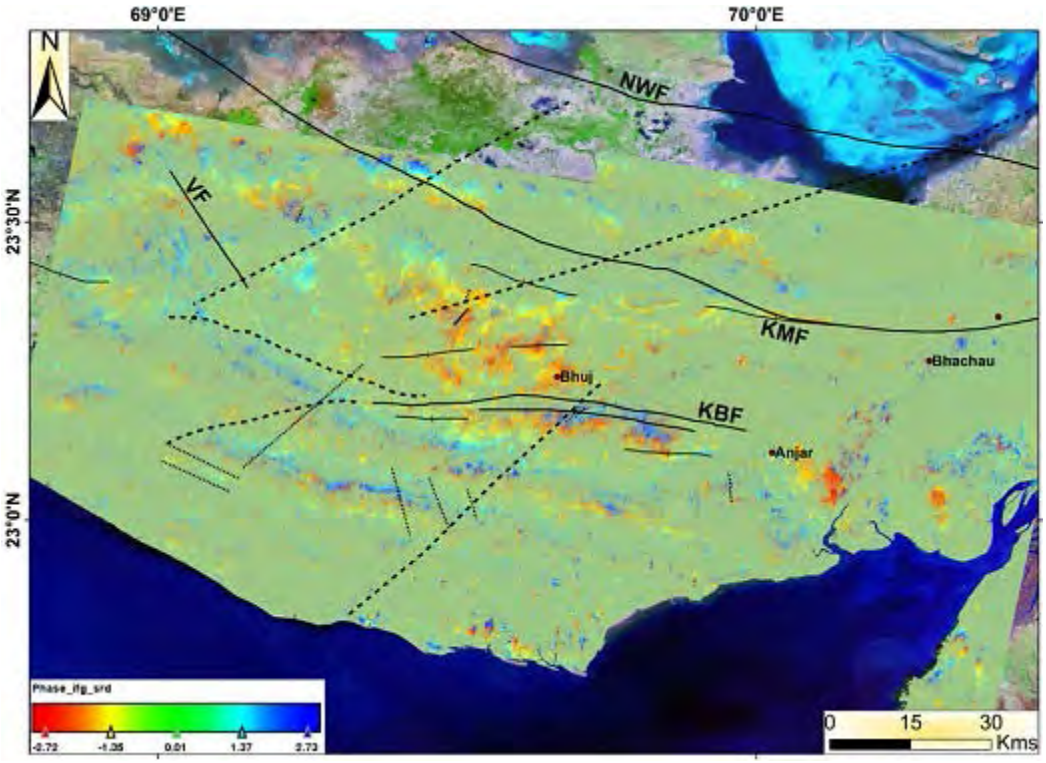

Figure 6.12: Interferogram generated from Sentinel 1-A 29th Dec 2014 and 07th Sept 2015 data pair.

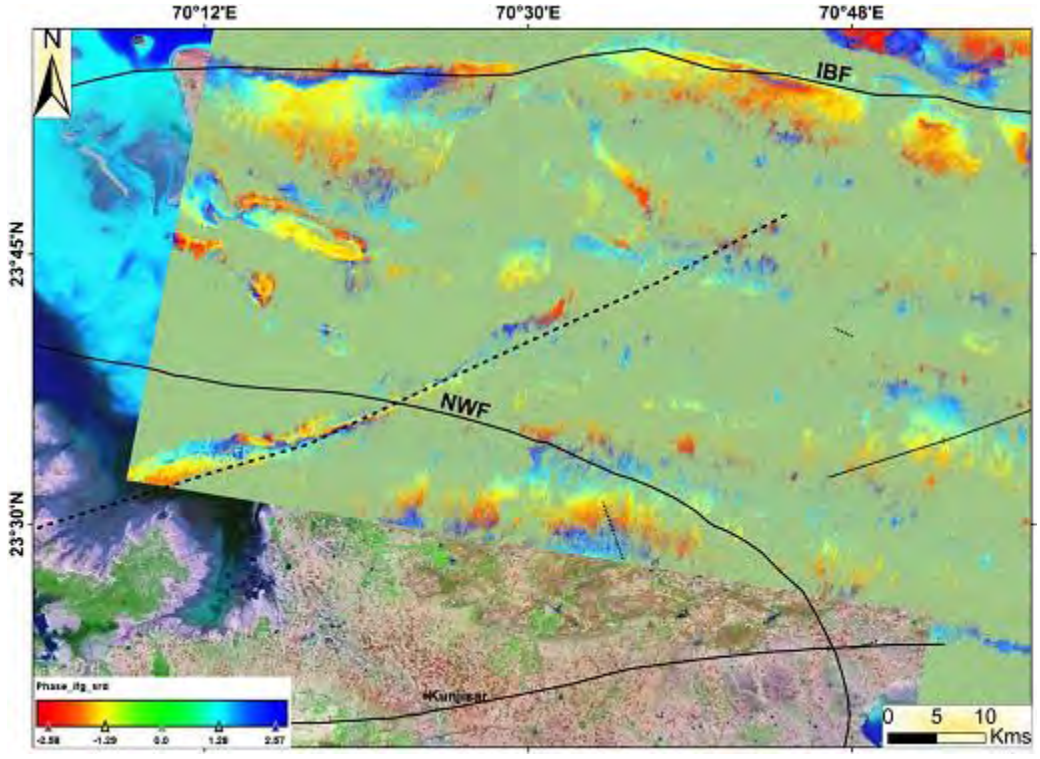

Figure 6.13: Interferogram generated from Sentinel 1-A 29th Feb 2016 and 19th Nov 2016 data pair.

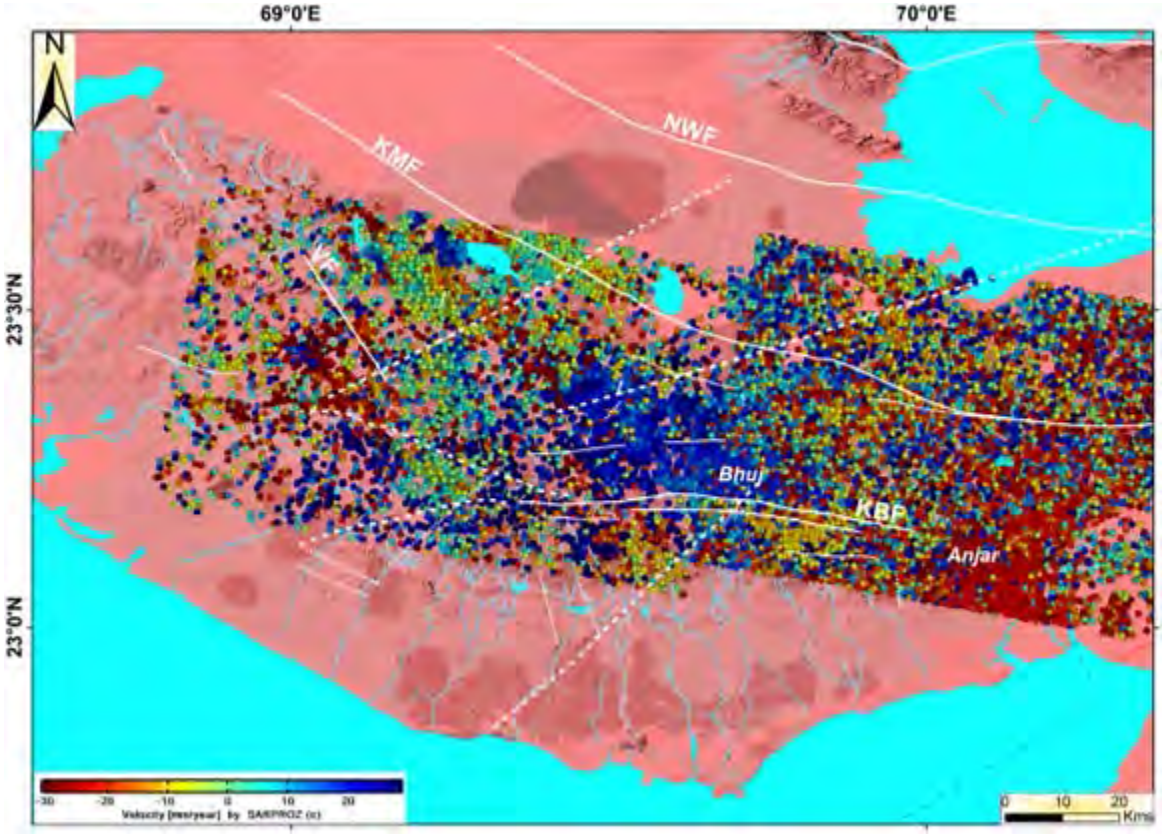

Figure 6.14: Persistent Scatterer map generated from Sentinel 1-A 2015-16 (11 Scenes).

Figure 6.15: Active fault map of Kutch (ISR 2010).

6.7 Terrain view

Terrain characteristics can well be visualized using DEM. In this study the ALOS PALSAR data has been used to generate DEM. Spatial resolution of DEM obtained is 12.5m. Figure 6.16 shows ALOS-PALSAR DEM overlain by shaded relied model of the Kutch region. Topographical features along with rivers are prominently displayed by this DEM. Further, in order to get more information about the terrain, three dimensional perspective views were generated for different areas as shown by the blocks marked as Location L1 to L6 (Figure 6.17 i to iii). The three dimensional topography within each block has been shown in the figures 6.17 L1 to L6).

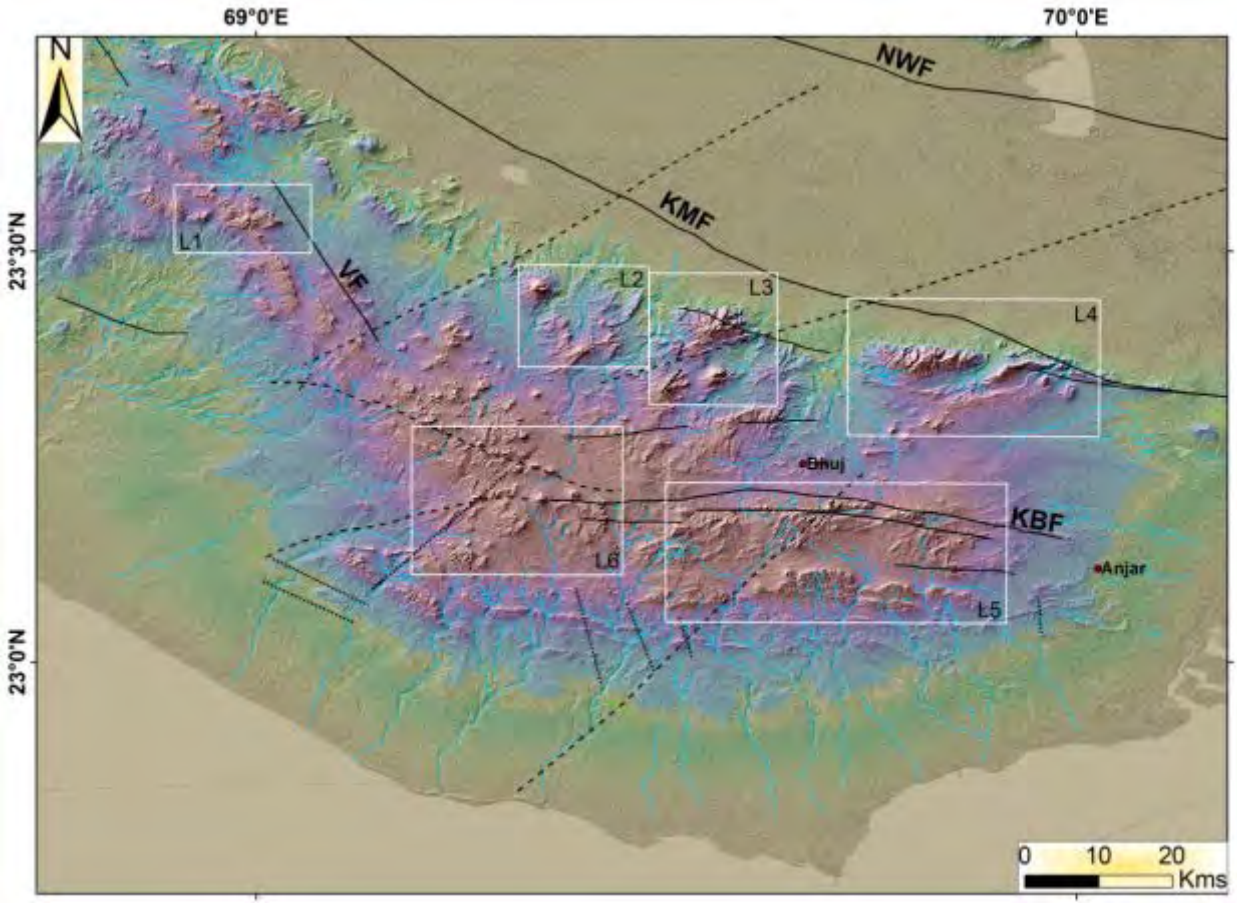

Figure 6.16: Hillshade map derived from ALOS PALSAR DEM with boxes showing the areas for which image draped 3D view has been derived.

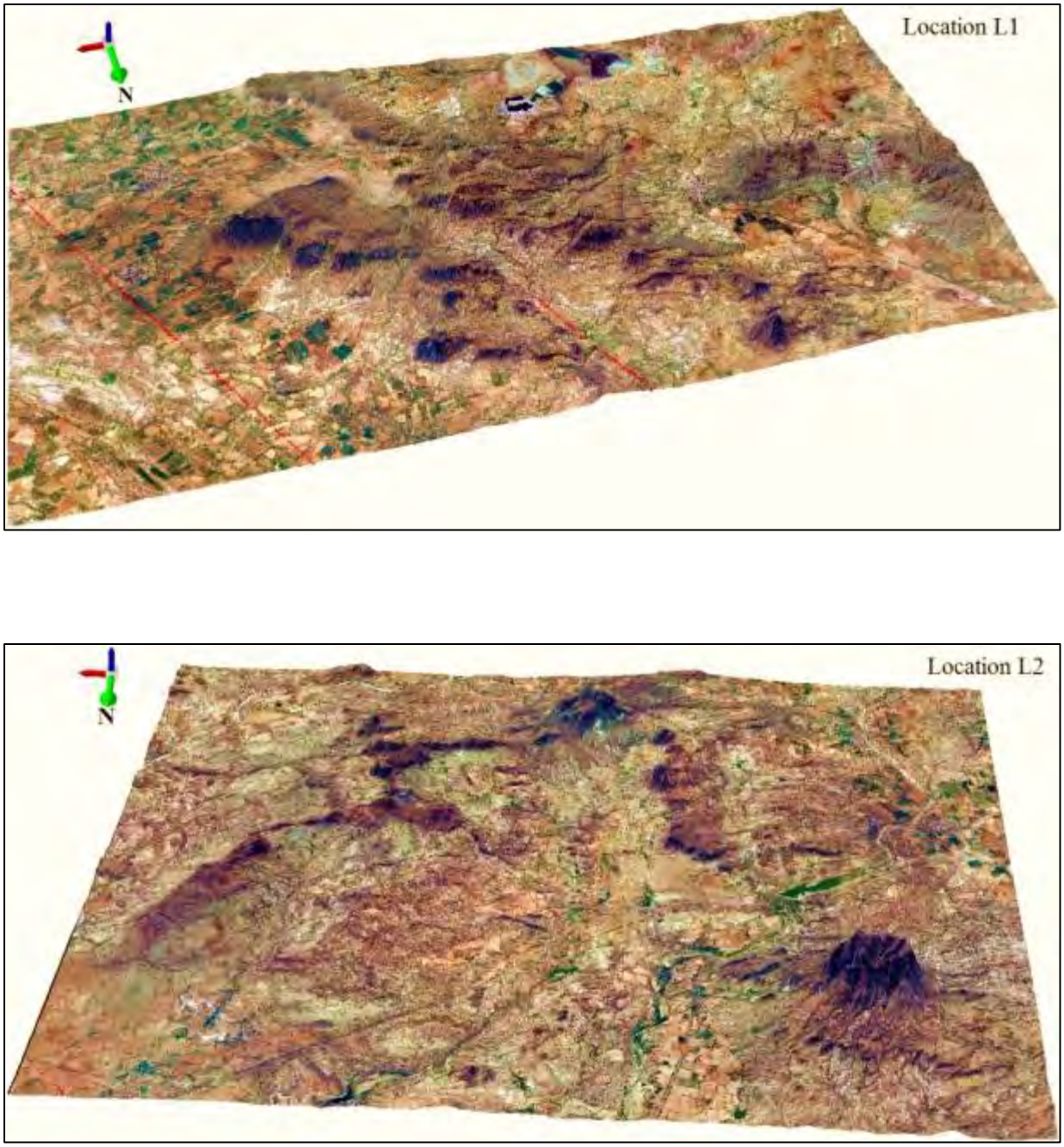

Figure 6.17(i): 3D view of Location L1 and L2 of figure 6.17 (exaggerated at 3x).

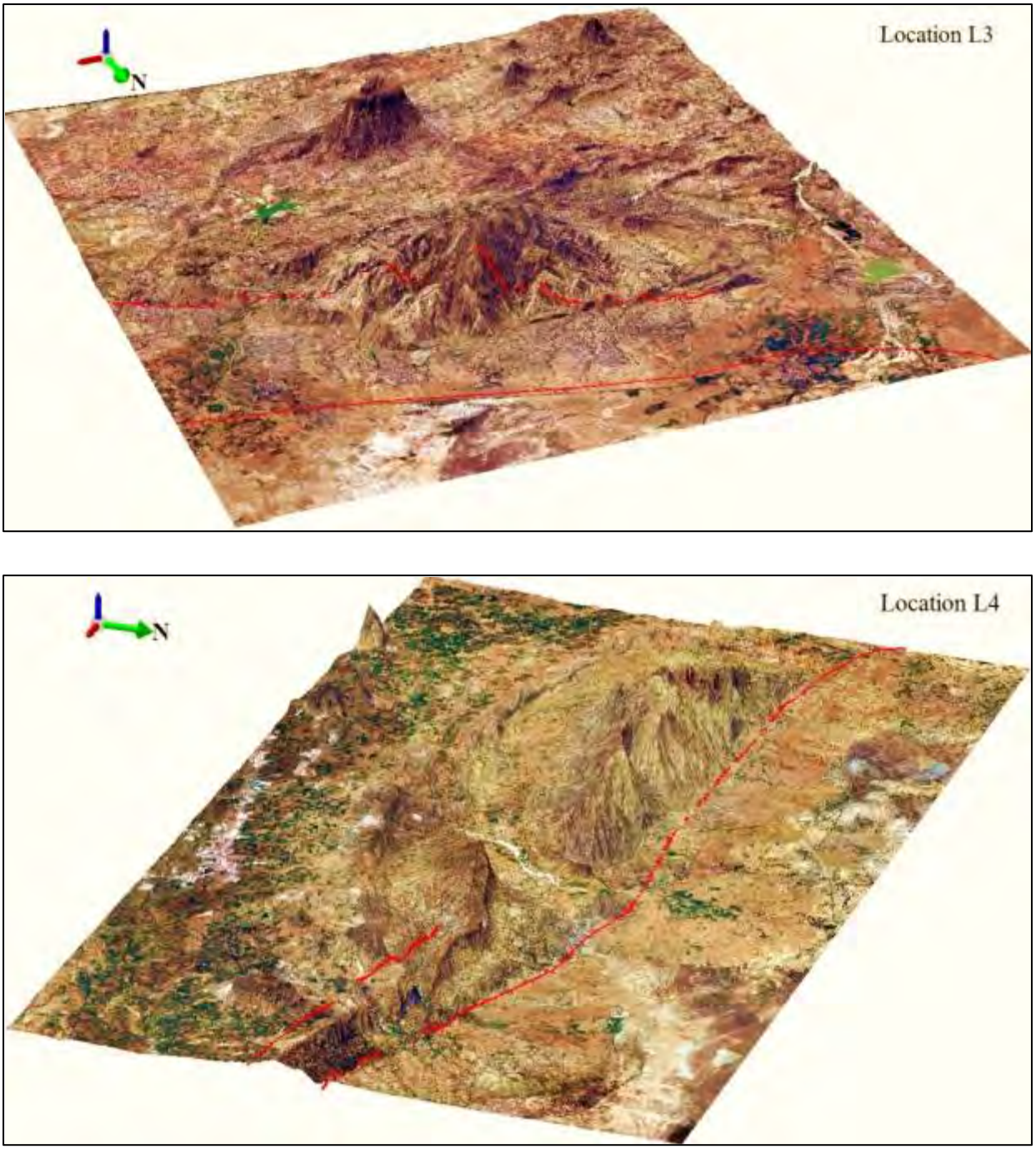

Figure 6.17(ii): 3D view of Location L3 and L4 of figure 6.17 (exaggerated at 3x).

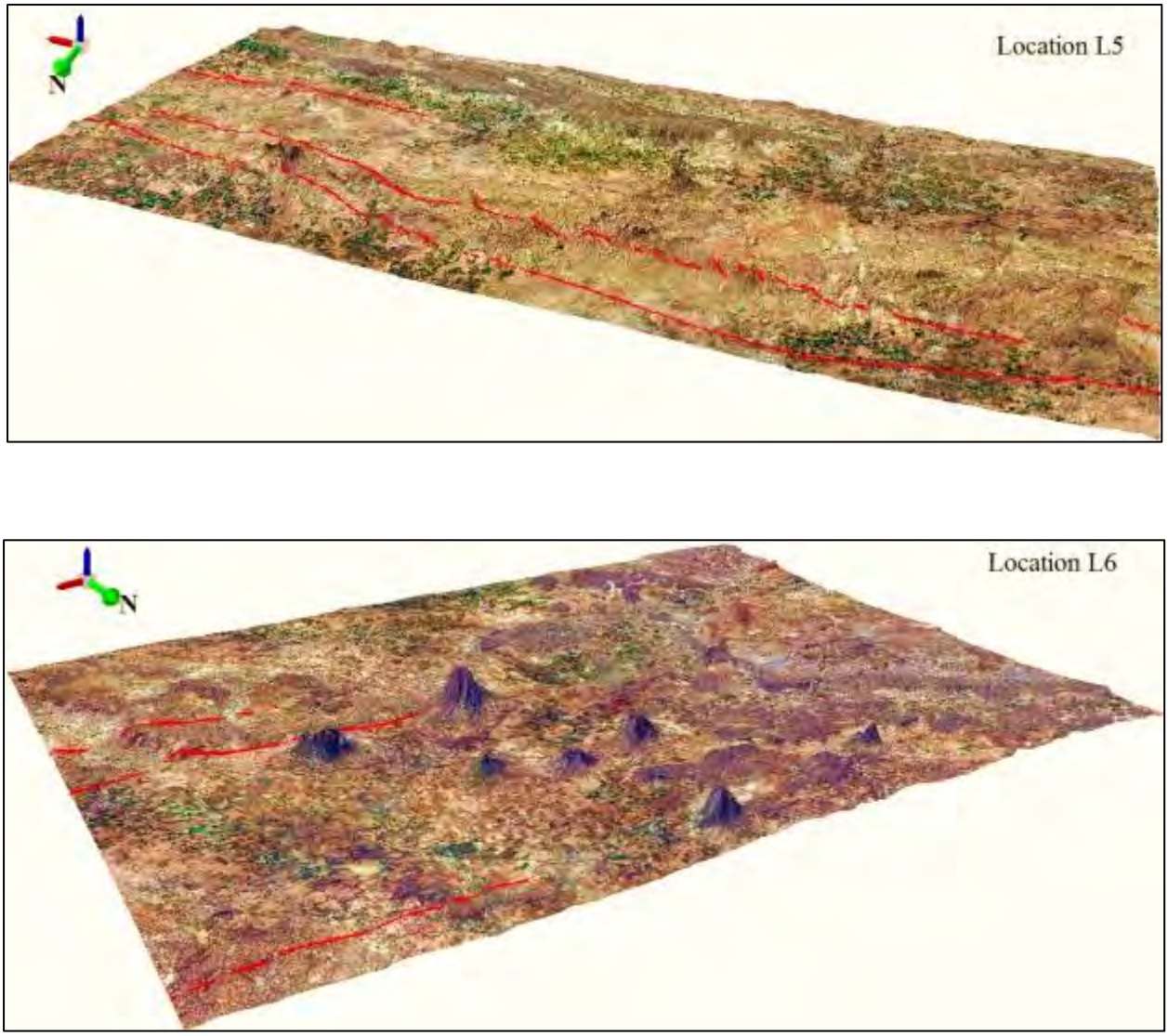

Figure 6.17(iii): 3D view of Location L5 and L6 of figure 6.17 (exaggerated at 3x).

Chapter 7

Geomorphic evidences of active faults in Kutch

7.1 Introduction

Relative movement between fractured rocks due to prevailing tectonic forces and the weight of the over burden rock results fault in geological environment. In active tectonic belts, potentially seismogenic zones are indicated by these faults. A number of deformation mechanisms are responsible for the underlying blind faults which causes an episodic earthquake-related movement. Those faults which have formed recurrently in the Quaternary time and may cause future rupture are called active faults (Morino *et al*., 2008). These faults bear certain geomorphic signatures which can explain the origin, stress condition and geometry of the fault and therefore survey across active faults can reveal idea about paleo seismic events.

In the Kutch peninsula, occurrence of a system of active faults leads to a crucial geodynamic phenomenon in the western part of continental margin of the Indian subcontinent. This region belongs to the seismically active zone-V as per Seismic Zoning Map of India outside the Himalayan seismic belt. The devastating earthquake of magnitude 7.7Ms (IMD), 7.7Mw (USGS) that struck Bhuj on January 26, 2001 is an example of such seismic activity. Numerous other large seismic events have occurred in Kutch in the past (Malik *et al*., 1999) as well. Kutch earthquake of almost similar magnitude in 1819 (Rajendran and Rajendran, 2001) and Anjar earthquake of magnitude 6.0 in 1956 (Chung and Gao, 1995) are significant among them. The Rann of Kutch earthquake of 1819 was the severest in the region which caused high destruction to the property in the epicentral area which extended from Ahmedabad in the east to Porbander in the west, Jaisalmer in the north, Bhuj and Anjar towns. In Bhuj alone, more than 7000 houses were overthrown. The earthquake was felt up to an average distance of 1280km from the centre of the epicentral tract over an area of the order of a million sq. Km. The most remarkable phenomenon associated with this shock was visible faulting on the earth surface which extended to more than 80km in length. A mound of earth at a distance of about 8km to the north of Sindri was observed in a place where the soil was previously low and level. This mound called “Allahbund” extended for a length of more than 80 to 100km in an approximately east-west direction. This earthquake was followed by a large number of

aftershocks which continued for nearly eight years. The Anjar earthquake of 1956 was widely felt in the region and caused considerable damage to the property in the epicentral tract.

The Kutch region had undergone rifting along the east-west line during the break-up of Gondwana land in the Jurassic (Biswas, 1980, 1987, Biswas and Deshpande, 1970). During the intense collision of the Indian continent with the Eurasia the Kutch region especially has suffered extensive compressive stresses, resulting in reactivation of the pre-existing rift faults and formation of new low-angle thrust faults. The focal mechanisms obtained from the occurred earthquakes indicate reverse faulting along the reactivated rift faults. The observed characteristic of uplift and subsidence caused by the 1819 Rann of Kutch earthquake is consistent with reactivation of such a fault. Similarly, the 2001 Gujarat earthquake was triggered by the tectonic slip on a previously unknown south-dipping fault genetically related to the inferred rift structures. They are related to the E-W oriented Island Belt Fault and eastern part of Kutch Mainland Fault. Even if numerous field studies have illustrated the depositional and geomorphic response to faulting; very less is known about the geomorphic response to active faults using remote sensing techniques in this area.

Sometime these features might be difficult to map in the field, but could be easily deciphered using remote sensing technique and different types of satellite images due to the obvious advantage of effective spatial coverage and quality governed by the image resolutions. Mapping of geological terrain based on the remote sensing technique has become an accepted tool for reconnaissance geological work for over decades. It has been used for producing active fault analysis, general geological maps and other tectonic analysis (Kaya, 2013). It is important for both seismic risk analysis and active tectonics where workers are challenged with predicting the geometry of otherwise inaccessible blind thrusts/faults. Small scale structures of the recent time can be compared with that of the structures present in the past images, where timing is poorly constrained. An attempt has been made to recognize the landforms using satellite remote sensing data sets and GIS tools and draw a correlation with the active faulting.

The studied areas have been marked as blocks, a to h on true colour composite image of Landsat-7 ETM and Sentinel 1-A SAR power or intensity image where faults have been identified followed by morphometric study using different geomorphic indices (Figure 7.1 and 7.2).

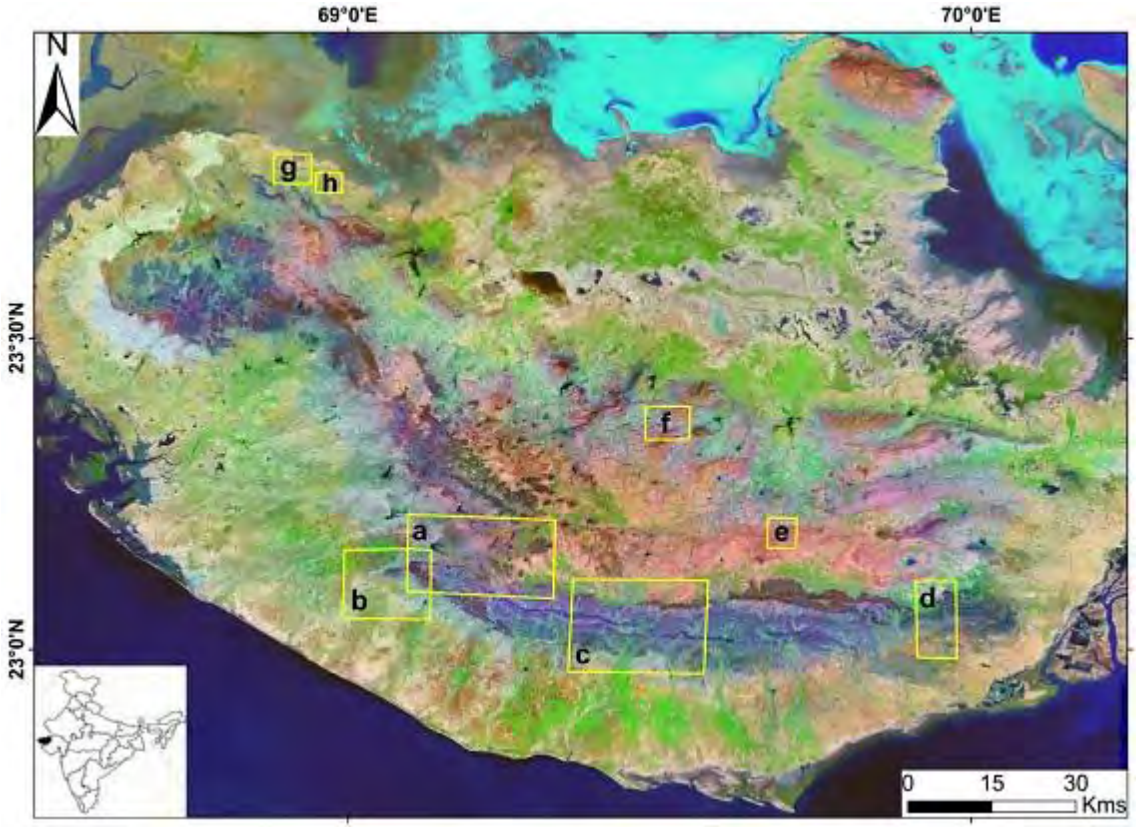

Figure 7.1: True Colour Composite Image of Landsat-7 ETM+ of study area showing the locations shown by the boxes a, b, c, d, e, f, g & h where active faults have been identified.

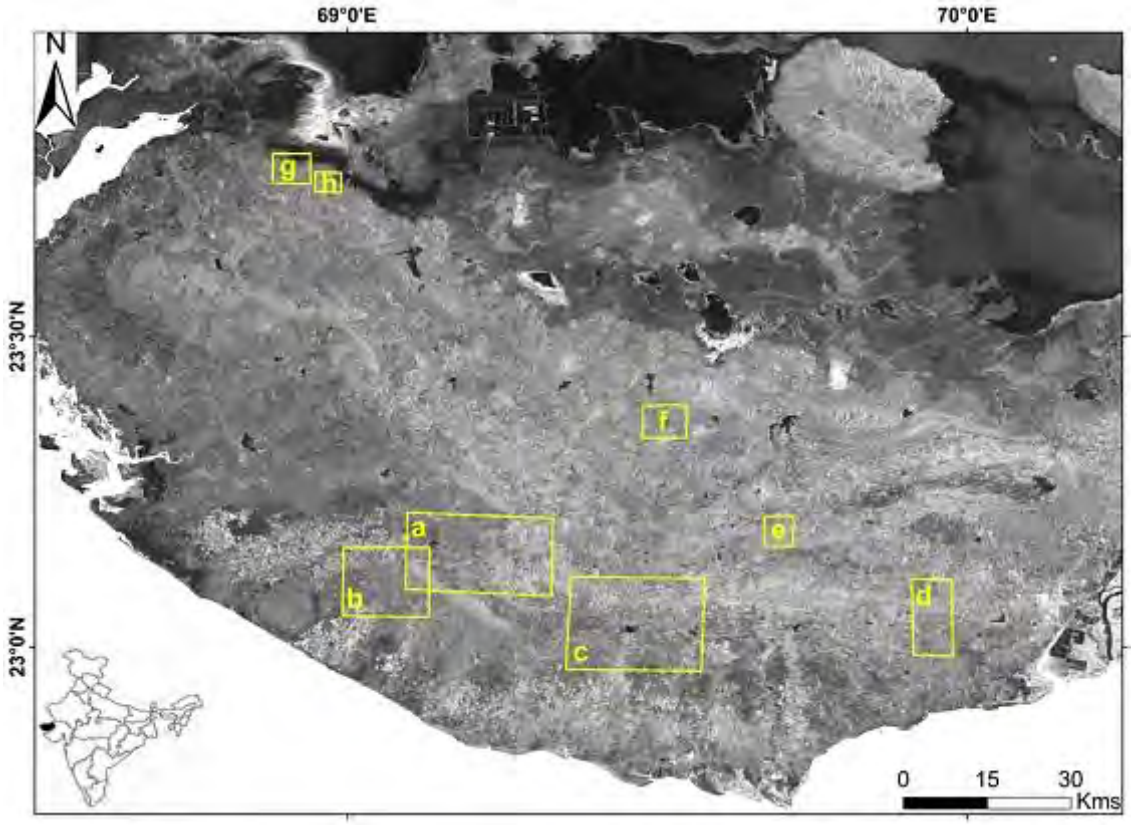

Figure 7.2: Power image derived from Sentinel-1 SAR image of study area showing the locations shown by the boxes a, b, c, d, e, f, g & h where active faults have been identified.

Remote Sensing analyses of morphological features provide important, though indirect clues for delineating active faults related to neotectonics. Offsetting and bending of streams, linear ridges, pressure ridges, beheaded streams, offset drainage, triangular facets, open rifts and prominent scarps along with their orientation in certain directions, are some peculiar and important patterns that can indicate the neo tectonic movement and the distribution of the fault patterns.

7.2 Location

The study area chosen for morphometric analysis lies between 22°40’ N and 24°0’ N latitudes and 68°30’ E to 70°30’ E longitudes. The Kutch region is bounded by the Arabian Sea to the west and the Rann of Kutch, a spreading but seasonal wetland, bounds to the north and east. In the past, the Rann of Kutch was an extension of the Arabian Sea. The Gulf of Kutch separates it from the Kathiawar peninsula and surrounds it to the south and southeast. A range of hills with east-west trend runs parallel to the Gulf of Kutch. The course of a section of the river Indus was partially altered as a result of the massive earthquake that hit Kutch on June 16, 1819 further causing a surface depression which became an inland sea (Figures 7.1 and 7.2).

From the geological point of view Kutch is categorized into four major E-W trending zones i.e.

A. Coastal Zone - demarcates the southern fringe.

B. Kutch Mainland –forms the central portion. It includes the northern hill range, rocky upland and coastal plains.

C. Banni Plains (less than 5m MSL) - It is represented by raised fluvio-marine sediments, salt pans and mud flats.

D. The two Ranns - (1) Great Rann (~ 2m MSL) in the north and (2) Little Rann in the east. Both the Rann is comprised of vast saline wasteland.

The boundaries of these geomorphic zones are bounded by the E-W trending faults. An array of tectonogenic geomorphic elements is marked in the Kutch landscape in the form of residual depressions and uplifts. The elevated landforms comprises of Mesozoic and Tertiary rocks whereas the depressions between the elevations are marked by mud-flats, Quaternary sediment successions, salt pans of Great and Little Ranns, Banni Plains along with marked alluvial river terraces. The uplifts are generally marked by asymmetric anticlines and domes.

All major uplifts are bounded, by a fault on one side, and by gently dipping peripheral plains, on the other side (Biswas, 1980).

A group of E-W trending uplifts are the significant structural features occurring in the region and these features were actively involved in the geological evolution (Merh, 1995).

7.3 Data Used and Methodology

7.3.1 Data Collection and Calibration:

The satellite data is now available with high pixel resolutions from Landsat and Indian Remote Sensing Satellites. Cloud free, multiband and high quality satellite images obtained by Landsat satellite series are readily available to the users. For the present study Landsat-7 ETM+ image with spatial resolution 30m having the path row combinations 150/44 and 151/44, Advanced Spaceborne Thermal Emission Reflection Radiometer (ASTER) data, Shuttle Radar Topographic Mission (SRTM) data and Sentinel-1 Level-0 product were used. The two Landsat scenes that cover the study area were obtained in different months and are recognized as:

Table 7.1: Landsat 7 ETM+ scenes with date of acquisition

PATH	ROW	SCENE IDENTIFIER	DATE OF ACQUISITION
150	44	LE71500442014156PFS00	05-JUNE-2014
151	44	LE71510442014147PFS00	27-MAY-2014

The first step carried out on the satellite images was to import them to ArcGIS 10.1. The required bands of 3, 2 and 1 of Landsat-7 ETM+ were stacked using ArcGIS 10.1 to generate standard True Colour Composite. This helped to decipher any remarkable alteration in the drainage pattern and other geomorphic features, which is then linked to active faulting. Two ETM+ scenes were mosaicked to generate one large single image with recalculated lines and columns.

7.3.2 Morphometric Analysis

Morphometric analysis is the quantitative assessment of form features of the earth surface and any landform unit. It can also be defined as the quantitative measurement of landscape shape. Landforms can be characterized in terms of their elevation, size and slope. The geomorphologists can compare different landforms and can calculate less straightforward parameters which are useful for identifying a particular characteristic of an area such as level of tectonic activity (Keller and Pinter, 1996). Morphometric analysis includes quantitative study of the various components such as hypsometric analyses, sinuosity, SL indices, basin shape indices, drainage basin asymmetry, etc., which indicates the nature of development of the basin. These are used as parameter of active tectonics (Keller and Pinter, 1996).

7.3.3 Hypsometric curve

For a drainage basin the hypsometric curve represents the relative proportion of the watershed area below (or above) a given height (Strahler, 1952). Under similar hydrological conditions, a relative understanding into the past soil movement of basins can be inferred by comparing the shape of the hypsometric curve for different drainage basins. Thus, the shape of the hypsometric curves is very useful in explaining the temporal changes in the slope of the original basin and in turn, provides information about the tectonic activities shaping out that basin.

- Convex hypsometric curves are typical of a youthful stage;
- S-shaped curves are related to a maturity stage, and
- Concave curves indicate a peneplain stage.

Frequent variation is observed in the shape of the hypsometric curve during the early geomorphic stages of development which is followed by minimal variation after the watershed attains a stabilized or mature stage (Figure 7.3). In the present study the hypsometric curves for the drainage basins of each location are generated from SRTM DEM using the watershed and hypsometric tools in ArcGIS.

7.3.4 Stream-Length gradient index

The stream-length gradient index reflects the relationship among rock resistance stream power, and tectonics (Hack, 1973). It is an important parameter to interpret if change in stream slope is due to tectonic deformation or rock resistance, especially if it has a vertical component (Keller and Pinter, 2002).

The stream gradient index is denoted by Hack (1973) as follows:

$$SL = (dH/dL)*L$$

where,

SL is the stream gradient index, dH/dL is the local gradient of the stream reach where the index is computed, dH is the drop in the elevation, dL is the length of the reach and L is the total length of the of the channel from the water divide to the centre of the reach measured along the channel (Figure 7.4).

The SL values are high in areas where: (a) active tectonics has resulted or, (b) rocks are particularly resistant. Therefore, high SL indices in rocks of low to uniform resistance are a possible indicator of active tectonics (Keller, 1986). An area of soft rocks having higher SL value represents recent tectonic activity, at the same time low SL values indicates movement along strike-slip faults (Keller and Pinter, 2002). In this study, SL index was calculated along a number of sections of streams and rivers of the different locations, where faults were recognized, using SRTM DEM and GIS and its standardized average value for the segments of each basin was calculated.

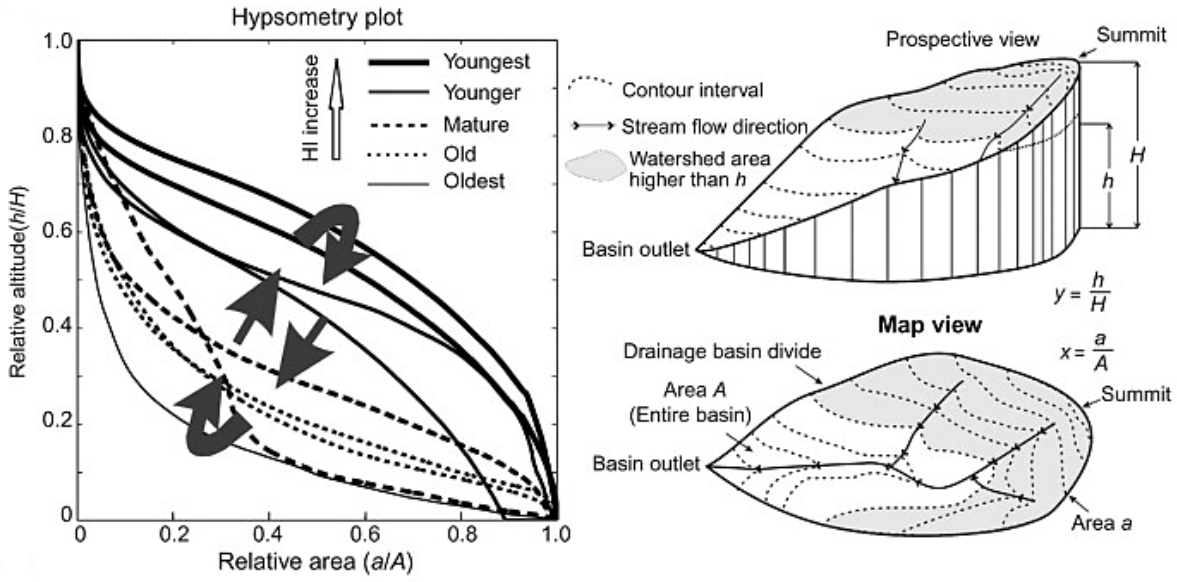

Figure 7.3: Typical hypsometric curves (HC) (Ritter *et al*., 2002 and Strahler, 1952) and geomorphic cycle development showing changes in hypsometric curves.

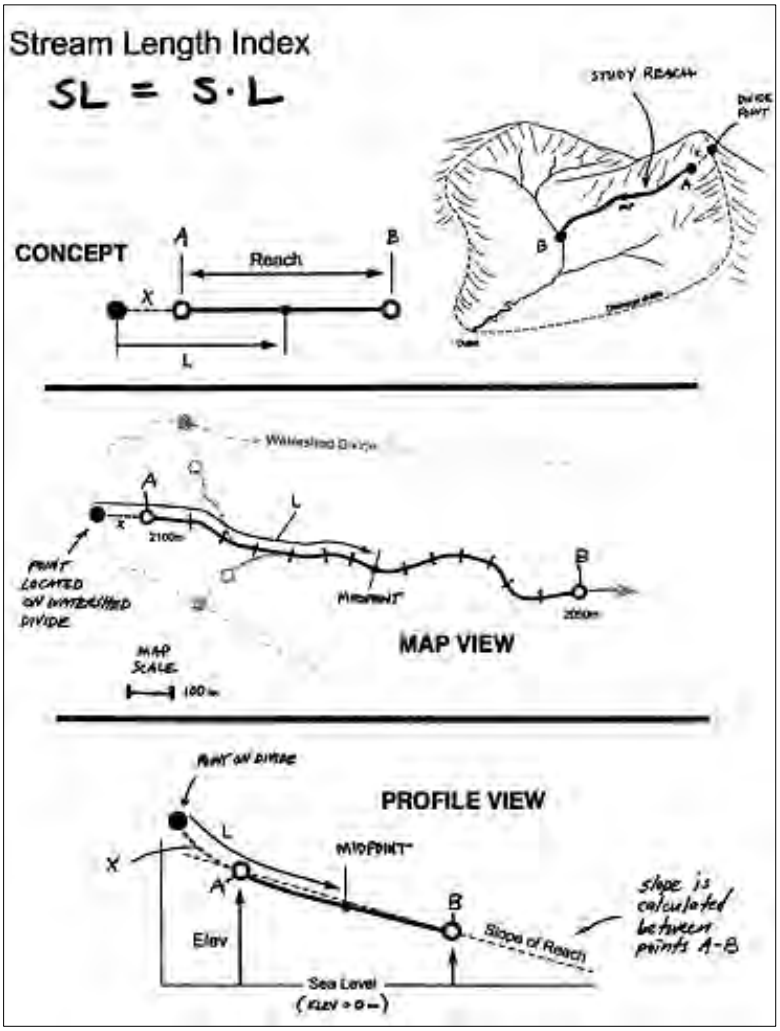

Figure7.4: SL mechanism (Mahmood and Gloaguen, 2012).

7.3.5 Sinuosity

Sinuosity deals with the arrangements of channel of a drainage basin. Sinuosity is defined as the ratio of channel length to channel valley length (Figure 7.5). Its value ranges from 1 to 4 or more. Rivers which have a sinuosity of 1.5 are called sinuous, and above 1.5 are called meandering (Leopold *et al*., 1964). It is a significant quantitative index for interpreting the significance of streams in the evolution of landscapes. It is a useful parameter for the rivers located in tectonically active areas (Gomez and Marron, 1991). The secondary effect of uplift can be measured by increasing or decreasing channel sinuosity. It is measured as:

Sinuosity= Channel length/Channel Valley length= C/V.

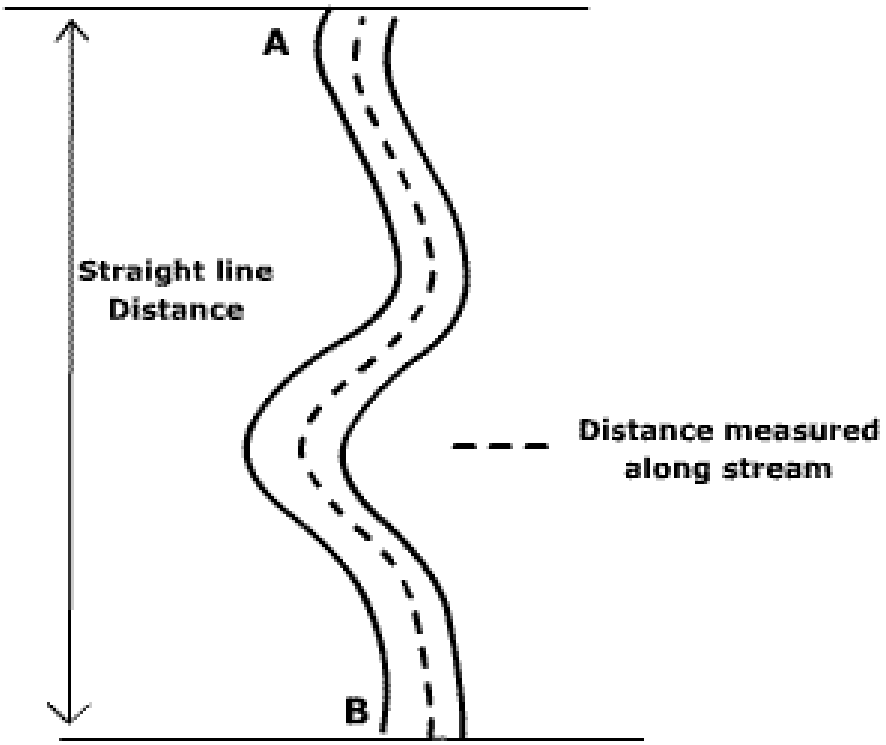

Figure7.5: Sinuosity measurements.

In this study, the drainage channels along the river are first digitized from world map base layer provided by ESRI online and then sinuosity of these drainage channels are calculated in ArcGIS.

7.3.6 Drainage Basin Asymmetry

The asymmetry factor (AF) was developed to identify tectonic tilting transverse to stream at drainage basin on larger scales (Hare and Gardner 1985; Keller and Pinter 2002).

The asymmetry factor is determined by the formula:

$$AF=100\ (A_r/A_t)$$

Where,

A_r is the area of the basin to the right of the trunk stream that is facing downstream and A_t is the total area of the drainage basin (Figure 7.6).

Asymmetry Factor (AF), greater or smaller than 50, shows effect of active tectonics, differential erosion or lithologic control (Hamdouni *et al*., 2008). Asymmetry Factor close to 50 is seen when there is no or little tilting perpendicular to the direction of the trunk channel.

The landforms are characterized by mountainous sides, relatively steep and flat floors in tectonically active topography. These steep sides are formed by displacement on faults such that the valley floor moves down relative to the surrounding margins, or, the boundaries move up relative to the floor. Then the consequence is basin sloping, causing the river to migrate and deviate from the basin midline (Cox, 1994). The drainage basin asymmetry factor is calculated from the watershed generated for each drainage basin in ArcGIS 10.2.

7.3.7 Basin shape index

In tectonically active areas, young drainage basins tend to be elongated shape parallel to the topographic slope of a mountain. These elongated shapes become circular shapes with time due to less tectonic activities and continued topographic evolution (Bull and McFadden, 1977). In tectonically active areas, the drainage basin widths are narrower near the mountain front than upstream from the mountain front. This is due to the energy of the stream near the mountain front concentrated primarily to down-cutting compared to the lack of continuing rapid uplift in the upstream which permits broadening of the basins.

The elongation ratio is expressed as:

$$Bs = B_l / B_w$$

Where,

B_l is the length of a basin measured from the headwaters point to the mouth, and

B_w is the width of a basin measured at its widest point (Figure 7.7).

High values of B_s are related with elongated basins which in turn are linked with relatively higher tectonic activity. On the other hand, low values of B_s indicate a more circular shaped basin, related with low tectonic activity. Hence, B_s reflects the rate of active tectonics. The basin shape index is calculated from the watershed generated for each drainage basin in ArcGIS.

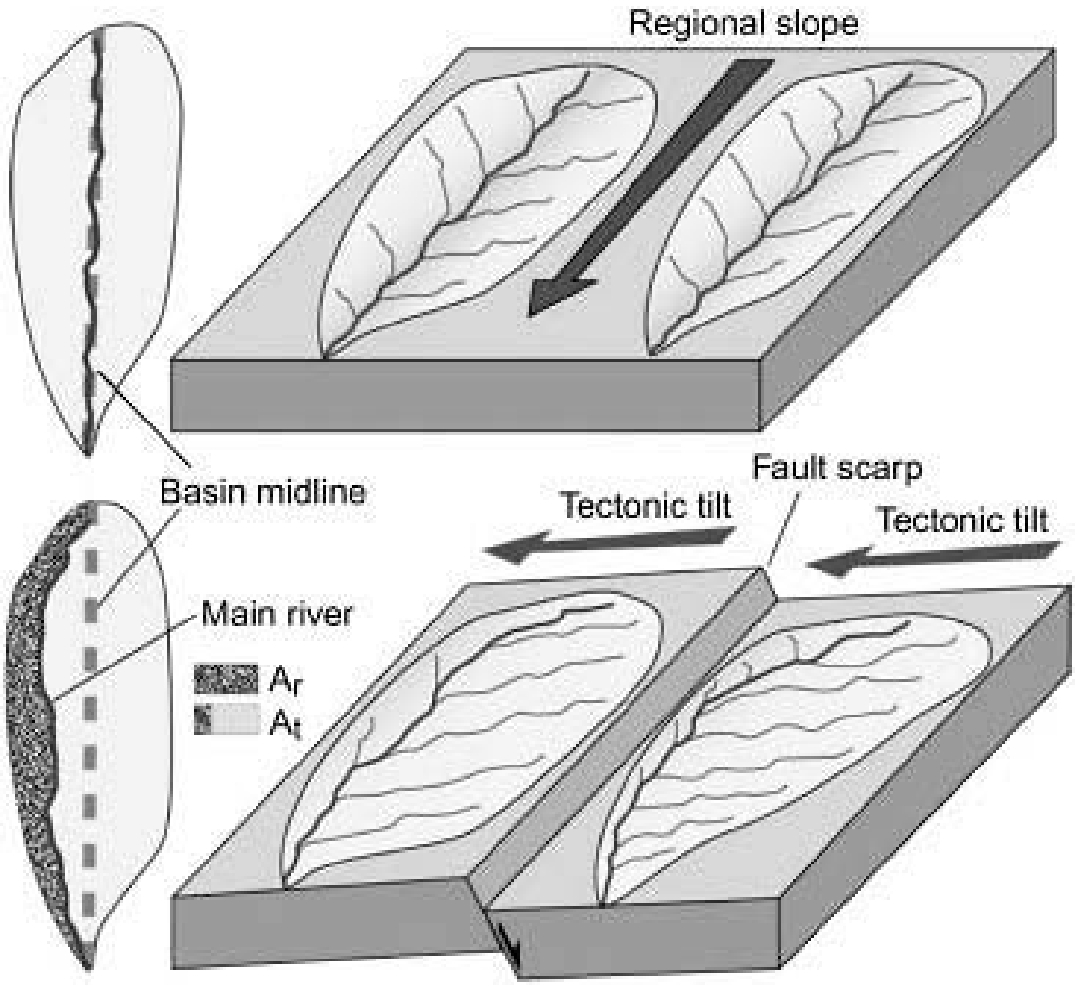

Figure7.6: Drainage response to uplift along a fault by migrating laterally in a down-tilt direction, A_r is the area of the basin to the right (looking downstream) of the trunk stream and A_t is the total area of the drainage basin (Keller and Pinter 2002).

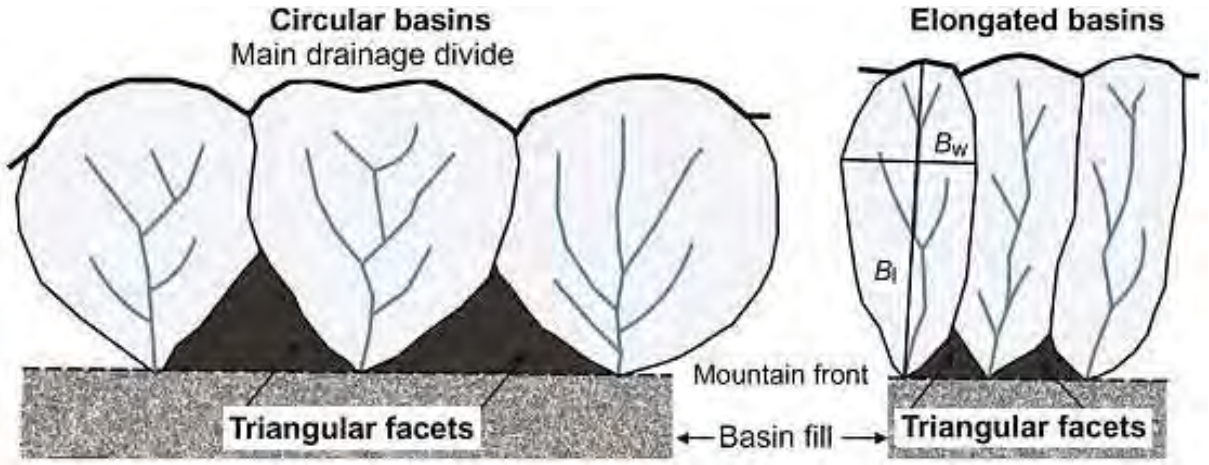

Figure 7.7: Basin shape index (Bs) calculation (Mahmood and Gloaguen, 2012).

7.4 Digital Elevation Model (DEM)

DEMs are storehouse of topographic information. DEMs denote terrain elevation as a function of geographic location (Burrough, 1986). They provide basic information required to characterize the topographic features of the terrain. Hence, to understand the Earth's surface in a better way, different viewing 3D ground elevation perceiving methods are used (Kaya, 2013). SRTM DEM of 30m resolution, ASTER DEM of 30m resolution and DEM generated from Sentinel-1 product using Sentinel-1 toolbox (SNAP) are used. The main products generated from DEM, which help in studying active faults in the present study area are:

7.4.1 Slope

Slope measures the steepness of the surface at any particular place. The DEM data were processed in ArcGIS to extract slope map.

7.4.2 Aspect

Aspect measures the direction of steepest slope for a location on the surface. The DEM data were processed in ArcGIS to extract aspect map. The aspect map allows a visual support to determine if the direction of the slope is affecting the orientations observed in the streams and faults.

7.4.3 Hillshade

Hill shading illuminates the surface from a particular sun position. Surfaces which are inclined away from light are darker than average, whereas surfaces inclined toward the light are brighter. The DEM were processed in ArcGIS 10.1 to extract a hillshade map. The controlling factors of hillshading are both light source elevation and azimuth. It is important to retain the elevation angles as low-elevation angles are noisy, highlighting streets as well as scarps; whereas high angles results in less contrast. Hence, for the present study a medium angle, such as 45°, proved useful. Azimuth, on the other hand, influences slope recognition. With the regional E-W fault trend, an azimuth of 315º is used to highlight the scarps in the locations 'a', 'b' and 'f'.

7.5 Interpretation and Discussion

The most important confirmation for fault identification has been given by the dislocation and displacement of mountain ridges and valleys, clearly recognizable lineaments, and drainage offsets observed in the true colour composite image of the area. Also, the

morphometric analysis and shaded relief models (SRMs) created from DEM, also further substantiates the presence of fault.

7.5.1 Evidence from geomorphic features observed in True Colour Composites

The geomorphic evidences of active faults are given in the highlighted boxes of figure 7.1 and 7.2 (enlarged in subsequent images). The main offset is observed within location 23°16’ N; 69°4’E and 23°6’ N; 69°24’ E (Box a, Figure 7.1) where the sedimentary rocks and intertrappean beds have been first displaced by one major fault striking approximately ENE-WSW, succeeded by another incidence of faulting (roughly NE-SW displacement) which affected both the rock groups and the first fault (Figure 7.8a and 7.10a).

A major offset in drainages is observed in the area marked (b) in figure 7.1, where a visible bending along the NW-SE direction is shown by three major drainage basins from NW corner of the area to SE corner. This observation infers to the presence of two faults striking NW-SE roughly, which resulted in the displacement of these three drainages along this particular direction (Figure 7.8b and 7.10b).

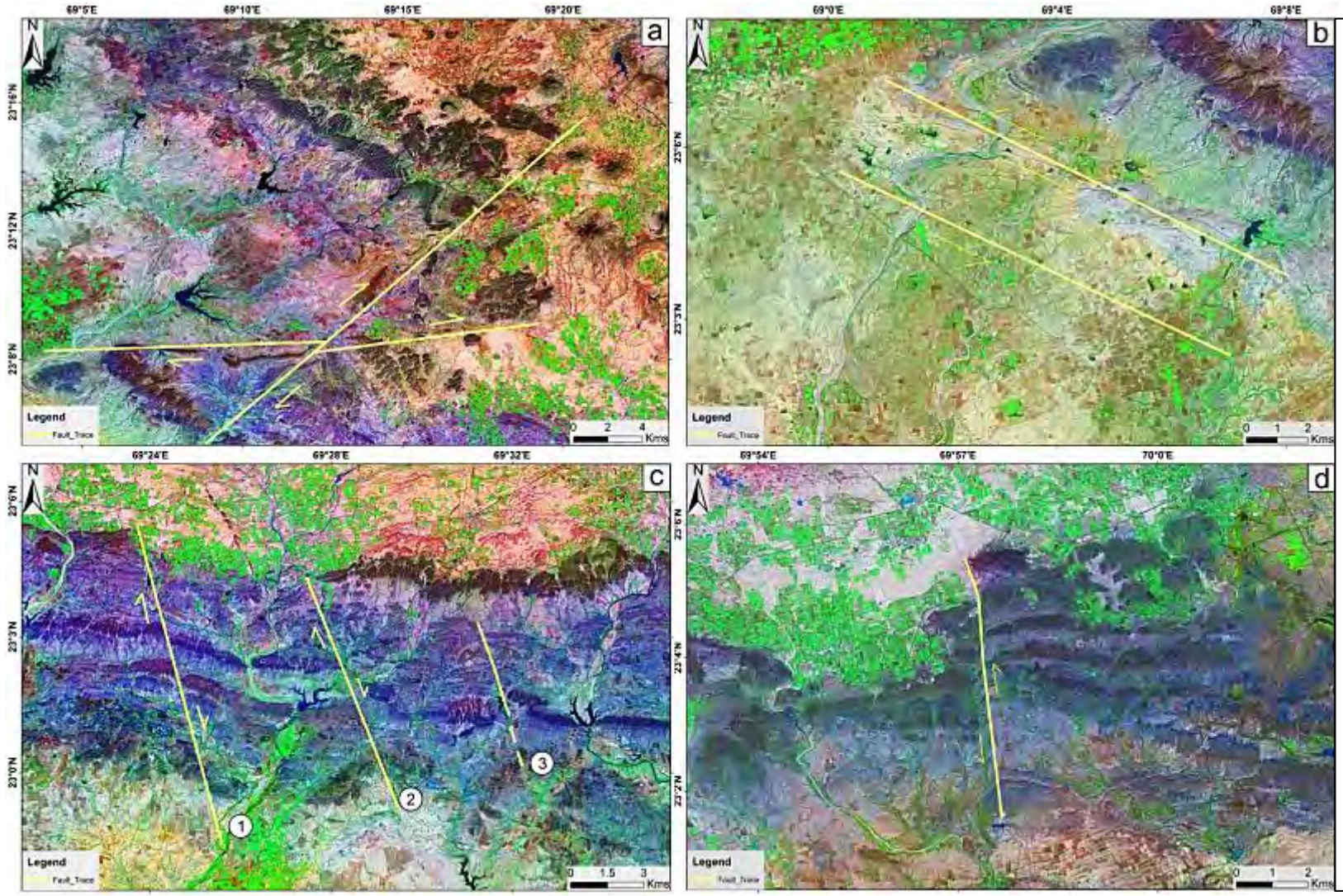

7.8(a) showing the displacement of sedimentary rocks and intertrappean beds along an offset which is further offset by another, thus inferring the presence of faults,

(b) showing drainage offset in three such parallel drainages indicating presence of two faults,

(c) showing displacement of the rock types along three parallel directions, inferring the presence of fault,

(d) showing the displacement of sedimentary rocks and intertrappean beds, inferring the presence of fault.

Figure 7.8: True Color Composite Image of Landsat-7 ETM+ of the area showed by boxes a, b, c and d in figure 7.1.

The sedimentary rocks and the intertrappean beds indicate another series of offsets (box c of Figure 7.1) along three lines (marked 1, 2 and 3 in Figure 7.8c and 7.10c), roughly parallel to each other and striking NNW-SSE. Apparent displacement towards south is observed by the eastern block of the fault while the western block shows displacement towards north. The drainage of this area tries to follow the fault morphology. While the first two faults from west (1 and 2) show noticeable effect of faulting, at the east the effect of 3rd fault (marked as 3), however, due to lack of evidences cannot be strongly inferred and hence has been traced in dashed lines (Figure 7.8c).

There is displacement of intertrappean beds and some other sedimentary rocks at the location 23°4'N, 69°57'E (Figure 7.8d and 7.10d) where the displacement is seen by the eastern block towards north and the western block has moved south (box d of Figure 7.1). The drainage in this area is offset along this fault.

The box (e) in figure 7.1 shows a lineament, step like fashion (en-echelon) which is displaced irregularly in series along its length. The faults strike roughly NE-SW (Figure 7.9e and 7.11e). The fault in the extreme NW can be traced further SW dependent on the drainage pattern which follows the strike of the fault.

Two prominent ridge displacement are seen near location 23°22'N, 69°31'E (box f of Figure 7.1), which concludes the presence of fault. The direction of displacement in both cases is roughly NE-SW and in both cases the eastern block, moved southward [Figure 7.9f(a)]. The two inferred faults may be the continuation of a single fault, but due to lack of evidence in between, it is described as two separate faults as it is difficult to comprehend the continuity. Based on drainage offset and a linear ponding along the offset [Figure 7.9f(b)] the fault at the lower side of the figure 7.9f(a) can be more clearly inferred. Two other sets of ridge displacements are observed (boxes g and h of Figure 7.1).where NW-SE ridge displacement is seen in area marked (Figure 7.9g and 7.11g). The sense of block displacement NW-SE, where the north-eastern blocks relocated southerly is observed in area marked (h) (Figure 7.9h and 7.11h). In addition to the ridge displacements, the drainage offset seen near 23°45' N, 68°58' E can also be concluded to have been modified by the faulting.

Further the faults are marked for the eight locations on a three dimensional prospective view obtained by draping high resolution Digital globe image over the ALOS PALSAR 12.5m resolution DEM [Figure 7.12 (i, ii ,iii)].

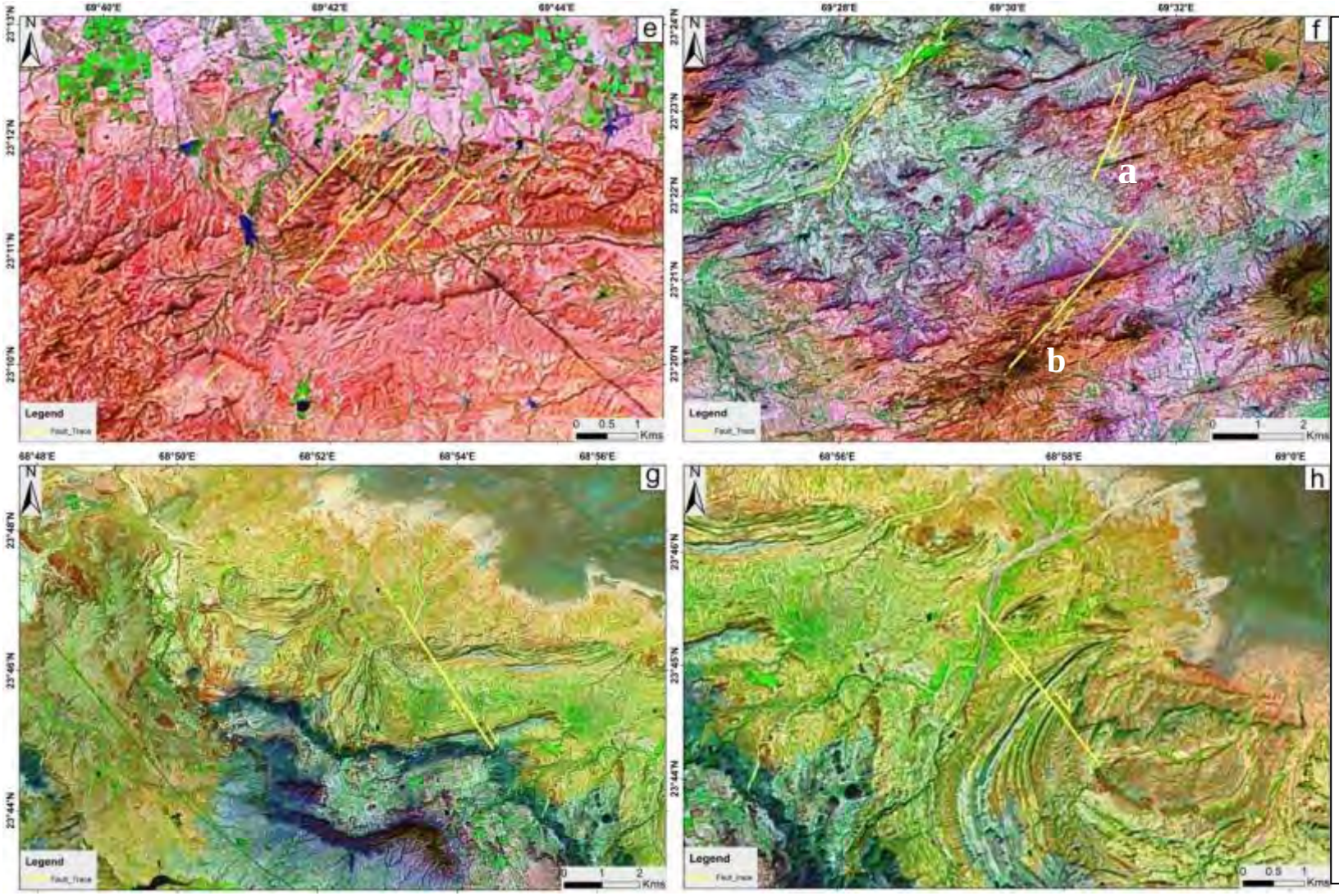

7.9 (e) showing a lineament affected by en-echelon type of offset, inferring the presence of fault,

(f) showing ridge displacement at two places, inferring the presence of faults [f(a)], including a drainage offset with prominent linear ponding [f(b)],

(g) showing the displacement of a ridge, indicating the presence of fault,

(h) showing the displacement of a ridge along with drainage offset along the same direction, inferring the presence of fault.

Figure 7.9: True Colour Composite image of landsat-7 ETM+ of areas showed by boxes e, f, g and h in figure 7.1

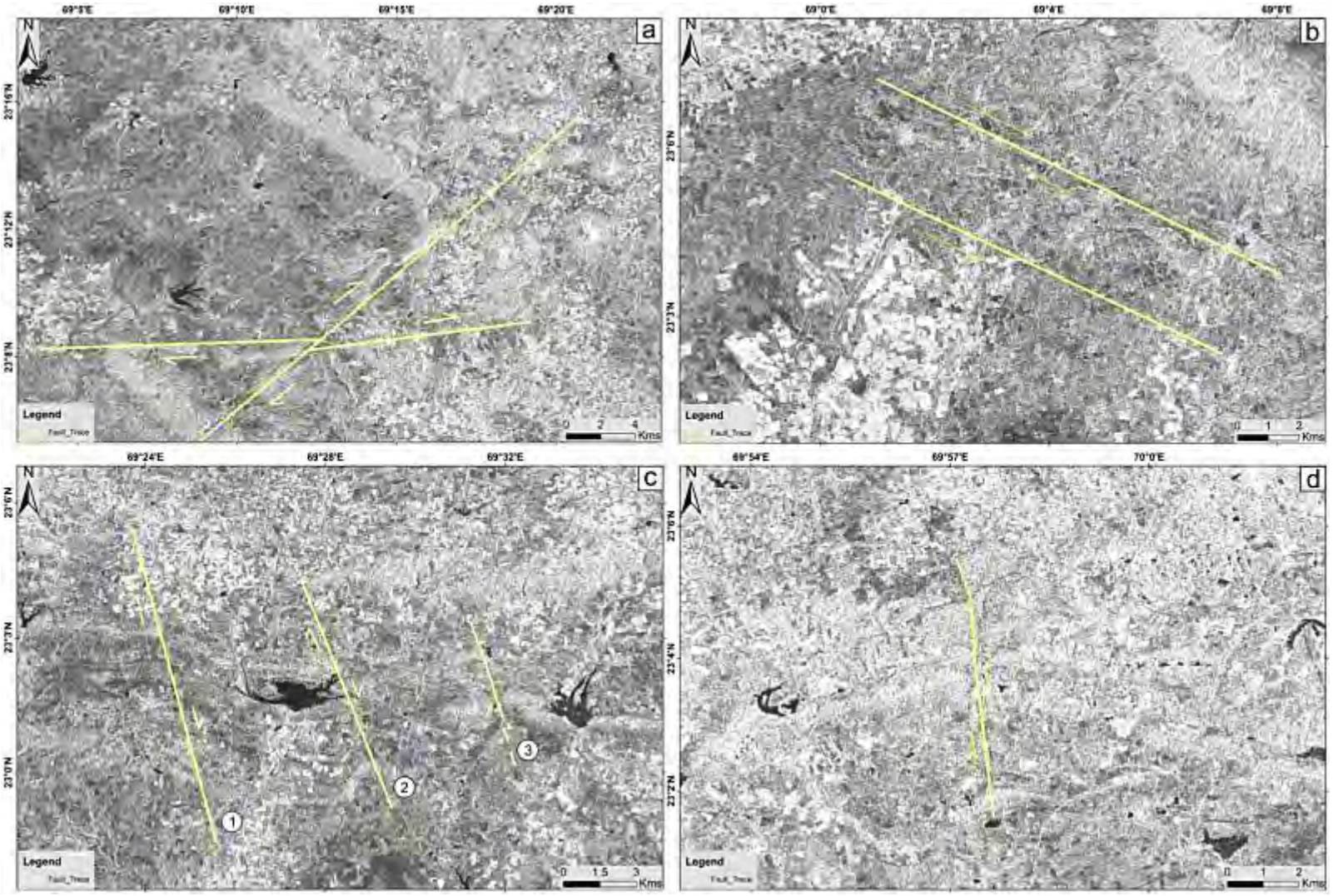

Figure 7.10: Sentinel-1 power image of areas showed by boxes a, b, c and d in figure 7.2.

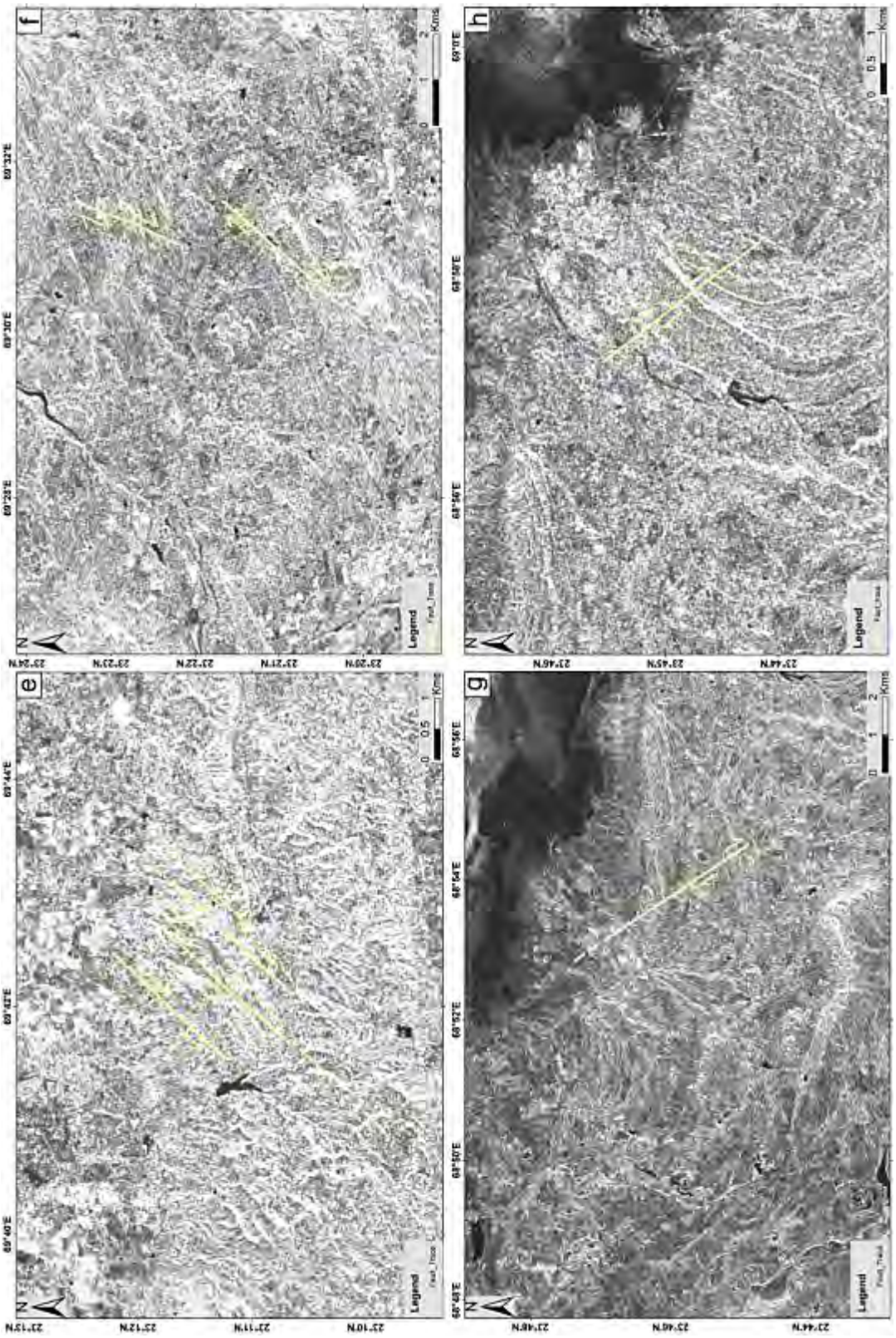

Figure 7.11: Sentinel-1 power image of areas showed by boxes e, f, g and h in figure 7.2.

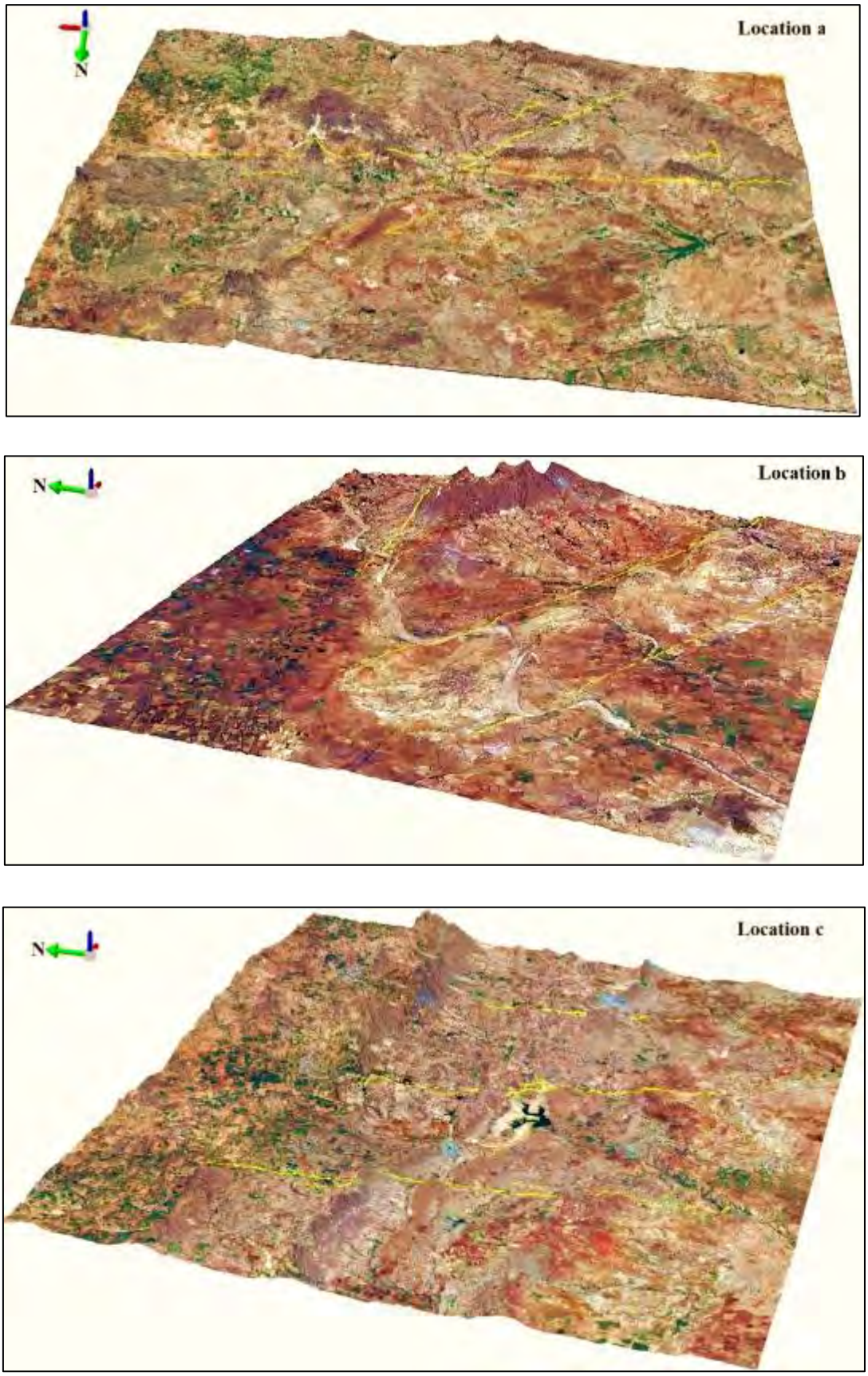

Figure 7.12 (i): 3D prospective view of Locations a, b, c.

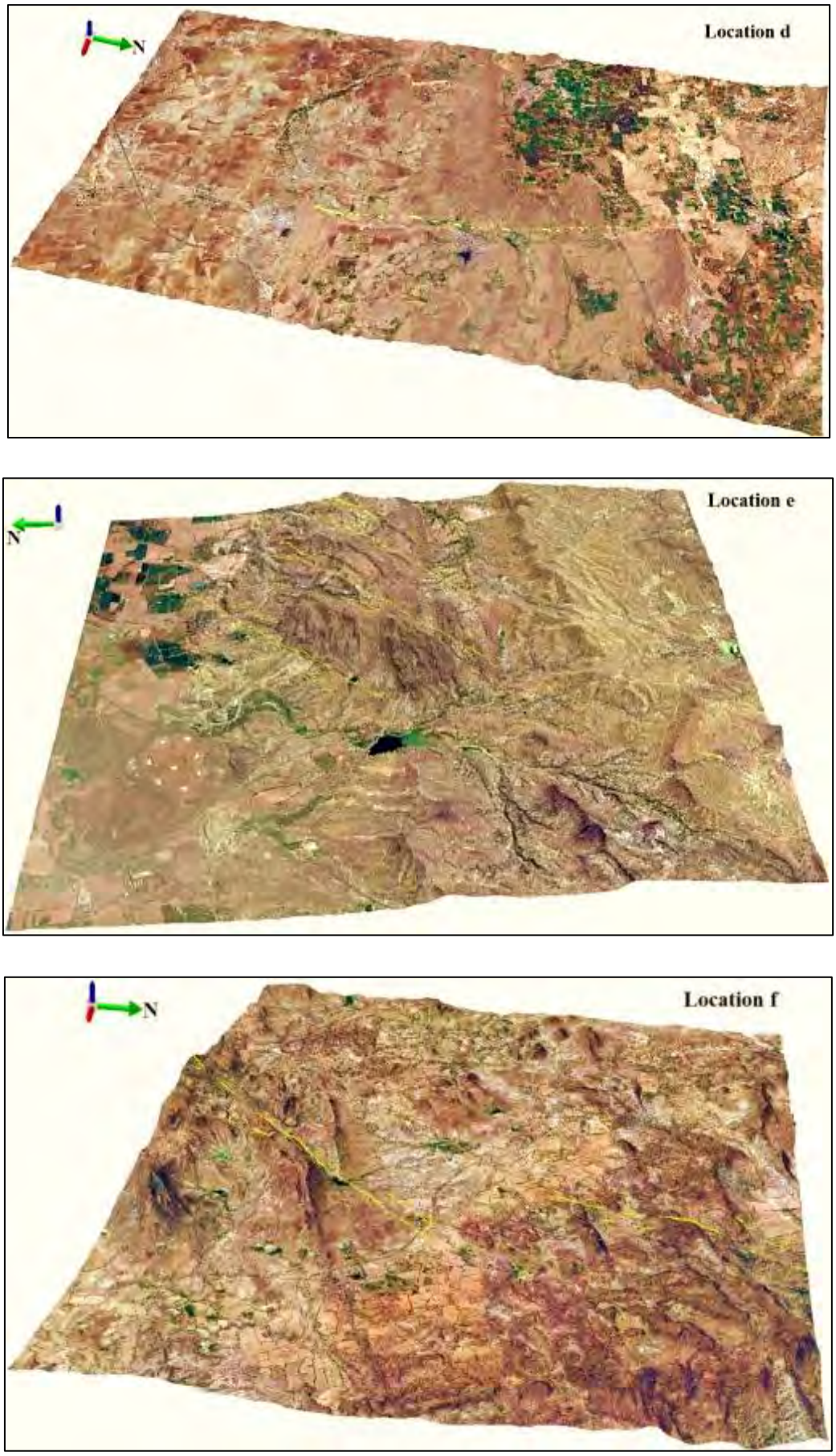

Figure 7.12 (ii): 3D prospective view of Locations d, e, f.

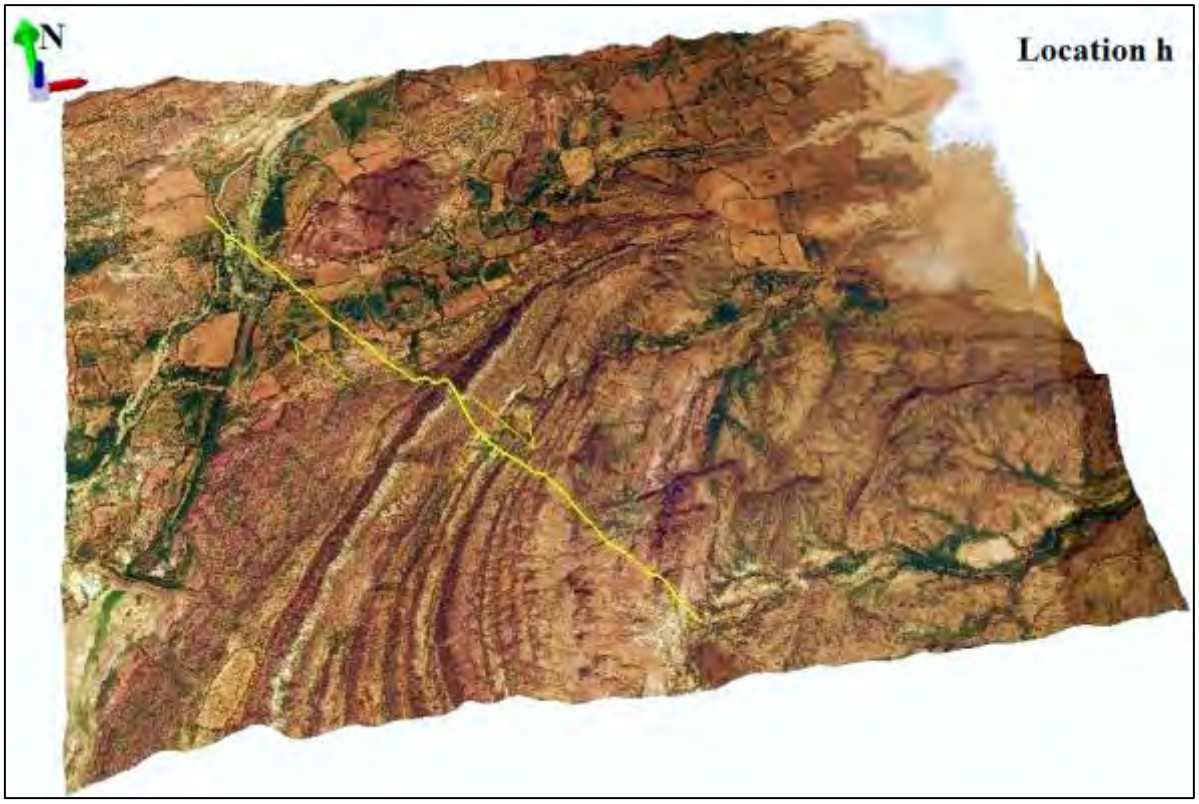

Figure 7.12(iii): 3D prospective view of Locations g, h.

7.6. Evidence from Morphometric analysis

7.6.1 Hypsometric analysis results

Hypsometric curves have been obtained for the different drainage basins: I, II, III and IV of locations ‘a’ and ‘b’; I, II, III and IV of locations ‘c’; DI, DII, FI and FII of locations ‘d’ and ‘f’; I, II, III and IV of locations ‘g’ and ‘h’ demarcated on DEM as shown in figure 7.13. Locations ‘a’, ‘b’, ‘c’,‘d’, ‘f’, ‘g’ and ‘h’ are as shown in figure 7.1. The hypsometric curves dominantly show concave and similar shapes in the first instance. However, for some basins at places, distinct convex up tendency is seen. This is observed in case of drainage basins I, III and IV of locations ‘a’ and ‘b’, II and III in case of location ‘c’, and I, II and IV of location ‘g’ and ‘h’ (Figure 7.13) Location ‘d’ indicates anomalous curves with strong convexity towards the right portion of the curve. Curves of location ‘f’ show rather smooth concave curves specifying lesser tectonic activity (Figure 7.14 i to iv).

The convexity of the hypsometric curve indicates the younger erosional stage of a basin (Strahler, 1952). This convexity may be attributed to tectonic factors. In turn, it validates the presence of the active faults in these locations which have been confirmed from the satellite images. These faults might have uplifted the area where the catchments are located. This results in a continuous base level depression in the rivers, thus maintaining high downward erosion rates. Therefore, these convex portions have been suffering continuous transformation process and conserving such convex profiles over time. The left over material after erosion is portrayed by the area below the curves. Hence, when the curve gradient becomes higher in its upper part, the amount of material left after erosion is smaller (Strahler, 1952; Harlin, 1978).

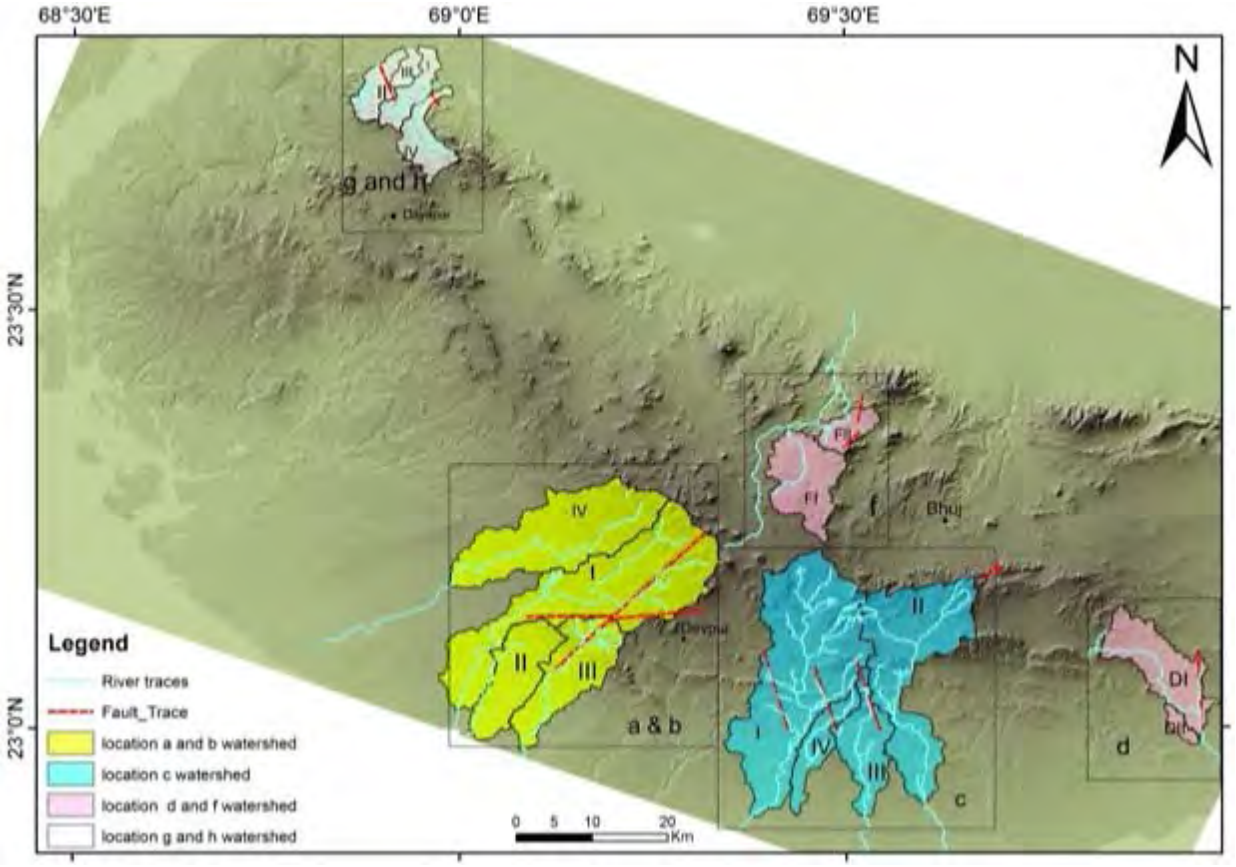

Figure 7.13: SRTM-DEM hillshade model showing the drainage basin of each location studied for hypsometric analysis and how the drainage patterns behave in relation to the inferred faults. The basins for each location are marked I, II, III and IV which shows their relative position with respect to the inferred faults which are also marked.

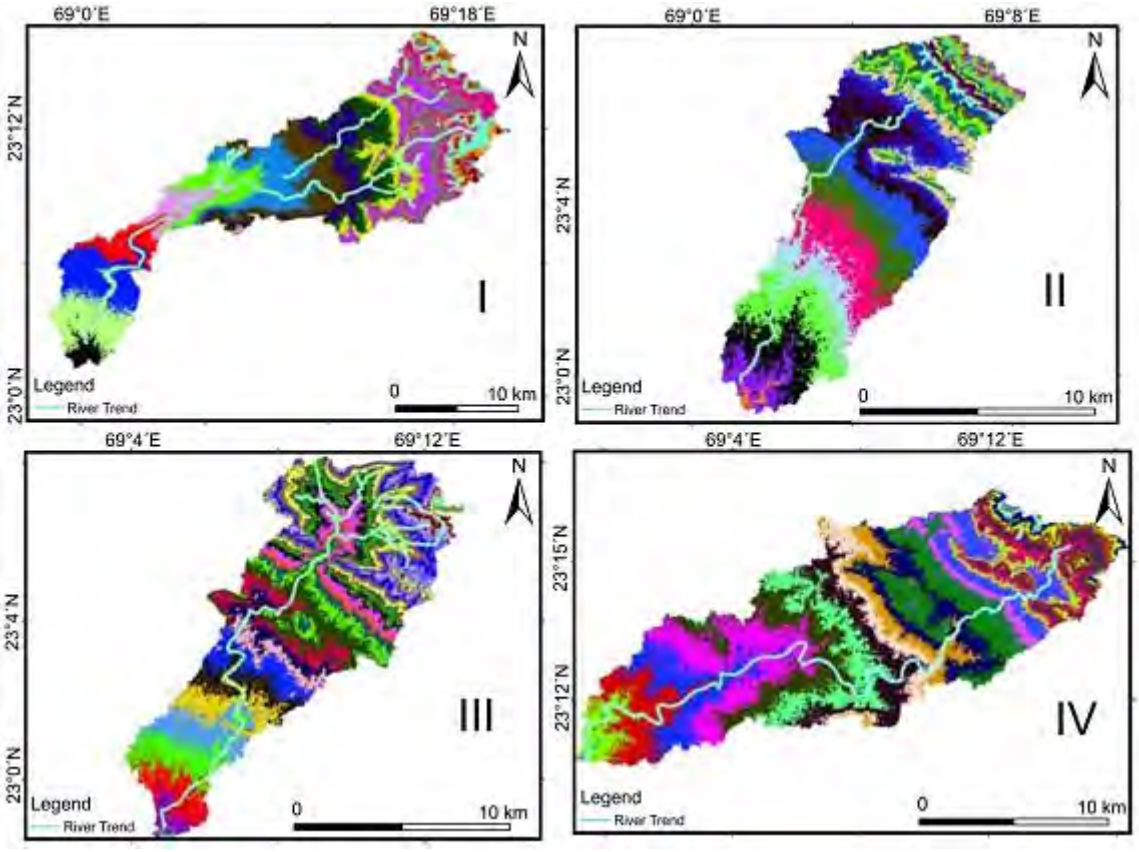

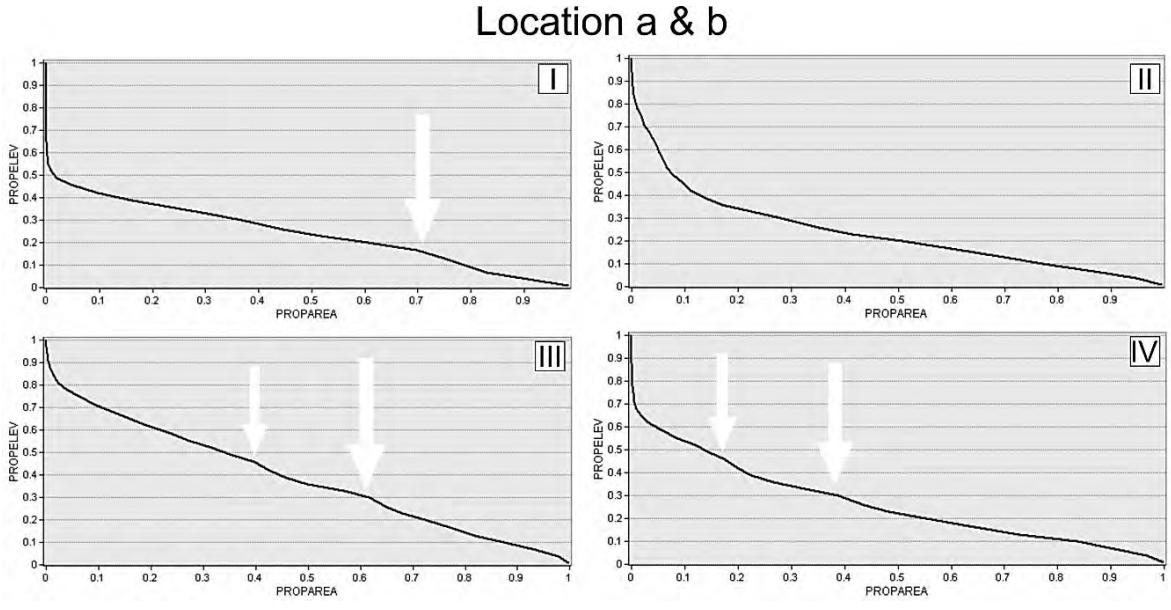

(A)

Figure 7.14 (i): Hypsometric graphs for the studied drainage basin of location (A) location 'a' and 'b'. (Arrows indicate the convex portion of the curve). Locations are as per figure 7.1.

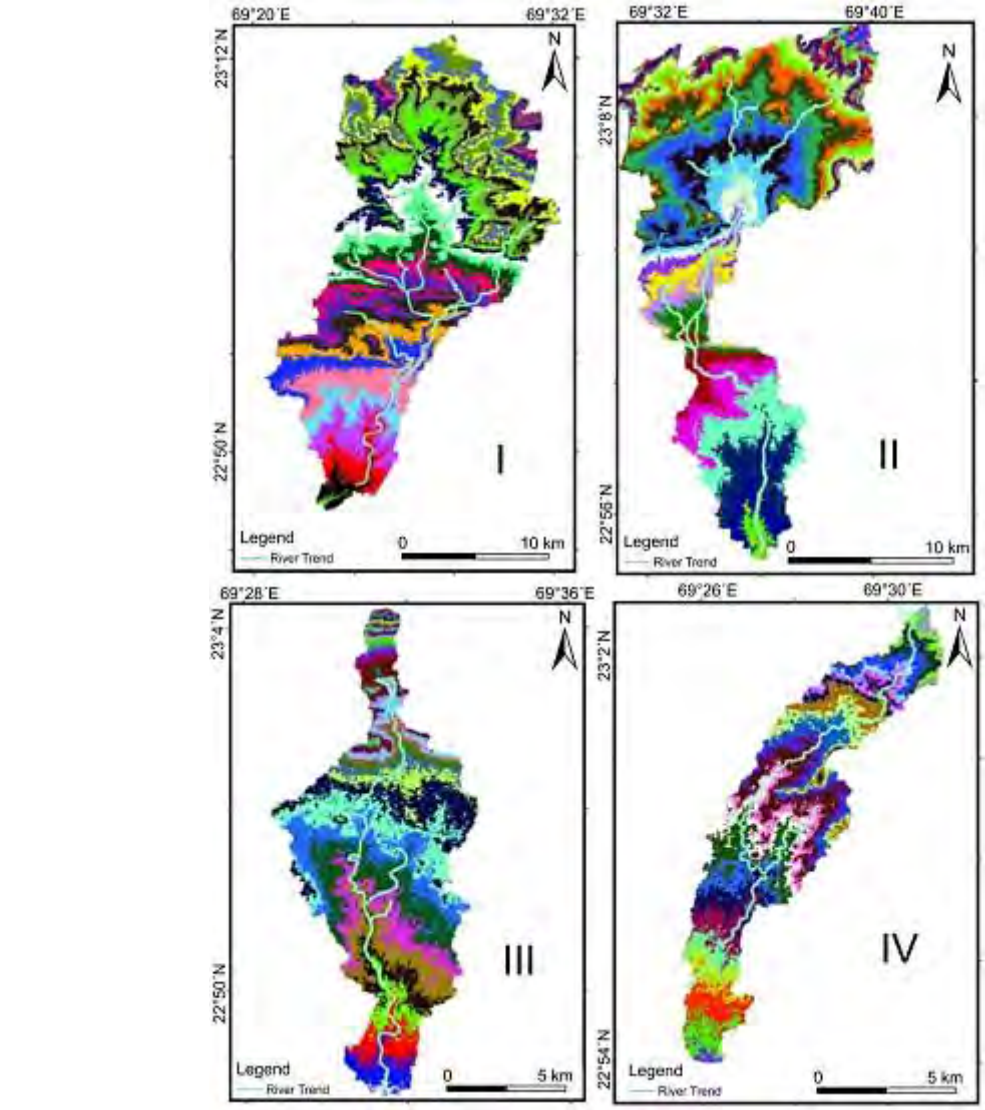

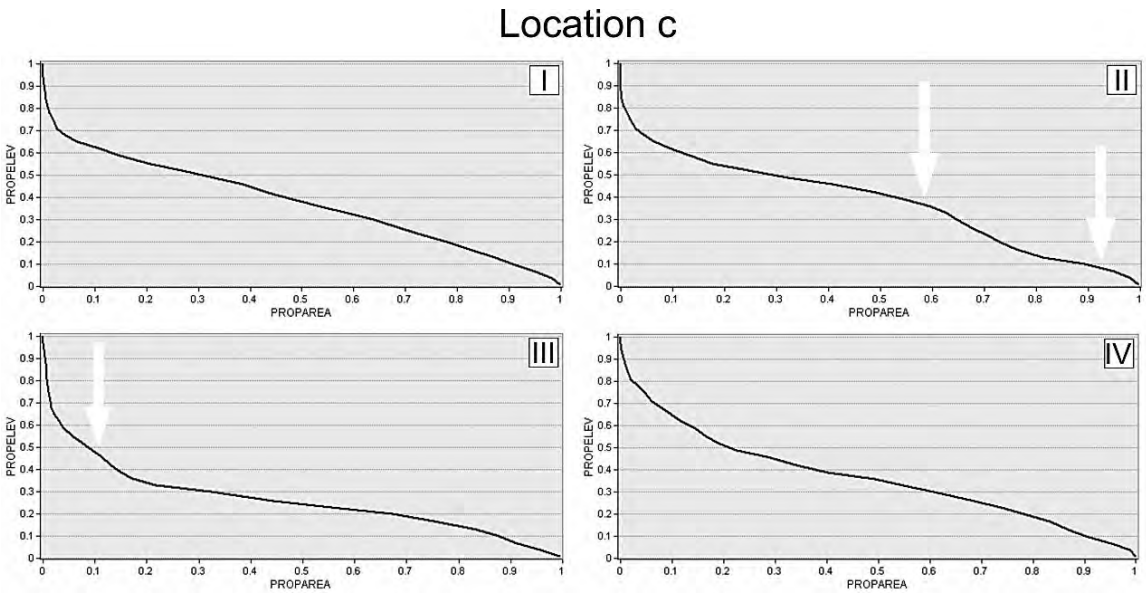

(B)

Figure 7.14 (ii): Hypsometric graphs for the studied drainage basin of location (B) location 'c'. (Arrows indicate the convex portion of the curve). Locations are as per figure 7.1.

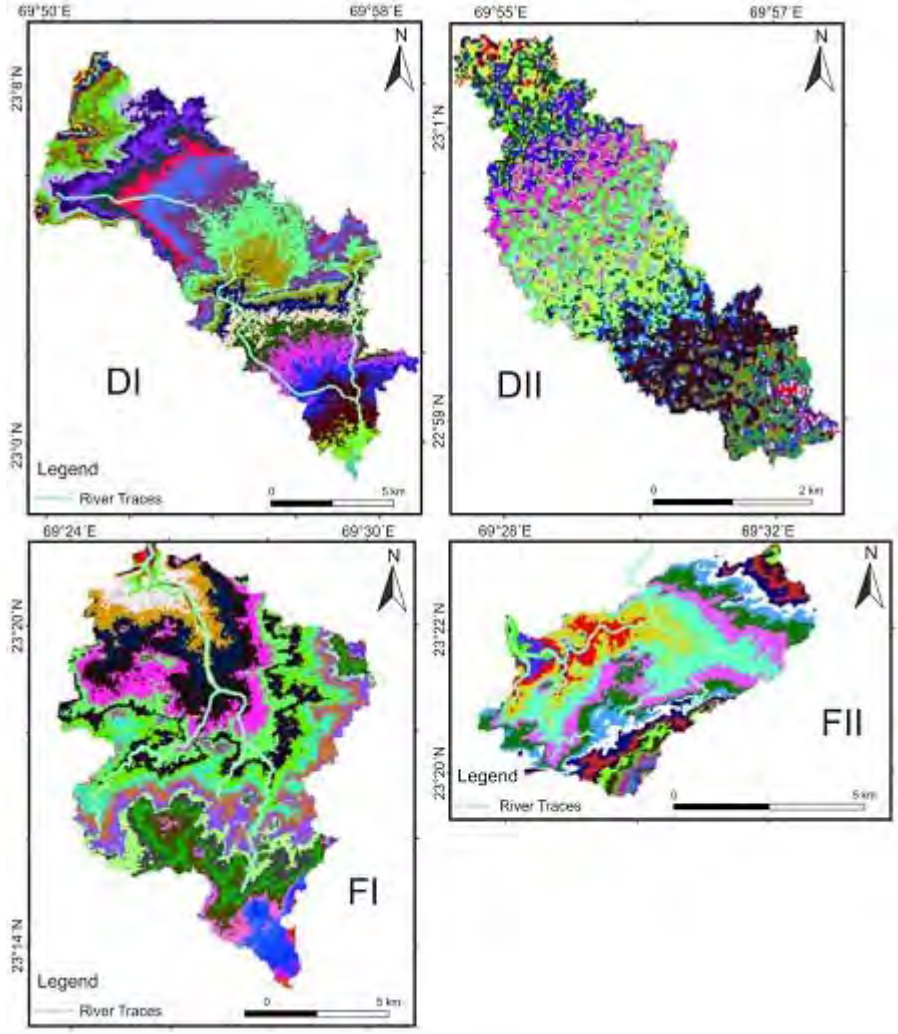

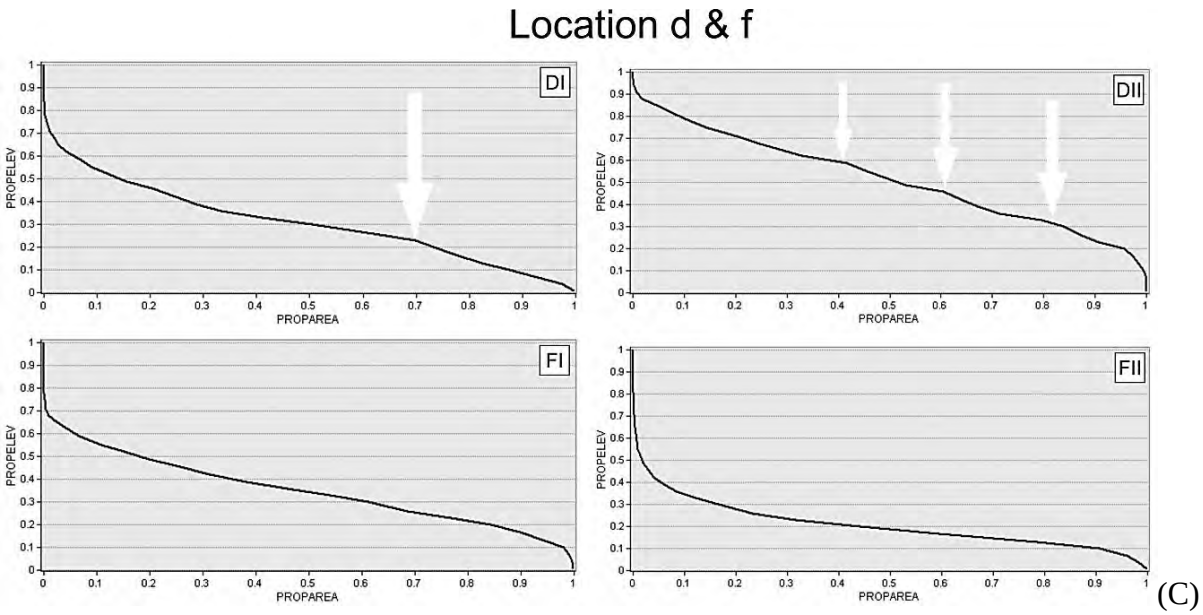

(C)

Figure 7.14 (iii): Hypsometric graphs for the studied drainage basin of location (C) location'd' and 'f'. (Arrows indicate the convex portion of the curve). Locations are as per figure 7.1.

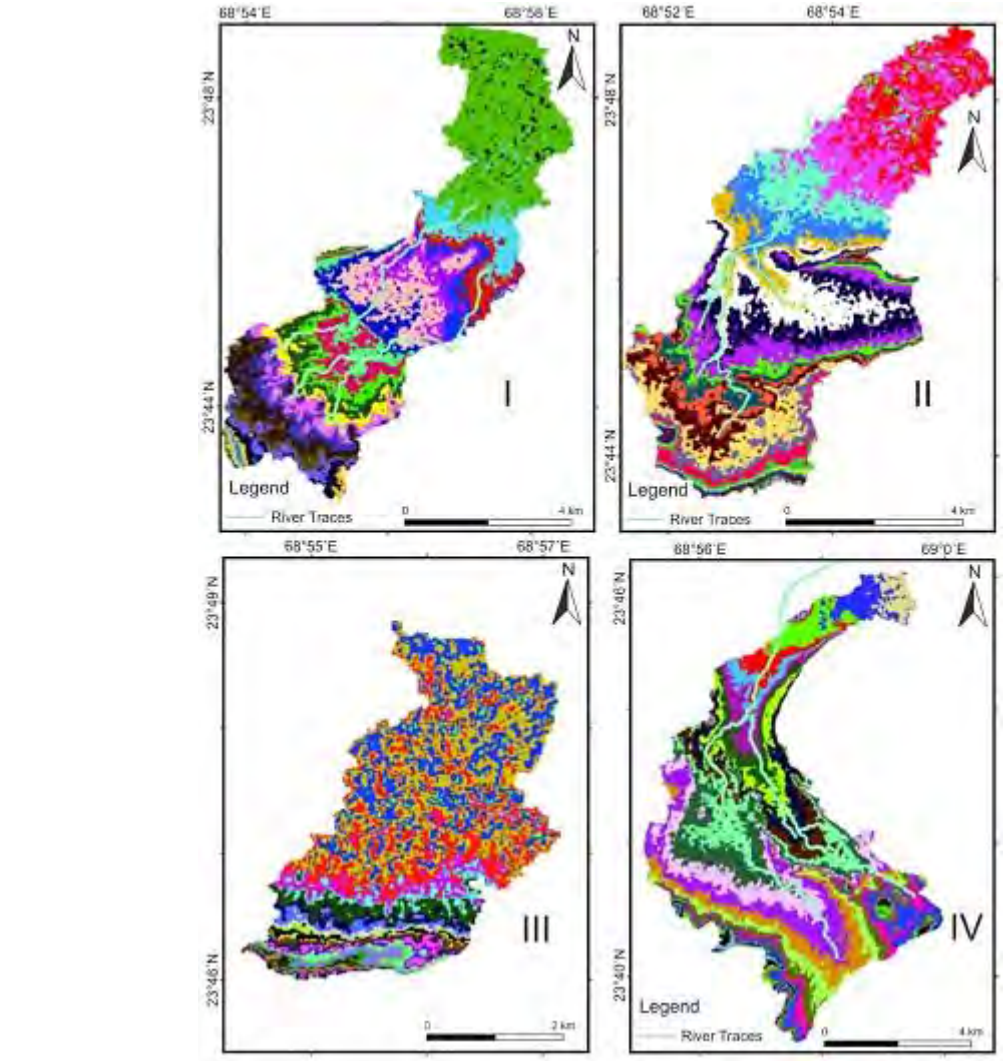

Location g & h

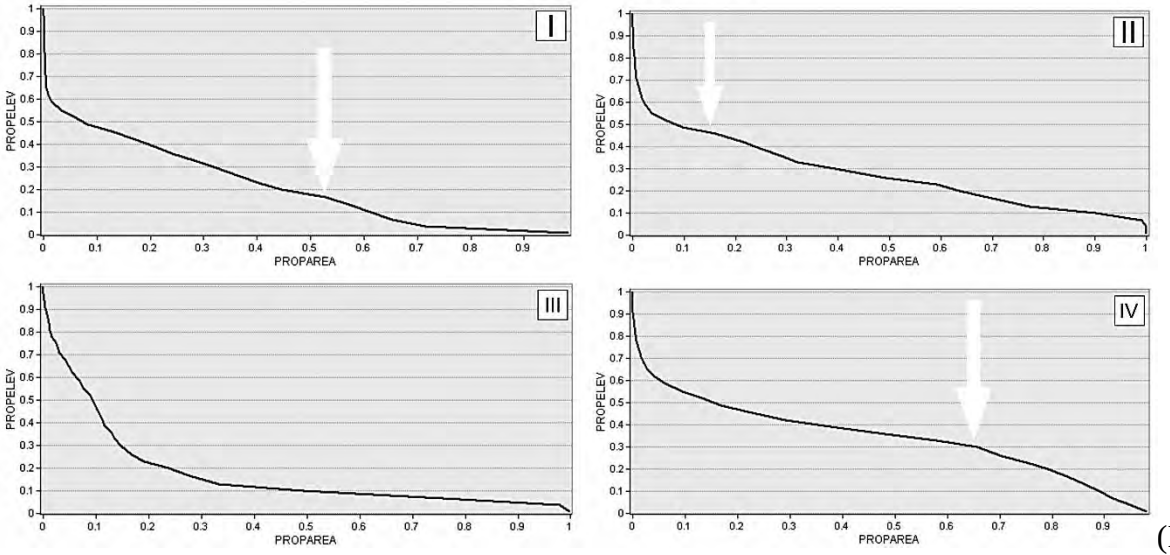

(D)

Figure 7.14 (iv): Hypsometric graphs for the studied drainage basin of location (D) location 'g' and 'h'. (Arrows indicate the convex portion of the curve). Locations are as per figure 7.1.

7.6.2 SL index results

The SL index value ranges from 5.5 (basin DII of location‘d’) to 132.8 (basin III of location ‘c’).

Table 7.2: Average SL index of the segments of drainage basins of each location (Figure 7.15).

Location	Basin No.	dL (in km)	dh (in km)	L (in km)	SL= (dh/dL)*L
a and b	I	16.6	48	36.4	105.4
	II	6.4	20	13.3	41.5
	III	8.0	31	12.2	46.9
	IV	11.3	38	21.7	73.1
c	I	17.9	69	21.9	84.1
	II	9.6	39	20.4	83.05
	III	3.8	28	18.1	132.8
	IV	2.7	10	17.3	63.5
d and f	DI	3.3	16	7.6	36.4
	DII	1.2	2	3.2	5.5
	FI	3.7	31	7.5	62.8
	FII	0.9	8	7.2	45.3
g and h	I	2.5	12	9.5	46.4
	II	2.1	5	5.0	11.8
	III	1.9	5	2.4	6.2
	IV	1.9	7	3.2	12.0

Those basins having values (from the table 7.2) above 50 show that SL indices increase when they cross the hill fronts related to these faults or wherever they come across the inferred faults. However, relatively lower SL values are also observed in basin DII of location ‘d’ and basins II, III and IV of location ‘g and h’. In these basins, the reason for these low SL values can be attributed to the strike slips nature of the above inferred faults even though the underlying rocks are resistant.

7.6.3 Sinuosity Results

All drainages where the faults are inferred, show sinuous channels (sinuosities of drainages from each location are given in the table 7.3) in the studied locations of the study area.

Table 7.3: The sinuosity values of the drainages near the inferred faults of each location (Figure 7.15).

Location	Basin No.	Drainage No.	Total Length C (km)	Shortest Path V (km)	Sinuosity (C/V)
a and b	I	1	61.3	46.0	1.3
		2	34.2	24.5	1.4
	II	1	18.2	14.7	1.2
	III	1	42.4	25.8	1.6
	IV		42.8	29.8	1.4
c	I	1	45.0	35.0	1.3
	II	1	41.6	27.7	1.5
	III	1	22.4	16.7	1.5
	IV	1	17.8	11.9	1.5
d and f	DI	1	21.6	16.3	1.3
	FI	1	31.7	20.8	1.5
		2	5.9	3.8	1.5
		3	7.1	5.0	1.4
		4	6.7	3.0	2.2
		5	2.6	1.5	1.7
g and h	I	1	9.6	7.8	1.2
	II	1	7.1	6.2	1.1
	IV	1	10.2	8.2	1.2
		2	3.6	3.3	1.1

The average sinuosity values of all the drainages of each location are around 1.2 to 1.5. The reason for lower sinuosity is that all rivers follow a straight deeply incised channel (faulted land) for a short distance because they emerge from the upland and flow onto the alluvial plain. Owing to such values, it can be understood that these drainages are fault modified and hence, further confirm the presence of fault. This is clearly understood from the satellite images given earlier as well where the drainages in vicinity of the faults or the drainages crosscutting the faults follow the fault trend near the faults and they emerge out of the fault resuming their path (Figure 7.8 b, c, d and 7.9 h). In some basins of location'd' and 'f', they roughly cross cut the fault and are also shifted during faulting process. In these regions around 2.0 sinuosity is observed.

7.6.4 Drainage basin asymmetry

The AF values calculated around the inferred faults, for the basins of each location, are given in the Table 7.4 below. There is a definite pattern in the AF values of this study area. From the table it is indicated that basins I and IV of location 'a' and 'b' show greater than 50 AF values signifying tilting towards west with respect to the 1st inferred fault in these locations. And the basins II and III of location 'a' and 'b' gives lower values of AF signifying their tilt towards the east with respect to the 1st fault. This is conformable with their position with respect to the fault. In case of location 'c' similar scenario is observed, where the basin II gives greater AF value whereas basins III and IV gives lower AF values, conformable with their position with respect to fault (Basin II suggests tilt towards west and are located west of the inferred faults and basin III and IV suggests tilt towards east with their position on the east of the fault).

All the basins show more or less low AF values in case of 'd' and 'f' location, suggesting tilt towards east (in case of Location 'd') and to the west (in case of Location 'f'). Since in both the locations 'd' and 'f', the asymmetrical drainages are located a bit far from the inferred fault, so the difference in their tilting and position with respect to the inferred faults can only be described due to the topography of the area.

Basins I, II and III of location 'g' and 'h' gives very high AF values, indicating their strong asymmetry towards east and these basins are located on the north-eastern block of the inferred fault. Lower AF values is shown by Basin IV of this location with respect to other three, still more than 50 and hence can be assumed to tilt slightly towards east but is relatively less affected by the faults than the other three. Such relationship between the AF values of the

basins and their position with respect to the trace of the inferred fault, from earlier sections, can only further substantiates the presence of fault at these locations.

Table 7.4: Drainage basin asymmetry values of the basins calculated for each location (Figure 7.15).

Location	Basin No.	A_r (sq. Km)	A_t (sq. Km)	AF= (A_r /A_t)*100
a and b	I	186.8	313.6	59.6
	II	25.6	95.9	26.7
	III	46.4	115.0	40.3
	IV	134.0	213.9	62.6
c	I	187.6	347.8	53.9
	II	159.1	227.4	69.9
	III	31.5	79.4	39.7
	IV	20.3	47.9	42.4
d and f	DI	25.1	102.8	24.4
	DII	4.5	10.6	42.4
	FI	38.4	95.3	40.3
	FII	14.4	30.6	47.1
g and h	I	27.4	35.2	77.8
	II	23.7	33.1	71.6
	III	10.9	13.1	83.2
	IV	24.6	45.5	54.06

7.6.5 Basin shape index results

Bs, computed from the DEM, can be classified into three classes:

Class 1 (>2.8), class 2 (2.1-2.7) and class 3 (1.4-2.0) (from table 7.5).

Table 7.5: Basin shape index of basins calculated for each location (Figure 7.15).

Location	Basin No.	B_l (in km)	B_w (in km)	Basin shape index $B_s = B_l/B_w$
a and b	I	39.9	11.9	3.3
	II	18.4	6.3	2.9
	III	21.3	9.3	2.2
	IV	31.8	11.8	2.7
c	I	36.4	15.1	2.4
	II	30.7	15.5	2.0
	III	19.8	8.7	2.3
	IV	22.9	4.1	5.6
d and f	DI	20.6	7.4	2.8
	DII	6.5	2.6	2.5
	FI	16.3	11.0	1.5
	FII	8.6	5.5	1.6
g and h	I	12.3	4.4	2.8
	II	11.1	5.1	2.2
	III	5.7	3.4	1.7
	IV	13.3	8.3	1.6

Most of the drainage basins of the location come under the classes 1 and 2, excepting basin FI, FII of location f; and basins III, IV of location g and h which come under the class 3. These basins have nearly circular shapes due to lower tectonic activity. This can be related well with the earlier observations from hypsometric analysis and drainage basin asymmetry where these particular basins indicate less affected by faults while the other basins with higher Bs values, hence elongated basin shapes, show effect of higher tectonic activity.

Apart from the geomorphic features happening in close proximity to the active faults showing their presence, the shaded relief models, slope and aspect are also studied.

The results obtained by analysing the different geomorphic indices (Table 7.2 to 7.5) have been reprensented in the figure 7.15 bar diagram.

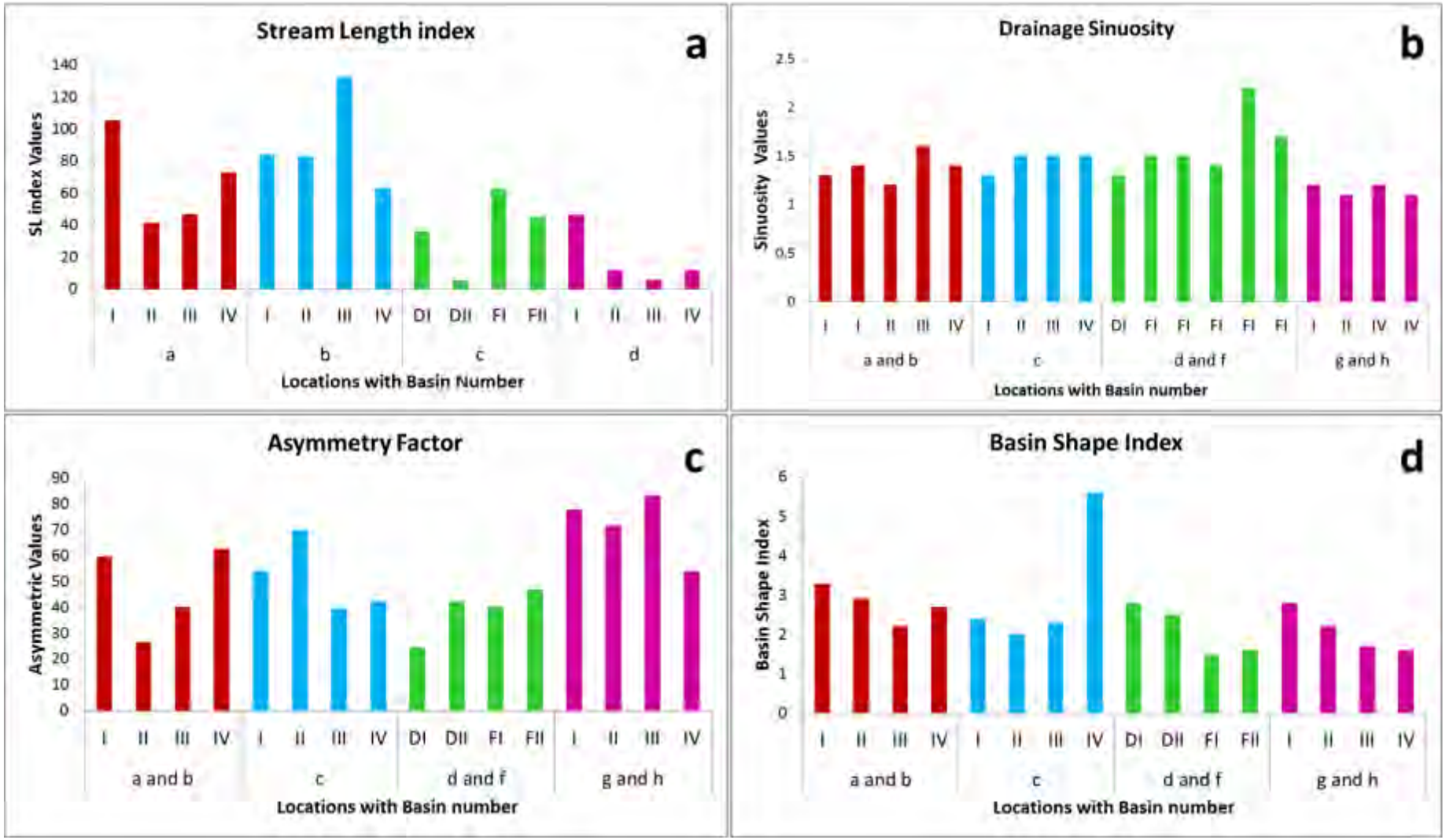

Figure 7.15: Graphs showing values for geomorphic indices (a) SL index (b) Sinuosity (c) Asymmetric factor (d) Basin shape index.

7.7 Evidence from Digital Elevation Model

Certain topographic features along the inferred faults were scrutinized using the shaded relief model derived from DEM (Figure 7.16) in order to confirm the existence of active faults in the study area. The Kutch Mainland Fault in the northern region indicate well-developed 'scarps' marked (A in Figure 7.16) and 'linear valley' (B) in the shaded relief image. Scarps are small offset on the ground surface where one side of fault has relocated vertically with respect to another. Linear valleys are formed due to simple deflections of streams along the fault trace.

The traces of faults inferred from figure 7.1 can also be proven from this hillshade image, enclosed in boxes in figure 7.16 which are further enlarged in Figure 7.17. These faults are mostly characterized by 'scarps', 'shutter ridges' 'triangular facets of dissected hills', and 'drainage offsets' which are the distinguishing features of presence of active fault. These shutter ridges are created as the fault displaced ridge crests on one side of the fault against gullies on other side of the fault. After erosion, V-shaped valley formations adjacent to the remaining fault spurs, give them a triangular shape forming a triangular facet. Triangular facets, shutter ridges and drainage offsets are demarcated by 'C', 'D' and 'E' respectively in figure 7.16 and 7.17.

This is supported by creating an aspect and slope map for the study area (Figure 7.18 and 7.19). The aspect map will permit for a visual aid to determine if the direction of the slope is affecting the orientations observed in the streams and faults GIS layers. Location 'a', 'b' and 'c' show prominent variation in slope which can be attributed to faulting.

While the general slope of the entire area is marked by green colour, the area along the inferred faults in the location 'a', 'b' and 'c' are marked by a red line along the fault (in case of location 'a' and 'b'; Figure 7.18(b)) and yellow line (in case of location 'c'; Figure 7.18(c)). The change in slope along the inferred faults is indicated by arrows.

The aspect map of location 'a', 'b', 'c' and 'f' validates the presence of faults as the blocks on either side of the inferred faults show similar aspects (Figure 7.19 (b) and (c)).

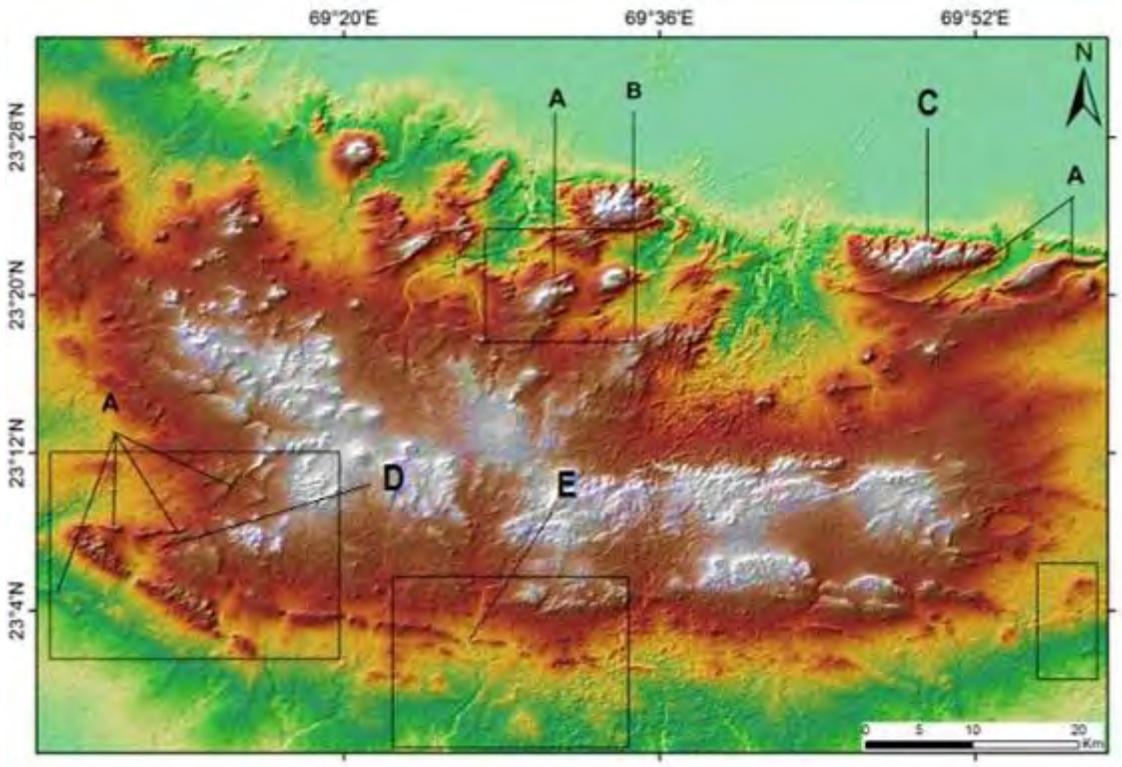

Figure 7.16: DEM hillshade model of the study area showing evidences of faults like Scarp (A), Linear Valley (B), triangular facets of dissected hills (C), Shutter Ridges (D) and drainage offsets (E). The rest scarps at the northeast corner of the image can be attributed to the presence of Kutch Mainland fault.

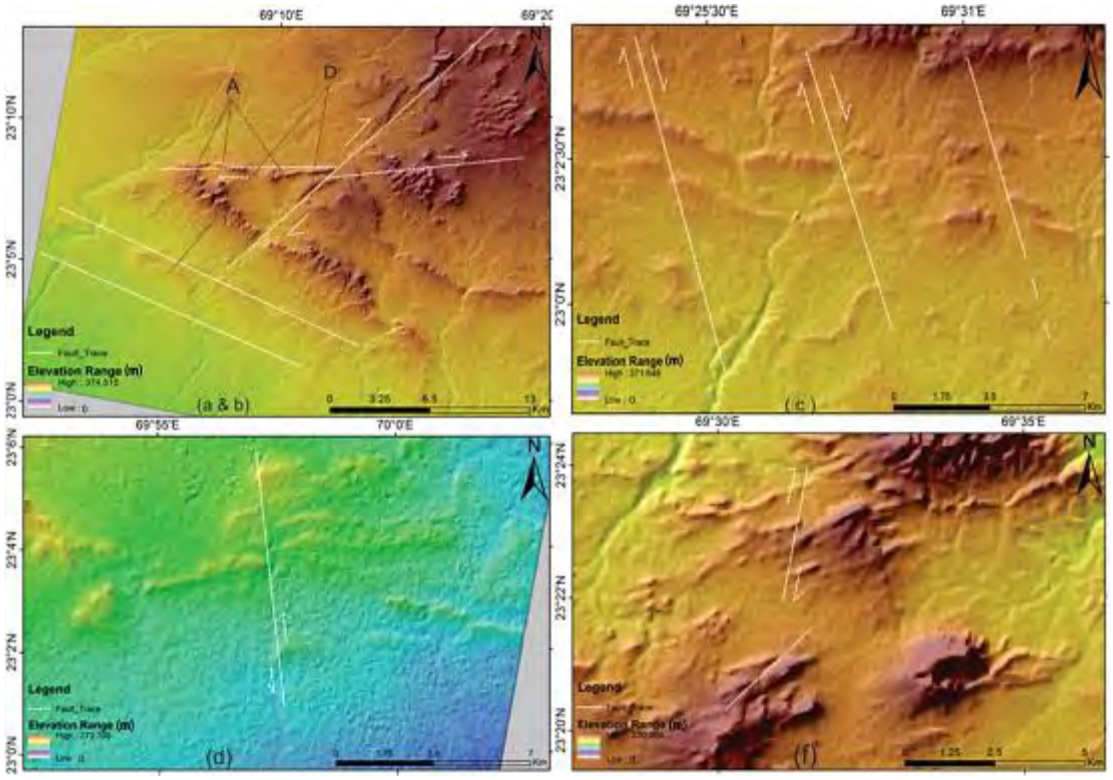

Figure 7.17: Hillshade model of the enlarged portions of location a,b,c,d and f, generated from the Sentinel-1 data using the Sentinel toolbox. The figures show evidences of faults Scarp (A), Shutter Ridges (D) and drainage offsets (E).

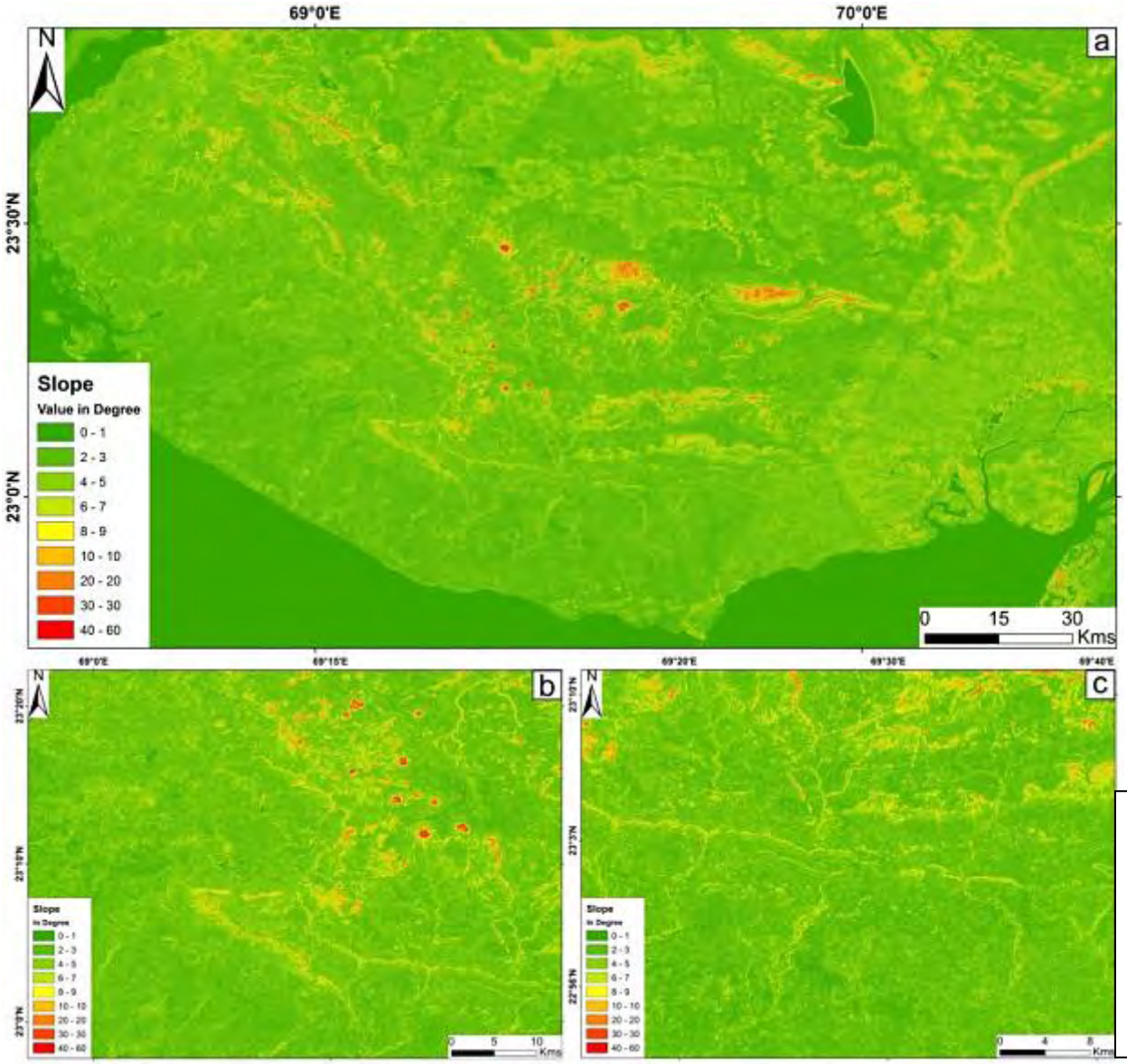

Figure 7.18: (a) Slope map of the Kutch area (b) enlarged slope map of location 'a' and 'b' (c) enlarged slope map of location 'c' (The slope with greater value indicates higher degree of slope)

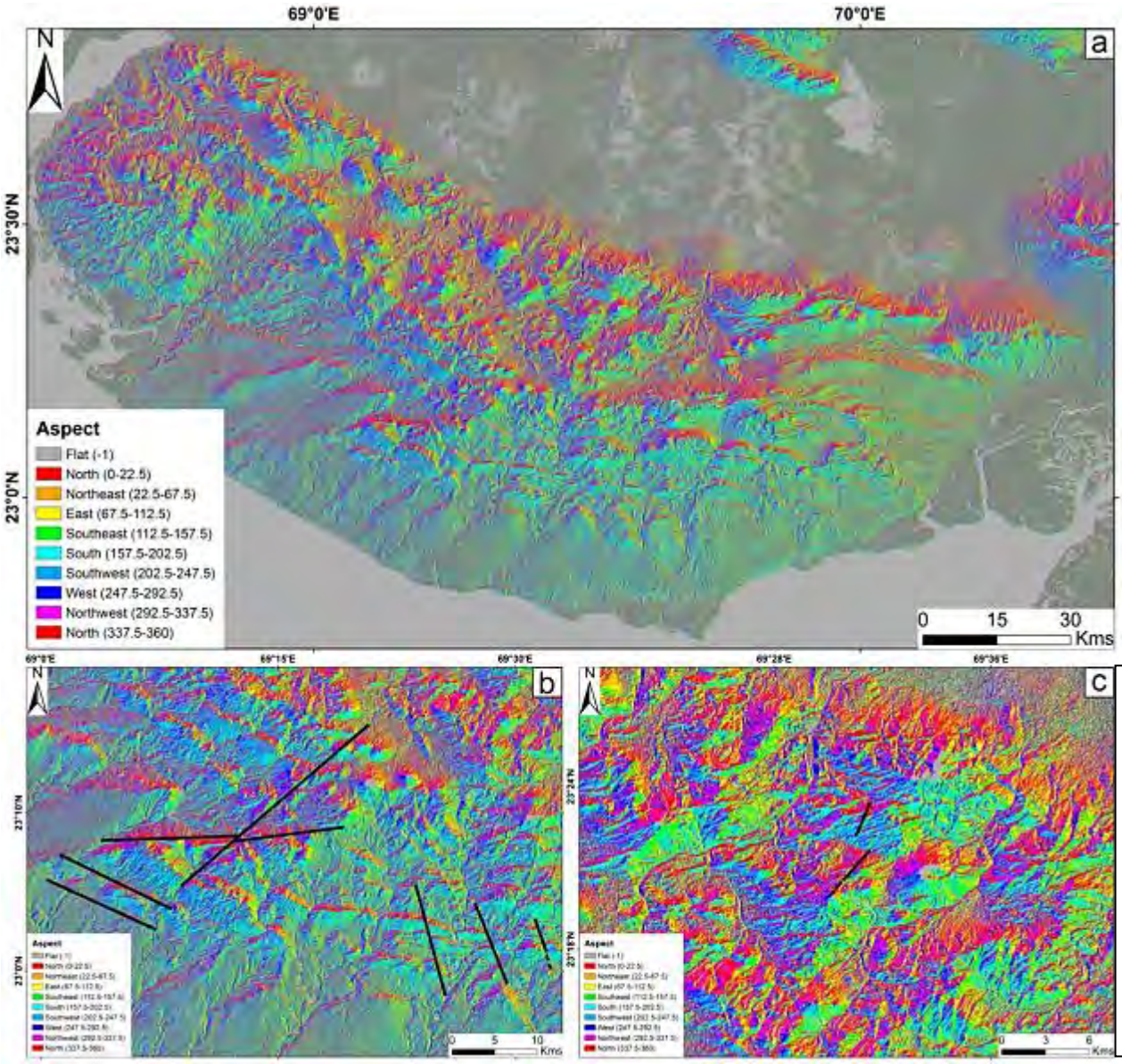

Figure 7.19: (a) Aspect map of the Kutch basin (b) enlarged aspect map of location 'a', 'b' and 'c' which brings out the effect of faults (c) enlarged aspect map of location 'f' showing the effect of fault.

7.8 Inferences

Satellite images study, morphometric analysis and DEM derivatives clearly elicit the presence of active faulting in the study area which is demonstrated through different geomorphic changes. The identified faults in this work are essential for descriptions of the tectonic setup of Kutch region, as deformation in the region plays important role in the overall deformation in western India.

The present study successfully demonstrated that remote sensing technique is a useful tool to map geomorphic features related to or affected by active faults and their further justification is easily proven using morphometric analysis and DEM based hillshade images. The change pattern in the hypsometry, drainage asymmetry and sinuosity is found to associate well with the faults inferred from geomorphic evidences. Thus, a strong control of these faults on the geomorphic diversity and drainage development in their vicinity is inferred.

For evaluating the influence of active tectonics the morphometric analysis is an effective tool. Utilizing the various analysis functions of GIS and remote sensing data (DEM and images) over large areas, geomorphic anomalies related to tectonic activity could be identified. Five morphometric evidences were calculated in this study such as Hypsometric curves, Sinuosity, SL index, Drainage Basin asymmetry and Basin shape index. The values of AF indicate widespread basin asymmetry related to tilt block tectonics. Higher values of Bs, HI and SL were found along the inferred faults. Evaluation of the active tectonics by Landsat imagery and DEM products also compared well with the morphometric analysis. Indeed, those areas indicating tectonic activities, interpreted through morphometric analysis, are steady with the areas having most ridge displacement, drainage offsets triangular facets, fault scarps, shutter ridges and linear valleys.

Chapter 8
Summary and Conclusion

8.1 Introduction

Earthquakes are much unexpected, may be powerful one, devastating and are one of the greatest mysteries of nature. Earthquakes are more frequent in tectonically active belts around the world which may be due to inter or intra plate activities. The plate margins of the world have produced some of most destructive and mightiest earthquakes. One such collisional tectonic zone is the Himalayan mobile belt (a constituent of Alpine-Himalayan belt) which has been generating earthquakes along the Himalayan zone along with different seismically active zones of India since times immemorial. As proposed by many researchers, the northward plunging of the Indian plate into the Eurasian plate is indirectly responsible for the intraplate activity in seismically active zones like Kutch in Gujarat. Since geological time, the Kutch basin has never attained stability and is continuously subjected to many phases of tectonic deformations.

It is now well established that in the field of remote sensing, microwave remote sensing is highly capable of detecting co-seismic and post-seismic surface deformations due to earthquakes. Employing InSAR and PSInSAR techniques surface deformations can be studied precisely with millimetre accuracy. The present research mainly deals with terrain change like ground deformations and ground settlements from SAR interferometry, morphotectonic and morphometric study followed by major and minor tectonic movements related to earthquakes. This study is the systematic effort, using satellite based InSAR, multispectral images, digital elevation models supported by topographical, geological, tectonic and seismic information to observe and interpret surface deformation associated with tectonic processes for the Kutch region (rift basin) India. The work is motivated by the relatively incomplete understanding of the post-seismic ground changes due to the occurrence of large intensity, damaging, earthquake in Bhuj on 26th January 2001 as well as subsequent earthquakes and earlier tectonically affected geological set up. Further the present study intends to provide a better understanding of the earthquake deformation cycle for the unstable continental plate region of Kutch basin.

A long-term time-series analysis technique has been used to improve the measurement of the post-seismic topographical change. As reported by Indian Seismological Research (ISR), Gujarat, the effect of small scale earthquakes distributed in the Kutch basin are some of the least investigated using InSAR and the present study demonstrates the capability of the technique to provide important observations on small-magnitude post-seismic events. PSI study involving almost a dozen of SAR scenes, area with significant land deformations for active Kutch region has been identified.

Morphometric analysis is the quantitative assessment of form features of the earth surface and any landform unit. It can also be defined as the quantitative measurement of landscape shape. Landforms can be characterized in terms of their elevation, size and slope. Morphometric analysis includes quantitative study of the various components such as hypsometric analyses, sinuosity, SL indices, basin shape indices drainage basin asymmetry, etc., which indicates the nature of development of the basin. These are used as parameter of active tectonics (Keller and Pinter, 1996). Quantitative assessment from morphotectonic and morphometric study of features of the Kutch basin shows the small scale change in landscape and activity of different basin associated with the numerous drainage patterns.

8.2 Interpretation from InSAR and PSI study

The multi-year time-series interferograms generated from descending InSAR data pair of the Envisat, ALOS-PALSAR and Sentinel 1-A satellite shown an inter-seismic ground deformation up to ±15-30 mm/yr for the Kutch region in the satellite-to-target line-of-sight direction.

The time series interferogram produced from Envisat and ALOS-PALSAR satellites images for a time period of 2003 to 2010 deciphers a long-term surface deformation processes for the Kutch, India. A specific deformation pattern is detected across the Kutch mainland, Island uplifted area along with the KBF and KMF associated areas to the South of Banni plains in the Central Kutch basin (Figures 5.5, 6.2, 6.3, 6.4, 6.6, 6.10, 6.12 and 6.13).

The interferograms generated for the study area suggest an interesting deformation pattern, where three identified regions indicate positive and negative ground deformations of about -35cm, -35cm and 24cm, respectively (Figure 5.5), which can be substantiated from the report of the Institute of Seismological Research (ISR), Gandhinagar where several seismic events occurred during the year 2007-2010 and the associated ground deformation is revealed

by the observational inference of clustering of interferometric fringes to the east and NE of the study area along with ground deformation (Figure 5.1).

A two phase episodic deformation is marked between the years 2003 to 2005 (right) from Envisat data pairs. The 2003-04 and 2004-05 data pair covering an area East of Bhuj with an almost flat terrain (to the North of Kutch Mainland Fault) suggests a negative deformation of about 8 cm around Kunjisar area along with 25 cm and 5 cm in the other two areas north of Kunjisar at Pachham and Khadir mounds and a positive deformation of 17 cm, 28 cm and 5 cm for the same locations respectively (Figure 6.2). The interferogram derived from 2003-05 pair (right) indicates resultant positive deformation (subsidence) in the mentioned area on ground to the NE, NW and south of Bhuj (Figure 6.3). Further deformation map generated from 2003 and 2005 Envisat data pair (left) deciphers a positive ground deformation up to 17 cm in and around the Bhuj region covering mostly the Mainland region of Kutch basin (Figure 6.4). In a sequel the Envisat data pair 2005-10 (left) and 2005-06 (right) shows a low scale ground deformation in terms of interferometric fringes (Figure 6.6). However comparing the interferometric image from 2003-05 with 2005-10, it can be well observed that the change in the ground topography has been reduced later period in comparison to the earlier which may be referred to the post relaxation phase of ground after the earthquake.

Elevation profiles derived from SRTM (2000) and ALOS PALSAR (2007) DEM for the above locations shown a change in trend and elevation value though such a small change was difficult to notice in the elevation profile. Therefore by employing change detection technique for the Bhuj area between the two DEMs, a relative elevation variation could also be inferred for Bhuj which marks the elevation difference (Figures 6.7, 6.8).

Displacement map generated from Sentinel 1-A data belonging to 2016 November-December shown a small scale ground subsidence up to 18 mm covering the northern part of the Kutch region (Figure 6.10). Again the interferogram generated from 2014-15 and 29 Feb 2016 and 19 November 2016 data pair of Sentinel 1-A image indicates small scale ground deformation up to mm scale around Bhuj, in the upper mainland, along KMF and KBF fault zones and a low rate deformation along the IBF in Khadir mound, laterally the major lineament cross cutting the KMF, east to the Khadir uplift (Figures 6.12 and 13).

The more accurate terrain change study based on the PSI technique inferred a negative ground displacement of 20 to 30 mm/yr in the W and NW of Bhuj city to the east of Mainland, the location south of the KBF region which was observed to be subsiding from InSAR study

also shown a subsidence with rate of 15 to 20 mm per year along the LOS. The extreme NW, NE locations of Bhuj and southern, eastern part of the Anjar city furthermore revealed a subsidence of 10 m and of 25-30 mm per year from the PSI study of the Sentinel images (Figure 6.14).

8.3 Interpretation from Morphometry study

Satellite images, morphometric analysis, DEM and its products, clearly elicit the presence of active faulting in the study area which is demonstrated through different geomorphic changes. The identified faults in this work are essential for descriptions of the tectonic setup of Kutch region, as deformation in the region plays important role in the overall topographical change in western India.

Tectonic features such as dislocation and displacement of mountain ridges, valleys, clearly recognisable lineaments, and drainage offsets have been identified in the Landsat true colour composite image which marks the presence of the faults. Also, the morphometric analysis and shaded relief models (SRMs) created from DEM, further substantiates the presence of faults. The geomorphic evidences of active faults are marked and highlighted in eight boxes denoted as a-h (Figure 7.1 and 7.2).

The main offset is observed to the west along KBF where the sedimentary rocks and intertrappean beds have been first displaced by one major fault striking approximately ENE-WSW, succeeded by another incidence of faulting (roughly NE-SW displacement) which affected both the rock groups and the first fault (Location a). A major offset in drainages is observed and marked to the extreme WWS along KBF, where distinct bending have been observed in three major basin. This observation infers about the presence of two faults striking NW-SE roughly, which resulted in the displacement of these three drainages along this particular direction (Location b). Another series of 3 offsets have been marked to the south of KBF roughly parallel to each other and striking NNW-SSE. The drainage of this area tries to follow the fault morphology (Location c). A displacement of intertrappean beds and some other sedimentary rocks is observed to the south of KBF where the displacement is seen by the eastern block towards north and the western block has moved south. The drainage in this area is also offset along this fault (Location d). A lineament is marked along the KBF having step like fashion (en-echelon) which is displaced along its length in series of intermittent distances. This fault strike roughly NE-SW (Figure 7.8). The fault in the extreme NW can be traced further SW based on the drainage pattern which follows the strike of the fault (Location e).

Two prominent ridge displacements are witnessed at the extreme north of KBF, which concludes the presence of fault. The direction of displacement in both cases is roughly NE-SW and in both cases the eastern block, moved southward. The two inferred faults may be the continuation of a single fault, but due to lack of evidence in between, it is described as two separate faults as it is difficult to comprehend the continuity. Based on drainage offset and a linear ponding along the offset the fault at the lower side can be more clearly inferred (Location f). Further two other sets of ridge displacements are observed at the extreme NW of Kutch basin. The blocks have been displaced along NW-SE, where the north-eastern blocks relocated southerly. In addition to the ridge displacements, the drainage offset can also be concluded to have been modified by the faulting (Location g and h) (Figure 7.9). The faults have been identified and marked on both the Landsat true colour image and Sentinel 1-A power image from which the DEM is also derived to infer the existence of faults on hillshade, slope and aspect maps (Figures 7.16, 7.18, 7.19). Further the faults have been identified and marked for the eight locations on a three dimensional prospective view obtained by draping high resolution Digital globe image over the ALOS PALSAR 12.5m resolution DEM (Figure 7.12 i, ii and iii).

8.4 Evidence from Morphometric analysis

Hypsometric curves have been obtained for the associated drainage basins from SRTM 30m resolution DEM for the eight locations where the faults have been identified. The locations a, b, c, d, g and h are found to be more tectonically active whereas smooth concave curves suggest lesser tectonic activity for location f (Figure 7.13).

The stream length (SL) index found to be highest for location c and lowest for d. The SL indices increase when a channel crosses the hill fronts related to these faults. However, relatively lower SL values are also observed in basins d, g and h. In these basins, the reason for these low SL values can be attributed to the strike slips nature of the above inferred faults even though the underlying rocks are resistant. The sinuosity value clearly indicates the presence of fault at all locations. The location d and f shown highest sinuosity as the channels roughly cross cut the fault and are also shifted during faulting process (Figure 7.16 a and b).

The basin asymmetry factor (AF) shown a proportioned tilting towards east and west controlled by the marked fault at locations a, b, and c. The AF is found to be low for locations d and f, as the drainages are located a bit far from the inferred fault. Basin g and h inferred to have very high AF values, indicating their strong asymmetry towards east and these basins are

located on the north-eastern block of the inferred fault. Estimated AF further substantiates the presence of fault (Figure 7.16 c).

The deciphered Basin shape index (Bs) for locations f, g and h exhibit nearly circular shape basins due to lower tectonic activity which was well correlated with hypsometric analysis and drainage basin asymmetry. These particular basins are less affected by faults while the other basins with higher Bs values represents elongated basin shapes hence showed effect of higher tectonic activity (Figure 7.16 d).

For evaluating the influence of active tectonics, the morphometric analysis is an effective tool. Utilizing the benefit of being calculated from GIS and remote sensing data (DEM and satellite images) over large areas, this can be used as a reconnaissance tool to identify the geomorphic anomalies related to tectonic activity. Five morphometric evidences were calculated in this study such as Hypsometric index, Sinuosity, SL index, Drainage Basin asymmetry and Basin shape index. The values of AF indicate widespread basin asymmetry related to tilt block tectonics. Higher values of Bs, HI and SL were found along the inferred faults. Evaluation of the active tectonics by Landsat images and DEM products also compared well with the morphometric analysis. Indeed, those areas indicating tectonic activities interpreted through morphometric analysis, are steady with the areas having most ridge displacement, drainage offsets, triangular facets, fault scarps, shutter ridges and linear valleys.

8.5 Conclusions

The Kutch region of Gujarat has witnessed prolonged tectonic and seismic activities which were instrumental in modifying the terrain features since ancient time. As the Kutch region is comprised of highly saturated soil and soft rocks the historical as well as very recent deformations caused by mainly earthquakes are very much evident and well recorded. The rate of deformation would naturally be very less when one tries to examine post-seismic deformation after a considerable time lapse and naturally occurring settlement of the ground.

It is always a challenging task to detect such low scale deformation. However, SAR interferometry can provide solution to such endeavour. InSAR is a unique geodetic technique capable of high precision and resolution measurement of surface deformation.

As the radar scenes for Kutch region generated by ALOS-PALSAR, Envisat and Sentinel 1-A were available, deformation studies for the region could be carried out. By

combining ALOS-PALSAR (2007-10), Envisat (2003-10) and Sentinel 1-A (2014-16) the total observation period could become 2003-2016. The Interferograms generated based on the Envisat and Sentinel 1-A data exhibits ground deformations in the area in and around KMF and KHF. These two faults are reported to be of active nature (ISR-2010) and hence, the observed deformations based on this study may be due to the active nature of the faults too. It is important to note that deformation measurement employing ALOS-PALSAR (L band ~23.8cm) and Envisat-Sentinel 1-A (C band ~ 5.6cm) are almost at the same order. Very negligible difference in measurement could be observed. Hence, the technique used for the purpose of deformation measurement is reliable.

The identified ground deformation areas could also be studied with the help of multispectral satellite images independently as well as in combination of DEM. Terrain characteristics are well displayed by the three dimensional perspective visuals created by draping Digital Globe satellite image over the ALOS-PALSAR DEM and radar power images. Multispectral satellite images also provided very clear characteristics of faults affecting the Mesozoic and Tertiary rocks.

The present study successfully demonstrated that remote sensing techniques is a powerful tool to map geomorphic features related to or affected by active faults and their occurrence is further proved using morphometric analysis and DEM interpretation. The change pattern in the hypsometry, drainage asymmetry and sinuosity is found to be well associate with the faults inferred from geomorphic evidences. Thus, a strong control of these faults on the geomorphic diversity and drainage development in their vicinity is inferred. Also it is clear from the present work that the Kutch region of Gujarat is still experiencing ground adjustment. After the occurrence of the 2001 Bhuj main shock and subsequent aftershocks, the region has still not attained complete relaxation of soft uppermost crustal layer preceded by compressional stress.

Observations on surface deformation, made possible by the use of InSAR and PSI techniques accompanied by morphometric study have provided some new insights into terrain change processes in the Kutch rift basin.

8.6 Future scope of work

This research work reports results on InSAR detection of post-seismic ground deformations, multispectral satellite images and radar power images based fault identification and morphometry. However, suitable radar scenes especially interferometric pair was not very

easily available. Naturally, the detection capability can be increased with better resolution radar data set, suitable interferometric pairs and longer coverage. The same is also applicable in case of multispectral satellite images and digital elevation model.

Topographic and geological maps provide basic information about any area. Therefore larger the scale of these maps it is better. Further, the InSAR detected land deformation areas may be visited for detailed field survey to improve the result although very small scale deformation would be very difficult to be noticed on the ground. In addition with the help of structural and geophysical modelling the findings can be corroborated and refined.

Bibliography

1. Anderson, R. C., and Beratan, K. K., 1993, Identification of geomorphic surfaces from Landsat data, Whipple Mountains, South-eastern California, Geological society of America Abstracts with Programs, 25, A-106.
2. Anderson, R. C., and Beratan, K. K., 1994, Identify characteristics of geomorphologic surfaces, Whipple Mountains, South-eastern California, Geological society of America Abstracts with Programs, 26, 34-35.
3. Anhert, F., 1973, COSLOPE 2- A comprehensive model program for simulating slope profile development, Geocommunication Programs, 8, 99-119, London.
4. Avena, G. C., Giuliano, G. and Lupia Palmieri, E., 1967, On the quantitative assessment of hierarchy and evolution of river networks, Bulletin of the Italian Geological Society, 86, 781 -796.
5. Avouac, J. P. and Peltzer, G., 1993, Active tectonics and southern Xinjiang, China: analysis of terrace riser and normal fault scarp degradation along the Hotan-Qira fault system, Journal of Geophysical Research, 98, 21773-21807.
6. Baghadi, N. and Zribi, M., 2016, Microwave Remote Sensing of Land Surfaces, Elsevier, France, 448.
7. Bamler, R. and Hartl, P., 1998, Synthetic aperture radar interferometry, Inverse Problems, 14, R1-R54.
8. Baral, S. S., Das, J., Saraf, A. K., Borgohain, S. and Singh, G., 2016, Comparison of Cartosat, ASTER and SRTM DEMs of Different Terrains, Asian Journal of Geoinformatics, 16 (1), 1-7.
9. Baral, S. S., Sharma, K., Saraf, A. K., Das, J., Singh, G., Borogohain, S. and Kar, E., 2016, Thermal anomaly from NOAA for Nepal Earthquake, Current Science, 110, 02: 150-153.
10. Bayuaji, L., Sumantyo, J.T.S. and Kuze, H., 2010, ALOS PALSAR DInSAR For land subsidence mapping in Jakarta, Indonesia, Canadian Journal of Remote Sensing, 36(1),1-8.
11. Beanland, S. and Clark, M.M., 1994, The Owens Valley fault zone, eastern California, and surface faulting associated with the1872 earthquake. U.S., Geological Survey Bulletin, 1982, 29.

12. Belisario, F., Del Monte, M., Fredi, P., Funiciello, R., Lupia Palmieri, E. and Salvini, F., 1999, Azimuthal analysis of stream orientations to define regional tectonic lines, Zeitschrift für Geomorphologie N. F., Supplement-Band, 118, 41-63.
13. Bhatt, C. M., Chopra, R. and Sharma, P. K., 2007, Morphotectonic analysis in Anandpur Sahib area, Punjab (India) using remote sensing and GIS approach, Journal of Indian Society of Remote Sensing, 35 (2), 129-139.
14. Bilham, R., 1998, Slip parameters for the Rann of Kachchh, India, 16 June 1819, earthquake, quantified from contemporary accounts. In: I.S. Stewart and C. Vita-Finzi (Eds) Coastal Tectonics, Geological Society London Special Publications, London, UK, 146, 295-319.
15. BIS (Bureau of Indian standards) 2002, Criteria for Earthquake Resistant Design of Structures: IS: 1893 (Part 1) General provisions and Buildings, BIS, New Delhi, 39. Available online at: http://www.bis.org.in/other/quake.htm.
16. Biswas, S. K. and Deshpande, S. V., 1970, Geological and tectonic maps of Kutch, In: Bulletin of Oil and Natural gas Commission, 7, 115-116.
17. Biswas, S. K., 1971, Note on the geology of Kutch, Quaternary Journal of Geology, Mineral, Metal Society, India, 43, 223-236.
18. Biswas, S. K., 1980, Structure of Kutch-Kathiawar region, Western India Proceeding 3rd Indian Geological Congress, Pune, 255-272.
19. Biswas, S. K., 1982, Rift basins in the western margin of India and their hydrocarbon prospects with special reference to Kutch basin, American Association of Petroleum Geologists, Bulletin, 66, 1497-1513.
20. Biswas, S. K., 1987, Regional tectonic framework, structure, and evolution of the western marginal basins of India, Tectonophysics, 135, 307-327.
21. Biswas, S. K., 2005, A review of structure and tectonics of Kutch basin, western India, with special reference to earthquakes, Current Science, 88 (10), 1592-1600.
22. Biswas, S. K., 2016, Tectonic framework, structure and tectonic evolution of Kutch basin, Western India, Special publication of the Geological Society of India, 6, 129-150.
23. Bocco, G., Mendoza, M. and Velazquez, A., 2001, Remote sensing and GIS based regional geomorphological mapping-a tool for land use planning in developing countries, Geomorphology, 39, 211-219.
24. Bodin, P. and Horton, S., 2004, Source parameters and Tectonic Implications of Aftershocks of the Mw 7.6 Bhuj Earthquake of 26 January 2001, Bulletin of the Seismological Society of America, 94, 818-827.

25. Brookfield, M. E., 1998, The evolution of the great river systems of Southern Asia during the Cenozoic India- Asia Collision Rivers draining southwards, Geomorphology, 22, 285-312.
26. Bull, W. B. and McFadden, L. D., 1977, Tectonic geomorphology north and south of the Garlock fault, California D.O. Doehring (Ed.), Geomorphology in Arid Regions, Proceedings of the Eighth Annual Geomorphology Symposium, State University of New York, Binghamton, 115-138.
27. Buonasorte, G., Ciccacci S., De Rita, D., Fredi P. and Lupia Palmieri, E., 1991, Some relations between morphological characteristics and geological structure in the Vulsini Volcani Complex (North Latium, Italy), Zeitschrift für Geomorphologie N. F, Supplement-Band, 82, 59-71.
28. Burbank, D. W. and Anderson, R. S., 2001, Tectonic Geomorphology, Blackwell Science, Cambridge, 274.
29. Burbank, D. W. and Pinter, N., 1999, Landscape evolution: The interaction between tectonics and surface processes, Basin Research, 11(1), 1-6.
30. Burrough, P. A., 1986, Principles of Geographical Information Systems for Land Resources Assessment (Oxford: Oxford University Press), 193.
31. Canuti, P., Casagli, N., Ermini, L., Fanti, R. and Farina, P., 2004, Landslide activity as a geoindicator in Italy: significance and new perspectives from remote sensing, Environmental Geology, 45, 907-919.
32. Cartier, K., Alt, D., 1982, The bewildering Bitterroot, the river that won't behave, Montana Magazine, 12, 52-53.
33. Centamore, E., Ciccacci S., Del Monte M., Fredi P., and Lupia Palmieri, E., 1996, Morphological and morphometric approach to the study of the structural arrangement of North-Eastern Arbuzzo (Central Italy), Geomorphology, 16, 127-137.
34. Chandrasekhar, D. V., Mishra, D. C., Singh, B., Vijayakumar, V. and Burgmann, R., 2004, Source parameters of the Bhuj earthquake, India of January 26, 2001 from height and gravity changes, Geophysical Research Letters, 31, L19608, doi:10.1029/2004GL020768, 1-4.
35. Chaudhary, B. S. and Aggarwal, S., 2009, Demarcation of paleochannels and integrated ground water resources mapping in parts of Hisar district, Haryana, Journal of Indian Society of Remote Sensing, 37, 251-260.

36. Chaudhary, B. S. and Toleti, B. V. M. Rao, 2006, Hydrogeomorphological Mapping and Delineation of Ground Water Potential Zones Using Satellite Data in Sonipat District, Haryana, Annals of Agri-Bio Research, 11(1), 7-14.
37. Chaudhary, B. S., Kumar, M., Roy, A. K. and Ruhal, D. S., 1996, Applications of remote sensing and geographical information system in ground water investigations in Sohna Block, Gurgaon District, Haryana, India, *Archives of International Society Photogrammetry and Remote Sensing,* 34(B-6), 18-23.
38. Chediya, O. K., 1986, Morphostructures and neo-tectonics of the Tien Shan, Frunze, Academia Nauk Kyrgyz CCP, 313.
39. Chen, Y. C., Sung, Q. C. and Cheng, K. Y., 2003, Along-strike variations of morphotectonic features in the western foothills of Taiwan: tectonic implications based on stream gradient and hypsometric analysis, Geomorphology, 56, 109-137.
40. Chorowicz, J., Dhonte, D. and Gundogdu, N., 1999, Neotectonics in the eastern North Anatolian Fault region (Turkey) advocates crustal extension: mapping from SAR ERS imagery and Digital Elevation Model, Journal of Structural Geology, 21, 511-532.
41. Chrowicz, J., Breard, J., Guillande, R., Moraase, C., Prudon, D. and Rudant, J., 1991, Dip and strike measured systematically on digitized three dimensional geological map, Photogrammetric Engineering and Remote Sensing, 57, 431-436.
42. Chung, W. Y. and Gao, H., 1995, Source parameters of the Anjar earthquake of July 21, 1956, India, and its seismotectonic implications for the Kutch rift basin, Tectonophysics, 242, 281-292.
43. Ciccacci S., Fredi, P., Lupia Palmieri, E. and Salvini, F., 1986, An approach to the quantitative analysis of the relationship between drainage pattern and fracture trend, International Geomorphology, 2, 49-68.
44. Colesanti, C., Ferretti, A., Novali, F., Prati, C., and Rocca, F., 2003a, SAR monitoring of progressive and seasonal ground deformation using the permanent scatterers technique, IEEE Transactions on Geoscience and Remote Sensing, 41, 1685-1701.
45. Cotilla, M. O. and Cordoba, D., 2004, Morphotectonics of the Iberian Peninsula, Pure and Applied Geophysics, 161, 755-815.
46. Cotilla, M. O., Cordoba, D. and Calzadilla M., 2007, Morphotectonic Study of Hispaniola, Geotectonics, 41 (5), 368-391.
47. Cox, R.T., 1994, Analysis of drainage-basin symmetry as a rapid technique to identify areas of possible Quaternary tilt-block tectonics: an example from the Mississippi Embayment, Geological Society of America Bulletin, 106, 571-581.

48. Cracknell, A. P. and Hayes, L., 1991, Introduction to Remote Sensing, Taylor & Francis, London, 304.
49. Cracknell, A. P., 1997, Advanced Very High Resolution Radiometer AVHRR, Taylor & Francis Books Ltd., London, 968.
50. Cracknell, A. P., 1998, Synergy in remote sensing – what's in a pixel? International Journal of Remote Sensing, 19(11), 2025-2047.
51. Cuong, N. Q. and Zuchiewicz, W. A., 2001, Morphotectonic properties of the Lo River fault near Tam Dao in North Vietnam, Journal of Natural Hazards and Earth System Sciences, 1, 15-22.
52. Curlander, J. and McDonough, R. N., 1991, Synthetic aperture radar : systems and signal processing, Wiley, New York.
53. Currado, C. and Fredi, P., 2000, Morphometric parameters of drainage basins and morphotectonic setting of eastern Abruzzo, Memorie della Societa Geologica ltaliana, 55, 411-419.
54. Dalati, M., 1994, Application of Remote Sensing for Tectonic purposes in EI-Rouge Depression, North West of the Syrian Arab Republic. Proceedings of the International Symposium on Spectral Sensing Research, ISSSR, II, 859-867, San Diego, California, USA.
55. Dasgupta, S., Pande, P., Ganguly, D., Iqbal, Z, Sanyal, K, Venkatraman, N.V., Dasgupta, S., Sural, B., Harendranath, L., Mazumdar, K., Sanyal, S., Roy, K., Das, L.K., Misra, P.S. and Gupta, H., 2000, Seismotectonic Atlas of India and its Environs, Geological Survey of India.
56. Delcaillau, B., 2004, Reliefs et Tectonique recente, In: Veubert (Ed.), 262.
57. Delcaillau, B., Deffontaines, B., Angelier, J., Deramond, J., Floissac, l., Souquet, P. and Chu, H. T., 1998, Morphotectonic evidence from lateral propagation of an active frontal fold: the Pakuashan anticline, foothills of Taiwan, Geomorphology, 24, 263-290.
58. Devi, R. K. M. and Singh, T., 2006, Morphotectonic setting of Ganga Lake, Itanagar Capital Complex, Arunachal Himalaya, Geomorphology, 76, 1-11.
59. Drury, S. A., 1998, Images of the Earth: A Guide to Remote Sensing, second Edition, Oxford Science Publications, New York, 203.
60. Dumont, J. F., Santana, E., Vilema, W., Pedoja, K., Ordonez, M., Cruz, M., Jemenez, N. and Zambrano, I., 2005, Morphological and microtectonic analysis of Quaternary deformation from Puna and Santa Clara Island, Gulf of Guayaquil, Ecuador (South America), Tectonophysics, 339, 331-350.

61. EERI (2016), EERI Earthquake Reconnaissance Team Report: M7.8 Gorkha, Nepal Earthquake on April 25, 2015 and its Aftershocks, Available online at: http://www.eeri.org.
62. Elachi, C., 1988, Spaceborne radar remote sensing: applications and techniques, The Institute of Electrical and Electronics Engineers, Inc., New York.
63. ESA Sentinel Online, 2015, Sentinel-1 SAR Technical Guide, Available online at: https://sentinel.esa.int/web/sentinel/technical-guides/sentinel-1-sar.
64. Evans, I. S., 1972, General geomorphometry, derivative of altitude and descriptive statistics, In Spatial Analysis in Geomorphology, edited by R. J. Chorley (London: Methuen), 17-90.
65. Fairbridge, R.W., 1968, The Encyclopedia of Geomorphology: Encyclopedia of Earth Science Series, Reinhold Book Corporation, New York, Amsterdam, London, 1295.
66. Ferretti, A., Fumagalli, A., Novali, F., Prati, C., Rocca, F. and Rucci, A., 2011, A New Algorithm for Processing Interferometric Data-Stacks: SqueeSAR, IEEE Transactions on Geoscience and Remote Sensing, 49(9), 3460-3470.
67. Ferretti, A., Prati, C. and Rocca, F., 2000, Nonlinear subsidence rate estimation using permanent scatterers in differential SAR interferometry., IEEE Transactions on Geoscience and Remote Sensing, IEEE Transactions on Geoscience and Remote Sensing, 38, 2202-2212.
68. Ferretti, A., Prati, C. and Rocca, F., 2001, Permanent Scatterers in SAR Interferometry, IEEE T Transactions on Geoscience and Remote Sensing, 39, 8-20.
69. Fletcher, K., 2007, InSAR Principles: Guidelines for SAR Interferometry Processing and Interpretation, European Space Agency (ESA) Publications, TM-19.
70. Florinsky, I. V., 1998, Combined analysis of digital terrain models and remotely sensed data in landscape investigations, Progress in Physical Geography, 22 (1), 33-6
71. Frisch, W., 1997, Tectonic Geomorphology. In proceeding of the Fourth International Conference on Geomorphology, Zeitschrift für Geomorphologie N. F., Supplementary Band, 118.
72. Gabriel, A. K. and Goldstein, R. M., 1988, Crossed orbit interferometry: theory and experimental results from SIR-B, International Journal of Remote Sensing, 9(5), 857-872.
73. Garcia-Melendez, E., Goy, J. L. and Zazo, C., 2003, Neotectonic and Plio-Quaternary landscape development within the easten Huercal-Overa basin (Betic Cordilleras Southeast Spain), Geomorphology, 50, 111-133.

74. Ge, L., Zhang, K. A., Dong, Y., Chang, H. C. and Rizos, C., 2008, Preliminary results of satellite radar differential interferometry for the co-seismic deformation of the 12 May 2008 Ms8.0 Wenchuan earthquake, International Association of Chinese Professionals in Geographic Information Science, 14, 12-19.
75. Gens, R. and van Genderen, J. L., 1996, SAR Interferometry - Issues, Techniques, Applications, International Journal of Remote Sensing, 17 (10), 1803-1835.
76. Gillespie, A. R., Kahle, A. B. and Polluconi, F. D., 1984, Mapping alluvial fans in Death Valley, California using multi-channel thermal infra-red image, Geophysical Research Letters, 11, 1153-1156.
77. Goldsworthy, M. and Jackson, J., 2000, Active normal fault evolution in Greece revealed by geomorphology and drainage patterns, Journal of the Geological Society, London, 157, 967-981.
78. Gomez, B. and Marron, D.C., 1991, Neotectonic effects on sinuosity and channel migration, Belle Fouche River, western South Dakota, Earth Surface Processes and Landforms, 16, 227- 235.
79. Graham, L., 1974, Synthetic Interferometer Radar for Topographic Mapping, Proceedings of the IEEE, 62 (6), 763-768.
80. Grandin, R., 2015, Interferometric processing of SLC Sentinel-1 TOPS data. Proceedings of ESA Fringe 2015 workshop, 1-14.
81. GSI 2001, Geology and mineral resources of Gujarat, Daman & Diu, Geological Survey of India Miscellaneous Publication No. 30, Part XIV, 102.
82. GSI 2003, Kutch (Bhuj) Earthquake. Geological Survey of India, Special Publication No. 76, 241.
83. GSI 2015, First Incidence Report of Geological Survey of India on the Major Nepal Earthquake, 2015, Available online at: http://www.portal.gsi.gov.in/gsiDoc/pub/nepal-earthquake-apr-2015.pdf.
84. Gupta, A., 2000, Information Technology and Natural Disaster Management in India, Available online at: http://www.gisdevelopment.net/aars/acrs/2000/ts8/hami0001pf.htm.
85. Gupta, R. P., 2003, Remote Sensing Geology, Second edition, Springer Publications, 656.
86. Gupta, S. and Ellis, M., 2004, Does the topography of actively ground folds mimic fold structures? The case of the Mohand Anticline, Frontal Himalaya, Geophysical Union, Annual meeting, April 2004.
87. Hack, J.T., 1973, Stream-profiles analysis and stream-gradient index, Journal of Research of the U.S. Geological Survey, 1, 421-429.

88. Hamdouni, E., Irigaray, C., Fernandez, T., Chacón, J. and Keller, E.A., 2008, Assessment of relative active tectonics, southwest border of Sierra Nevada (Southern Spain), Geomorphology, 96, 150-173.
89. Hanssen, R. F., 2001, Radar Interferometry: Data interpretation and error analysis, Kluwer Academic Publishers, Dordrecht, 308.
90. Hantke, R. and Scheidegger, A. E., 1998, Morphotectonics of the Massacre Island, Annali di Geofisica, 41 (2), 165-181.
91. Hare, P.W. and Gardner, T.W., 1985, Geomorphic indicators of vertical neotectonism along converging plate margins, Nicoya Peninsula, Costa Rica, in Morisawa, M., and Hack, J. T., eds., Tectonic geomorphology: Proceedings of the 15th Geomorphology Symposia Series, Binghamton, 76-104.
92. Harlin, J.M., 1978, Statistical moments of the hypsometric curve and its density function, Mathematical Geology, 10, 59-72.
93. Hayakawa M., Molchanov, O. A., Kodama, O. A., Tanaka, T. and Igarashi, T., 2000, On a possibility to monitor seismic activity using satellites, Advances in Space Research, 26(6), 993-996.
94. Higgitt, D. L. and Warburton, J., 1999, Applications of differential GPS in upland fluvial geomorphology, Geomorphology, 29, 121-134.
95. Hilley, G. E., Bu¨rgmann, R., Ferretti, A., Novali, F. and Rocca, F., 2004, Dynamics of slow-moving landslides from permanent scatterer analysis, Science, 304, 1952-1955.
96. Hobbs, W. H., 1912, earth Features and their Meaning. McMillan Co., New York, 506.
97. Hong, Y., Adler, R. and Huffman, G., 2007, Use of satellite remote sensing data in the mapping of global landslide susceptibility, Natural Hazards, 43, 23-44.
98. Hooke, J. M., 1995, River channel adjustment to meander cut-offs on the River Bollin and River Dane, NW England, Geomorphology, 14, 235-253.
99. Humphrey, N. F., and Heller, P. L., 1995, Natural oscillations in coupled geomorphic systems: An alternative origin for cyclic sedimentation, Geology, 23, 499-502.
100. Husson, L. and Mugnier, J. L., 2003, Three Dimensional horizon reconstruction from outcrop structural data, restoration and strain field of the Baisahi anticline, western Nepal, Journal of Structural Geology, 25(1), 79-90.
101. ISR (Institute of Seismological Research) 2007-2008, 2008-2009, 2009-2010 Annual Report, Government of Gujarat, India : http://www.isr.gujarat.gov.in/.
102. Iyengar, R. N. and Raghu Kanth, S. T. G., 2002, Strong ground motion at Bhuj city during the Kutch earthquake, Current Science, 82, 1366-1372.

103. Jackson, J. and Leeder, M., 1994, Drainage system and the development of normal faults-An example from Pleasant Valley, Nevada, Journal of Structural Geology, 16 (8), 1041-1059.
104. Jacobs, A., Sandwell, D., Fialko, Y. and Sichoix, L., 2002, The 1999 (Mw 7.1) Hector Mine, California, earthquake: near-field post seismic deformation from ERS interferometry, Bulletin of the Seismological Society of America, 92, 1433-1442.
105. Jain, M., Woodcock, N. H. and Tandon, S. K., 1998, Neotectonics of Western India: evidence from deformed Quaternary fluvial sequences, Mahi River, Gujarat, Journal of the Geological Society, 155, 897-901.
106. Jain, S., and Verma, P. K., 2006, Mapping of active tectonics intensity zones using remote sensing and GIS, Journal of Indian Society of Remote Sensing, 34, 131-142.
107. Jasrotia, A. S., Kumar, A. and Bhat, A., 2012, Morphometric analysis and hydrogeomorphology for delineating groundwater potential zones of Western Doon Valley, Uttarakhand, International Journal of Geomatics and Geosciences, 2(4), 1078-1096.
108. Jasrotia, A. S., Kumar, R. and Saraf, A.K., 2007, Delineation of groundwater recharge sites using integrated remote sensing and GIS in Jammu district, India. International Journal of Remote Sensing, 28 (22), 5019-5036.
109. Jasrotia, A.S., 2007, Landslide Hazard Zonation along the NH-IA between Udhampur to Kud using remote sensing and GIS techniques, Natural Hazard, Special Vol. of Indian Geological Congress, 129-144.
110. Jordan, G., Meijninger, B. M. L., van Hinsbergen, D. J. J., Meulenkamp, J. E. and van Dijk, P. M., 2005, Extraction of morphotectonic features from DEMs: Development and applications for study areas in Hungary and NW Greece, International Journal of Applied Earth Observation and GeoInformation, 7. 163-182.
111. Kahle, A. B., Shumate, M. S. and Nash, D. B., 1984, Active airborne infrared laser system for identification of surface rocks and minerals, Geophysical Research Letters, 11, 1149-1152.
112. Karanth, R. V., Sohoni, P. S., Mathew, G. and Khadikar, A. S., 2001, Geological observations of the 26 January, 2001, Bhuj earthquake, Journal of Geological Society of India, 58, 193-202.
113. Kaya, G.T., 2013, A hybrid model for classification of remote sensing images with linear SVM and support vector selection and adaptation, Selected Topics in Applied Earth Observations and Remote Sensing, IEEE Journal, 6 (4), 1988-1997.

114. Kayal, J. R., De, R., Ram, S., Srirama, B. V. and Gaonkar, S. G., 2002, Aftershocks of the 26 January, 2001 Bhuj earthquake in western India and its seismotectonic implications, Journal of Geological Society of India, 59, 395-417.
115. Keller, E. A., Rockwell, T. K., Clark, M. N., Dembroff, G. R. and Johnson, D. L., 1982, Tectonic geomorphology of Ventura, Ojai, santa Paula areas, western Transverse Ranges, California. In: Cooper, J. D. (Ed.), Neotectonics in Southern California: Geologic Society of America Cordilleran Section Field Guidebook, 25-42.
116. Keller, E., 1986, Investigation of active tectonics: use of surfacial earth processes. In: Wallace, R. E. (eds). Active tectonics studies in geophysics, National Academy Press, Washington, D. C. 136-147.
117. Keller, E.A. and Pinter, N., 1996, Active tectonics: Earthquakes Uplift and Landscapes, Prentice Hall, New Jersey.
118. Keller, E.A. and Pinter, N., 2002, Active tectonics: Earthquakes Uplift and Landscapes, Second edition, Prentice Hall, New Jersey, 362.
119. Kimura, K., 2004, Comparative morphotectonics in the Himalayan foreland and the forearc of Southwest Japan, Himalayan Journal of Sciences, 2 (4) (special issue).
120. Kobor, J. S. and Roering, J. J., 2004, Systematic variation of bedrock channels gradient in the central Oregon Coast Range: implication for rock uplift and shallow landslideing, Geomorphology, 62, 239-256.
121. Kocak, G., Buyuksalih, G. and Oruc M., 2005, Accuracy assessment of interferometric digital elevation models derived from the shuttle radar topography mission X- Band and C-Band data in a test area with rolling topography and moderate forest cover, Optical Engineering, 44(3), 036201.
122. Koike, K.., Nagano, S. and Kawaba, K., 1998, Construction and analysis of interpreted fracture plain through combination of satellite image derived lineaments and digital elevation model data, Computer Geosciences, 24, 573-583.
123. Krishna, A. P. and Rai, L. K., 1996, GIS and remote sensing for natural resources management at watershed level in the mountain environment: a conceptual approach, Asian-Pacific Remote Sensing and GIS Journal, UN-ESCAP, Thailand, 9(1), 93-99.
124. Krishna, A. P., 1996, Land Cover Change Dynamics of a Himalayan Watershed Utilizing Indian Remote Sensing Satellite (IRS) Data, 0-7803-3068-4/96 IEEE, 221-223.

125. Krishna, A. P., 2005, Snow and glacier cover assessment in the high mountains of Sikkim Himalaya, Hydrological Processes, John Wiley & Sons Ltd Country of publication, Great Britain, ISSN0885-6087, 19 (12), 2375-2384.
126. Le Turdu, C., Coussement, C., Tiercelin, J. J., Renaut, R. W., Rolet, J., Richert, J. P., Xavier, J. P. and Coqulet, D., 1995, Rift basin structure and depositional patterns interpreted using 3-D remote sensing approach: The Barongo and Bogoria basins, Central Kenya rift, East Africa, Bulletin Centres Re'cherches, 19, 1-37.
127. Leopold, L. B., Wolman, M. G. and Miller, J. P., 1964, Fluvial processes in geomorphology, San Francisco, W. H. Freeman and Co., 522.
128. Li, F. and Goldstein, R., 1990, Studies of Multibaseline Spaceborne Interferometric Synthetic Aperture Radars, IEEE Transactions on Geoscience and Remote Sensing, 28(1), 88-97.
129. Lifton, N. A. and Chase, C. G., 1992, Tectonic, climatic and lithologic influences on landscape fractal dimension and hypsometry: implication for landscape evolution in the San Gabriel Mountains, California, Geomorphology, 5, 77-114.
130. Lillesand, T. and Kiefer, R. W., 2000, Remote Sensing and Image Interpretation, 4th Edition, John Wiley, New York, 736.
131. Lupia Palmieri, E., Biasini, A., Caputo, C., Centamore, E., Ciccacci S., Del Monte M., Fredi P. and Pugliese, F., 2001, Quantitative geomorphology and morphodynamics of Abruzzo. III. II catchment area of the Saline River, Physical Geography and Quaternary Dynamics, 24, 157-176.
132. Lupia Palmieri, E., Centamore, E. Ciccacci S., D 'Alessandro L., Del Monte M., Fredi P. and Pugliese, F., 1998, Quantitative geomorphology and morphodynamics of Abruzzo. III. II Tordino River catchment, Physical Geography mica Dina, 21, 113-129.
133. Lupia Palmieri, E., Ciccacci S., Civitelli, G., Corda, L., D 'Alessandro L., Del Monte M., Fredi P. and Pugliese, F., 1995, Quantitative geomorphology and morphodynamics of Abruzzo. I. II River basin Sinello, Physical Geography and Quaternary Dynamics, 18, 31-46.
134. Lyons, S. and Sandwell, D., 2003, Fault creep along the southern San Andreas from interferometric synthetic aperture radar, permanent scatterers, and stack- ing, Journal of Geophysics Research, 108.
135. Madsen, S., Zebker, H. and Martin, J., 1993, Topographic Mapping Using Radar Interferometry: Processing Techniques, IEEE Transactions on Geoscience and Remote Sensing, 31(1), 246-256.

136. Mahmood, S. A. and Gloaguen, R., 2012, Appraisal of active tectonics in Hindu Kush: insights from DEM derived geomorphic indices and drainage analysis, Geoscience Frontiers, 3 (4), 407-428.
137. Maiti, S. and Bhattacharya, A. K., 2011, A three-unit-based approach in coastal-change studies using Landsat images, International Journal of Remote Sensing, 32, 209-229.
138. Maiti, S. and Bhattacharya, A., 2009, Shoreline change analysis and its application to prediction: a remote sensing and statistics based approach, Marine Geology, 257, 11-23.
139. Maiti, S., 2013, Interpretation of coastal morphodynamics of Subarnarekha estuary using integrated cartographic and field techniques, Current Science, 104(12), 1709-1713.
140. Malik, J. N., Sohoni, P. S., Karanth, R. V. and Merh, S. S., 1999, Modern and historic seismicity of Kachchh Peninsula, Western India, Journal of Geological Society of India, 54, 545-550.
141. Mandal, P., Rastogi, B. K., Satyanarayana, H. V. S., Kousalya, M., Vijayraghavan R., Satyamurty, C., Raju, I. P., Sarma, A. N. S. and Kumar, N., 2004, Characterization of the causative fault system for the 2001 Bhuj earthquake of Mw 7.7, Tectonophysics , 378, 105-121.
142. Mansor, S., Cracknell, A. P., Shilin, B. V. and Gornyi, V. I., 1994, Monitoring of underground coal fires using thermal infrared data, International Journal of Remote Sensing, 15(8), 1675-1685.
143. Mansor, S., Pradhan, B., Daud, M., Khuzaimah, Z. and Lee, S., 2007, Utilization of optical Remote sensing data and GIS tools for regional landslide hazard analysis in Malaysia, Journal of Institution of Surveyors Malaysia (Peer Reviewed Journal), 51, 50-55.
144. Mantovani, F., Soeters, R. and Van Westen, C. J., 1996, Remote sensing techniques for landslide studies and hazard zonation in Europe, Geomorphology, 15, 213–225.
145. Mark, D. M., 1975, Geomorphometric parameters- a review and evaluation, Geografiska Annaler, 57A, 165-77.
146. Marple, R. T. and Talwani, P., 1993, Evidence of possible tectonic upwarping along the South Carolina coastal plain from an examination of river morphology and elevation data, Geology, 21, 651-654.
147. Marshall, J. S. and Anderson, R. S., 1995, Quaternary uplift and seismic cycle deformation, Peninsula de Nicoya, Costa Rica, Geological Society of America, 107, 463-473.

148. Martha, T., Kerle, N., van Westen, C. J. and Kumar, K., 2010, Characterizing spectral, spatial and morphometric properties of landslides for semi-automatic detection using object-oriented methods, Geomorphology, 116, 24-36.
149. Massonnet, D. and Fiegl, K. L., 1998, Radar interferometry and its application to changes in the earth's surface, Reviews of Geophysics, 36 (4), 441-500.
150. Massonnet, D., Feigl, K., Rossi, M. and Adragna, F., 1994, Radar interferometric mapping of deformation in the year after the Landers earthquake, Nature, 369, 227-230.
151. Mayer, L., 1990, Introduction to Quantitave Geomorphology, Prentice Hall, Englewood Cliffs, New Jersey, 380.
152. McCalpin, J. P. and Thakkar, M. G., 2003, 2001 Bhuj-Kuchchh earthquake: surface faulting and its relation with neotectonics and regional structures, Gujarat, Western India, Annals of Geophysics, 46, 937-956.
153. McFadden, L. D., Tinsley, J. C., and Bull, W. B., 1982, Late quaternary pedogenesis and alluvial chronologies of the Los Angeles basin and St. Gabriel mountain areas, southern California in Tinsley, J. C., and McFadden, L. D., eds., Late quaternary pedogenesis and alluvial chronologies of the Los Angeles basin and St. Gabriel mountain areas, southern California, and Holocene faulting and alluvial stratigraphy within the Cucamonga fault zone, Field Trip 12, Cordilleron Section of the Geological Society of America, 1-13.
154. Medwedeff, D. A., 1992, Geometry and Kinematics of an Active, Laterally Propagating Wedge Thrust, Wheeler Ridge, California. In: Mitra, S., Fisher, G. W., (Eds.) Structural Geology of Fold and Thrust Belts, John Hopkins Studies in Earth and Space Sciences, 5, 1-28.
155. Merh, S. S., 1995, Geology of Gujarat, Geological Society of India, 222.
156. Merritts, D. J. and Vincet, K. R., 1989, Geomorphic responses of coastal streams to low, intermediate, high rates of uplift, Mendocino Triple Junction region, Northern California, Geological Society of America, 110, 1373-1388.
157. Merritts, D. J., Vincet, K. R. and Wohl, E. E., 1994, Long River profiles, tectonism and eustasy: a guide to interpreting fluvial terraces, Journal of Geophysical Research, 99 (B7), 14031-14050.
158. Miliaresis, G. C. and Paraschou, C. V. E., 2005, Vertical accuracy of the SRTM DTED level 1 of Crete, International Journal of Applied Earth Observation and Geoinformation, 7(1), 49-59.
159. Molnar, P., Brown, E. T., Burchfiel, B. C., Deng, Q., Feng, X., Li, J., Raisbeck, G. M., Shi, J., Wu, Z., Yiou, F. and You, H., 1994, Quaternary climate change and the formation

of river terrace across growing anticlines on the north flank of the Tien Shan China, Journal of Geology, 102, 583-602.

160. Morino, M., Malik, J. N., Mishra, P., Bhuiyan, C. and Kaneko, F., 2008, Active fault traces along Bhuj Fault and Katrol Hill Fault, and trenching survey at Wandhay, Kachchh, Gujarat , India, Journal of Earth System Science, 117 (3), 181-188.
161. Mueller, K. and Talling, P., 1997, Geomorphic evidence for tear faults accommodating lateral propagation of an active fault bend fold, Wheeler Ridge, California, Journal of Structural Geology, 19 (3-4), 397-411.
162. Mukherji, A. D. and Iyer, S. D., 1999, Synthesis of morphotectonics and volcanics of the central Indian Ocean Basin, Indian Journal of Marine Sciences, 19, 13-16.
163. Muller, J. E., 1968, An introduction to the hydraulic and topographic sinuosity indexes, Annual Association of American Geographers, 58, 371-385.
164. Murthy C. V. R., 2004, Learning earthquake design and construction, IIT Kanpur-BMTPC.
165. Oilier, C. D., 1981, Tectonics and landforms, Longman Group Limited, Harlow, England, 324.
166. Okeke, F. I., 2006, InSAR Operational and Processing Steps for DEM Generation, in Promoting Land Administration and Good Governance, 5th FIG Regional Conference, Accra, Ghana, March 8-11, 2006, 1-13.
167. Oldham, R. D., 1926, The Kutch earthquake of 16th June 1891 with a revision of the great earthquake of 12th June 1897, Member of Geological Survey of India, 46, 71-74.
168. Onorati, G., Poscolieri, M., Ventura R., Chiarini, V. and Crucilla, A., 1992, A digital elevation model of Italy for geomorphology and structural geology. Catena, 19, 147-178.
169. Ouchi, S., 1985, Response of alluvial rivers to slow tectonic movement, Geological Society of America, 96, 504-515.
170. Pande, P., 2007, Evaluation of seismotectonics of Kachchh rift basin, Gujarat, India and assessment of seismic hazard potential of the region. PhD Thesis, 144.
171. Pande, P., 2009, The 2001 Bhuj Earthquake, Gujarat, India: Societal Issues and Aspects of Disaster Management. Geological Survey of India (GSI).
172. Pati, J. K., 2005, The Dhala Structure, Bhundelkhand Craton, Central India – A New Large Paleoproterozoic Impact Structure, Meteoritics & Planetary Sciences, Supplement, Proceedings of 68th Annual Meeting of the Meteoritical Society, between 12-16 September in Gatlinburg, Tennessee, 40, 5092.

173. Pati, J. K., Lal, J., Prakash, K. and Bhusan, R., 2008, Spatio-temporal shift of Western bank of the Ganga river Allahabad city and its implications, Journal of Indian Society of Remote sensing, 36, 289-297.
174. Pati, J. K., Malviya, V. P. and Prakash, K., 2006, Basement reactivation and its relation to neotectonic activity in and around Allahabad, Ganga plain, Journal of the Indian Society of Remote Sensing, 34 (1), 47-56.
175. Pedrera, A., Perez-Pena, J. V., Galindo- Zaldivar, J., Azanon, J. M. and Azor, A., 2009, Testing the sensitivity of geomorphic indices in areas of low rate active folding (Eastern Betic Cordillera, Spain), Geomorphology, 105, 218-231.
176. Penck, A. and Bruckner, E., 1909, The Alps in the Ice Age: Leipzing, Tauchnitz, 1199.
177. Philips, L. F. and Schumm, S. A., 1987, Effect of regional slope on drainage networks, Geology, 15, 813-816.
178. Pike, R. J., 1993, A bibliography of geomorphometry, with a topical key to the literature and an introduction to the numerical characterization of topographic form, U.S. Geological Survey Open-file Report, 93-262-A, 132.
179. Pirasteh, S., Mahmoodzadeh, A. and Mahtab, A., 2008, Integration of Geoinformation Technology and Survey Analysis for Development in Mitigation Study against Earthquake: A Case Study for Esfahan Iran, International Disaster Advances Journal, 1 (2), 20-26.
180. Pirasteh, S., Rizvi, S. M. A., Ayazi, M. H. and Mahmoodzadeh, A., 2010, Using Microwave Remote Sensing for Flood study in Bhuj Taluk, Kuchch District Gujarat, India, International Geoinformatics Research and Development Journal, 1 (1), 13-24.
181. Pirasteh, S., Woodbridge, K. and Rizvi, S. M., 2009, Geo-information technology (GiT) and tectonic signatures: the River Karun & Dez, Zagros Orogen in south-west Iran, International Journal of Remote Sensing, 30 (1-2), 389-404.
182. Rabus, B., Eineder, M., Roth, A. and Balmer, R., 2003, The shuttle radar topography mission-a new class of digital elevation models acquired by spaceborne radar, ISPRS Journal of Photogrammetry & Remote Sensing, 57, 241-262.
183. Rai, D. C., Singhal, V., Bhushan, R. S. and Sagar, S. L., 2015, Reconnaissance of the Effect of the M7.8 Gorkha (Nepal) Earthquake of April 25, 2015, Geomatics Natural Hazards and Risk, Taylor & Francis, 7(1), 1-17.
184. Rajendran, C.P., and Rajendran, K., (2001), Characteristics of deformation and past seismicity associated with the 1819 Kutch earthquake, northwestern India, Bulletin of the Seismological Society of America, 91, 407-426p.

185. Rajendran, K. and Rajendran, C. P., 1999, Seismogenesis in the stable continental interiors: An appraisal based on two examples from India, Tectonophysics, 305, 355-370.
186. Rajendran, K., Rajendran, C. P., Thakkar, M. G. and Tuttle, M. P., 2001, The 2001 Kutch (Bhuj) earthquake: Coseismic surface features and their significance, Current Science, 80, 1397-1405.
187. Ramasamy, S. M., 2005, Remote sensing in Geomorphology, New India Phlishing Agency, New Delhi, 276.
188. Ramasamy, S. M., 2006, Remote Sensing and Active Tectonics of South India, International Journal of Remote Sensing, 27 (20), 4397-4431.
189. Ramasamy, S. M., Kumaran, C. J., Selvakumar, R., and Saravanavel, J., 2011, Remote sensing revealed drainage anomalies and related tectonics of South India, Tectonophysics, 501, 41-51.
190. Ramsay, L. A., Walker, R. T. and Jackson, J., 2007, Geomorphic constrains on the active tectonics of Southern Taiwan, Geophysical Journal International, 170, 1357-1372.
191. Rao, D.P., 2002, Remote sensing application in geomorphology, Tropical Ecology, 48, 49-59.
192. Raucoules, D., Colesanti, C. and Carnec, C., 2007, Use of SAR interferometry for detecting and assessing ground subsidence, Comptes Rendus Geoscience, 339(5), 289-302.
193. Rhea, S., 1989, Evidence of uplift near Charleston, South Carolina, Geology, 17, 311-315.
194. Ritter, D. F., Kochel, R. C. and Miller, J. R., 2002, Process geomorphology, McGraw Hill, Boston.
195. Rockwell, T. K., Keller, E. A., Clark, M. N., and Johnson, D. L., 1984, Chronology and rates of faulting of Ventura River terraces, California,. Geological Society of America Bulletin, 95, 1466-1474.
196. Roy, A. B., Chatterjee, A., Chauhan, N. K., Sinha, J. and Rakshit, D., 2012, Satellite imegery study of Kachchh, Western Indian subcontinent: Evidence for fault development and associated landform pattern, Indian Journal of Geosciences, 65(4), 287-296.
197. Sabins, F. F., 2007, Remote Sensing Principles and Interpretations. W. H. Freeman & Co. Publishers, 464.
198. Sabins, F. F., 1997, Remote Sensing: Principles and Interpretation, Third edition, Geological Magazine, Cambridge University Press, New York, 494.
199. Sadybakasov, I., 1990, Neotectonics of High Asia: Moscow, Nauka, 176.

200. Saraf, A. K., Das, J., Biswas, A., Rawat, V., Sharma, K. and Suzat, Y., 2012, SAR interferometry in post-seismic ground deformation detection related to the 2001 Bhuj earthquake, India. International Journal of Remote Sensing, 33, 1296-1308.
201. Satyabala, S. P. and Bilham, R., 2006, Surface deformation and subsurface slip of the 28 March 1999 Mw = 6.4 west Himalayan Chamoli earthquake from InSAR analysis, Geophysical Research Letters, 33, L23305, doi: 10.1029/2006GL027422.
202. Satyabala, S. P., 2006, Coseismic ground deformation due to an intraplate earthquake using synthetic aperture radar interferometry: the Mw 6.1 Killari, India, earthquake of 29 September 1993, Journal of Geophysical Research, 111, B02302, doi: 10.1029/2004JB003434.
203. Scaioni, M., Longoni, L., Melillo, V. and Papini, M., 2014, Remote Sensing for Landslide Investigations: An Overview of Recent Achievements and Perspectives, Remote Sensing, 6, 1-53.
204. Scheidegger, A. E., 1961, Mathematical models of slope development. Geological society of American Bulletin, 72, 37-50.
205. Schmidt, D. A. and Burgmann, R., 2003, Time-dependent land uplift and subsi- dence in the Santa Clara valley, Califoria, from a large interferometric synthetic aperture radar data set, Journal of Geophysics Research, 108.
206. Schumm, S. A., and Khan, H. R., 1972, Experimental study of channel patterns, Geological Society of America, 83, 1755-1770.
207. Seeber, L. and Gotnitz, V., 1983, River profile along the Himalayan Arc as indicators of active tectonics, Tectonophysics, 92, 335-367.
208. Shah, A., Kulkarni, M. N., Tomar, V. S. and Likhar, S., 2004, Some Recent Results from GPS Studies for the January 2001 Bhuj Earthquake, Map Asia Conference 2004.
209. Sharma, K., Saraf, A. K., Das, J. D., Rawat, V. and Shujat, Y. 2010, SRTM and ASTER DEM characteristics of two areas from Himalayan region, International Geoinformatics Research and Development Journal, 1 (3), 25-31.
210. Sharma, V. K., 2001, Gujarat earthquake - some emerging issues. Disaster Prevention and Management, 10, 349-355.
211. Singhroy, V., 1995, SAR integrated techniques for geohazard assessment, Advance Space Research, 15, 67-78.
212. Slaymaker, O., 2001, The role of remote sensing in geomorphology and terrain analysis in the Canadian Cordillera, International Journal of Applied Earth Observation and Geoinformation, 3, 11-17.

213. Smith, M. and Pain, C., 2009, Applications of remote sensing in geomorphology, Progress in Physical Geography, 33, 568-582.
214. Sparling, D. R., 1967, Anomalous drainage pattern and crustal tilting in Ottawa country, Ohio. Ohio Journal of Science, 67, 378-381.
215. Strahler, A. N., 1952, Hypsometric (area–altitude) analysis of erosional topography, Geological Society of America Bulletin, 63, 1117-1142.
216. Stramondo, S., Bignami, C., Chini, M., Pierdicca, N. and Tertulliani, A., 2006, Satellite radar and optical remote sensing for earthquake damage detection: results from different case studies, International Journal of Remote Sensing, 27(20), 4433-4447.
217. Stramondo, S., Chini, M., Salvvi, S. and Bignami, C., 2008, Ground deformation imagery of the May Sichuan earthquake, EOS Transactions American Geophysical Union, 89, 1-2.
218. Stramondo, S., Moro, M., Doumaz, F. and Cinti, F. R., 2005, The 26 December 2003, Bam, Iran earthquake: surface displacement from Envisat ASAR interferometry, International Journal of Remote Sensing, 26, 1027-1034.
219. Sun, G., Ranson, K. J., Kharuk, V. I. and Kovacs K., 2003, Validation of surface height from shuttle radar topographic mission using shuttle laser Altimeter, Remote Sensing of Environment, 88, 401-411.
220. Susan, R., 1993, Geomorphic observations of rivers in the Oregon coast range from a regional reconnaissance perspective, Journal of Geomorphology, 6, 135-150.
221. Tate, A., Muller, K. J. and Golombek, M. P., 2002, Geomatics and kinematics wrinkle ridges of lunae and soils plana Mars: implications for fault/fold growth history, Lunar and Planetary Sciences XXXIII.
222. Thakkar, M. G., Maurya, D. M., Raj, R. and Chamyal, L. S., 1999, Quaternary Tectonic history and terrain evolution of the area around Bhuj, Mainland Kachchh, Western India, Journal of Geological Society of India, 53, 601-610.
223. Tripathi, N. K. and Singh, P., 2000, Integrated GIS and Remote Sensing Approach to Map Pollution in Upper Lake, Bhopal, India, Geocarto International, 15(4), 49-55.
224. Tripathi, N. K. and Soomro, A. S., 2007, A GIS Approach to Tsunami Disaster Risk Zonation, Krabi, Thailand, International journal of Geoinformatics, 3(3): 9-16.
225. Tripathi, N. K., Siddiqi, M.U. and Gokhale, K. V. G. K., 2000, Directional morphological image transforms for lineament extraction from remotely sensed images, International Journal of Remote Sensing, 21(17), 3281-3292.
226. Tronin, A. A., 1996, Satellite thermal survey-A new tool for the studies of seismoactive regions, International Journal of Remote Sensing, 17, 1439-1455.

227. Tronin, A. A., 2006, Remote sensing and earthquakes: A review, Physics and Chemistry of Earth, 31, 138-142.
228. Tronin, A. A., Hayakawa, M. and Molchanov, O. A., 2002, thermal IR satellite data application for earthquake research in Japan and China, Journal of Geodynamics, 33, 519-534.
229. Tsimi, C., Ganas, A., Soulakellis, N., Kairis, O. and Valmis S., 2007, Morphotectonics of the Psathopyrgos active fault, western Corinth Rift, Greece. International Conference of the Geological Society of Greece, Athens 24-26 May 2007.
230. Ulaby, F., 2013, Microwave Radar and Radiometric Remote Sensing, 2nd edition, University of Michigan, USA, 1116.
231. Van Westen, C. J., Castellanos, E. and Kuriakose, S. L., 2008, Spatial data for landslide susceptibility, hazard, and vulnerability assessment: An overview, Engineering geology, 102(3), 112-131.
232. Verrios, S., Zygouri, V. and Kokkalas, S., 2004, Morphotectonic analysis in the Eliki fault zone (Gulf of Cornith, Greece). Bulletin of the Geological society of Greece. V-XXXVI. Proc. 10th International Congress, Thessaloniki, 1706-1715.
233. Verstappen, H. Th., 1977, Remote Sensing in Geomorphology, Elseviers, Amersterdam, 214.
234. Walker, R. and Jackson, J., 2002, Offset and evolution of Gowk fault, S. E. Iran: a major intra continental strike-slip system, Journal of Structural Geology, 24, 1677-1698.
235. Weldon, R. J., 1986, Late Cenozoic geology of Cajon Pass, implication for tectonics and sedimentation along the San Andreas fault (Ph. D. Thesis), California Institute of Technology, Pasadena.
236. Whipple, K. X., and Dunne, T., 1992, Debris flow fans in Owen Valley, California, Geological Society of America, 104, 39-43.
237. Woodhouse, H., 2006, Introduction to Microwave Remote Sensing, First edition, CRC Press, 400.
238. Woodhouse, L. H., 2005, Introduction to Microwave Remote Sensing, Taylor and Francis, New York, 400.
239. Wright, T., Fielding, E. and Parsons, B., 2001, Triggered slip: observations of the 17 August 1999 Izmit (Turkey) earthquake using radar interferometry, Geophysical Research Letter, 28, 1079-1082.

240. Yague-Martinez, N., Prats-Iraola, P., Gonzalez, F. R., Brcic, R., Shau, R., Geudtner, D., Eineder, M. and Bamler, R., 2016, Interferometric Processing of Sentinel-1 TOPS Data, IEEE Transactions on Geoscience and Remote Sensing, 54 (4), 2220-2233.
241. Yarai, H., Ozawa, T., Nishimura, T., Tobita, M. and Imakiire, T., 2004, Crustal deformation associated with the northern Miyagi earthquake detected by RADARSAT-1 and ENVISAT SAR interferometry, Earth, Planets and Space, 56, 103-107.
242. Zebker, H. A., Rosen, P. A. and Hensley, S., 1997, Atmospheric effects in interferometric synthetic aperture radar surface deformation and topographic maps, Journal of Geophysics Research, 102, 7547-7563.
243. Zebker, H. and Goldstein, R., 1986, Topographic Mapping From Interferometric Synthetic Aperture Radar Observations, Journal of Geophysical Research, 91(5), 4993-4999.
244. Zebker, H., Rosen, P. A., Goldstein, R., Gabriel, A. and Werner, C., 1994, On the derivation of coseismic displacement fields using differential radar interferometry: The Landers earthquake, Journal of Geophysical Research, 99 (10), 617-634.
245. Ziqi, G., Guiwen, H. and Shuqing, Q., 2001, Spatial Detect Technology Applied on Earthquake impending Forecast, 22nd Asian Conference on Remote Sensing, 5-9 November 2001, Singapore.
246. Zizioli, D., 2008, DEM based morphotectonic analysis of Western Ligurian Alps., Scientifica Acta, 2 (2), 44-47.

WEB PAGES

URL Links:

1. http:// cct.nrcan.gc.ca/resource/tutor/
2. http:// envisat.esa.int/handbooks/asar/CNTR4.html
3. http:// www.aero.org/.../crosslink/summer2004/04.html
4. http:// www.geocities.com/.../ 8361/Quake2001India.htm
5. http:// www.physics.nus.edu.sg.htm
6. http:// www.radartutorial.eu/20.airborne/ab06.en.html
7. http://asc-india.org/lib/20010126-kachchh.htm
8. http://asc-india.org/seismi/seis-gujarat.htm#3
9. http://doris.tudelft.nl/
10. http://earthexplorer.usgs.gov
11. http://earthquake.usgs.gov/earthquakes/world/historical.php
12. http://en.wikipedia.org/ wiki/Interferometric_Synthetic_aperture_radar
13. http://en.wikipedia.org/wiki/Interferometric_synthetic_aperture_radar
14. http://en.wikipedia.org/wiki/Radar
15. http://envisat.esa.int/instruments/asar/
16. http://glcf.umd.edu/data/landsat/
17. http://gujarat-earthquake.gov.in/final/seismic.html
18. http://landsat.usgs.gov/landsat8.php
19. http://mrs.eecs.umich.edu/sensors.html
20. http://peer.berkeley.edu/pdf/2713_Other200104GujaratEQTR0101.pdf
21. http://pubs.usgs.gov/gip/earthq1/where.html

22. http://pubs.usgs.gov/gip/earthq1/where.html

23. http://pubs.usgs.gov/gip/earthq1/where.html

24. http://srtm.csi.cgiar.org/

25. http://www.esri.com/arcview

26. http://www.globalchange.umich.edu/globalchange1/current/lectures/evolving_earth/evolving_earth.html

27. http://www.gsdma.org/hazard-risk-mitigation-studies/hrva.aspx/ Gujrat online access on 28-04-2017

28. http://www.jpl.nasa.gov/srtm

29. http://www.mapsofindia.com/maps/india/majorearthquake.html

30. http://www.mapsofindia.com/maps/india/majorearthquake.html

31. http://www.photogrammetry.ethz.ch/general/persons/jana/isprs/tutradar/3_radar1_1.ppt

32. http://www.sarproz.com/

33. https://earthengine.google.com/datasets/)

34. https://scihub.copernicus.eu/

35. https://sentinel.esa.int/web/sentinel/toolboxes/sentinel-1

36. https://www.sarproz.com/processing-modules-options/

37. informationOverload-http://informoverload.com/wp-ontent/uploads/2015/05/ASAH_L.jpg

38. informationOverload-http://informoverload.com/wp-ontent/uploads/2015/05/ASAH_L.jpg.

39. USGS- earthquake.usgs.gov

40. USGS-earthquake.usgs.gov

LIST OF PUBLICATIONS OUT OF RESEARCH WORK

Publication in Journals

1. Mohammed Zia, Kanika Sharma, Arun Kumar Saraf, Josodhir Das, **Suman Baral**, Mrinmoy Das (2014) "Ground deformational studies using ALOS PALSAR data between 2007 and 2010 of the central Kutch area, Gujarat, India". Natural Hazards, 71 (3): 1379–1388.
2. **S. S. Baral**, K. Sharma, A. K. Saraf, J. Das, G. Singh, S. Borogohain, E. Kar (2016) "Thermal anomaly from NOAA for Nepal Earthquake". Current Science, 110 (02): 150-153.
3. Eirin Kar, **Suman Sourav Baral**, Arun Kumar Saraf, Josodhir Das, Gaurav Singh, Susanta Borogohain (2016) "Remote Sensing and GIS based analysis of Geomorphic Evidences and Morphometry of active faults in Kachchh area". Indian Society of Remote Sensing, doi:10.1007/s12524-016-0588-z.
4. **Baral, S. S**., Das, J., Saraf, A. K., Borgohain, S. and Singh, G. (2016) "Comparison of Cartosat, ASTER and SRTM DEMs of Different Terrains" Asian Journal of Geoinformatics, 16 (1): 1-7.
5. S. Borgohain, J. Das, A. K. Saraf, G. Singh and **S. S. Baral** (2016) "Morph dynamic Changes of Lohit River, NE India: GIS Based Study". Current Science, 110 (09):1810-1816.
6. S. Borogohain, J. Das, A. K. Saraf, G. Singh, **S. S. Baral** (2017) "Structural controls on topography and river morphodynamics in Upper Assam Valley, India ". Geodinimica Acta, 29(1):62-69.
7. **Baral, S. S**., Das, J., Saraf, A. K., Borgohain, S. and Singh, G. "InSAR and PS based post-earthquake surface deformation studies for Kutch and the expected neo-tectonic activity", Manuscript Submitted.

Published Articles

1. K. Sharma, A. K. Saraf, J. Das, **Suman S. Baral**, S. Borgohain, G. Singh (2016) "Change Detection Study of Nepal-2015 Earthquakes Induced Landslides" Manuscript Article published in BHOO-KAMPAN, "Indian Society of Earthquake Science".

Conference and Seminars

1. Participated in the National GeoResearch Scholars Meet 2016 (NGEOSM2016) during June 1-4, 2016 at Wadia Institute of Himalayan Geology, Dehradun, India followed by an

Oral Presentation on “InSAR Technique in post-earthquake surface deformation studies for Bhuj and the expected neo-tectonic activity”.

2. Presented the Research Paper entitled “Morph dynamic Changes of Lohit River, NE India: GIS Based Study" in National conference-2014 organized by Mizoram University, India.
3. Presented the Research Paper entitled “Flood Induced Changes in Kedarnath Valley (Uttarakhand) Using Remote Sensing and GIS” in National conference-2014 organized by Mizoram University, India.
4. Attended National Conference “ESICET” organized by IIT Roorkee held in November 2011 for 10days.
5. Presented the Research Paper entitled “Comparison of DEM for different terrain in India” in ESICET, IIT Roorkee November 2011.